UNIVERSIDAD COMPLUTENSE DE MADRID

FACULTAD DE CIENCIAS FÍSICAS
Departamento de Física Teórica II

PROPIEDADES ESPECTRALES, TRANSPORTE, Y NO EQUILIBRIO QUÍMICO EN GASES DE MESONES LIGEROS.

MEMORIA PARA OPTAR AL GRADO DE DOCTOR

PRESENTADA POR

Daniel Fernández Fraile

Bajo la dirección del doctor

Ángel Gómez Nicola

Madrid, 2010

- **ISBN: 978-84-693-3475-1**

Propiedades espectrales, transporte, y no-equilibrio químico en gases de mesones ligeros

Daniel Fernández Fraile

Memoria de Tesis Doctoral presentada al Departamento de Física Teórica II para optar al grado de Doctor en Física

Tesis doctoral dirigida por el Dr. Ángel Gómez Nicola

Departamento de Física Teórica II
Universidad Complutense de Madrid

2009

A mi madre,
que deseaba estar presente el día de la defensa de esta tesis,
con cariño.

Agradecimientos

Agradezco a mis padres y a mi hermana el apoyo que he recibido por su parte durante todos estos años. Esta tesis es en gran medida un logro suyo también. Quiero agradecer además a mi profesor del instituto y buen amigo Carlos González Blanco el haberme enseñado de forma tan auténtica sobre ciencia, en particular física, y haberme apoyado desde entonces.

A mi director de tesis, Ángel, y a Ramón Fernández Álvarez-Estrada, les agradezco mucho el haberme ofrecido la oportunidad de realizar un doctorado en una disciplina tan bonita como es la física teórica de partículas. Ángel ha sido un director de tesis estupendo, apoyándome y mostrándose comprensivo en todo momento. Los temas de física en los que me ha introducido han despertado en mí un gran interés, y espero que sigamos colaborando estrechamente en el futuro.

Estoy encantado de haber tenido durante estos años un gran número de discusiones científicas e intercambio de ideas con mis colaboradores Daniel Cabrera Urbán, Kevin Dusling, Ramón Fernández Álvarez-Estrada, Ángel Gómez Nicola, Dima Kharzeev, Rob Pisarski, Elena Tomás Herruzo, y Raju Venugopalan.

Finalmente, quiero hacer especial mención a los compañeros de los Departamentos de Física Teórica I y II de la Universidad Complutense de Madrid, a mis familiares, y al resto de mis amigos. Todos ellos han influido de forma muy positiva en mí.

Índice general

Resumen

R.1 Introducción

Esta tesis está constituida por tres líneas principales de investigación: resonancias, coeficientes de transporte, y no-equilibrio químico en el gas de mesones. En los Capítulos 2, 3, y 4 se discuten en gran detalle cada uno de estos temas. El tratamiento presentado es en principio válido para un gas de mesones compuesto por varias especies (piones, kaones, etas, y las correspondientes resonancias), pero nuestra exposición se particularizará para el caso más simple en el que los grados de libertad del gas son piones, sigmas ($f_0(600)$), y rhos ($\rho(770)$) únicamente[1]. Nuestro análisis se llevará a cabo en el contexto de la Teoría de Perturbaciones Quiral (ChPT), que es una teoría de campos efectiva para QCD en el régimen de bajas energías y temperaturas (por debajo de la transición de fase quiral).

En primer lugar, en el Capítulo 1, repasamos parte del material necesario para entender los resultados presentados en los capítulos sucesivos. Se hace especial énfasis en la teoría cuántica de campos a temperatura finita (Sección 1.4), así como en coeficientes de transporte, siendo este último punto descrito tanto desde el punto de vista de teoría cinética como desde el punto de vista de teoría de campos (Secciones 1.5 y 1.6 respectivamente).

En el Capítulo 2 presentamos nuestro análisis de resonancias térmicas en el gas de mesones. Discutimos ahí la necesidad de unitarizar las amplitudes de dispersión de Teoría de Perturbaciones Quiral para poder reproducir resonancias. El comportamiento con la temperatura y la densidad nuclear de las resonancias presentes en el gas de piones es analizado. Empleamos dos métodos distintos para incorporar densidad nuclear: por un lado el re-escaleo de la constante de desintegración del pión F_π, y por otro lado un método diagramático más preciso basado en la ecuación de Bethe-Salpeter. También analizamos la naturaleza "molecular" de estas resonancias, así como la relación entre su evolución en el medio y la restauración de la simetría quiral. Como aplicaciones de este análisis, comparamos con resultados experimentales sobre aumento en el umbral de amplitudes de dispersión, y comentamos sobre la relación entre la evolución en el medio de la ρ y la producción de dileptones.

En el Capítulo 3 desarrollamos un método diagramático para calcular coeficientes de

[1]El caso con número de sabores igual a tres es técnicamente más complicado, pero a su vez es también más interesante desde el punto de vista fenomenológico para temperaturas cercanas a la transición de fase quiral, donde todos los mesones ligeros juegan un papel importante. Para temperaturas bajas, el gas de piones constituye una buena aproximación.

transporte en el contexto de la Teoría de Perturbaciones Quiral. Comenzamos repasando resultados previos sobre el cálculo de coeficientes de transporte en teoría cinética, en teorías escalares de campos, y en teorías gauge a temperaturas altas, y establecemos la conexión con nuestro análisis diagramático para el gas de mesones a temperaturas bajas. Posteriormente, en la Sección 3.3, presentamos el análisis general de diagramas en ChPT para el cálculo de coeficientes de transporte, que nos permitirá obtener en las siguientes secciones la contribución dominante a la conductividad eléctrica DC, la conductividad térmica, la viscosidad de cizalla, y a la viscosidad de volumen. Analizamos también varias aplicaciones fenomenológicas de los resultados obtenidos para coeficientes de transporte, tales como la conexión entre la conductividad DC y el espectro de fotones de baja energía, la verificación de la cota inferior propuesta para el cociente η/s, la relación entre la anomalía de traza y la viscosidad de volumen, y un análisis en el límite de gran $N_{\rm c}$ que proporciona una comprobación de la consistencia de nuestros resultados.

Finalmente, en el Capítulo 4, analizamos el régimen de no-equilibrio químico para el gas de mesones. Se asume que el número de mesones es (aproximadamente) conservado, de modo que debe introducirse un potencial químico asociado a esta carga. Esta aproximación es válida por ejemplo en el contexto de una colisión de iones pesados, donde el equilibrio químico en el gas de hadrones es perdido (a la temperatura de "freeze-out" químico $T_{\rm CFO}$) antes de que se alcance el "freeze-out" térmico (a $T_{\rm TFO} < T_{\rm CFO}$), de modo que el número de mesones es aproximadamente conservado durante ese intervalo de temperaturas. Puesto que los mesones (piones en nuestro caso) corresponden a campos escalares neutros, es necesario modificar las reglas de Feynman estándar de temperatura finita para poder tener en cuenta esta situación fuera del equilibrio. Este punto es analizado en la Sección 4.2 en términos del formalismo de integrales de camino holomorfas. Una vez que las reglas de Feynman han sido deducidas, en la Sección 4.3 se calculan fuera del equilibrio químico para un gas de piones algunas cantidades de interés fenomenológico: la función de partición (y algunas otras cantidades termodinámicas derivadas de ella, como por ejemplo la presión y el condensado quiral), y la auto-energía del pión (masa térmica y anchura).

Al final de cada uno de los capítulos 2, 3, y 4 incluimos una sección donde se resumen las principales conclusiones del mismo. Además, tras el Capítulo 4, hay una sección que repasa los puntos principales de esta tesis y comenta posibles líneas de investigación para el futuro relacionadas con el material aquí presentado. Finalmente, en los cuatro apéndices se pueden encontrar varias fórmulas complementarias, otros detalles técnicos, aclaraciones sobre la notación empleada, y una lista de las abreviaturas usadas.

Los análisis y resultados presentados en esta tesis han sido esencialmente recogidos en los trabajos [FF06, GN07, FF07c, FF07a, FF07b, Cab08, FF09b, FF09c, FF09a].

A continuación, presentamos un resumen de esta tesis estructurado en secciones que se corresponden directamente con los Capítulos 2, 3, y 4 de la misma. Muchos detalles y aspectos técnicos han sido omitidos, por lo que se remite al lector al correspondiente capítulo de la tesis para una explicación más detallada.

R.2 Propiedades espectrales de resonancias térmicas y simetría quiral

Las resonancias mesónicas más ligeras, la $\rho(770)$ y la $f_0(600)$ ó σ, juegan un papel crucial en diferentes fenómenos relacionados con la materia caliente y/o densa creada en experimentos de colisiones de iones pesados y de materia nuclear. Por un lado, las modificaciones de la función espectral de la resonancia ρ son cruciales para entender correctamente la emisión de dileptones en este tipo de experimentos [Aga05, Arn06a]. A este respecto, los dos principales escenarios teóricos propuestos en la literatura pueden clasificarse en un cambio de la masa de esta resonancia, y en un ensanchamiento de la misma, de acuerdo con el efecto dominante resultante. Los modelos de cambio de la masa están inspirados por la hipótesis de escaleo de Brown-Rho (BR) [Bro91], que predice que las masas de los mesones vectoriales debe escalear del mismo modo que el condensado de quarks y por lo tanto, la principal modificación espectral de la resonancia estaría dictada por la restauración de la simetría quiral. Por su parte, el escenario de ensanchamiento es respaldado mediante diferentes análisis teóricos [Her92, Pis95, Pet98, Rap97, Rap00], incluyendo tratamientos quirales unitarizados [Cab02, Dob02]. Los resultados experimentales parecen favorecer el escenario de ensanchamiento [Aga05, Arn06a, Nas07], aunque la reducción en la masa podría también ser apreciable [Ada04b, Aga05, Nar06].

Por otro lado, la posible modificación en el medio de la resonancia $f_0(600)/\sigma$ es interesante porque este estado tiene los mismos números cuánticos que el vacío y por lo tanto sería sensible a la restauración de la simetría quiral. En este sentido, una propuesta inicial [Hat85] sugería que la σ podría dar lugar a un aumento de la sección eficaz de dispersión $\pi\pi$ debido a su posible acercamiento al eje real cuando se encuentra cerca del umbral, que podría ser interpretado como une señal precursora de la restauración de la simetría quiral. En este argumento se asume implícitamente i) que la σ es dominada por su componente $\bar{q}q$ de modo que su valor esperado se comporta como el condensado de quarks y ii) que la σ es lo suficientemente estrecha como para que su anchura se anule cuando su masa se aproxima al umbral. Ninguna de estas suposiciones previas parecen estar respaldadas por los datos experimentales referentes al estado $f_0(600)$ registrado en el Particle Data Group [Ams08], que es medido en dispersión de piones y resulta tener una anchura de desintegración grande. Aunque es comúnmente aceptado que este estado es miembro del nonete escalar, su naturaleza $\bar{q}q$ ha sido criticada en base a resultados del retículo [Alf00] y a análisis de gran-N_c [Pel04]. De hecho, es de esperar que el estado físico contenga una componente importante no-$\bar{q}q$ del tipo tetraquark, glueball o mesón-mesón, esta última comúnmente referida como un estado "molecular" (estado ligado $\pi\pi$). Sin embargo, el aumento de las amplitudes de dispersión en el umbral sí es observado en experimentos de materia nuclear a densidades altas, en reacciones $\pi A \to \pi\pi A'$ [Bon00, Sta00] y en $\gamma A \to \pi\pi A'$ [Mes02], especialmente en el canal escalar. Sin embargo, análisis de temperatura finita muestran que este estado permanece ancho incluso cerca de la transición de fase a pesar de la proximidad del polo al umbral de dos piones [Pat03, Hid04], lo cual no produce en la práctica aumento de la sección eficaz en el umbral. Otro efecto de gran interés a ser explorado es la posibilidad de que al incrementar la influencia del medio, bien aumentando considerablemente la densidad o la temperatura, la σ pudiera convertirse en

un estado ligado $\pi\pi$, como fue sugerido en [Sch88] y confirmado recientemente en otros trabajos [Pat03, Hid04].

A continuación analizamos estos aspectos de las resonancias σ y ρ en el contexto de la Teoría de Perturbaciones Quiral unitarizada.

R.2.1 Resonancias a temperatura finita con el IAM

Uno de los métodos más simples y potentes de unitarización para teorías quirales es el llamado Método de la Amplitud Inversa (IAM) [Dob90, Dob93, Dob97]. Su nombre se debe al hecho de que el requerimiento de unitariedad implica la siguiente condición sobre el inverso la amplitud t_{IJ} asociada a una onda parcial en el proceso de dispersión $\pi\pi \to \pi\pi$:

$$\hat{S}^\dagger \hat{S} = 1 \quad \Rightarrow \quad \mathrm{Im}\, t_{IJ}(s) = \sigma_0(s)|t_{IJ}(s)|^2 \quad \Rightarrow \quad \mathrm{Im}\, \frac{1}{t_{IJ}(s)} = -\sigma_0(s) \ , \tag{R.1}$$

para $s > 4M_\pi^2$, donde s es la energía de c.m. al cuadrado y $\sigma_0(s) = \sqrt{1-4M_\pi^2/s}$ es el espacio de fases de dos piones. Consideremos el desarrollo de ChPT para las ondas parciales

$$t_{IJ}(s) = t_{IJ}^{(2)}(s) + t_{IJ}^{(4)}(s) + \mathcal{O}(p^6) \ , \tag{R.2}$$

donde I denota el isospín, J el momento angular orbital, p denota genéricamente un momento de mesón, masa o temperatura (p debe ser pequeño comparado con la escala quiral $\Lambda_\chi \sim 1$ GeV, mientras que la temperatura T debe estar por debajo de la temperatura crítica $T_c \sim 200$ MeV), y $t_{IJ}^{(k)}$ es la contribución de orden $\mathcal{O}(p^k)$. Para las energías y temperaturas de interés aquí, sólo las ondas parciales que involucran $J \leq 1$ son relevantes. De acuerdo con el contaje estándar de ChPT, $t^{(2)}$ corresponde a los diagramas a nivel árbol obtenidos a partir del lagrangiano $\mathcal{L}_2$. Esta amplitud de orden más bajo es independiente de la temperatura, y tiene la siguiente forma:

$$t_{IJ}^{(2)}(s) = A_{IJ}(s - s_2^{IJ}) \ , \qquad \begin{array}{|c|c|c|} \hline IJ & 16\pi F_\pi^2 A_{IJ} & s_2^{IJ}/M_\pi^2 \\ \hline 00 & 1 & 1/2 \\ 11 & 1/6 & 4 \\ 20 & -1/2 & 2 \\ \hline \end{array} \tag{R.3}$$

donde s_2 es el llamado cero de Adler (el punto donde la amplitud se anula) a segundo orden. A este orden, la amplitud depende únicamente de la masa del pión $M_\pi \simeq 140$ MeV y de su constante de desintegración $F_\pi \simeq 93$ MeV. El orden $t^{(4)}$ incluye diagramas a un lazo provenientes de $\mathcal{L}_2$ y los diagramas a nivel árbol de $\mathcal{L}_4$ que son necesarios para renormalizar las divergencias que surgen de los primeros.

La expansión quiral (R.2) satisface sólo perturbativamente la relación de unitariedad (R.1), esto es,

$$\mathrm{Im}\, t_{IJ}^{(4)}(s) = \sigma_0(s)|t_{IJ}^{(2)}(s)|^2 \ , \tag{R.4}$$

y análogamente para órdenes superiores, lo que significa que, eventualmente, los desarrollos quirales no son compatibles con las cotas impuestas por unitariedad sobre las ondas

parciales. Esto implica en particular que las resonancias no son correctamente reproducidas por estas ondas parciales. Los métodos de unitarización en cambio, permiten construir amplitudes quirales que respetan de forma exacta unitariedad, a su vez demandando que a energías bajas se reproduzca la expansión quiral estándar. De acuerdo con el IAM, las ondas parciales unitarizadas a orden $\mathcal{O}(p^4)$ están dadas por

$$t_{IJ}^{\mathrm{U}}(s) = \frac{\left[t_{IJ}^{(2)}(s)\right]^2}{t_{IJ}^{(2)}(s) - t_{IJ}^{(4)}(s)} \ . \tag{R.5}$$

En cuanto a las resonancias, además de aparecer como picos en la sección eficaz de dispersión, también son identificadas como polos en la amplitud de dispersión continuada a la segunda hoja de Riemann (SRS), definida a partir de la amplitud en la primera hoja como $\mathrm{Im}\, t^{(\mathrm{II})}(s - \mathrm{i}0^+) = \mathrm{Im}\, t^{(\mathrm{I})}(s + \mathrm{i}0^+)$, para $s > 4M_\pi^2$. En el caso de la amplitud (R.5), su continuación analítica a la SRS viene dada por

$$t^{(\mathrm{II})}(s) = \frac{t^{(\mathrm{I})}(s)}{1 - \mathrm{i}2\sigma_0(s)t^{(\mathrm{I})}(s)} \ . \tag{R.6}$$

La masa y anchura de la correspondiente resonancia vienen dadas en términos de la posición del polo en la SRS como $s_{\mathrm{polo}} = (M_{\mathrm{R}} - \mathrm{i}\Gamma_{\mathrm{R}}/2)^2$ [Ams08].

Hay sin embargo un requerimiento técnico extra para estas amplitudes unitarizadas, y es que las amplitudes del IAM deben anularse en los mismos valores de energía y con la mismas potencias que las amplitudes perturbativas. Estos valores son los llamados ceros de Adler y se encuentran por debajo del umbral. Puesto que un cero en la amplitud corresponde a un polo en la amplitud inversa, esto afecta a la estructura analítica de $1/t$. Tener en cuenta esta corrección es importante cuando se trata con efectos del medio que pueden llevar los polos al eje real cerca del umbral, ya que de otro modo habría polos espurios en ambas hojas de Riemann por debajo del umbral.

El IAM se puede extender a temperatura finita incluyendo correcciones térmicas a la amplitud de dispersión, que han sido calculadas en [GN02b] a orden un lazo en ChPT. La relación de unitariedad (R.4) permanece válida reemplazando en el caso térmico $\sigma_0 \mapsto \sigma_T(s) \equiv \sigma_0(s)[1 + 2n_{\mathrm{B}}(\sqrt{s}/2)]$, con $n_{\mathrm{B}}(x) \equiv [\exp(x/T) - 1]^{-1}$ (distribución de Bose-Einstein). Finalmente, teniendo en cuenta los efectos mencionados en el párrafo anterior, uno obtiene la siguiente expresión para las ondas parciales térmicas unitarizadas:

$$\begin{aligned} t^{\mathrm{IAM}} &= \frac{(t^{(2)}(s))^2}{t^{(2)}(s) - t^{(4)}(s,T) + A(s,T)} \ , \\ \text{con} \quad A(s,T) &\equiv t^{(4)}(s_2,T) - \frac{(s_2 - s_4)(s - s_2)}{s - s_4}\left[t^{(2)\prime}(s_2) - t^{(4)\prime}(s_2,T)\right] \ , \end{aligned} \tag{R.7}$$

donde la función A corresponde a la contribución del cero de Adler, s_k denota el cero de Adler (que depende de T para $k > 2$) a $\mathcal{O}(p^k)$, con $s_4 = s_2 - t^{(4)}(s_2,T)/t^{(2)\prime}(s_2)$.

Realizando la continuación analítica de esta amplitud unitarizada a la SRS, encontramos polos en los canales $I = J = 0$ y $I = J = 1$, que son identificados como las resonancias $f_0(600)$ y $\rho(770)$ respectivamente. En la Figura R.1 mostramos los resultados

de la posición de los polos para varias temperaturas. Observamos que el polo de la ρ muestra un comportamiento predominante de ensanchamiento. Por otro lado, la σ experimenta un importante decrecimiento en su masa, presumiblemente debido a la restauración de la simetría quiral, mientras que su anchura aumenta para temperaturas bajas pero decrece a partir de $T \simeq 100$ MeV.

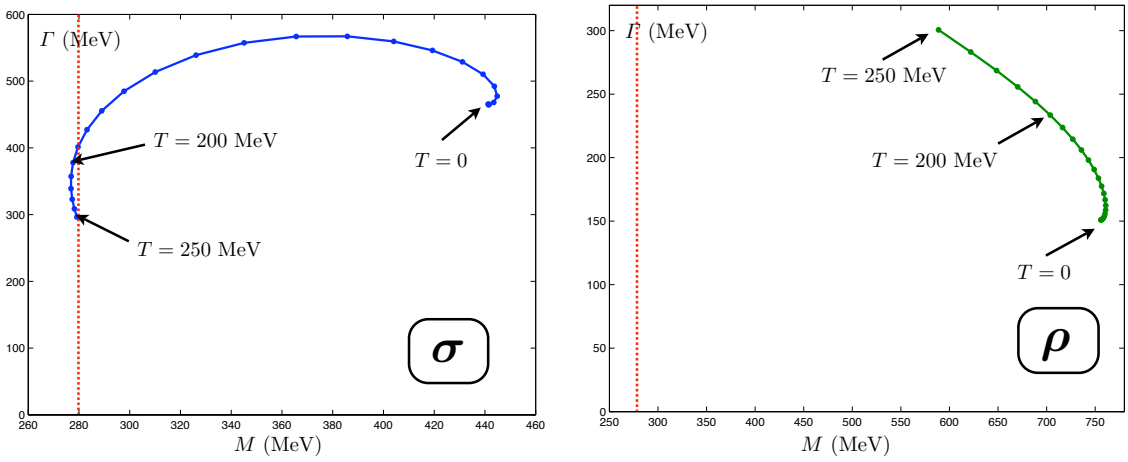

Figura R.1: Dependencia con la temperatura de los polos complejos correspondientes a la $f_0(600)$ y la ρ, obtenidos unitarizando mediante el IAM. Los puntos son obtenidos variando la temperatura en intervalos de 10 MeV.

El mesón ρ a temperatura finita: ensanchamiento frente a escaleo de la masa en dispersión $\pi\pi$ y sondas de dileptones

El polo correspondiente a la ρ obtenido en nuestro tratamiento con el IAM a temperatura finita experimenta un significativo ensanchamiento. La principal fuente de este ensanchamiento es el incremento del espacio de fases térmico debido a la presencia del factor de Bose-Einstein. Sin embargo, este no es el único efecto, de hecho, usando la parametrización Breit-Wigner ($\Gamma_{\rm p} \ll M_{\rm p}$) para el intercambio de una ρ en $\pi\pi \to \rho \to \pi\pi$, uno obtiene [Dob02]:

$$\frac{\Gamma_T}{\Gamma_0} = [1 + 2n_{\rm B}(M_T/2)]\ \frac{g_T^2 M_T}{g_0^2 M_0}\ , \tag{R.8}$$

donde g es el vértice efectivo $\rho\pi\pi$. En la Figura R.2 (izquierda) mostramos en detalle la dependencia con la temperatura de la masa, anchura, y vértice efectivo, y claramente se observa que la anchura aumenta aproximadamente según el espacio de fases hasta $T \simeq 100$ MeV y a partir de ahí el ensanchamiento se debe al aumento del vértice efectivo $\rho\pi\pi$. Este ensanchamiento está también presente en el factor de forma electromagnético del pión [GN05], que entra directamente en el ritmo de emisión de dileptones. Nuestro resultado es por tanto compatible con el escenario de ensanchamiento observado claramente por la colaboración NA60 [Arn06a]. La masa del polo cambia muy poco en nuestro caso. Esto parece contradecir el escenario según el cual la masa decrece del mismo modo que el condensado de quarks $M_T/M_0 \simeq \langle\bar{q}q\rangle_T/\langle\bar{q}q\rangle_0$ [Bro91, Bro05b]. Sin embargo, es importante

mencionar que análisis más recientes basados en la misma hipótesis de escaleo [Har06, Bro05a, Bro05b] sugieren que el decrecimiento de la masa podría hacerse efectivo sólo muy cerca de la temperatura de transición, lo que en la práctica significaría que esas predicciones no son estrictamente incompatibles con los datos de dileptones.

Con el objetivo de clarificar nuestros resultados con respecto a este punto, hemos representado también en la Figura R.2 (derecha) la masa del polo y el condensado de quarks calculado a partir de la expansión del virial [Dob99] usando las amplitudes de dispersión de piones a $\mathcal{O}(p^4)$, que dan una temperatura crítica de $T_c \simeq 230$ MeV. No observamos un patrón de escaleo para la masa análogo al del condensado, además, $T_0 \simeq 310$ MeV permanece lejos del valor crítico donde el condensado se anula.

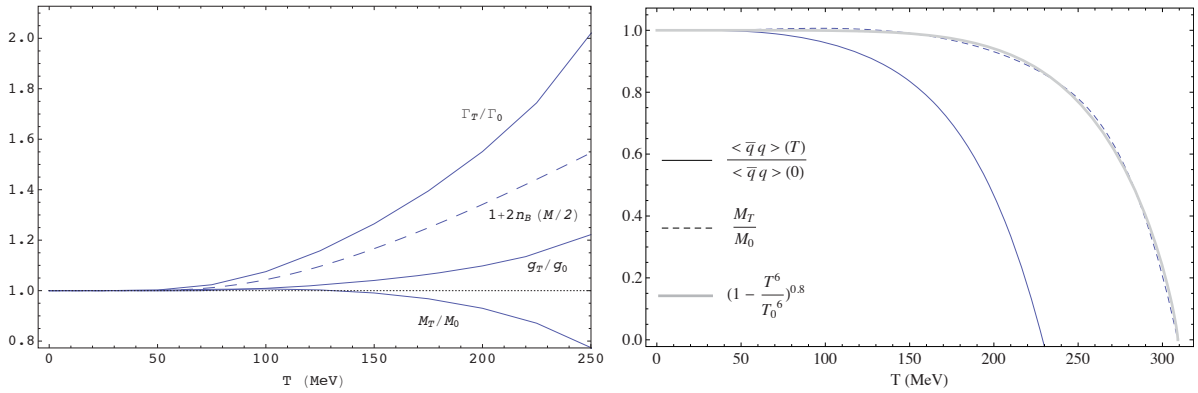

Figura R.2: Masa y anchura térmicas de la ρ obtenidas a partir de su polo en el IAM. En el gráfico de la izquierda también representamos la dependencia con T del vértice efectivo $\rho\pi\pi$. En el gráfico de la derecha comparamos la masa con el condensado de quarks. La masa se anula a $T_0 \simeq 310$ MeV.

El mesón $f_0(600)/\sigma$ térmico: comportamiento en el umbral y naturaleza $\bar{q}q$

La dependencia con la temperatura que obtenemos en la Figura R.1 muestra que la masa decrece significativamente en este canal, indicando restauración de la simetría quiral. De hecho, este es en este caso el efecto dominante para temperaturas $T \simeq 100$ MeV y superiores, por encima del aumento del espacio de fases térmico. Sin embargo, el polo permanece ancho incluso cuando su parte real ha alcanzado el umbral de dos piones.

Para un estado ancho como $f_0(600)$ a temperatura finita siempre hay una rivalidad entre los efectos de aumento del espacio de fases térmico, que no está relacionado con la restauración de la simetría quiral, y el decrecimiento de la masa y anchura debidos a la propia simetría. Dependiendo de cómo de ancha la resonancia sea, los efectos de restauración de simetría jugarán un papel más o menos importante, y el polo se moverá más o menos deprisa hacia el umbral. No hay modo de saber a priori si se localizará suficientemente próxima al eje real cerca de la transición de fase de modo que los efectos de aumento en la sección eficaz en el umbral sean apreciables. Como hemos visto, según nuestro método, esto no ocurre a temperatura finita, aunque la situación puede cambiar a densidad finita, como veremos en breve.

El papel del polo de la σ como precursor de la transición está fuertemente ligado a su naturaleza $\bar{q}q$. En la Figura R.3 comparamos la masa del polo con la raíz cuadrada del condensado de quarks, del mismo modo que hicimos en el caso de la ρ. Recuérdese que, en un modelo $O(4)$, $M_\sigma \sim \langle\sigma\rangle \sim F_\pi$ y, por otro lado, $F_\pi^2 = -m_{\rm q}\langle\bar{q}q\rangle/M_\pi^2$ a partir de la relación de Gell-Mann-Oakes Renner (GOR) [GM68]. También representamos los resultados próximos al límite quiral, para los que el condensado se anula a temperaturas más bajas y los efectos de ruptura explícita de la simetría son reducidos considerablemente. En cualquier caso, no observamos un patrón de escaleo según el condensado, como era de esperar a partir de nuestros resultados de un estado con anchura térmica grande. Cerca del límite quiral, la masa del polo ni siquiera llega al umbral cerca de la temperatura crítica, dado que la anchura térmica es aumentada notablemente debido al hecho de que hay mayor espacio de fases disponible. A partir de nuestro análisis de los efectos térmicos, podemos también concluir que la componente no-$\bar{q}q$ de la resonancia $f_0(600)$ debe ser de crucial importancia. Esta misma conclusión ha sido alcanzada en otros estudios [Alf00, Pel04]. La novedad aquí es el uso de argumentos térmicos. A continuación veremos que los efectos de densidad finita, que llevan a los polos de las resonancias por debajo del umbral, permiten también extraer conclusiones interesantes acerca de su naturaleza $\bar{q}q$.

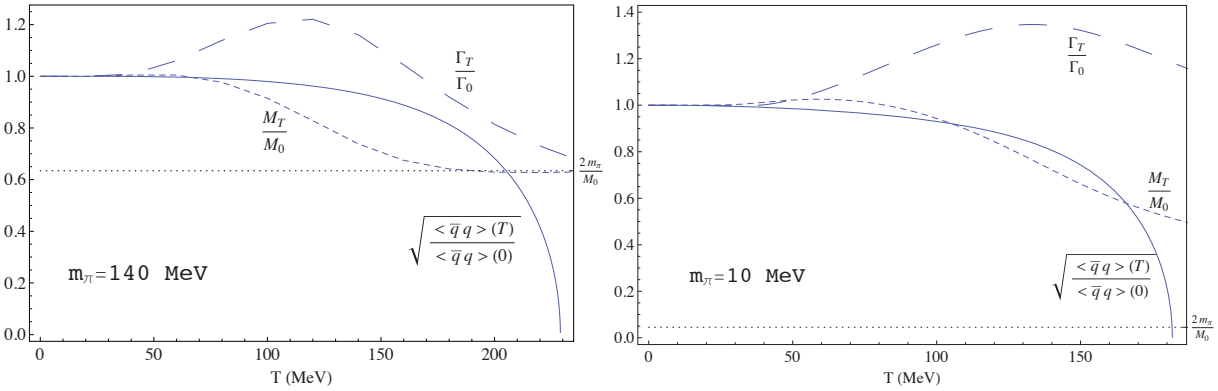

Figura R.3: Comparación entre la masa de la $\sigma/f_0(600)$ extraída a partir del polo IAM a temperatura finita y la raíz del condensado, para la masa física del pión (izquierda) y cerca del límite quiral (derecha).

R.2.2 Efectos de restauración de la simetría quiral a densidad finita y $T = 0$ a través del escaleo de F_π en el IAM

El modo más simple de incorporar efectos de densidad nuclear finita a $T = 0$ en el contexto de teoría quiral unitarizada es, de modo efectivo a orden lineal en la densidad, mediante la variación del valor de la constante de desintegración del pión según la relación de GOR a densidad finita [Tho95, Mei02]:

$$\frac{F_\pi^2(\rho)}{F_\pi^2(0)} \simeq \frac{\langle\bar{q}q\rangle(\rho)}{\langle\bar{q}q\rangle(0)} \simeq \left(1 - \frac{\sigma_{\pi N}}{M_\pi^2 F_\pi^2(0)}\rho\right) \simeq \left(1 - 0{,}35\frac{\rho}{\rho_0}\right) \ , \qquad \text{(R.9)}$$

donde ρ es la densidad nuclear, $\sigma_{\pi N} \simeq 45$ MeV es el término sigma de la interacción pion-nucleón y $\rho_0 \simeq 0{,}17$ fm^{-3} es la densidad de saturación nuclear. Por lo tanto, variando F_π en

nuestro análisis con el IAM, simulamos efectos de restauración quiral debidos a densidad nuclear. Este método ignora correcciones de interacción de muchos cuerpos, como el acoplo de piones a excitaciones partícula-agujero (ph) y Delta-agujero (Δh). Esta aproximación es más adecuada para la σ que para la ρ puesto que, como hemos visto a temperatura finita, la restauración de la simetría quiral tiende a dominar el comportamiento del polo de la σ bajo la influencia de efectos del medio. De hecho, cambiando sólo F_π, no se produce ensanchamiento debido al medio, lo cual probablemente no es realista en el caso de la ρ, como se ha enfatizado en otros trabajos que tienen en cuenta la interacción de muchos cuerpos [Her92, Pet98, Cab02]. Esto debe tenerse en cuenta al interpretar nuestros resultados usando (R.9) para la ρ en términos de escaleo BR.

En las Figuras R.4 y R.5, mostramos los resultados obtenidos variando F_π en las amplitudes del IAM para las trayectorias de los polos en el plano complejo y el escaleo de la masa respectivamente en los canales $IJ = 00, 11$. En la Figura R.6 (derecha) también mostramos el efecto sobre la amplitud de dispersión en el canal de la σ. A medida que F_π decrece, el polo de la σ se vuelve lo suficientemente estrecho como para que la reducción en la masa debida a la restauración quiral lo lleve al eje real, lo cual produce aumento de la amplitud en el umbral, aunque a densidades considerablemente superiores a ρ_0. En relación con la reducción en la masa, se produce ahora de forma análoga a la variación del condensado (ver Fig. R.5). En la Figura R.7 mostramos $|t_{00}|^2$ considerando simultáneamente efectos de temperatura y densidad según Eq. (R.9) para F_π. Observamos que el efecto neto de introducir la temperatura es, por un lado, un ensanchamiento efectivo de las amplitudes de dispersión, como era de esperar a partir de los argumentos de espacio de fase térmico comentados anteriormente. Por otro lado, para un valor dado de F_π (suficientemente pequeño), la temperatura amplifica el aumento en el umbral, dado que la amplitud es suavizada notablemente a energías más altas, lo que hace que la región de energías bajas sea relativamente más importante.

En el caso del canal de la ρ, ahora sí sigue el patrón de escaleo de tipo BR. De hecho, nuestro polo para el mesón ρ se mueve gradualmente desde la curva $\langle\bar{q}q\rangle^{1/2}$ a la curva $\langle\bar{q}q\rangle$, como se ha obtenido en [Bro04]. Sin embargo, uno debe ser cauteloso sobre esta conclusión, ya que estamos ignorando efectos de ensanchamiento debidos al medio que podrían cambiar esta imagen de escaleo que hemos obtenido.

Comparación con experimentos de materia nuclear

Como hemos comentado anteriormente, además de los experimentos de colisiones relativistas de iones pesados, hay otros experimentos dedicados a las reacciones de producción en núcleos donde nuestro análisis puede ser de utilidad. En concreto, en experimentos relacionados con aumento en el umbral de la sección eficaz de producción de pares de piones, y en la modificación del espectro de dileptones producido a partir de desintegraciones de ρ's. El aumento en el umbral observado en [Bon00, Sta00, Mes02] para el canal $I = J = 0$ es reproducido cualitativamente con nuestro método variando F_π para emular los efectos de densidad. Comparando con nuestro análisis de temperatura finita, nuestra principal conclusión es que, debido a la naturaleza ancha de la σ a temperatura finita, el aumento en el umbral no es visible a T finita y sólo puede tener lugar si los efectos de restauración quiral debidos a densidad nuclear son suficientemente intensos, comparados por

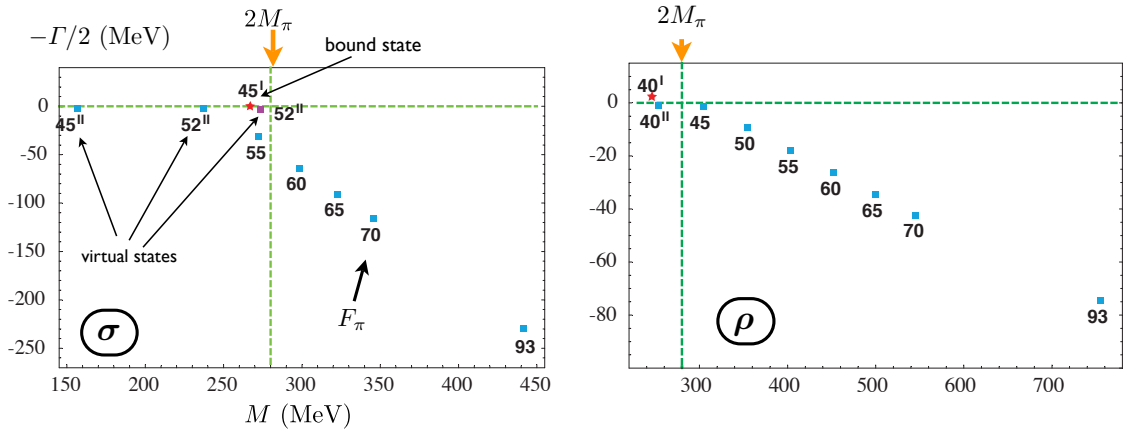

Figura R.4: Polos en el IAM variando F_π. Los números junto a las posiciones de los polos indican el valor de $F_\pi(\rho)$ en MeV según (R.9). Los polos en la primera y segunda hoja están indicados.

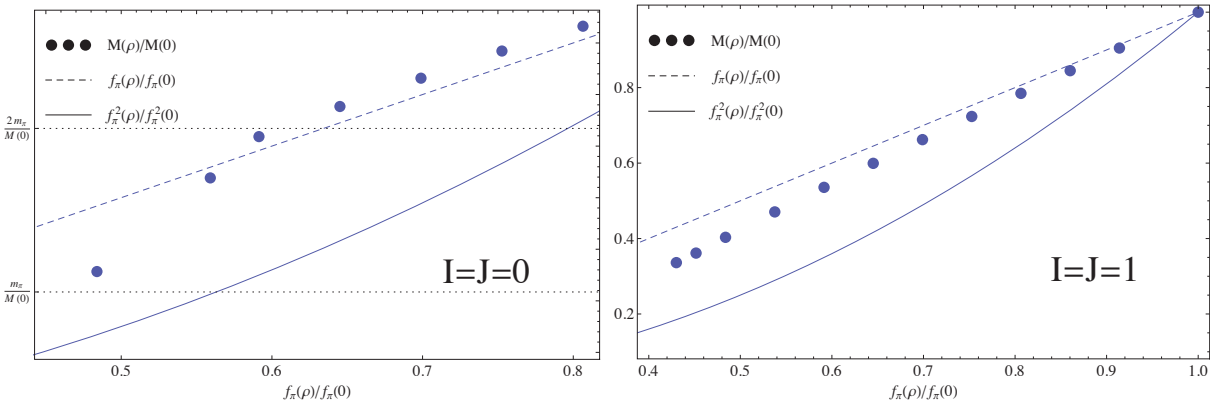

Figura R.5: Escaleo de la masa, comparado con $F_\pi^2(\rho)/F_\pi^2(0) \sim \langle\bar{q}q\rangle(\rho)/\langle\bar{q}q\rangle(0)$ y con $F_\pi(\rho)/F_\pi(0)$. En el caso $I = J = 0$, las masas representadas corresponden a las masas más bajas de los polos en la segunda hoja de Riemann.

ejemplo con los efectos de medio que hemos ignorado y que podrían incrementar también la anchura de la σ, evitando que el polo se aproxime al eje real eliminando el aumento en el umbral. Éste parece no ser el caso cuando las interacciones de muchos cuerpos son consideradas adecuadamente [Chi98a, Roc02], lo cual apoya esta simple aproximación. De hecho, el efecto observado está en razonable acuerdo cuantitativo con los resultados de trabajos teóricos previos [Dav00, Jid01, Pat03], y no es muy fuerte para densidades $\rho \lesssim \rho_0$ (rango disponible experimentalmente), en línea con los resultados experimentales en [Sta00].

En el caso de dileptones en materia nuclear, un parámetro que es directamente medible en esos experimentos es el coeficiente del término lineal en la densidad para la masa del mesón $\rho(770)$:

$$\frac{M(\rho)}{M(0)} = 1 - \alpha\frac{\rho}{\rho_0} \ . \tag{R.10}$$

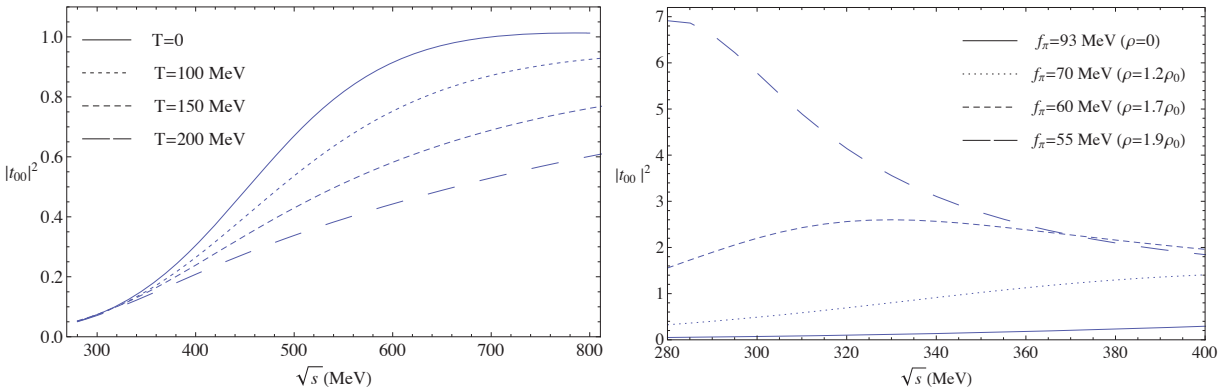

Figura R.6: Módulo al cuadrado de la onda parcial a temperatura finita en el canal $I = J = 0$ (izquierda), y a $T = 0$ y variando F_π (derecha) para simular restauración quiral a densidad finita.

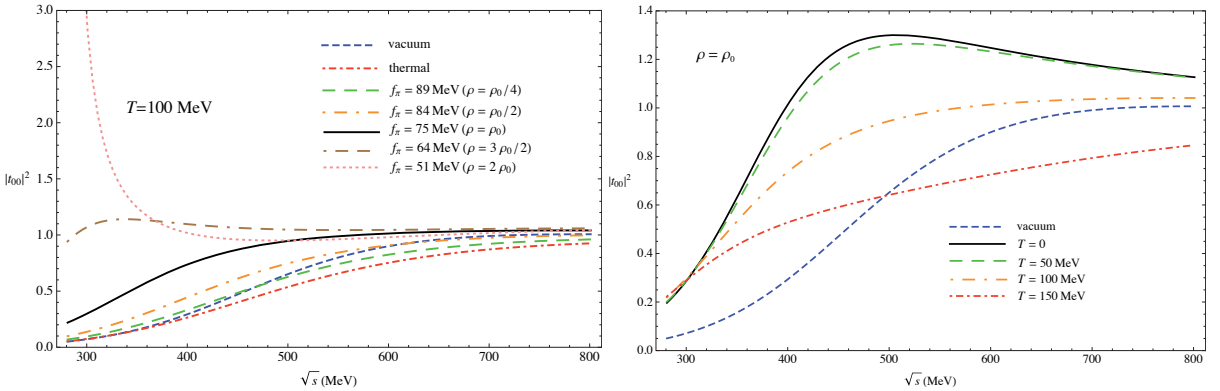

Figura R.7: Módulo al cuadrado de la onda parcial en el canal $I = J = 0$ a $T = 100$ MeV para varias densidades (izquierda), y a densidad normal de materia nuclear ($F_\pi = 75$ MeV) para varias temperaturas (derecha).

Los valores experimentales disponibles hasta ahora son $\alpha = 0{,}092 \pm 0{,}002$ obtenido por la colaboración E325-KEK [Nar06], y $\alpha = 0{,}02 \pm 0{,}02$ medido por el experimento JLab-CLAS [Nas07]. Hemos realizado un ajuste lineal de nuestros resultados del polo en el canal $I = J = 1$ para $F_\pi = 93, 85, 80, 75$ MeV, esto es, hasta $\rho \lesssim \rho_0$ para comparar con los experimentos. Nuestro ajuste da $\alpha = 0{,}2$, que es más próximo al resultado en [Nar06] que al de [Nas07], aunque por encima del valor experimental. Nuestro resultado también está de acuerdo con el escaleo de BR [Bro02] y las reglas de suma de QCD en [Hat95] que predicen $\alpha \simeq 0{,}1 - 0{,}2$. Es importante recordar de nuevo que hasta el momento hemos ignorado todos los efectos de ensanchamiento del medio a temperatura cero que, a diferencia del caso de la σ, pueden ser cruciales para la ρ. De hecho, en [Leu98] se encontró que las reglas de suma de QCD por sí mismas no proporcionan una ligadura única para la variación de la masa y anchura en el medio, a menos que hagan otras suposiciones adicionales. En particular, se muestra que si uno asume que la anchura no aumenta, entonces automáticamente la masa cae. Éste es el escenario que hemos recuperado en el presente análisis, que como hemos comentado varias veces puede

no corresponder al caso físicamente relevante.

Clasificación "molecular" de resonancias

Se puede obtener información muy útil sobre la naturaleza de las resonancias estudiando el comportamiento de los polos cerca del umbral. Nuestro argumento se apoya en la clasificación de resonancias que se encuentran cerca del umbral dada en [Mor91, Mor92] y que está basada en una "expansión de rango efectivo". Aunque generalmente es difícil extraer propiedades sobre la naturaleza "interna" de resonancias a partir de sus productos de desintegración (polos en la amplitud de dispersión), en esos trabajos se establece que cuando el polo permanece cerca del umbral se puede aplicar la siguiente regla: *una resonancia "potencial" o "molecular" aparece como un único polo cerca del umbral, mientras que en el caso de un estado de tipo $\bar{q}q$ aparecen dos polos cerca del umbral muy juntos entre sí en diferentes hojas de Riemann.*

Por consiguiente, vemos que el polo de la σ sigue un claro patrón molecular, ya que el polo permanece cerca del umbral y eventualmente se convierte en un estado ligado alejado del polo en la SRS que permanece debajo del umbral. Interpretamos esto como la coexistencia de dos estados a altas densidades: una "molécula" $\pi\pi$ y un estado virtual que se comporta como el compañero quiral del pión, en el sentido de que tiende a degenerarse con él en masa (aunque tienen distintos números cuánticos) siguiendo el comportamiento del condensado. Nótese que el polo que representamos en la Figura R.5 es precisamente este estado virtual. Esta imagen contrasta con lo que observamos en el canal de la ρ, donde dos polos cercanos permanecen por debajo del umbral, uno de ellos moviéndose a la primera hoja convirtiéndose en un estado ligado. Esto es claramente un escenario de tipo $\bar{q}q$ no-molecular, según la clasificación anterior. Sin embargo, este criterio de clasificación sólo es aplicable en principio a resonancias escalares. De todos modos, la naturaleza $\bar{q}q$ de la ρ ha sido defendida en otros trabajos por medio de diversos argumentos, como por ejemplo el escaleo con N_c grande [Pel04, Pel06]. Una imagen parecida para los polos en el eje real fue obtenida en [Pat03], donde la dependencia en densidad se parametrizó también variando F_π, y en [Han08], incrementando la masa de los quarks para así poder comparar con resultados del retículo (extrapolación quiral).

R.2.3 Temperatura y densidad nuclear finitas en un análisis de interacción de muchos cuerpos

Hemos extendido también nuestros resultados previos en el canal $I = J = 0$ incorporando efectos de densidad nuclear y temperatura finitas usando una descripción de la dinámica del pión en el medio teniendo en cuenta las interacciones de muchos cuerpos (many-body interactions). Por razones técnicas, es conveniente usar un método diferente al IAM para la unitarización de la matriz de dispersión T, que sin embargo proporciona resultados en vacío similares a los del IAM, esto es, las resonancias mesónicas son generadas dinámicamente en el canal escalar y muchos observables son descritos en un buen grado de acuerdo con experimentos dispersión [Oll97, Oll99b, Oll98].

La idea es resolver la ecuación de Bethe-Salpeter (BS) para la amplitud de dispersión:

$$T = V + \overline{VGT} \ , \tag{R.11}$$

donde hemos usado una notación abreviada para esta ecuación integral: T, V, y G son matrices con índices correspondientes a los diferentes canales de dispersión (nosotros sólo consideramos uno aquí), y la barra sobre el producto VGT representa la integración del lazo correspondiente en el diagrama de Feynman.

El potencial (núcleo) V de la ecuación viene dado por la amplitud de orden más bajo obtenida a partir del lagrangiano quiral. En la Eq. (R.11), G representa el producto de dos funciones de Green correspondientes a las líneas mesónicas intermedias. Se demuestra que, V y T se pueden evaluar en la capa de masas, factorizándose y dejando la integración en cuadrimomento sólo para el producto de los propagadores mesónicos. Esto nos permite escribir (R.11) como una (en el caso de un un único canal) ecuación lineal algebraica con solución trivial,

$$T = [1 - VG]^{-1} V \ . \tag{R.12}$$

La principal diferencia entre el presente método y el IAM se encuentra en la contribución de orden $\mathcal{O}(p^4)$, que aquí viene dada por el lazo mesón-mesón en canal s, mientras que los canales t y u presentes en el IAM aquí están ausentes. A temperatura finita, la contribución de los términos que se encuentran fuera de la capa de masas (off-shell) a la amplitud de dispersión para el diagrama a un lazo viene dada por:

$$\delta V^T_{\rm off}(s) = \frac{4}{3F_\pi^2}\left(V_{\rm on}(s) + \frac{s}{3F_\pi^2}\right)\ I_0^T \ , \tag{R.13}$$

donde $I_0^T \equiv (2\pi^2)^{-1}\int_0^\infty {\rm d}q\ \boldsymbol{q}^2\ n_{\rm B}(\omega_q)/\omega_q$, $V_{\rm on}(s) = -(s - M_\pi^2/2)/F_\pi^2$ es la amplitud a nivel árbol, y $\omega_q^2 = \boldsymbol{q}^{\,2} + M_\pi^2$. Por otro lado, la contribución de los diagramas "tadpole" es

$$\delta V^T_{\rm tad}(s) = \left[\frac{20}{9}\, s\, I_0^T - \frac{25}{6}\, I_2^T\right]/F_\pi^4 + V_{\rm on}(s)\frac{4}{3F_\pi^2}\, I_0^T \ , \tag{R.14}$$

con $I_2^T \equiv M_\pi^2\, I_0^T$.

En la Figura R.8 (izquierda) mostramos la trayectoria del polo de la σ para el cálculo térmico usando la ecuación de BS con el núcleo a orden $\mathcal{O}(p^2)$. Como podemos ver, la evolución del polo sigue un patrón muy parecido al del IAM, aunque la posición de la masa de la σ alcanza valores inferiores por debajo del umbral a temperaturas bajas. Como en el IAM, el polo de la sigma permanece lejos del eje real con una anchura considerable hasta temperaturas de 200 MeV. La atracción sentida por la σ hacia el umbral con este método en comparación con lo que ocurría con el IAM parece reflejar que las contribuciones de canal t y u son relevantes en esta región de energías y proporcionan una contribución repulsiva. Sin embargo, el resultado es cualitativamente parecido en ambos métodos. Como test adicional, hemos calculado también la trayectoria del polo variando F_π, que representamos en la parte derecha de la Figura R.8. Obtenemos un resultado parecido al de IAM en cuanto a que el polo colapsa en el eje real para valores de F_π inferiores a 50 MeV. Además, observamos el efecto de doblado del polo que sigue el patrón "molecular" discutido anteriormente. Por otro lado, también hemos estudiado el aumento en el umbral de la amplitud de dispersión $\pi\pi$ para valores decrecientes de F_π, que omitimos al ser los resultados muy parecidos a los representados en las Figuras R.6 y R.7 para el IAM.

Por último, hemos llevado a cabo la introducción de efectos de densidad nuclear mediante la renormalización del propagador del pión incluyendo interacciones con bariones

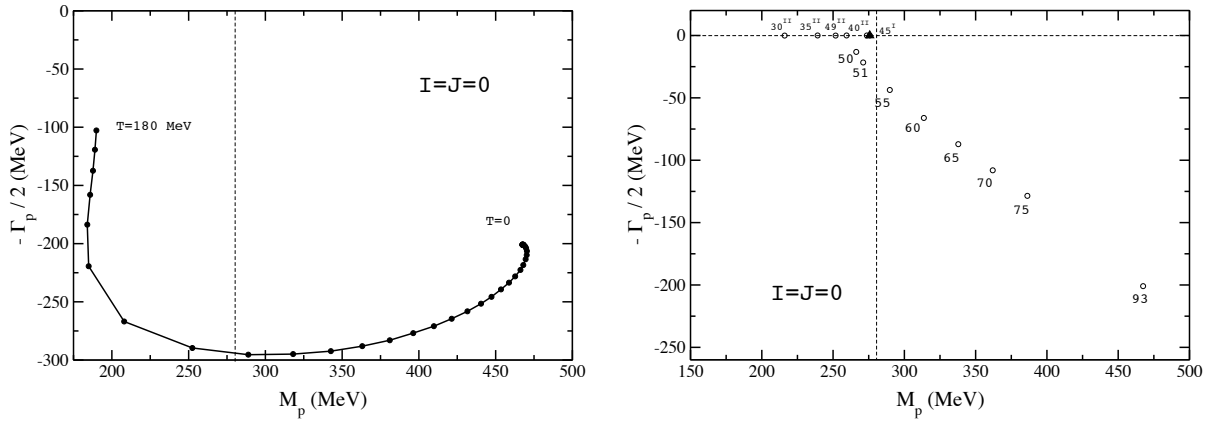

Figura R.8: (Eje vertical invertido con respecto a la Fig. R.1) Izquierda: Dependencia con la temperatura del polo de la σ calculado con la ecuación de BS incluyendo correcciones térmicas al núcleo de orden $\mathcal{O}(p^2)$ (el intervalo de temperaturas entre cada punto es 5 MeV). Derecha: Trayectoria del polo variando F_π. Los números junto a cada punto indican el valor de F_π en MeV.

a temperatura finita. En materia nuclear fría, la función espectral del pión exhibe una mezcla del modo de cuasi-partícula del pión y excitaciones en onda p partícula-agujero (ph) y Delta-agujero (Δh) [Ose82]. Al orden más bajo en la expansión en densidades la amplitud pión-pión a un lazo incluye el diagrama (a) en Fig. R.9 (ver también la Fig. R.10), en el que uno de los piones intermedios excita un ph (ó Δh). Además del diagrama (a), la simetría quiral requiere el conjunto de términos de contacto representados en los diagramas (b-d), que pueden verse como contribuciones a la amplitud $\pi\mathrm{N} \to \pi\pi\mathrm{N}$ cortando los correspondientes propagadores. Se demuestra que la solución algebraica de la ecuación (R.11) permanece inalterada en este caso, y sólo es necesario remplazar los propagadores en G por los correspondientes que incluyen la interacción bariónica.

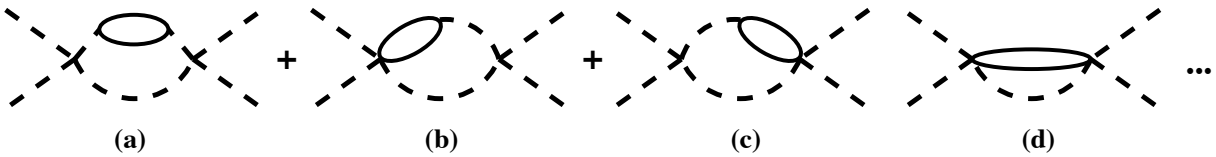

Figura R.9: Inserción barión-agujero al orden más bajo incluyendo las correcciones de vértice.

En la Figura R.11 mostramos la parte imaginaria de la amplitud $\pi\pi$ para diferentes densidades y temperaturas. Recordamos que en vacío y en el caso térmico $\mathrm{Im}\, T$ se anula por debajo del umbral. Nuestro resultado, obtenido a partir de un cálculo dinámico que tiene en cuenta interacciones de muchos cuerpos para los estados intermedios de dos piones, exhibe una apreciable acumulación de intensidad para y por debajo de $P^0 = 2M_\pi$ incluso a temperatura cero, aunque el aumento es comparativamente menor que el obtenido variando F_π. Con respecto al cálculo térmico, la densidad finita suaviza la

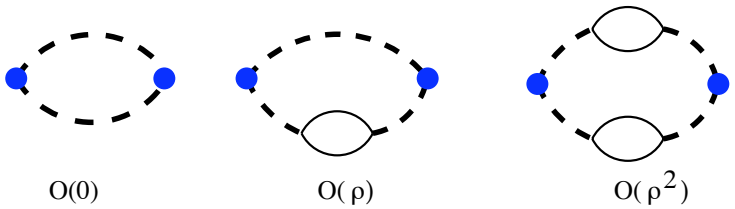

Figura R.10: Contribuciones de orden $\mathcal{O}(0, \rho, \rho^2)$ en densidad bariónica al lazo mesónico a partir de inserciones de auto-energía irreducibles.

amplitud a energías altas e incrementa la intensidad por debajo del umbral de vacío, efecto que está relacionado con la excitación de modos colectivos piónicos. La combinación de estos efectos acelera el desplazamiento de la σ hacia el umbral y el eje real pero, a pesar de esto, sigue permaneciendo ancha cerca de la transición de fase.

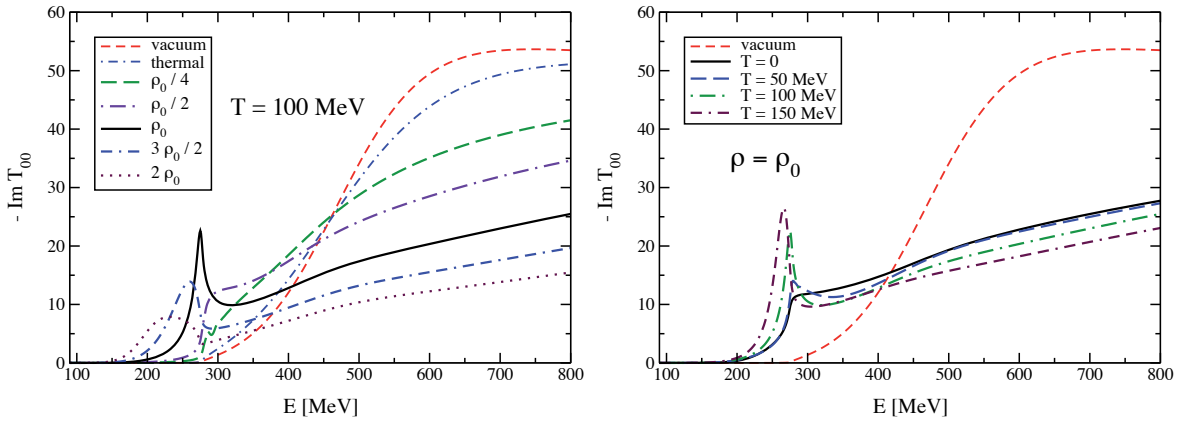

Figura R.11: Parte imaginaria de la amplitud $\pi\pi$ en el canal $I = J = 0$ a temperatura y densidad nuclear finitas. También incluimos el resultado en vacío como referencia.

R.3 Coeficientes de transporte en Teoría de Perturbaciones Quiral

El análisis de coeficientes de transporte en el contexto de colisiones relativistas de iones pesados se ha convertido en una línea de investigación muy activa, con varias aplicaciones fenomenológicas y teóricas. Los coeficientes de transporte proporcionan la respuesta lineal del sistema ante la acción de gradientes en magnitudes termodinámicas del mismo. Gradientes en velocidades se relacionan con las viscosidades de cizalla y volumen, mientras que la conducción de carga eléctrica y calor se codifica en las conductividades eléctrica y térmica respectivamente.

El papel de las viscosidades en colisiones de iones pesados es especialmente interesante. Aunque la materia que se produce tras la colisión inicial de los dos iones se comporta

aproximadamente como un fluido perfecto [Ada04a], hay desviaciones medidas, principalmente por medio del *flujo elíptico*, que son razonablemente bien explicadas por medio de un cociente viscosidad de cizalla entre la densidad de entropía pequeño [Rom07]. En estos análisis, la viscosidad de volumen es normalmente ignorada, en base a varios estudios teóricos en los regímenes de bajas y altas temperaturas [Arn06b, Pra93, Dav96]. Sin embargo, recientemente [Kha08, Kar08] se ha contemplado la posibilidad de que la viscosidad de volumen fuera mayor de lo esperado cerca de la transición de fase de QCD, por el efecto de la anomalía de traza. Por otra parte, el cociente de la viscosidad de cizalla sobre la densidad de entropía presumiblemente tiene un mínimo en esa región de temperaturas. Si los dos coeficientes de viscosidad fueran comparables a las temperaturas de interés, entonces habría varias consecuencias físicas interesantes tales como supresión del flujo radial, modificación del mecanismo de hadronización [Kar08], o "clustering" en el "freeze-out" [Tor08].

Los análisis de coeficientes de transporte en el retículo son técnicamente complicados y computacionalmente costosos, dado que implican el límite de momento y energía tendiendo a cero de funciones espectrales [Aar02, Mey08b, Hue08, Gup04], y no hay resultados concluyentes disponibles en estos momentos. Es por lo tanto muy interesante y útil considerar regímenes que son accesibles al análisis teórico con el objetivo de proporcionar información complementaria acerca de coeficientes de transporte. El análisis teórico de coeficientes de transporte ha sido llevado a cabo tradicionalmente desde dos puntos de vista: teoría cinética (KT), y el análisis diagramático. El cálculo en teoría cinética involucra la resolución de una ecuación de tipo Boltzmann linearizada, y ha sido exitosamente llevado a cabo en QCD a temperaturas altas [Arn00, Arn03, Arn06b], en el sector mesónico [Pra93, Dav96, Dob04, Dob07a, Dob07b, Dob09], y también aplicado a la materia de tipo "color-flavor locked" presente en el núcleo de las estrellas de neutrones [Man05, Man07, Man08], mientras que el método diagramático ha sido desarrollado para teorías escalares y gauge a altas temperaturas [Jeo95, Jeo96, MR01, VB02, Aar02, Aar03, Aar04, Aar05]. En ambos formalismos, es crucial incluir adecuadamente la anchura de colisión de las partículas, tras identificar el proceso de re-equilibración dominante en el plasma.

R.3.1 Cálculo diagramático de coeficientes de transporte

A diferencia del cálculo de teoría cinética, que es aplicable cuando el gas es diluido, el método diagramático es en principio aplicable en todo rango de temperaturas (aunque el número de diagramas a considerar podría variar). El método diagramático fue analizado exhaustivamente en el caso de teorías escalares renormalizables en [Jeo95, Jeo96], con especial énfasis en el régimen alta temperatura, donde una formulación en términos de una teoría cinética efectiva es también posible. La conclusión es que para obtener el orden dominante en teoría de perturbaciones estándar de un cierto coeficiente de transporte, es necesario sumar un número infinito de diagramas a cualquier temperatura. Por simplicidad, para explicar la filosofía general del método diagramático, consideramos una teoría $\lambda\phi^4$. Un coeficiente de transporte viene dado en Teoría de la Respuesta Lineal (LRT) tomando el límite de momento externo yendo a cero de la densidad espectral correspondiente. Este proceso de tomar el límite implica la aparición de los llamados *pinching poles*, que son productos de propagadores avanzado y retardado compartiendo el mismo

cuadrimomento:

$$G_{\rm R}(p)G_{\rm A}(p) \simeq \frac{\pi}{4E_p^2\Gamma_p}\left[\delta(p^0-E_p)+\delta(p^0+E_p)\right] \ , \quad \text{para} \quad \Gamma_p \ll E_p \ , \tag{R.15}$$

donde la anchura de la partícula (inverso del tiempo de colisión en el plasma) Γ_p está relacionada con la auto-energía mediante

$$\Gamma_p = -\frac{\mathrm{Im}\,\Pi_{\rm R}(E_p,\boldsymbol{p})}{2E_p} \ . \tag{R.16}$$

Nótese que el producto (R.15) está mal definido cuando las partículas se propagan libremente, esto es, cuando $\Gamma_p = 0$. Un "pinching pole" corresponde a la contribución que proviene de un par de líneas en el diagrama que comparten el mismo cuadrimomento cuando el cuadrimomento externo es cero. Como vemos a partir de la ecuación (3.2), esas líneas están aproximadamente en la capa de masas en ese límite, que es razonable si el tiempo de colisión es grande. Para una teoría $\lambda\phi^4$, la contribución de orden más bajo a la anchura proviene del diagrama de la Figura R.15, que es de orden $\mathcal{O}(\lambda^2)$. Por lo tanto, *diagramas de escalera* como el representado en la Figura R.12 cuentan todos lo mismo, $\mathcal{O}(1/\lambda^2)$, en cuanto a las potencias de la constante de acoplo, y por lo tanto deben ser resumados a toda temperatura.

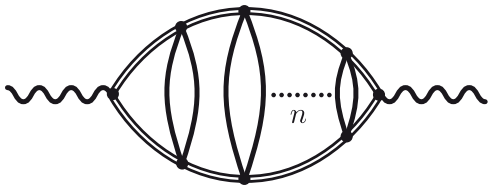

Figura R.12: Un diagrama de escalera con n *peldaños*.

Otro tipo de diagramas, los *diagramas de burbujas* (ver Fig. R.13), aparentemente darían lugar a una contribución mayor a medida que se incrementa el número de "burbujas", de acuerdo con el contaje anterior (intuitivamente son de orden $\mathcal{O}((1/\lambda^2)^n\lambda^{n-1}) = \mathcal{O}(1/\lambda^{n+1})$). Sin embargo, tras un cuidadoso análisis [Jeo95], puede demostrarse que pueden resumarse todos dando lugar en realidad a una contribución subdominante con respecto a los de escalera (salvo en el caso de la viscosidad de volumen). Además, se demostró en [Jeo95] que la contribución dominante para la viscosidad de volumen viene dada por diagramas de escalera con peldaños que involucran procesos que cambian el número de partículas (ver comentarios en los resultados relativos a la viscosidad de volumen del gas de piones más abajo).

Por lo tanto, es interesante desde el punto de vista teórico analizar lo que ocurre en el contexto de ChPT para un gas de mesones, donde no hay una constante de acoplo explícita, y por lo tanto no es evidente si una resumación de diagramas es necesaria para obtener el orden dominante de los distintos coeficientes de transporte.

R.3.2 Anchura de colisión

Como hemos mencionado, es crucial para el cálculo de coeficientes de transporte tener líneas con anchura de colisión no nula en el diagrama genérico de la Fig. R.14 (representadas mediante líneas dobles), para poder tener en cuenta las colisiones entre las partículas

Figura R.13: Un diagrama de burbujas con n "burbujas".

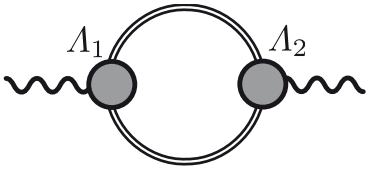

Figura R.14: Representación genérica de un diagrama de escalera/burbujas en términos de dos vértices efectivos distintos, Λ_1 y Λ_2.

del fluido, como también ocurre en el análisis de teoría cinética. Si la anchura de la partícula es cero, significa que ésta puede propagarse indefinidamente por el plasma y por lo tanto el correspondiente coeficiente de transporte sería infinito. Podemos aproximar la interacción entre partículas en el medio considerando la siguiente densidad espectral que incluye una anchura finita Γ_p:

$$\rho(p^0, \boldsymbol{p}) = \frac{1}{E_p}\left[\frac{\Gamma_p}{(p^0 - E_p)^2 + \Gamma_p^2} - \frac{\Gamma_p}{(p^0 + E_p)^2 + \Gamma_p^2}\right] . \tag{R.17}$$

Esta aproximación mediante una lorentziana será apropiada en el caso de que la anchura sea lo suficientemente pequeña. La anchura se calcula de forma genérica para una colisión de dos cuerpos mediante [Goi89]:

$$\Gamma(k_1) = \frac{\sinh(\beta E_1/2)}{4E_1}\int \mathrm{d}\nu_2\,\mathrm{d}\nu_3\,\mathrm{d}\nu_4\ (2\pi)^4\delta^{(4)}(k_1 + k_2 - k_3 - k_4)|T(s,t)|^2 , \tag{R.18}$$

con $\mathrm{d}\nu_i \equiv \mathrm{d}^3\boldsymbol{k}_i/[(2\pi)^3 2E_i \sinh(\beta E_i/2)]^{-1}$, $T(s,t)$ es la amplitud de dispersión, y $s \equiv (k_1 + k_2)^2$ y $t \equiv (k_1 - k_3)^2$ son las correspondientes variables de Mandelstam. Si el gas es diluido, esto es $\beta E \gg 1$, la formula anterior adopta la forma:

$$\Gamma(k_1) \simeq \frac{1}{2}\int \frac{\mathrm{d}^3\boldsymbol{k}_2}{(2\pi)^3}\ \mathrm{e}^{-E_2/T}\ \sigma_{\mathrm{tot}}(s) v_{\mathrm{rel}}(1 - \boldsymbol{v}_1 \cdot \boldsymbol{v}_2) , \tag{R.19}$$

donde σ_{tot} es la sección eficaz total de dispersión, $\boldsymbol{v}_i$ es la velocidad de cada una de las dos partículas que colisionan, y v_{rel} es su velocidad relativa. La contribución dominante a la anchura del pión viene dada por el diagrama de la Figura R.15. Como se ha comentado en la Sección R.2, hasta energías del orden de 1 GeV (suficientes para temperaturas por debajo de T_{c}) puede mostrarse [GN02a] que para dispersión $\pi\pi$ sólo los canales $IJ = 00, 11, 20$ de isospín y momento angular son relevantes y puede entonces aproximarse:

$$\sigma_{\mathrm{tot}}(s) = \frac{32\pi}{3s}\sum_{I,J}(2J+1)(2I+1)|t_{IJ}(s)|^2 \simeq \frac{32\pi}{3s}\left[|t_{00}(s)|^2 + 9|t_{11}(s)|^2 + 5|t_{20}(s)|^2\right] , \tag{R.20}$$

donde $t_{IJ}(s)$ son las ondas parciales de dispersión.

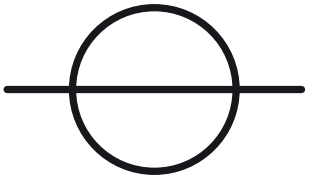

Figura R.15: Contribución dominante a la anchura del pión.

R.3.3 Análisis general de diagramas para coeficientes de transporte en ChPT

En el caso de ChPT, análogamente a como ocurría en $\lambda\phi^4$, también encontramos contribuciones no-perturbativas del tipo $\propto 1/\Gamma$ (con $\Gamma = \mathcal{O}(p^5)$), debido a la presencia de "pinching poles". Esto indica que el contaje estándar para diagramas de ChPT, dictado por el Teorema de Weinberg (1.43), tiene que modificarse de algún modo pues, en caso contrario, a medida que un diagrama tuviera más inserciones del tipo "pinching poles" su contribución sería arbitrariamente grande a temperaturas bajas. En realidad, como veremos, a temperaturas bajas los diagramas de escalera son dominantes, pero perturbativamente pequeños en comparación con el diagrama de una única burbuja representado en la Figura R.16.

Figura R.16: Contribución dominante para coeficientes de transporte en ChPT.

De nuevo, los mismos argumentos topológicos de una teoría $\lambda\phi^4$ son aplicables en el caso de ChPT, de modo que esperamos que la contribución dominante para los coeficientes de transporte provenga de diagramas de escalera y de burbujas, que son las topologías con un mayor número de "pinching poles". De acuerdo con el trabajo [VB02], el límite de frecuencia cero de la derivada de la densidad espectral correspondiente al diagrama R.14 viene dada por:

$$\lim_{\omega\to 0^+} \frac{\rho^{AA}(\omega,\mathbf{0})}{\omega} = -\theta\beta \int \frac{\mathrm{d}^3\boldsymbol{p}}{(2\pi)^3} \int_{-\infty}^{\infty} \frac{\mathrm{d}\xi}{2\pi}\, n_{\mathrm{B}}(\xi)[1+n_{\mathrm{B}}(\xi)] G_{\mathrm{R}}(\xi,\boldsymbol{p}) G_{\mathrm{A}}(\xi,\boldsymbol{p}) \times \Lambda_1^A(\xi-\mathrm{i}0^+,\xi+\mathrm{i}0^+;\boldsymbol{p})\Lambda_2^A(\xi+\mathrm{i}0^+,\xi-\mathrm{i}0^+;\boldsymbol{p}) \,, \tag{R.21}$$

donde $\theta = 1/2, 1$ dependiendo de si los propagadores en el lazo son partículas autoconjugadas o no respectivamente. Con objetivo de dar una primera estimación intuitiva de la contribución a temperaturas bajas de un diagrama genérico de escalera/burbuja, asignamos un factor Y, que esperamos que sea no-perturbativo, a cada par de líneas que comparten el mismo cuadrimomento, y un factor X, que esperamos que sea de orden $X_1 \equiv [M_\pi/(4\pi F_\pi)]^2$ (X_1 es la contribución típica de un lazo quiral) a cada lazo ordinario

en nuestro diagrama. Por tanto, de acuerdo con este contaje intuitivo, la contribución de una diagrama con n peldaños sería de orden

$$\mathcal{O}(X^n Y^{n+1}) \ , \tag{R.22}$$

así que los diagramas de escalera podrían en principio volverse más importantes a medida que la temperatura se reduce para un Y no perturbativo (ver más adelante), región en la cual se espera que ChPT funcione mejor. Evidentemente, la contribución que proviene del diagrama de la Figura R.16 sería de orden $\mathcal{O}(Y)$ en lugar de $\mathcal{O}(X)$, que es la estimación dada por el contaje de potencias de Weinberg (para líneas piónicas sin anchura). En el análisis siguiente de diagramas de escalera y burbuja, comprobaremos el contaje (R.22) para el caso particular de la conductividad eléctrica DC, aunque los resultados son extensibles a otros coeficientes de transporte. Veremos que a temperaturas muy bajas, los diagramas de escalera están suprimidos perturbativamente mientras que los de burbujas pueden ignorarse. Sin embargo, cerca de la temperatura crítica, en principio, la suma de estos diagramas podría ser relevante.

Diagramas de escalera

A continuación analizamos diagramas de escalera con los vértices externos correspondientes a inserciones de corrientes electromagnéticas (estamos interesados por tanto en la auto-energía del fotón), para así obtener la conductividad eléctrica DC. Usando (R.21), la contribución correspondiente al diagrama de la Figura R.16, viene dada por

$$\sigma^{(0)} = \frac{e^2}{3T} \int \frac{\mathrm{d}^3 \boldsymbol{p}}{(2\pi)^3} \ \frac{|\boldsymbol{p}|^2}{E_p^2 \Gamma_p} n_{\mathrm{B}}(E_p)[1 + n_{\mathrm{B}}(E_p)] \ , \tag{R.23}$$

donde e es la carga del electrón y $E_p \equiv \sqrt{M_\pi^2 + |\boldsymbol{p}|^2}$. Para temperaturas muy bajas ($T \ll M_\pi$), esta expresión adopta la forma simple

$$\sigma^{(0)} \simeq 14 \ \frac{e^2 F_\pi^4}{T^{1/2} M_\pi^{5/2}} \ . \tag{R.24}$$

Este comportamiento, $\lim_{\omega \to 0^+} \rho(\omega)/\omega \sim \sqrt{M_\pi/T}$ (de modo que en el caso de la conductividad eléctrica $Y \sim \sqrt{M_\pi/T}$), para la densidad espectral a temperaturas bajas indica que podría haber importantes contribuciones no-perturbativas provenientes de diagramas de orden superior en este régimen de temperaturas (diagramas de escalera con un número más alto de peldaños). Sin embargo, tras analizar detalladamente esta posibilidad, se obtiene que, para $T \ll M_\pi$, la contribución a la conductividad DC de un diagrama con k

peldaños viene dada en términos de la contribución del diagrama con $k-1$ peldaños por

$$\sigma_{\rm LT}^{(k)} = e^2\alpha^{(k)}\frac{M_\pi}{3}\left(\frac{F_\pi}{M_\pi}\right)^4\sqrt{\frac{M_\pi}{T}}\int\frac{{\rm d}^3\boldsymbol{y}_1}{(2\pi)^3}\frac{y_1^2}{f(y_1)}A_{\rm LT}^{(k)}\left(\sqrt{M_\pi T}y_1\right)\exp\left(-\frac{y_1^2}{2}\right)\ , \quad \text{(R.25)}$$

$$A_{\rm LT}^{(k)}\left(\sqrt{M_\pi T}y_1\right) \equiv \frac{1}{32\pi y_1^2}\int\frac{{\rm d}^3\boldsymbol{y}_2}{(2\pi)^3}\frac{\boldsymbol{y}_1\cdot\boldsymbol{y}_2}{|\boldsymbol{y}_1-\boldsymbol{y}_2|f(y_2)}A_{\rm LT}^{(k-1)}(\sqrt{M_\pi T}y_2)\exp\left(-\frac{y_2^2}{2}\right)$$

$$\times\left\{\frac{|\boldsymbol{y}_1-\boldsymbol{y}_2|^2}{4}+\exp\left[\frac{1}{4}\left(y_1^2+y_2^2-\frac{1}{2}\frac{(y_1^2-y_2^2)^2}{|\boldsymbol{y}_1-\boldsymbol{y}_2|^2}-\frac{1}{2}|\boldsymbol{y}_1-\boldsymbol{y}_2|^2\right)\right]\right\}\ , \quad \text{(R.26)}$$

con $\alpha^{(k)}$ un factor combinatorio, y la función f definida como:

$$f(x) \equiv \frac{23}{512\pi^3}\left[\exp(-x^2/2)+\sqrt{\frac{\pi}{2}}\frac{1+x^2}{x}\,{\rm erf}(x/\sqrt{2})\right]\ , \quad \text{(R.27)}$$

y hemos re-escaleado $\boldsymbol{p}_{1,2} = \sqrt{M_\pi T}\boldsymbol{y}_{1,2}$ ($y_{1,2} \equiv |\boldsymbol{y}_{1,2}|$). A partir de la ecuación, (R.26) podemos extraer nuestras conclusiones principales: el vértice efectivo a baja temperatura $A_{\rm LT}^{(k)}\left(\sqrt{M_\pi T}y_1\right)$ es independiente de T y, a partir de (R.25), el orden correcto de la contribución a la conductividad de la escalera con k peldaños en nuestro contaje de potencias es $\sigma_{\rm LT}^{(k)} = e^2M_\pi\mathcal{O}(X^k\sqrt{M_\pi/T}) = e^2M_\pi\mathcal{O}(X^kY)$, en lugar de la estimación intuitiva inicial $\mathcal{O}(X^kY^{k+1})$. La independencia del vértice de baja temperatura con T se sigue de (R.26) por inducción, ya que $A^0 = 1$. Por consiguiente, la única dependencia con la temperatura en $\sigma_{\rm LT}^{(k)}$ es $1/\sqrt{T}$, la misma que en el orden más bajo (R.24). Podemos también comprender por qué el contaje intuitivo "olvida" k potencias de Y. La razón es que la contribución que procede de las funciones espectrales de los peldaños introduce un factor extra $\sqrt{T/M_\pi}$ dentro del integrando en (R.26). La contribución de orden $\mathcal{O}(X^k)$ restante se debe a los k lazos quirales. Para comprobar explícitamente nuestras conclusiones, hemos evaluado numéricamente la contribución del diagrama con un peldaño y obtenemos $\sigma_{\rm LT}^{(1)}/\sigma_{\rm LT}^{(0)} \simeq 0{,}06$. Podemos por tanto concluir que los diagramas de escalera a muy bajas temperaturas, aunque representan la contribución principal más allá del orden dominante, son perturbativos en nuestro análisis de ChPT. Además, siguiendo los argumentos anteriores, no es difícil concluir que diagramas de escalera con peldaños mas complejos o vértices que provengan del lagrangiano quiral $\mathcal{L}_d$ con $d > 2$ están también suprimidos perturbativamente.

Sin embargo, la correcta contribución de los diagramas de escalera resulta ser mucho mayor que la estimada por contaje estándar de ChPT (Teorema de Weinberg), esto es, su contribución es de orden $\sigma^{(k)}/\sigma^{(0)} = \mathcal{O}(p^{2k})$ en lugar de $\mathcal{O}(p^{4k})$. La razón es la presencia de los factores Y no-perturbativos, como hemos visto. Siguiendo nuestros argumentos de contaje quiral, para temperaturas del orden de M_π, nos damos cuenta primero que ahora $Y \sim \mathcal{O}(1)$ alrededor de $T \sim M_\pi$. Para esas temperaturas, la simplificación de reducir cualquier diagrama de escalera a uno con vértices constantes no es posible. De hecho, esperamos que para temperaturas más altas los vértices derivativos comiencen a ser cada vez más importantes. De todos modos, siempre que T permanezca dentro del rango de aplicabilidad de ChPT, podemos considerar todos esos diagramas perturbativamente suprimidos.

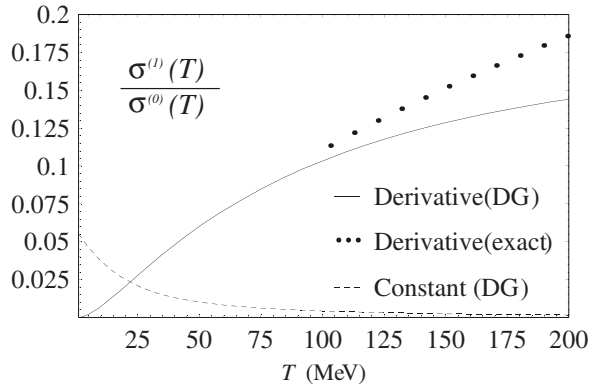

Figura R.17: Estimación de la contribución de los diagramas de escalera para temperaturas más altas, con y sin vértices derivativos. Los puntos corresponden a las expresiones exactas sin usar la aproximación de gas diluido.

Con el fin de comprobar los comentarios previos, hemos evaluado numéricamente los diagramas de escalera con un peldaño y vértices constantes, usando $k = 1$ y $\alpha^{(1)} = 1$, y efectuando sólo la aproximación de gas diluido. Hemos también considerado, por comparación, la contribución de un diagrama de escalera con sólo un peldaño y una posible configuración de vértices derivativos, esto es, la obtenida remplazando factor constante $(M_\pi/F_\pi)^4$ en el vértice por $|\boldsymbol{p}_1|^4/F_\pi^4$ en el integrando. Los resultados se muestran en la Figura R.17, donde para comparar hemos representado algunos puntos calculados sin usar la aproximación del gas diluido. Claramente, los vértices derivativos se convierten en los importantes a moderadas y altas temperaturas, indicando que la suma de diagramas de escalera podría ser necesaria en ese régimen.

Diagramas de burbuja

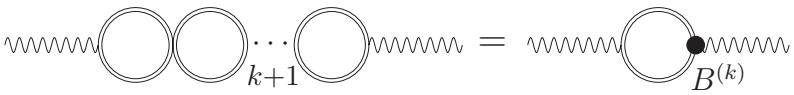

Figura R.18: Diagrama genérico de burbujas con $k+1$ "burbujas" ($k \geq 1$).

En el caso del diagrama de burbujas representado en la Figura R.18, que en principio podría dar una contribución no-perturbativa de orden $\mathcal{O}(Y^n)$, resulta que su contribución a la conductividad es en realidad subdominante con respecto al orden $\mathcal{O}(1/\Gamma)$. Para ver esto, definimos un vértice efectivo con $k \geq 1$ burbujas $\boldsymbol{B}^{(k)}$ (ver Figura R.18). Dada la estructura de los vértices de burbuja, uno se da cuenta rápidamente de que, a diferencia de los de escalera, $\boldsymbol{B}^{(k)}(\mathrm{i}\omega_n + \mathrm{i}\nu_m, \mathrm{i}\omega_n, \boldsymbol{p})$ es independiente de la frecuencia y momento $(\mathrm{i}\omega_n, \boldsymbol{p})$ de la pata externa piónica si sólo se consideran vértices constantes de cuatro piones. Por tanto, la contribución de esos diagramas a la conductividad se anula por paridad. De hecho, siguiendo el argumento de la paridad, las únicas contribuciones de un diagrama con $k+1$ burbujas que no se anulan por paridad son aquellas en las que todos los vértices

de cuatro piones contienen el factor $\boldsymbol{p}_i \cdot \boldsymbol{p}_{i+1}$ $(i = 1, \ldots, k)$, donde p_i es el momento que "corre" a través de la burbuja i. Enfatizamos que consideramos sólo vértices piónicos del lagrangiano $\mathcal{L}_2$, vértices de orden más alto están suprimidos por contaje de Weinberg y lo mismo pasa para burbujas formadas por más líneas piónicas (así que contienen vértices de más de cuatro piones). Por lo tanto, el vértice efectivo de burbujas satisface una relación de recurrencia de la forma:

$$\boldsymbol{B}^{(k)}(\mathrm{i}\nu_m, \boldsymbol{p}) = \int \frac{\mathrm{d}^3\boldsymbol{p}_2}{(2\pi)^3} \, \frac{\boldsymbol{p}\cdot\boldsymbol{p}_2}{F_\pi^2} \, T \sum_{n=-\infty}^{\infty} \boldsymbol{B}^{(k-1)}(\mathrm{i}\nu_m, \boldsymbol{p}_2) \Delta_\Gamma(\mathrm{i}\omega_n, |\boldsymbol{p}_2|) \Delta_\Gamma(\mathrm{i}\omega_n + \mathrm{i}\nu_m, |\boldsymbol{p}_2|) \ . \tag{R.28}$$

La forma simple de los vértices de burbujas permite sumarlos todos explícitamente, puesto que constituyen básicamente una serie geométrica. Entonces, la contribución a la conductividad de la suma de diagramas de burbujas es de la forma:

$$\begin{aligned} \sigma_{\mathrm{bub}} &= \frac{e^2}{3} \lim_{\omega\to 0^+} \frac{1}{T} \int \frac{\mathrm{d}^3\boldsymbol{p}}{(2\pi)^3} \frac{n_{\mathrm{B}}(E_p)\,[1+n_{\mathrm{B}}(E_p)]}{4E_p^2\Gamma_p} \,\mathrm{Re} \sum_{k=1}^{\infty} 2\boldsymbol{p}\cdot\boldsymbol{B}^{(k)}(\omega,\boldsymbol{p}) \\ &= 2e^2 \lim_{\omega\to 0^+} \mathrm{Re} \sum_{k=1}^{\infty} F^{(k)}(\omega) = \sigma^{(0)}(T) \lim_{\omega\to 0^+} \mathrm{Re}\, \frac{\mathrm{i}\omega I(T)/F_\pi^2}{1-\mathrm{i}\omega I(T)/F_\pi^2} \\ &= \mathcal{O}(\omega^2)\sigma^{(0)}(T) \ . \end{aligned} \tag{R.29}$$

Tras considerar la contribución total de diagramas que involucran piones neutros y cargados, obtenemos $\sigma_{\mathrm{bub}} = \mathcal{O}(\omega^2)\sigma^{(0)}(T)$. Queremos enfatizar que el orden dominante en los vértices de burbujas proviene de los "pinching poles" en los productos $G_{\mathrm{R}}G_{\mathrm{A}}$ y da lugar a las contribuciones $\mathcal{O}(\omega/\Gamma)$ analizadas anteriormente. El siguiente orden al dominante podría dar lugar a una contribución no nula en el límite $\omega \to 0^+$, pero no a términos $1/\Gamma$ (las integrales $I(T)$ mostradas anteriormente) y por tanto suprimida por contaje ordinario de ChPT, así que típicamente los factores $\omega I(T)$ en la suma (R.29) serían remplazados por una contribución $\mathcal{O}(p^2)$. Así que nuestra conclusión es que los diagramas de burbujas son subdominantes a toda temperatura dentro del rango de validez de ChPT.

R.3.4 Resultados para coeficientes de transporte

Conductividad eléctrica DC

Hemos visto que la contribución dominante a la conductividad DC a temperaturas bajas, correspondiente al diagrama R.16, está dada por la fórmula (R.23). Es interesante comparar nuestro resultado con el comportamiento esperado de teoría cinética. De acuerdo con teoría cinética, $\sigma \sim e^2 n_{\mathrm{ch}} \tau / M_\pi$ (n_{ch} es la densidad de partículas cargadas, τ es el tiempo medio de colisión, y e es la carga de la partícula), y $\tau \sim 1/\Gamma$, $\Gamma \sim nv\sigma_{\pi\pi}$ (v es la velocidad media de las partículas). En el límite no-relativista ($T \ll M_\pi$), $n \sim (\sqrt{M_\pi T})^3 \mathrm{e}^{-M_\pi/T}$, $v \sim \sqrt{T/M_\pi}$, y $\sigma_{\pi\pi}$ es una constante, por tanto $\sigma \sim 1/\sqrt{T}$. Así que nuestro resultado en ChPT es consistente con teoría cinética para $T \ll M_\pi$.

En la Figura R.19 representamos la contribución dominante a la conductividad eléctrica como función de la temperatura para distintas elecciones de las amplitudes de dispersión que entran en la anchura del pión. Vemos que la unitariedad (resonancias) hace que

la conductividad crezca a partir de cierta temperatura en adelante, de otro modo decrecería con T asintóticamente hacia cero. El comportamiento creciente con T es también obtenido en cálculos en el retículo [Gup04]. Los puntos en la Figura corresponden a unitarizar las amplitudes de dispersión a temperatura finita. Vemos que la evolución térmica de las resonancias no afecta mucho a la conductividad. Un efecto más significativo se observa al introducir densidad nuclear de modo efectivo variando F_π según (R.9), pero únicamente a temperaturas bajas (como podemos ver en la Fig. R.19, a temperaturas altas $\sigma^{(0)}$ es aproximadamente constante, indicando que los efectos del medio podrían no ser importantes en ese régimen).

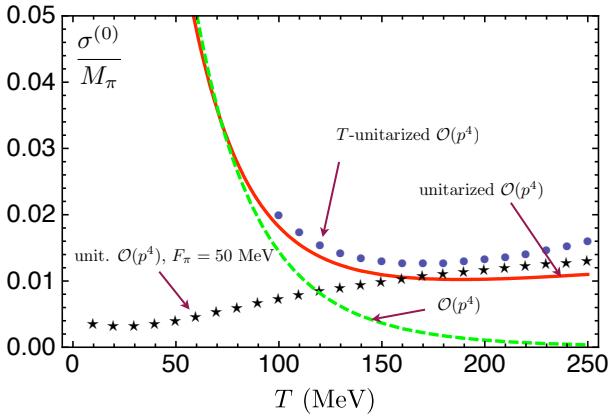

Figura R.19: Contribución dominante a la conductividad DC como función de la temperatura. La línea discontinua corresponde a considerar ondas parciales no-unitarizadas a orden $\mathcal{O}(p^4)$ en la anchura del pión, la línea roja representa el caso unitarizado a orden $\mathcal{O}(p^4)$, y los puntos corresponden a unitarizar a temperatura finita a $\mathcal{O}(p^4)$. Las estrellas corresponden a ondas parciales unitarizadas a orden $\mathcal{O}(p^4)$ con $F_\pi = 50$ MeV ($\rho \simeq 2\rho_0$) simulando densidad nuclear de acuerdo con (R.9).

Espectro de fotones a muy baja energía

Como aplicación fenomenológica del cálculo de la conductividad eléctrica, consideramos ahora el espectro de fotones producidos por un gas hadrónico en el límite de muy bajas energías. El ritmo diferencial de emisión de fotones por parte de un plasma termalizado está relacionado directamente con la función espectral del correlador de dos corrientes electromagnéticas [Ala01] mediante:

$$\omega \frac{\mathrm{d}R_\gamma}{\mathrm{d}^3\boldsymbol{p}} = \frac{1}{8\pi^3} n_{\mathrm{B}}(\omega) \rho^\mu{}_\mu(\omega = |\boldsymbol{p}|) \ . \tag{R.30}$$

La identidad de Ward $p^\mu \rho_{\mu\nu} = 0$ implica $\rho_{00}(\omega \neq 0, \boldsymbol{p} = 0) = 0$, de modo que la conductividad eléctrica proporciona información directa sobre el límite cero de energías ($\omega \to 0^+$) en la región estática [Gup04, Bla05] simplemente como $\omega \mathrm{d}R_\gamma/\mathrm{d}^3\boldsymbol{p}(\omega \to 0^+, \boldsymbol{p} = 0) = 3T\sigma(T)/(4\pi^3)$, esto es, una conductividad no nula implica un valor constante del espectro de fotones cerca del origen.

Con esta motivación en mente, compararemos nuestros resultados para la conductividad a las temperaturas de relevancia física en una colisión de iones pesados con análisis

recientes, tanto teóricos como experimentales, del espectro de fotones hadrónico a bajas energías. Usando la anchura unitarizada, obtenemos a energía cero $3T\sigma/(4\pi^3) \simeq 3{,}7 \times 10^{-3}$ GeV^{-2}fm^{-4} para $T = 150$ MeV. Por lo tanto, predecimos un valor apreciable para el espectro de fotones hadrónico en el origen. Una extrapolación lineal de la curva de baja energía ($\omega \simeq 200$ MeV) en [Tur04] hasta el origen da un valor de aproximadamente 2×10^{-3}GeV^{-2}fm^{-4} para $T = 150$ MeV. Esto indica que nuestra predicción se encuentra en el rango de valores correcto.

Estableceremos ahora una comparación más directa con los datos experimentales, teniendo en cuenta que nuestro método sólo proporciona información para energías muy próximas al origen. Uno entonces debe integrar el ritmo de emisión en (R.30) sobre la evolución espacio-temporal del plasma y promediar sobre la "rapidity" del fotón [Tur04] para así obtener el espectro de fotones medido $\omega \mathrm{d}N_\gamma/\mathrm{d}^3\boldsymbol{p}$ como función de p_T, la componente del momento del fotón transversa al eje de colisión en el sistema de referencia del laboratorio. Obviamente, los resultados dependen fuertemente de la evolución hidrodinámica en el espacio-tiempo para las condiciones aplicables a un experimento particular. Aquí daremos simplemente una primera estimación, asumiendo una simple descripción hidrodinámica de Bjorken [LB96, Pei02] ignorando el efecto del flujo transverso. De modo que $\omega = p_\mathrm{T}\cosh(y-\eta)$, con y y η las "rapidities" del fotón y el fluido respectivamente. Por tanto, nuestro valor para $\omega \to 0^+$ se traduce directamente en el valor del flujo de emisión para $p_\mathrm{T} \to 0^+$. En cuanto a la integración espacio-temporal, usamos el valor típico [LB96, Pei02] para el radio transverso nuclear $R_A \simeq 1{,}3 \text{ fm } A^{1/3} \simeq 7{,}7$ fm para ^{208}Pb y cambiamos a coordenadas de tiempo propio τ y rapidez η. En el límite de Bjorken y para $p_\mathrm{T} \to 0^+$, no hay dependencia con la rapidez de modo que simplemente tenemos que multiplicar por la velocidad de expansión [Pei02] $\Delta\eta_\mathrm{nucl} = 2\mathrm{arccosh}(\sqrt{s}/2A \text{ GeV}) \simeq 10{,}1$, para las energías de colisión de WA98 $\sqrt{s} = 158A$ GeV. Con estas aproximaciones, el espectro de fotones en el origen está dado por:

$$\omega\frac{\mathrm{d}N_\gamma}{\mathrm{d}^3\boldsymbol{p}}(p_\mathrm{T}\to 0^+) \simeq \pi R_A^2 \Delta\eta_\mathrm{nucl}\int_{\tau_\mathrm{i}}^{\tau_\mathrm{f}} \frac{3T(\tau)\sigma(T(\tau))}{4\pi^3}\,\tau\mathrm{d}\tau\ . \tag{R.31}$$

Una estimación burda se obtiene asumiendo una fase hadrónica a temperatura constante en el tiempo. Tomando los valores de tiempo propio $\tau_\mathrm{i} = 1$ fm/c y $\tau_\mathrm{f} = 13$ fm/c [Tur04] y $T = 150$ MeV, esto da un valor para el espectro en el origen de $\mathrm{d}N_\gamma/\mathrm{d}^3\boldsymbol{p}(p_\mathrm{T}=0) \simeq 5{,}8\times 10^2$. Una aproximación más realista consiste en considerar la ley de enfriamiento de un gas ideal $T(\tau) = T_\mathrm{i}(\tau_\mathrm{i}/\tau)^{1/3}$ [LB96], que es probablemente todavía demasiado exagerada para mesones a temperaturas moderadas y altas. Tomando $\tau_\mathrm{i} = 3$ fm/c, para la fase hadrónica, $\tau_\mathrm{f} = 13$ fm/c y $T_\mathrm{i} = 170$ MeV, obtenemos $T_\mathrm{f} = 104$ MeV que es del mismo orden que la temperatura de "freeze-out" térmico. Insertando esta ley en (R.31) junto con la conductividad unitarizada de la Figura R.19 resulta $\mathrm{d}N_\gamma/\mathrm{d}^3\boldsymbol{p}(p_\mathrm{T}=0) \simeq 5{,}6 \times 10^2$ (indicamos este valor en la gráfica de la Fig. R.20) aunque este resultado es muy sensible a variaciones en la temperatura.

Tomando los dos puntos experimentales de más bajo p_T en [Agg04] y simplemente extrapolando linealmente desde ellos al origen tenemos $\mathrm{d}N_\gamma/\mathrm{d}^3\boldsymbol{p}(p_\mathrm{T}=0) \simeq 5 \times 10^2$. Por consiguiente, nuestros resultados a energías muy bajas, para las que la componente hadrónica del gas se espera que domine, son compatibles con los datos experimentales recientes en el sentido de una simple extrapolación lineal. Nuestro análisis del gas de

piones también sugiere que considerar una anchura térmica no-nula para el fotón, no considerada en análisis previos [Ste96, Ste97, Ala01, Rap99, Tur04], puede ser relevante para disminuir el valor del espectro de fotones a energías muy bajas y eventualmente hacerlo finito en el origen (esencialmente debido al efecto LPM [Liu07]).

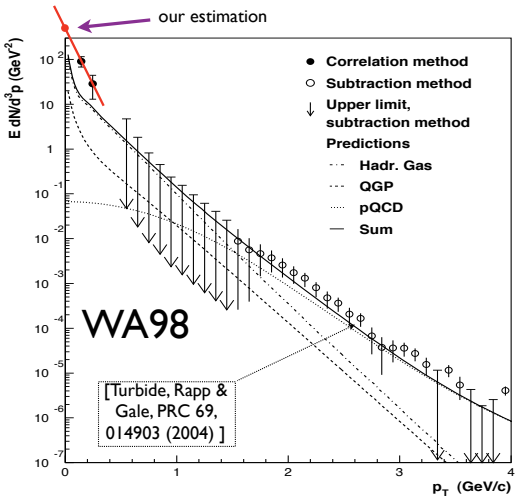

Figura R.20: Espectro de fotones obtenido por el experimento WA98 [Agg04]. Nuestra estimación en el origen es compatible con una extrapolación lineal a partir de los dos puntos experimentales de energía más baja.

Conductividad térmica

Aunque en el caso del pión la única carga que es estrictamente conservada es la energía, en el régimen de temperaturas y energías para el gas de hadrones propio de una colisión relativista de iones pesados, es una buena aproximación asumir que colisiones $2 \to 2$ son los únicos procesos relevantes, que en la práctica significa que el número de piones es aproximadamente conservado (ver Capítulo 4 de la tesis), dando lugar a una conductividad térmica no nula incluso cuando el potencial químico es muy pequeño [Gav85]. La conductividad térmica se calcula mediante la relación

$$\kappa = -\frac{\beta}{6} \lim_{\omega \to 0^+} \lim_{|\boldsymbol{p}| \to 0^+} \frac{\rho_\kappa(\omega, |\boldsymbol{p}|)}{\omega} \ , \tag{R.32}$$

donde

$$\rho_\kappa(\omega, |\boldsymbol{p}|) = \int \mathrm{d}^4x \ \mathrm{e}^{\mathrm{i}p\cdot x} \langle [\hat{\mathcal{T}}^i(x), \hat{\mathcal{T}}_i(0)] \rangle \ , \tag{R.33}$$

con $\mathcal{T}^i \equiv T^{i0} - hN^i$. Bajo la suposición de un número de partículas aproximadamente conservado, los promedios térmicos contendrán ahora sumas sobre estados de número bien definido de partículas, $|N\rangle$. Por tanto, puesto que para el diagrama de la Figura R.16, el tensor energía-impulso entra al orden más bajo (sin interacción), y basándonos en las

expresiones de teoría cinética en equilibrio:

$$T^{i0} = \int \frac{\mathrm{d}^3\boldsymbol{p}}{(2\pi)^3}\, E_p v^i n_{\mathrm{B}}(E_p) \ , \tag{R.34}$$

$$N^{i} = \int \frac{\mathrm{d}^3\boldsymbol{p}}{(2\pi)^3}\, v^i n_{\mathrm{B}}(E_p) \ , \tag{R.35}$$

con $v^i = p^i/E_p$, definimos el operador $\hat{N}^i$ por medio de su regla de Feynman para el vértice en espacio de momentos heurísticamente como $N^i \equiv T^{i0}/E_p$ (se entiende implícitamente el límite de momento externo igual a cero). De acuerdo con esta definición, la contribución de orden más bajo a la conductividad térmica viene dada por:

$$\kappa^{(0)} = \frac{1}{8\pi^2 T^2} \int_0^\infty \mathrm{d}|\boldsymbol{p}|\ \frac{|\boldsymbol{p}|^4 (E_p - h)^2}{E_p^2 \Gamma_p} n_{\mathrm{B}}(E_p)[1 + n_{\mathrm{B}}(E_p)] \ , \tag{R.36}$$

siendo h el resultado *exacto* para la entalpía por partícula. Sin embargo, en nuestros cálculos aproximaremos $h \equiv (\epsilon + P)/n = Ts/n$ (s es la densidad de entropía y n la densidad de partículas) por el resultado obtenido para un gas ideal, ya que esperamos que esta aproximación sea razonable para temperaturas bajas. A muy baja temperatura, $T \ll M_\pi$, tenemos:

$$\kappa^{(0)} \simeq 63\ \frac{T^{1/2} F_\pi^4}{M_\pi^{5/2}} \ . \tag{R.37}$$

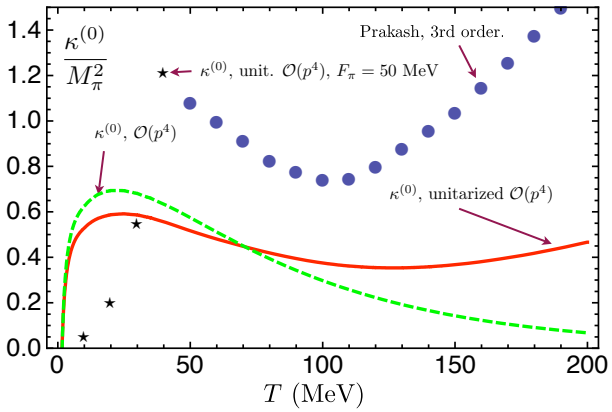

Figura R.21: Contribución de orden más bajo a la conductividad térmica como función de la temperatura. Comparamos con el análisis de [Pra93], basado en teoría cinética.

Por teoría cinética [Lif81], $\kappa \sim T^{-1}(\bar{e} - h) l v$ ($\bar{e}$ es la energía media por partícula y $l \sim 1/(\sigma_{\pi\pi} n)$ es el recorrido libre medio). En el límite no-relativista, $\bar{e} \sim M_\pi$, $h \sim 5T/2 + M_\pi$, y entonces $\kappa \sim T^{1/2}$, de modo que es compatible con nuestros resultados para temperaturas muy bajas. En la Figura R.21 comparamos nuestros resultados para κ con el análisis de teoría cinética en [Pra93]. De nuevo, la unitariedad hace que cambie el comportamiento de la conductividad térmica con la temperatura, mostrando un mínimo cerca de $T = 140$ MeV. Los efectos de densidad modifican apreciablemente la conductividad térmica a temperaturas altas, como es de esperar al introducir una carga conservada extra (el número bariónico).

Viscosidad de cizalla

La viscosidad de cizalla viene dada en LRT por

$$\eta = \frac{1}{20} \lim_{\omega\to 0^+} \lim_{|\boldsymbol{p}|\to 0^+} \frac{\rho_\eta(\omega,|\boldsymbol{p}|)}{\omega} \ , \tag{R.38}$$

con

$$\rho_\eta(\omega,|\boldsymbol{p}|) = \int \mathrm{d}^4x \ \mathrm{e}^{\mathrm{i}p\cdot x}\langle[\hat{\pi}^{ij}(x),\hat{\pi}_{ij}(0)]\rangle \ , \tag{R.39}$$

y $\pi^{ij} \equiv T^{ij} - g^{ij}T^k{}_k/3$. La contribución de orden más bajo es:

$$\eta^{(0)} = \frac{1}{10\pi^2 T}\int_0^\infty \mathrm{d}|\boldsymbol{p}| \ \frac{|\boldsymbol{p}|^6}{E_p^2\Gamma_p} n_{\mathrm{B}}(E_p)[1+n_{\mathrm{B}}(E_p)] \ . \tag{R.40}$$

Para temperaturas muy bajas, $T \ll M_\pi$, esta expresión adopta la forma

$$\eta^{(0)} \simeq 37\frac{T^{1/2}F_\pi^4}{M_\pi^{3/2}} \ . \tag{R.41}$$

En la Figura R.22 comparamos nuestros resultados para la viscosidad de cizalla con el obtenido por Prakash y colaboradores usando un análisis de teoría cinética [Pra93]. Nuestro resultado también está en buen acuerdo con el obtenido en el trabajo [Dob04] basado en teoría cinética con amplitudes del IAM. Observamos que los efectos de densidad nuclear sólo implicarían un cambio significante en la viscosidad de cizalla a temperaturas bajas. Por otra parte, por teoría cinética no relativista, esperamos el comportamiento $\eta, \zeta \sim M_\pi vnl$, de modo que $\eta, \zeta \sim \sqrt{T}$ y ambas viscosidades serían del mismo orden a temperaturas muy bajas[2].

La unitariedad hace que el cociente η/s (s es la densidad de entropía) para el gas de piones respete la cota $1/(4\pi)$ conjeturada por Kovtun y colaboradores para todo tipo de materia [Kov05], como podemos ver en Fig. R.23. Sin implementar la unitarización, el Principio de Incertidumbre sería también violado eventualmente, puesto que $\eta/s \sim \epsilon\tau/n \sim E\tau \gtrsim 1$. Además, cerca de T_c nuestro valor para η/s no se encuentra lejos de estimaciones recientes en el retículo y otros modelos teóricos [Nak05]. Aunque no lo representamos en la figura, obtenemos que η/s comienza a crecer muy suavemente con la temperatura para $T > 550$ MeV, aunque son temperaturas donde nuestro tratamiento es claramente no aplicable. Un comportamiento lentamente creciente para este cociente se obtiene también mediante cálculos de alta temperatura en la fase de Plasma de Quarks y Gluones (QGP) [Cse06]. Es también notable el hecho de que el resultado obtenido en AdS/CFT, $\eta/s = 1/(4\pi)$, es independiente de la temperatura [Kov05]. Sin embargo, un análisis reciente predice un incremento pronunciado de la viscosidad de cizalla cerca de la transición de fase, en la llamada fase de semi-QGP [Hid08b, Hid08a]. Es bien conocido

[2]Sin embargo, a esas temperaturas deben tenerse en cuenta procesos inelásticos en el cálculo de la viscosidad de volumen, que cambian cualitativamente su comportamiento. Ver comentarios en la Secciones 3.1.2 y 3.4.4 de la tesis.

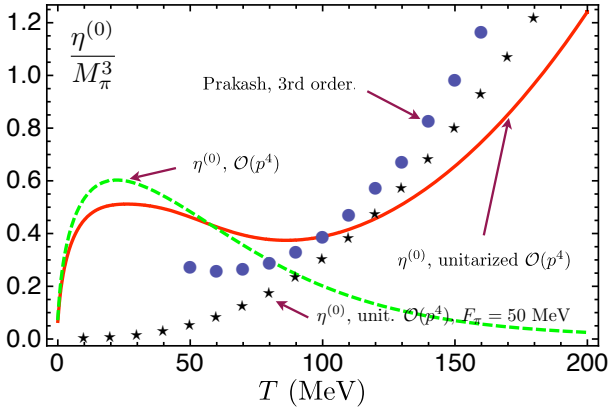

Figura R.22: Contribución de orden más bajo a la viscosidad de cizalla como función de la temperatura para varias aproximaciones en la amplitud de dispersión. También se compara con los resultados basados en teoría cinética de [Pra93] (puntos).

que la cantidad η/s presenta un mínimo en la temperatura de una transición de fase para varias sustancias comunes [Cse06, Dob09], y por tanto se espera que este mínimo también ocurra en QCD a la temperatura crítica. Más adelante, veremos que el comportamiento de η/s con el número de colores en el límite de gran-N_c a ambos lados de la transición de fase es también compatible con la existencia de un mínimo.

Con la curva obtenida para η/s podemos calcular también la longitud de atenuación del sonido, como comprobación extra de la consistencia de nuestro resultado, que viene dada por (despreciando la contribución de la viscosidad de volumen) $\Gamma_s \simeq 4\eta/(3sT)$, y está directamente relacionada con efectos fenomenológicos tales como *flujo elíptico* o *radios de HBT*. Obtenemos por tanto, para $T = 180$ MeV, el valor $\Gamma_s \simeq 0{,}55$ fm, que es compatible con la estimación de Teaney en [Tea03].

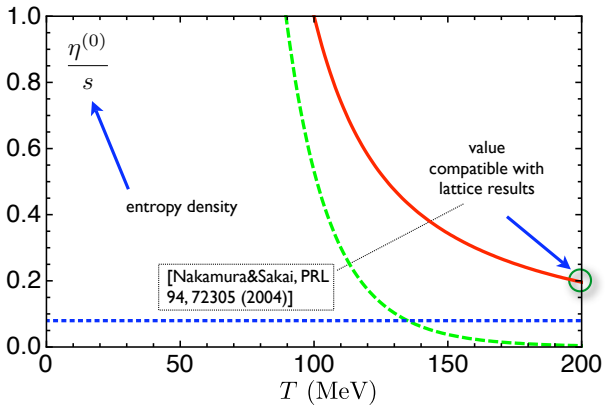

Figura R.23: Viscosidad de cizalla dividida por la densidad de entropía como función de la temperatura. La línea horizontal discontinua corresponde a la cota $1/(4\pi)$ de AdS/CFT.

Viscosidad de volumen y anomalía de traza

Como hemos mencionado, se ha propuesto recientemente que la viscosidad de volumen, ζ, podría ser mayor de lo esperado cerca de la transición de fase de QCD. Los autores de [Kar08], usando reglas de suma de QCD [Ell98, Shu99], establecen la siguiente relación entre la viscosidad de volumen y la anomalía de traza de QCD:

$$\zeta(T) = \frac{1}{9\omega_0(T)} \left[T^5 \frac{\partial}{\partial T} \frac{\langle\theta\rangle_T - \langle\theta\rangle_0}{T^4} + 16|\epsilon_{\rm v}| \right] , \tag{R.42}$$

donde $\omega_0 \sim 1$ GeV es un parámetro del ansatz utilizado para la densidad espectral, $\epsilon_{\rm v}$ es la densidad de energía del vacío, $\langle\theta\rangle_T \equiv \langle T^\mu_\mu\rangle_T = \epsilon - 3P \equiv$ es la anomalía de traza a temperatura finita, con T^μ_μ el tensor energía-impulso, ϵ la densidad de energía, y P la presión. Esta ecuación implica que la viscosidad de volumen sería importante cerca de la transición de fase de QCD, dado que el valor de $\langle\theta\rangle_T$ calculado en el retículo presenta un pico a esas temperaturas [Che08], más o menos pronunciado dependiendo del orden de la transición [Kar08].

Es por tanto de gran importancia intentar clarificar la validez de la relación (R.42) en regímenes de QCD donde los cálculos analíticos son robustos y así no necesitar recurrir a resultados del retículo. En el régimen de acoplo débil, válido a temperaturas altas, se sabe que ζ/η es paramétricamente pequeño [Arn06b]. En el régimen de QCD de bajas energías y temperaturas (por debajo de la transición), donde el sistema consiste principalmente de mesones, uno también puede llevar a cabo cálculos analíticos por medio de la Teoría de Perturbaciones Quiral [Ger89].

La viscosidad de volumen se define en LRT en completo equilibrio termodinámico (térmico + químico). Para un gas de piones masivos, a temperaturas muy bajas, ζ está dominada por procesos inelásticos en el gas [Jeo95] (y esto juega un importante papel en la resumación de los diagramas de escalera). Sin embargo, nosotros ignoraremos los procesos inelásticos $2\pi \leftrightarrow 4\pi$, suprimidos en nuestro contaje de ChPT (de acuerdo con el análisis diagramático de la Sección R.3.3), y consideraremos en su lugar la situación de no-equilibrio químico en la que sólo ocurren procesos de dispersión elástica en el gas de piones. Esta aproximación es razonable en el contexto de una colisión relativista de iones pesados donde, para temperaturas comprendidas entre el "freeze-out" químico y térmico, el número de partículas se mantiene aproximadamente conservado [Hun98, Kol03]. A partir de la fórmula de Kubo para la viscosidad de volumen (ver Sección 1.6.3 de la tesis), que involucra el correlador de la traza del tensor energía-impulso, obtenemos el siguiente resultado al orden más bajo:

$$\zeta^{(0)} = \int_0^\infty {\rm d}p \; \frac{3p^2(p^2/3 - c_{\rm s}^2 E_p^2)^2}{4\pi^2 T E_p^2 \Gamma_p} \, n_{\rm B}(E_p)[1 + n_{\rm B}(E_p)] \; , \tag{R.43}$$

donde $c_{\rm s}$ es la velocidad del sonido en el gas, que calculamos a partir de la presión P usando el cálculo perturbativo a $\mathcal{O}(T^8)$ en [Ger89]. En la Figura R.24 vemos que a orden $\mathcal{O}(T^6)$, el calor específico y la velocidad del sonido aumentan monótonamente con la temperatura, aproximándose $c_{\rm s}^2$ al límite ultra-relativista 1/3 correspondiente a un gas de

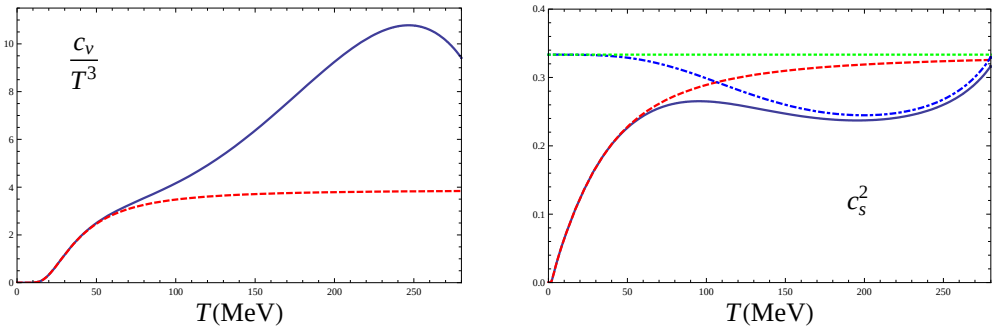

Figura R.24: Calor específico (izquierda) y velocidad del sonido al cuadrado (derecha) para el gas de piones. La línea roja discontinua corresponde al cálculo a $\mathcal{O}(T^6)$, mientras que la línea azul continua es el cálculo a $\mathcal{O}(T^8)$. La línea punteada verde corresponde al límite ultra-relativista $c_s^2 = 1/3$. La línea de punto y rayas es el resultado en el límite quiral a orden $\mathcal{O}(T^8)$.

piones masivos libres. A temperaturas altas, $T \gg M_\pi$ (estrictamente nuestro resultado no es aplicable en ese régimen), el momento es de orden $p \sim T$, y vemos que (R.43) se anula asintóticamente con la temperatura, como es de esperar en un sistema invariante conforme [Arn06b, Hos84, Gav85, Pra93]. De hecho, a partir de (R.43) obtenemos que para un gas de piones sin masa (límite quiral):

$$\zeta^{(0)} = 15(1/3 - c_s^2)^2 \eta^{(0)} \ , \tag{R.44}$$

consistentemente con [Hor87] y paramétricamente consistente con QCD a altas temperaturas [Arn06b]. El punto crucial aquí es que considerando un orden más en la presión c_v crece, alcanzando un máximo aproximadamente en $T_c \simeq 220$ MeV [3]. La velocidad del sonido tiene un mínimo entonces en T_c que alterará el comportamiento de $\zeta(T)$. Nótese que, aunque en el caso masivo T_c es próximo a la temperatura de restauración quiral T_c^χ donde el parámetro de orden $\langle \bar{q}q \rangle_T$ se anula[Ger89], en el límite quiral $T_c^\chi \simeq 170$ MeV, mientras que T_c permanece prácticamente inalterada, lo cual indica que la restauración de la simetría quiral no es la principal fuente de este pico.

Representamos nuestro resultado para la viscosidad de volumen en la Figura R.25. El efecto de incluir el orden $\mathcal{O}(T^8)$ en c_s^2 da lugar a un pico en torno a T_c, no presente en el resultado a orden $\mathcal{O}(T^6)$. La velocidad del sonido no es el único efecto relevante que da lugar a un pico apreciable: la unitarización de la sección eficaz de dispersión, que entra en Γ_p, es también crucial a orden $\mathcal{O}(T^8)$. Consistentemente, hemos escogido los valores de las constantes de baja energía $\bar{l}_i$ que entran en las amplitudes de dispersión de piones de modo que la masa y anchura de la ρ coincidan con sus valores físicos para $T = 0$. Como comentamos más abajo, la dependencia en las constantes $\bar{l}_i$ es crucial en el presente análisis. Nuestros resultados en el límite quiral están en acuerdo razonable con un análisis reciente de teoría cinética [Che09]. También obtenemos en la viscosidad de volumen un pico a bajas temperaturas, que desaparece en el límite quiral. En el régimen

[3] Denotamos en esta sección con T_c a la temperatura del pico anómalo en la anomalía de traza, no confundir con T_c^χ, la temperatura crítica de la transición de fase quiral.

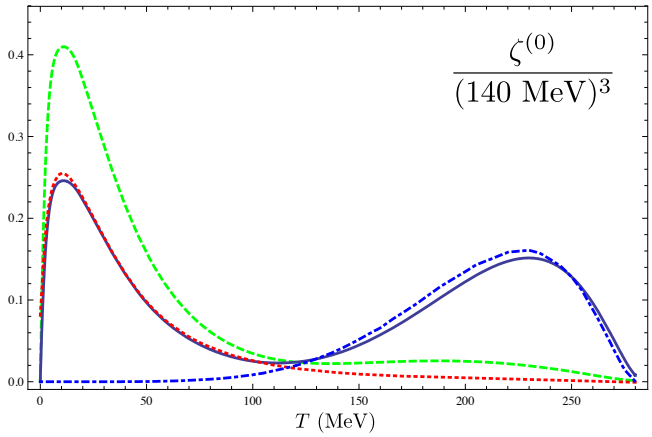

Figura R.25: Viscosidad de volumen para el gas de piones. La línea azul continua corresponde al resultado unitarizado con c_s^2 a orden $\mathcal{O}(T^8)$, y la línea azul de puntos y rayas corresponde al mismo cálculo en el límite quiral. La línea discontinua verde es el resultado no-unitarizado al mismo orden. La línea roja punteada es el el unitarizado con c_s^2 a orden $\mathcal{O}(T^6)$ y permanece muy cerca a la curva no-unitarizada, que no mostramos.

de muy bajas temperaturas, $T \ll M_\pi$, el orden más bajo (R.43) adopta la forma:

$$\zeta^{(0)} \simeq 13{,}3\,\frac{F_\pi^4\sqrt{T}}{M_\pi^{3/2}}\ , \quad \text{para} \quad T \ll M_\pi\ . \tag{R.45}$$

El comportamiento anterior es consistente con otros resultados de teoría cinética no-relativista [Gav85] donde se obtenía que ζ y η eran del mismo orden a temperaturas muy bajas (asumiendo únicamente procesos elásticos). De este modo, $\zeta(T)$ aumenta con T para temperaturas muy bajas, mientras que decrece para temperaturas muy altas al alcanzar el límite conforme asintóticamente, por lo que en algún punto intermedio debe haber un máximo, lo cual explica el máximo a bajas temperaturas debido a la ruptura explícita de la simetría de escala por parte de la masa del quark. El máximo anómalo en cambio tiene su origen puramente en la interacción. Calculemos ahora para el gas de piones las contribuciones que rompen la simetría conforme para el gas de piones. Primero, es instructivo recordar el resultado de la anomalía de traza de QCD [Col77]:

$$\partial_\mu s^\mu = T^\mu{}_\mu = \frac{\beta(g)}{2g}G^a_{\mu\nu}G_a^{\mu\nu} + (1+\gamma_m(g))\bar{q}Mq\ , \tag{R.46}$$

donde $s^\mu = T^{\mu\nu}x_\nu$ es la corriente de "dilatación", y las funciones del grupo de renormalización son, perturbativamente, $\beta(g) = \mathcal{O}(g^3)$, $\gamma_m(g) = \mathcal{O}(g^2)$. El primer término, que es proporcional al condensado de gluones, es la anomalía conforme. El segundo término proviene de la ruptura explícita en el lagrangiano de QCD, siendo M la matriz de masas de los quarks. A temperatura finita, el promedio térmico de la anomalía de traza viene dado en términos de cantidades termodinámicas, $\langle\theta\rangle_T \equiv \langle T^\mu{}_\mu\rangle_T = \epsilon - 3P$, y ha sido calculado en el retículo para la teoría con sólo gluones (sin quarks) [Boy96], así como para QCD con quarks de masa próxima a los valores físicos [Che08]. Para el gas de piones, usando

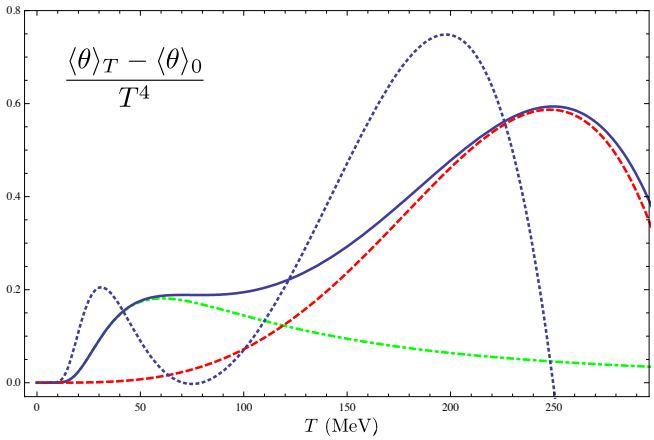

Figura R.26: Promedio térmico de la anomalía de traza para un gas de piones. Las línea verde de puntos y rayas y la línea continua azul son, respectivamente, los resultados a orden $\mathcal{O}(T^6)$ y $\mathcal{O}(T^8)$. La línea discontinua roja corresponde al resultado a orden $\mathcal{O}(T^8)$ para un gas de piones sin masa (el orden $\mathcal{O}(T^6)$ se anula para $M_\pi = 0$). La línea punteada azul es $T\frac{\partial}{\partial T}\frac{\langle\theta\rangle_T - \langle\theta\rangle_0}{T^4}$.

la relación entre la anomalía de traza y la presión

$$\langle\theta\rangle_T = T^5 \frac{\mathrm{d}}{\mathrm{d}T}\left(\frac{P}{T^4}\right), \tag{R.47}$$

representamos en la Figura R.26 la anomalía de traza para diferentes órdenes en la presión, así como el miembro de la derecha de la fórmula (R.42). Los diagramas que contribuyen a orden $\mathcal{O}(T^8)$ en el contaje de ChPT son los representados en la Figura R.31. Observamos claramente la misma estructura de dos picos que en la viscosidad de volumen, con características parecidas. El pico de baja temperatura desaparece en el límite quiral. Su contribución proviene de la ruptura explícita de la simetría de escala. En el límite quiral, la anomalía de traza tiene una expresión simple a este orden [Ger89, Leu88, Leu92]:

$$\langle T^\mu{}_\mu \rangle^* = \frac{\pi^2}{270}\frac{T^8}{F_\pi^4}\left(\ln\frac{\Lambda_\mathrm{p}}{T} - \frac{1}{4}\right), \tag{R.48}$$

con $\Lambda_\mathrm{p} \sim 400$ MeV para nuestra elección de $\bar{l}_i$.

El pico en la transición sólo aparece a orden $\mathcal{O}(T^8)$ y sobrevive en el límite quiral, donde su origen es puramente anómalo. Proviene de interacciones en ChPT que involucran acoplos dimensionales, tales como F_π, y es por tanto suprimido a temperaturas bajas [Leu92]. Para piones masivos, el valor del pico y su posición permanecen prácticamente inalterados con respecto al caso en el límite quiral. La contribución fermiónica también es pequeña en los análisis en el retículo [Che08]. Estos resultados muestran de nuevo que la naturaleza de este efecto probablemente no está relacionada con restauración de la simetría quiral, sino más bien con el confinamiento. La correlación con la viscosidad de volumen es de nuevo clara. De hecho, en el límite quiral, la función entre paréntesis en (R.42) y $15(c_\mathrm{s}^2 - 1/3)^2 = \zeta/\eta$ tienen su máximo en a la misma temperatura $T_\mathrm{c} = \mathrm{e}^{-5/8}\Lambda_\mathrm{p}$ con Λ_p dado en [Ger89] en términos de $\bar{l}_1 + 4\bar{l}_2$. Recordamos que para poder establecer la

posible correlación entre la anomalía conforme y la viscosidad de volumen, hemos usado el mismo conjunto de $\bar{l}_i$ en ambas gráficas. Para esos valores unitarizados, $T_c \simeq 220$ MeV. Usando los valores perturbativos, por ejemplo los dados en [Ger89], fijados para reproducir las longitudes de dispersión de piones, el pico crítico es unas tres veces más pequeño y $T_c \simeq 148$ MeV, mientras que T_c^χ varía tan solo unos 10 MeV de un conjunto de $\bar{l}$'s al otro. Obtenemos exactamente la misma reducción drástica del pico crítico y al desplazamiento de T_c en la viscosidad de volumen. La presencia de resonancias es por tanto crucial para conseguir un efecto apreciable en el pico anómalo, cuya contribución dominante proviene del condensado de gluones.

Los valores numéricos de la anomalía de traza en la Figura R.26 no están lejos de los valores del retículo [Che08] para temperaturas bajas, pero son un factor 10 más pequeños cerca de T_c. El aumento de los grados de libertad debido a estados más pesados, no incluidos en nuestro análisis, es claramente importante en esa región. De hecho, usando la Aproximación del Gas de Resonancias (HRG), la contribución a la anomalía por parte de los estados $\{\pi, \rho, \sigma\}$ equivale sólo a un 5 % de la de todos los estados bariónicos y mesónicos en el espectro hasta 2,5 GeV. De hecho, aunque obtenemos $\zeta/s \simeq 0{,}02$ en el pico de la transición, aún obtendríamos un valor mayor si asumimos que la introducción de estados más pesados aumenta la anomalía, lo que reduce c_s^2 [Kar08]. Como un indicativo, tomando $c_s^2 = 0$ en (R.43) obtenemos $\zeta/s \sim 1$ en T_c.

En la Figura R.27 representamos la medida de interacción, $(\langle\theta\rangle_T - \langle\theta\rangle_0)/T^4$, usando varias amplitudes de dispersión en la aproximación del gas del virial (VGA). El pico anómalo se obtiene cuando consideramos amplitudes $\mathcal{O}(p^4)$, y su altura es prácticamente igual a la obtenida con el cálculo diagramático de la Fig. R.26. También observamos que la evolución de $f_0(600)$ y $\rho(770)$ a temperatura y/o densidad finitas no cambia significativamente la altura de este pico. Como se ha comentado en secciones anteriores, es de esperar que la resonancia $f_0(600)/\sigma$ esté relacionada con la restauración de la simetría quiral. Dado que el pico anómalo no sufre apenas modificaciones al tomar el límite quiral, nuestro resultado sobre el efecto en la anomalía de traza de la evolución en el medio de las resonancias es también consistente con que el pico anómalo esté principalmente relacionado con el confinamiento (pues de hecho aparece en la teoría con gluones únicamente, donde no existe simetría quiral por definición).

Finalmente, en la Figura R.29 representamos la viscosidad de volumen dividida por la densidad de entropía. Mostramos explícitamente la importancia de introducir amplitudes de dispersión unitarizadas (resonancias) para poder reproducir el pico cerca de la transición de fase. Comparando con la Figura R.23, nuestro resultado para el cociente $\zeta^{(0)}/s$ es aún menor que $\eta^{(0)}/s$ cerca de la transición, aunque la correlación con la anomalía conforme es clara, y ello permite predecir una ζ/s mayor si los estados más pesados son incluidos. Sin embargo, estas son extrapolaciones basadas en un análisis de temperaturas bajas, y deben tomarse con cautela.

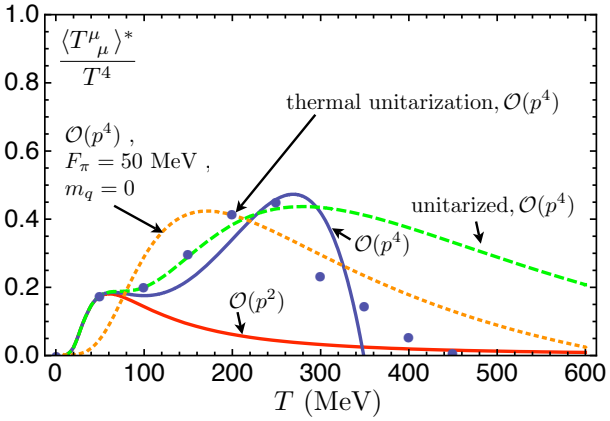

Figura R.27: Medida de interacción calculada en la VGA para varias amplitudes de dispersión. La evolución en el medio de las resonancias $f_0(600)$ y $\rho(770)$ no cambia significativamente la altura del pico de interacción.

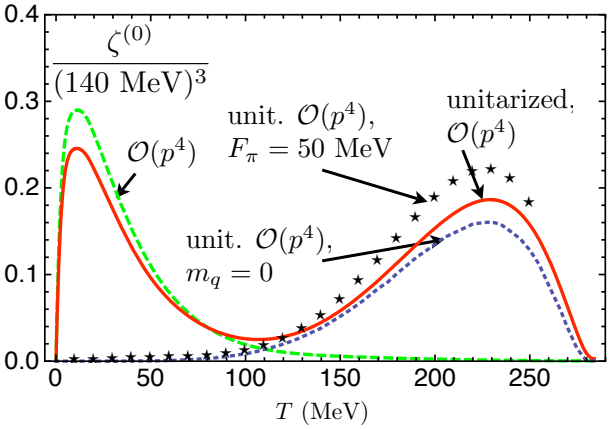

Figura R.28: Contribución al orden más bajo para la viscosidad de volumen de un gas de piones considerando diferentes aproximaciones en las amplitudes de dispersión.

R.3.5 Comportamiento de los coeficientes de transporte para N_c grande

El análisis del comportamiento con el número de colores, N_c, para $N_c \to \infty$ permite extraer interesante información cualitativa sobre diversas cantidades no-perturbativas en QCD [Man99]. En nuestro caso de ChPT, el contaje para gran N_c de las constantes de baja energía $\bar{l}_i$ puede extraerse a partir de las de SU(3), L_i [Man99, Gas84], mientras que $F_\pi^2 = \mathcal{O}(N_c)$. Esto implica que las amplitudes de dispersión $\pi\pi$ son $|T|^2 \sim \mathcal{O}(1/N_c^2)$, independientemente de si están unitarizadas o no, y por tanto obtenemos que la anchura es $\Gamma_p \sim \mathcal{O}(1/N_c^2)$. Este resultado, junto con el escaleo N_c de las cantidades termodinámicas $P \sim \epsilon \sim c_s^2 \sim s \sim \mathcal{O}(1)$, que extraemos de [Ger89], implica que todos los coeficientes de transporte escalean como $\mathcal{O}(N_c^2)$ para $M_\pi \neq 0$.

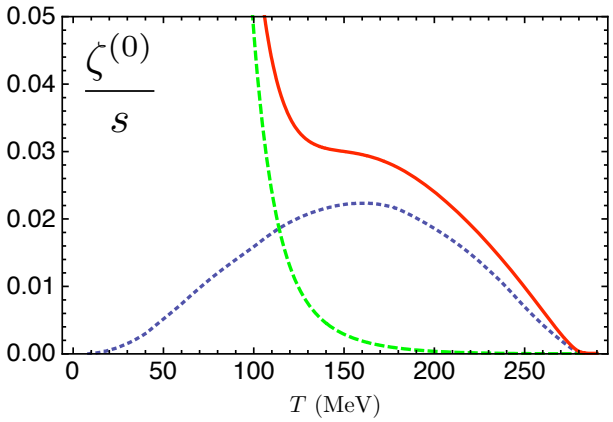

Figura R.29: Contribución al orden más bajo a la viscosidad de volumen dividida por la densidad de entropía para un gas de piones. Las curvas corresponden a los mismos casos que en la Figura R.28.

Sin embargo, en el límite quiral, a partir de la expresión de la presión [Ger89]

$$P = \frac{\pi^2}{30} T^4 \left[1 + \frac{T^4}{36 F_\pi^4} \ln \frac{\Lambda_\mathrm{p}}{T} + \mathcal{O}(T^6) \right] , \tag{R.49}$$

y teniendo en cuenta que $\ln \Lambda_\mathrm{p} \sim \bar{l}_1 + 4\bar{l}_2 \sim \mathcal{O}(N_\mathrm{c})$, obtenemos que en este límite $c_\mathrm{s}^2 - 1/3 \sim \mathcal{O}(\ln \Lambda_\mathrm{p}/F_\pi^4) \sim \mathcal{O}(1/N_\mathrm{c}) \sim \langle\theta\rangle_T$. Ahora, dado que $\zeta/\eta \sim \mathcal{O}(c_\mathrm{s}^2 - 1/3)^2$ en el límite quiral, y puesto que el contaje anterior para la anchura es también válido en este límite, esto significa que para $M_\pi = 0$, el escaleo de la viscosidad de volumen es $\zeta \sim \mathcal{O}(1)$, a diferencia de otros coeficientes que todavía escalean como $\mathcal{O}(N_\mathrm{c}^2)$. Resumiendo:

$$\sigma \sim \kappa \sim \zeta \sim \eta \sim \zeta/s \sim \eta/s \sim \mathcal{O}(N_\mathrm{c}^2) \qquad (M_\pi \neq 0) , \tag{R.50}$$

$$\sigma \sim \kappa \sim \eta \sim \eta/s \sim \mathcal{O}(N_\mathrm{c}^2) , \quad \zeta \sim \zeta/s \sim \mathcal{O}(1) \quad (M_\pi = 0) . \tag{R.51}$$

Estas relaciones de escaleo son consistentes con los resultados obtenidos previamente para los coeficientes de transporte. La viscosidad de volumen está suprimida con respecto a la viscosidad de cizalla en el límite quiral, como consecuencia de la invariancia de escala, aunque esto es sólo una dependencia paramétrica y no tiene en cuenta la ruptura anómala cerca de la transición. Para $M_\pi \neq 0$, la ruptura explícita de la invariancia conforme vuelve a los dos coeficientes comparables, como obtenemos a temperaturas bajas, donde los términos de masa dominan. Para temperaturas más altas, el resultado del límite quiral se alcanza asintóticamente. Nótese también que el escaleo en N_c para $M_\pi \neq 0$ es compatible con nuestras expresiones al orden más bajo (R.24), (R.37), (R.41) y (R.45). El comportamiento con N_c es también útil para entender el origen de los distintos términos que rompen la simetría conforme cerca de la transición de fase. Teniendo en cuenta el comportamiento crítico, obtenemos $T_\mathrm{c} \sim \mathcal{O}(\mathrm{e}^{N_\mathrm{c}})$ y $\langle\theta\rangle_{T_\mathrm{c}} \sim \mathcal{O}(\mathrm{e}^{N_\mathrm{c}}/N_\mathrm{c}^2)$. Esta dependencia exponencial con N_c es otra indicación del dominio de confinamiento sobre la restauración quiral, comparando con la temperatura quiral $T_\mathrm{c}^\chi = \mathcal{O}(N_\mathrm{c})$. Además, $\langle\theta\rangle \propto L_3$, que en el límite de gran N_c incluye un término proporcional al condensado de gluones [Esp90]. En el caso de piones masivos, el escaleo anterior del límite quiral se alcanza sólo asintóticamente para T grande, mientras que para cualquier T obtenemos $\zeta/\eta \sim \mathcal{O}(1) \sim \langle\theta\rangle_T - \langle\theta\rangle_0$ con

$\zeta \sim \mathcal{O}(N_c^2)$, compatible con (R.45). Finalmente, comparando con los resultados de QCD a temperaturas altas, a partir de las expresiones dadas en [Arn00, Arn06b] con el escaleo $\alpha_s = \mathcal{O}(1/N_c)$, se obtiene $\eta/s \sim \mathcal{O}(1)$. Esto es cualitativamente compatible con la idea de que η/s se aproxima a un mínimo desde la fase de temperaturas bajas a medida que T se acerca a la temperatura crítica, como comentamos al analizar la viscosidad de cizalla. Por otro lado, en el régimen de altas temperaturas ζ/η está suprimida por un factor $(c_s^2 - 1/3)^2$ adicional.

R.4 No-equilibrio químico en el gas de mesones

Una de las líneas de investigación actuales en el contexto de Colisiones de Iones Pesados es la evolución térmica y química de un gas hadrónico en expansión. En líneas generales, la imagen aceptada es que la evolución térmica del sistema en enfriamiento alcanza el "freeze-out" químico antes que el térmico, de modo que cuando los hadrones se desacoplan completamente (dejan de interactuar fuertemente) los potenciales químicos asociados a la conservación de número de partículas son no nulos. La composición química del gas puede determinarse experimentalmente analizando las abundancias de las diferentes especies hadrónicas y su espectro [Kat90, Beb92, Hun98, Kol03, BM04]. La presencia de dicha fase no-equilibrada químicamente es más probable que ocurra para las energías de colisión que se alcanzan en RHIC o LHC que para las de los experimentos SPS o AGS [BM04]. Para la componente piónica, diferentes estimaciones basadas en equilibrio térmico local predicen $\mu_\pi \sim 50 - 100$ MeV a la temperatura de "freeze-out" térmico $T_{\rm TFO} \sim 100 - 120$ MeV, con el "freeze-out" químico teniendo lugar a $T_{\rm CFO} \sim 180$ MeV aproximadamente [Beb92, Hun98, Kol03, Let08, Son97].

A temperaturas bajas y moderadas, la componente dominante es la fase piónica. En esa fase, el recorrido libre medio de piones es pequeño comparado con el tamaño del sistema, de modo que el equilibrio térmico prevalece [Goi89, Beb92, Sch93]. Por otra parte, el ritmo de relajación química por medio de procesos $2\pi \leftrightarrow 4\pi$ es muy pequeño [Goi93, Son97] debido a la fuerte supresión en espacio de fases. Por tanto, en el rango de temperaturas $T_{\rm TFO} < T < T_{\rm CFO} \lesssim T_c$, con T_c la temperatura crítica de restauración de la simetría quiral, el sistema está en equilibrio y dominado por colisiones elásticas de modo que $\mu_\pi \neq 0$. En ese rango de temperaturas, es válido usar el marco teórico de la Teoría de Perturbaciones Quiral, y es también razonable adoptar una descripción de gas diluido, ya que la densidad media de partículas es pequeña. Además, despreciando efectos disipativos tales como las viscosidades, la entropía es conservada durante la evolución del plasma.

Consideramos a continuación un gas de piones interactuantes (aunque el análisis puede extenderse directamente a un gas de mesones en general) en el régimen donde el equilibrio térmico ha sido alcanzado pero sin embargo el sistema permanece fuera del equilibrio químico. Implementamos la conservación aproximada del número de partículas por medio de un potencial químico asociado al número de piones μ_π usando un tratamiento diagramático de teoría de campos a temperatura finita, válido en principio para cualquier teoría bosónica neutra (esto es, campos reales) en este régimen. Las reglas de Feynman resultantes las aplicamos en el contexto de la Teoría de Perturbaciones Quiral, con el objetivo de analizar cantidades termodinámicas de interés en el gas de piones, tales como la

energía libre, el condensado de quarks y la auto-energía térmica. En particular, derivamos la generalización a $\mu_\pi \neq 0$ de las relaciones de tipo Luscher y Gell-Mann-Oakes-Renner. Prestamos especial atención a la comparación con teoría cinética convencional, que nos proporciona una comprobación de la consistencia de nuestro método. Se analizan también varias aplicaciones fenomenológicas, en relación con la restauración de la simetría quiral, condiciones de "freeze-out", y condensados de Bose-Einstein de piones.

Hasta ahora, los efectos de potencial químico en sistemas como el que nosotros consideramos han sido incorporados básicamente de dos formas. Una es el límite de partículas libres (donde realmente el número de partículas es conservado), usado para la evaluación de la función de partición, incluyendo resonancias explícitamente [Beb92, Son97]. Esto permite, mediante requerimientos de conservación de la entropía, describir con bastante precisión la dependencia $\mu_\pi(T)$ en el rango de temperaturas de relevancia fenomenológica indicadas anteriormente. El otro método consiste en usar argumentos de teoría cinética e incluir entonces la dependencia en $\mu_\pi \neq 0$ a través de las funciones de distribución. Este último camino ha sido seguido por ejemplo para el cálculo de la anchura térmica en [Goi89], en el cálculo de coeficientes de transporte [Pra93, Dob04], o en la aproximación del virial a densidades bajas [Dob99]. Finalmente, conviene mencionar que hay análisis fenomenológicos, tales como [Bai97] para el espectro de dileptones, donde se sigue la misma prescripción, esto es, se reemplaza la función de distribución pero en los propagadores de diagramas, inspirado en la formulación de no-equilibrio de teoría de campos a temperatura finita [Cho85].

R.4.1 Potencial químico para un campo escalar neutro

Para una teoría bosónica con campos reales, el número de partículas se conserva solamente en el caso libre. Sin embargo, estamos interesados en el régimen donde los procesos relevantes en el sistema son los elásticos. Nuestro objetivo es pues proporcionar una descripción diagramática de dicho sistema, al cual no podemos aplicar la reglas de Feynman derivadas para campos con cargas conservadas de forma exacta (esto es, a nivel del lagrangiano). Para obtener nuestra formulación diagramática, emplearemos la técnica de las integrales de camino holomorfas, donde el operador número de partículas tiene una representación bien definida en términos de operadores de creación y destrucción incluso para campos escalares reales.

El punto de partida es la función de partición del sistema en la colectividad grancanónica:

$$\tilde{Z}_\beta \equiv \mathrm{Tr}\left\{ \mathrm{e}^{-\beta(\hat{H}-\mu\hat{N})} \right\} \ , \tag{R.52}$$

con H el hamiltoniano del sistema, N el número de partículas, y donde las cantidades indicadas con una tilde se referirán al caso con $\mu \neq 0$ en lo sucesivo. No es difícil mostrar que la afirmación de conservación aproximada del número de partículas (en un cierto intervalo de tiempo) equivale a la condición $[\hat{H}, \hat{N}] \simeq 0$. Usando la técnica de integrales de camino holomorfas [ZJ02], y a partir de la condición de conservación aproximada del número de partículas, es posible demostrar (ver detalles en el Capítulo 4 de la tesis) que

el funcional generador en nuestro caso toma la forma

$$\tilde{Z}_\beta[j] = \tilde{Z}^0_\beta \ \exp\left(-\mathrm{i}\int\limits_C \mathrm{d}^4x\ \mathcal{V}\left(\frac{\delta}{\mathrm{i}\delta j(x)}\right)\right) \exp\left(-\frac{1}{2}\int\limits_C \mathrm{d}^4x \int\limits_C \mathrm{d}^4x'\ j(x)\tilde{G}(x-x')j(x')\right)\ , \tag{R.53}$$

donde $\int\limits_C \mathrm{d}^4x \ \equiv \int_C \mathrm{d}t \int \mathrm{d}^3\boldsymbol{x}$, C es el contorno representado en la Figura R.30 (resulta ser el mismo que en el caso $\mu \equiv 0$), y el propagador $\tilde{G}$ viene dado por

$$\tilde{G}(t) = \frac{1}{2\omega}\left[\mathrm{e}^{-\mathrm{i}\omega|t|}(1+n_\mathrm{B}(\omega-\mu)) + \mathrm{e}^{\mathrm{i}\omega|t|}n_\mathrm{B}(\omega-\mu)\right]\ . \tag{R.54}$$

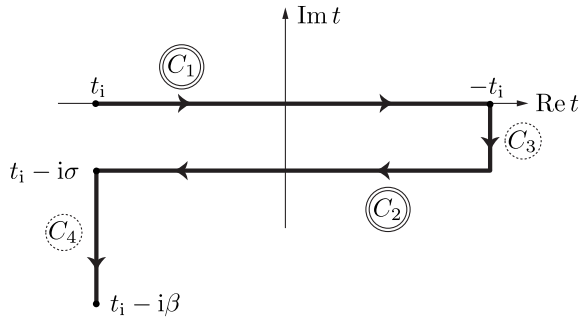

Figura R.30: Contorno de tiempo complejo para el caso $\mu \neq 0$, donde $\sigma \in [0, \beta]$.

El Formalismo de Tiempo Imaginario (ITF) corresponde a la elección $t_\mathrm{i} = \sigma = 0$ para el contorno de la Figura R.30, de modo que uno se limita a los tiempos puramente imaginarios $t = -\mathrm{i}\tau$ con $\tau \in [0, \beta]$. Sin embargo, el correspondiente propagador para $\mu \neq 0$ muestra una característica peculiar que complica los cálculos diagramáticos en este formalismo, generando en algunos casos resultados mal definidos. El origen del problema está en el hecho de que el propagador libre en tiempo imaginario no es periódico, por lo que no existe una relación de KMS global en este caso. Aunque en la representación mixta el propagador satisface $\tilde{\Delta}_T(\tau + \tilde{\beta}_p, p) = \tilde{\Delta}_T(\tau, p)$. Esta periodicidad dependiente del momento hace imposible definir adecuadamente una representación de Matsubara en el espacio de Fourier. La alternativa es emplear el Formalismo de Tiempo Real (RTF), que en cambio sí está bien definido.

Formalismo de Tiempo Real

Consideramos ahora el contorno completo de la Figura R.30 y, siguiendo la notación estándar, denotamos los propagadores mediante $\tilde{D}_{ij} = \tilde{G}(t_i - t_j)$ con $t_i \in C_i, t_j \in C_j$. Tenemos por tanto para los segmentos $C_{1,2}$ del contorno:

$$\begin{aligned}
\tilde{D}_{11}(t-t') &= \tilde{G}^>(t-t')\theta(t-t') + \tilde{G}^<(t-t')\theta(t'-t)\ , \\
\tilde{D}_{22}(t-t') &= \tilde{G}^<(t-t')\theta(t-t') + \tilde{G}^>(t-t')\theta(t'-t)\ , \\
\tilde{D}_{12}(t-t') &= \tilde{G}^<(t-t'+\mathrm{i}\sigma) = \tilde{D}_{21}(t'-t)\ ,
\end{aligned} \tag{R.55}$$

donde $t, t' \in \mathbb{R}$ y $\tilde{G}^{>}, \tilde{G}^{<}$ dados en (D.10)-(D.11), y análogamente para los otros segmentos. Para formular adecuadamente el RTF a $\mu \neq 0$ tomamos primero, como de costumbre, $t_i \to -\infty$. En principio esta elección implica, tras imponer ciertas condiciones asintóticas para las corrientes j y para la función espectral (que se cumplen también en nuestro caso con $\mu \neq 0$), que el funcional generador para $\mathcal{V} = 0$ puede factorizarse como [Lan87]:

$$\tilde{Z}^{\mathcal{V}=0}_{\beta,C}[j] = \mathcal{N}\ \tilde{Z}^{\mathcal{V}=0}_{\beta,C_{12}}[j]\ \tilde{Z}^{\mathcal{V}=0}_{\beta,C_{34}}[j]\ , \tag{R.56}$$

de modo que uno puede calcular funciones de correlación en tiempo real sin considerar las contribuciones que provienen de los segmentos verticales del contorno C. Además, consideraremos por simplicidad el contorno con $\sigma \to 0^+$ (se demuestra que los resultados físicos no dependen de la elección de σ [Lan87]). Veremos que la mayoría de los resultados pueden escribirse como funcionales de $\tilde{n}_{\mathrm{B}}(x) \equiv n_{\mathrm{B}}(x-\mu)$, que codifica toda la dependencia con T y μ.

Los propagadores (R.55) en el espacio de momentos para nuestra elección de contorno adoptan la forma (nótese que la componente $\tilde{D}_{11}$ corresponde al propagador libre $\tilde{G}$ en (D.19)):

$$\begin{aligned}
\tilde{D}_{11}(p_0,p) &= \frac{\mathrm{i}}{p_0^2 - E_p^2 + \mathrm{i}0^+} + 2\pi\delta(p_0^2 - E_p^2) n_{\mathrm{B}}(|p_0| - \mu)\ , \\
\tilde{D}_{22}(p_0,p) &= \frac{-\mathrm{i}}{p_0^2 - E_p^2 + \mathrm{i}0^+} + 2\pi\delta(p_0^2 - E_p^2) n_{\mathrm{B}}(|p_0| - \mu)\ , \\
\tilde{D}_{12}(p_0,p) &= 2\pi\delta(p_0^2 - E_p^2)\left[\theta(p_0) + n_{\mathrm{B}}(|p_0| - \mu)\right]\ , \\
\tilde{D}_{21}(p_0,p) &= 2\pi\delta(p_0^2 - E_p^2)\left[\theta(-p_0) + n_{\mathrm{B}}(|p_0| - \mu)\right]\ .
\end{aligned} \tag{R.57}$$

Puede comprobarse fácilmente que estos propagadores para $\mu \neq 0$ en el RTF coinciden con los empleados en [Bai97] y usados para analizar la emisión térmica de dileptones, donde fueron obtenidos asumiendo una sustitución directa de las funciones de distribución en equilibrio por las correspondientes fuera del equilibrio a $\mu \neq 0$.

Es importante enfatizar que las propiedades espectrales de la teoría en interacción vienen dadas a partir de funciones de Green retardadas y no a partir de los valores esperados de productos ordenados temporalmente. En el ITF a $\mu \equiv 0$, los correladores retardados se obtienen mediante continuación analítica. Sin embargo, hemos visto que este no es un procedimiento bien definido para $\mu \neq 0$. La solución al problema de encontrar funciones de Green retardadas en el RTF fue dada en el trabajo [Kob90], y es directamente extensible a nuestro caso. Las reglas diagramáticas obtenidas allí nos permitirán por ejemplo calcular la anchura del pión, dada por la auto-energía retardada del diagrama R.35(b).

En cuanto al cálculo de cantidades termodinámicas con nuestro formalismo de tiempo real, tales como la función de partición, otro conjunto de reglas diagramáticas propuesto en [Fuj84, Mat85] nos permitirá calcular la contribución de diagramas de vacío, en los cuales no hay "patas" externas. El procedimiento consiste en fijar uno de los vértices del diagrama de vacío asumiendo que es de tipo 1 y entonces sumar sobre el resto de vértices considerando todas las posibilidades (tipo 1 ó 2). Este método es igualmente válido para el caso $\mu \neq 0$ que nos interesa.

R.4.2 Aplicaciones al gas de piones

Evaluación de la energía libre en ChPT

Aplicamos ahora nuestros resultados previos al gas de piones, descrito en ChPT con dos sabores ligeros. En nuestros cálculos usamos los mismos valores centrales para las constantes de baja energía $\bar{l}_i$ que en [Gas84, Ger89], para así poder comparar con más facilidad con los resultados en [Ger89].

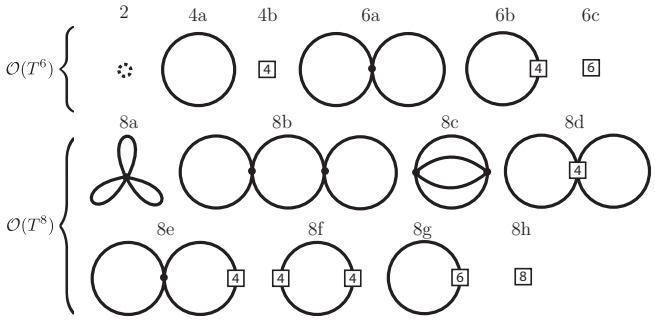

Figura R.31: Diagramas de Feynman que contribuyen a la función de partición del gas de piones hasta orden $\mathcal{O}(T^8)$. La primera fila incluye diagramas de orden hasta $\mathcal{O}(T^6)$ mientras que la segunda y la tercera corresponden a las contribuciones de orden $\mathcal{O}(T^8)$. Los puntos denotan vértices que provienen de $\mathcal{L}_2$, mientras que los vértices de lagrangianos superiores se indican con un cuadrado. La etiqueta encima de cada diagrama sigue la notación de [Ger89].

La energía libre z, a partir de la cual se obtienen observables termodinámicos, viene dada por:

$$\tilde{z}(T,\mu_\pi) = -\lim_{V\to\infty}\frac{T}{V}\ln\tilde{Z}_\beta(T,\mu_\pi)\ . \tag{R.58}$$

Y entonces la presión se puede puede obtener a partir de z como:

$$\tilde{P}(T,\mu_\pi) = \tilde{z}_0 - \tilde{z}(T,\mu_\pi)\ , \quad \tilde{z}_0 = \lim_{T\to 0^+}\tilde{z}\ . \tag{R.59}$$

Los diagramas que contribuyen a la energía libre en ChPT son los diagramas cerrados que se muestran en la Figura R.31. El número asignado a cada diagrama indica el orden de su contribución en la expansión quiral. El orden dominante $\tilde{z}_2 = -F_0^2M_0^2$ proviene del término de contacto en $\mathcal{L}_2$. El orden siguiente corresponde a los diagramas 4a y 4b, y equivale a la función de partición de un gas de piones libres. El primer orden en el que la interacción entre piones entra es el $\mathcal{O}(T^6)$, y los diagramas que contribuyen son los 6(a,b,c) en la Figura R.31. El diagrama 6c renormaliza la energía del vacío, mientras que el diagrama 6b es de la misma forma que el 4a y por tanto da lugar a una contribución a la función de partición libre pero con la masa cambiada. En el caso del diagramas 6a, su contribución viene dada por:

$$\tilde{z}_{6\mathrm{a}} = \frac{3M_0^2}{8F_0^2}\tilde{G}^2(0)\ . \tag{R.60}$$

Después de renormalizar, la contribución total a la presión a orden $\mathcal{O}(T^6)$ es:

$$\tilde{P} = \frac{3}{2}\tilde{g}_0(M_\pi, T, \mu) - \frac{3}{8}\frac{M_0^2}{F_0^2}\left[\tilde{g}_1(M_0, T, \mu)\right]^2 + \mathcal{O}(T^8) \ , \tag{R.61}$$

donde $\tilde{g}_0$ y $\tilde{g}_1$ están dadas en el Apéndice D de esta tesis, y donde M_π es la masa física del pión a $T = \mu_\pi = 0$.

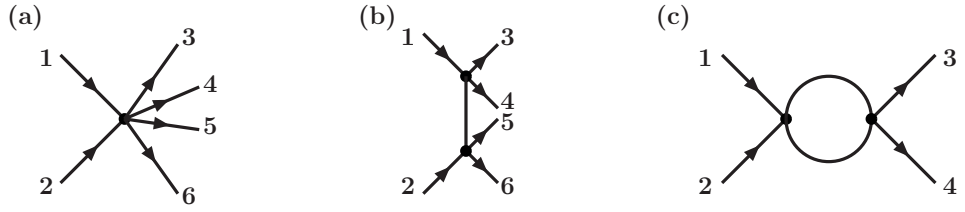

Figura R.32: (a,b) Diagramas que contribuyen al orden dominante (a nivel árbol) a los procesos $2\pi \to 4\pi$. (c) Contribución a un lazo a la dispersión elástica pión-pión.

Consideramos ahora las contribuciones a orden $\mathcal{O}(T^8)$ mostradas en la Figura R.31. A este orden esperamos que la aproximación de conservación del número de partículas comience a fallar, dado que los diagramas de vacío correspondientes pueden ser formados "cerrando" procesos inelásticos (ver Fig. R.32). Las contribuciones de este orden comenzarán a ser importantes para temperaturas próximas a T_c. Para estas temperaturas, el potencial químico es pequeño, y la dependencia en μ_π está suprimida en potencias de μ_π/T y μ_π/M_π. Además, tomar μ_π/T pequeño justifica emplear las expresiones calculadas con el ITF en [Ger89] a $\mu = 0$ y cambiar los propagadores por los correspondientes a $\mu \neq 0$. Las distintas contribuciones de los diagramas 8(a,b,c,d,e) vienen entonces dadas por [Ger89]:

$$\tilde{z}_{8a} = -\frac{25M_0^2}{48F_0^4}\tilde{G}^3(0) \ , \tag{R.62}$$

$$\tilde{z}_{8b} = \frac{M_0^2}{16F_0^4}\tilde{G}^2(0)\left(8 + 3M_0^2\frac{\partial}{\partial M_0^2}\right)\tilde{G}(0) \ , \tag{R.63}$$

$$\tilde{z}_{8c} = \frac{1}{48F_0^4}\left[3M_0^4\tilde{J}_1 - 72\tilde{J}_2 + 16M_0^2\left(\tilde{G}(0)\right)^3\right] \ , \tag{R.64}$$

$$\tilde{z}_{8d+8e} = -\frac{3}{F_0^4}\left\{(2l_1 + 4l_2)\left[\tilde{G}_{\mu\nu}\right]^2 + \tilde{G}(0)\left[(3l_1 + l_2 + l_3)\,M_0^4\tilde{G}(0) - \frac{l_3 M_0^6}{2}\frac{\partial}{\partial M_0^2}\right]\tilde{G}(0)\right\} \ , \tag{R.65}$$

donde $\tilde{G}_{\mu\nu} \equiv \partial_\mu\partial_\nu\tilde{G}(0)$, y

$$\tilde{J}_1 = \mathrm{i}\int \mathrm{d}^4x\left[\tilde{D}_{11}^4(x) - \tilde{D}_{12}^4(x)\right] = \int \mathrm{d}^3\boldsymbol{x}\int_0^\infty \mathrm{d}t\left\{\left[\tilde{G}^>(t,\boldsymbol{x})\right]^4 - \left[\tilde{G}^<(t,\boldsymbol{x})\right]^4\right\} \ ,$$

$$\tilde{J}_2 = \mathrm{i}\int \mathrm{d}^4x\left[\left(\partial_\mu\tilde{D}_{11}(x)\partial^\mu\tilde{D}_{11}(x)\right)^2 - \left(\partial_\mu\tilde{D}_{12}(x)\partial^\mu\tilde{D}_{12}(x)\right)^2\right] \ . \tag{R.66}$$

La renormalización de las distintas contribuciones se lleva a cabo de forma idéntica a como se hizo en el trabajo [Ger89].

Resultados para observables termodinámicos

A partir de la energía libre obtenemos el condensado de quarks (el parámetro de orden de la transición de fase quiral), la densidad de entropía, y la densidad de número de piones del modo estándar:

$$\langle\bar{q}q\rangle(T,\mu_\pi) = \langle\bar{q}q\rangle(0,0)\left[1+\frac{c}{F_0^2}\frac{\partial\tilde{P}(T,\mu_\pi)}{\partial M_\pi^2}\right] \ , \quad \tilde{s}(T,\mu_\pi) = \frac{\partial\tilde{P}(T,\mu_\pi)}{\partial T} \ ,$$
$$\tilde{n}(T,\mu_\pi) = \frac{\partial\tilde{P}(T,\mu_\pi)}{\partial\mu_\pi} \ , \tag{R.67}$$

donde $c = 1 - M_0^2(4\bar{h}_1 + \bar{l}_3 - 1)/(32\pi^2 F_0^2) + \mathcal{O}(M_0^4)$.

En la Figura R.33 mostramos nuestros resultados. La primera característica que observamos es que las curvas de orden $\mathcal{O}(T^6)$ y del gas ideal están muy cerca la una de la otra para todo el rango de temperaturas y potenciales químicos mostrados. Efectos apreciables debidos a la interacción sólo aparecen numéricamente cuando se incluye el orden $\mathcal{O}(T^8)$. Esta es también una característica del cálculo a $\mu_\pi = 0$ [Ger89]. Por ejemplo, en el límite quiral ($M_\pi = 0$) y para $\mu_\pi = 0$, el orden $\mathcal{O}(T^6)$ en (R.61) se anula idénticamente, mientras que el $\mathcal{O}(T^8)$ sobrevive, produciendo contribuciones conformemente anómalas a la presión (como hemos visto anteriormente en relación con la viscosidad de volumen). En la Figura R.33 también comparamos nuestros resultados con la aproximación del gas del virial [Dob99], donde la presión puede escribirse a densidades bajas en términos de los desfasajes de dispersión de piones. En las curvas mostradas en la Figura R.33, los desfasajes han sido calculados perturbativamente a orden $\mathcal{O}(p^4)$ en ChPT. Vemos que nuestros resultados a orden $\mathcal{O}(T^8)$ con $\mu_\pi \neq 0$ se encuentran razonablemente cerca de los del virial, al menos para μ_π no muy grande. Esto es una comprobación de la consistencia de nuestro método. Por otro lado, las curvas para el condensado de quarks muestran que la temperatura de restauración quiral disminuye para $\mu_\pi \neq 0$. Esto es razonable pues introducir un potencial químico es un modo efectivo de reducir la masa y aumentar los efectos térmicos.

Un observable muy interesante de cara a la descripción de la evolución de $\mu_\pi(T)$ es el cociente entre la densidad de entropía y la densidad de número de piones, también representado en la Figura R.33. Como se enfatizaba en los trabajos [Beb92, Son97], se espera que este cociente permanezca aproximadamente constante durante la expansión del gas hadrónico. Esta es la aproximación de expansión isentrópica, que es exacta en el límite de altas temperaturas, $T \gg M_\pi, \mu_\pi$, para el gas ideal. La idea consiste entonces en fijar s/n a un valor dado a la temperatura de "freeze-out" químico $T_{\rm CFO}$ donde $\mu_\pi = 0$. Disminuyendo la temperatura uno puede mantener s/n fijo incrementando μ_π, como puede verse en la Figura R.33. Esto proporciona la dependencia $\mu_\pi(T)$, que se obtiene en [Beb92, Son97] para la aproximación de gas ideal. En la Figura R.34, se representan las curvas isentrópicas $\mu_\pi(T)$ con valor de referencia $s/n = 4$, con $T_{\rm CFO} \simeq 190$ MeV para la curva correspondiente al gas ideal. El efecto más significativo que observamos es la

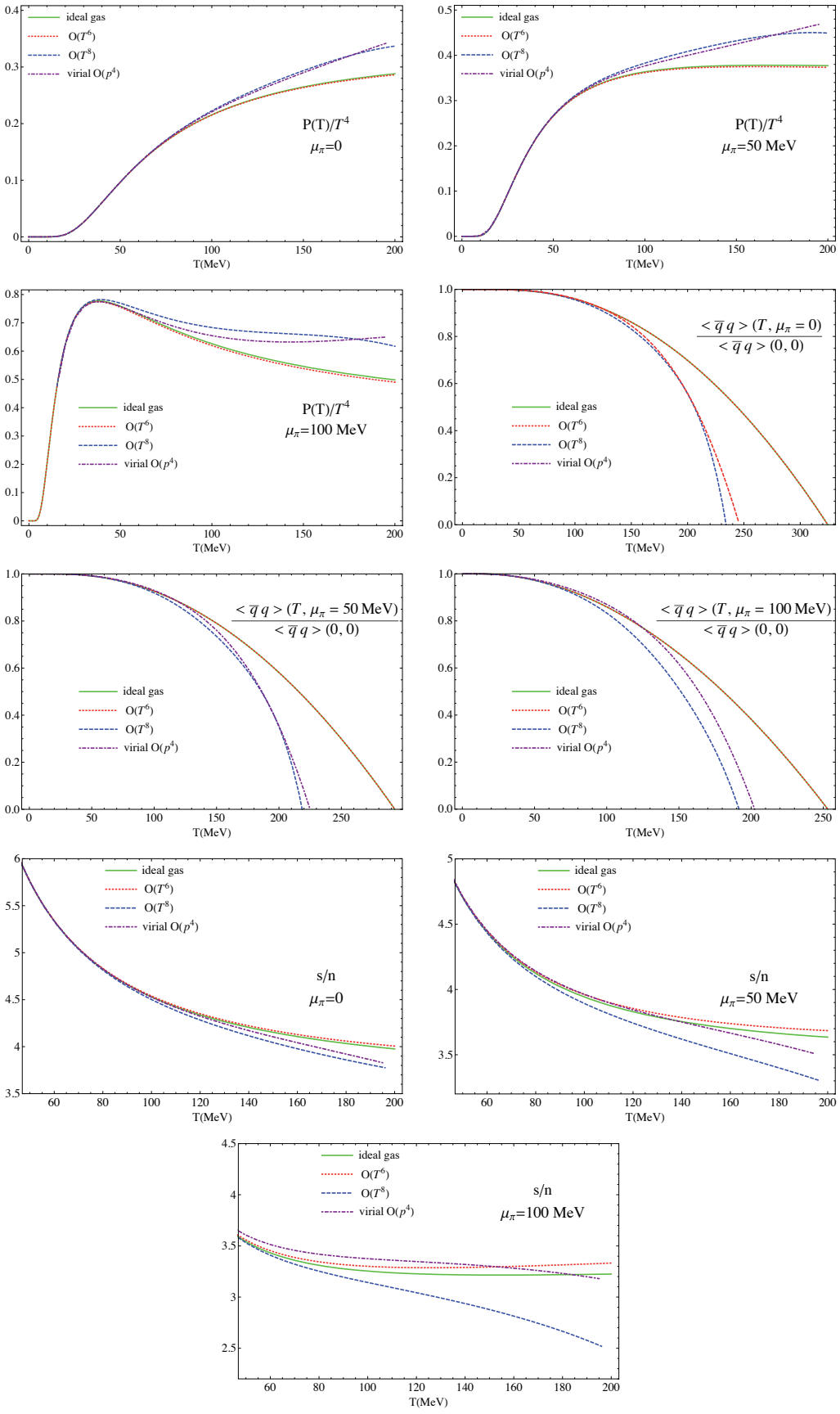

Figura R.33: Resultados para observables termodinámicos a diferentes valores del potencial químico y diferentes órdenes en las interacciones de ChPT.

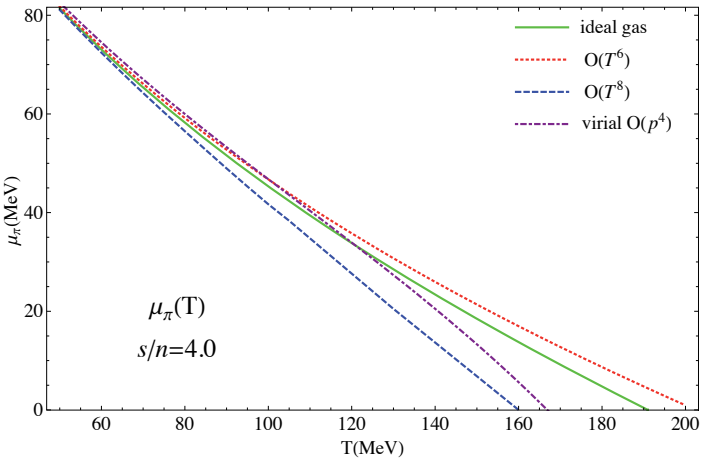

Figura R.34: Dependencia de $\mu_\pi(T)$ en la aproximación isentrópica con el valor fijo $s/n = 4$.

reducción de $T_{\rm CFO}$ cuando las interacciones a orden $\mathcal{O}(T^8)$ se incluyen. Éste es un efecto muy natural ya que, a este orden en la interacción, los procesos que cambian el número de partículas comienzan a ser relevantes y llevan al sistema al equilibrio químico de nuevo. La curva del virial permanece razonablemente cerca de nuestro resultado perturbativo a orden $\mathcal{O}(T^8)$, puesto que los dos métodos se diferencias significativamente sólo a valores altos de μ_π y T, que no son alcanzados a lo largo de la curva $\mu_\pi(T)$.

Auto-energía: masa y anchura térmicas del pión

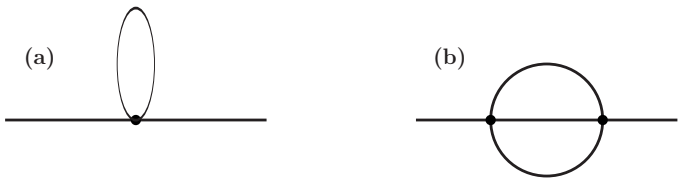

Figura R.35: Diagramas que contribuyen al orden más bajo a las partes real (a) e imaginaria (b) de la auto-energía.

A continuación calculamos la auto-energía del pión, para la que el orden dominante a su parte real e imaginaria viene dado por los diagramas en la Figura R.35(a) y R.35(b) respectivamente, con todos los vértices pertenecientes al lagrangiano $\mathcal{L}_2$. Usando las reglas mencionadas anteriormente, la contribución del primer diagrama en la Figura R.35(a) viene dada por:

$$M_\pi^2(T,\mu_\pi) = M_\pi^2 + \frac{M_0^2}{2F_0^2}\tilde{g}_1(M_0,T,\mu_\pi) + \mathcal{O}(M_0^4)\ , \tag{R.68}$$

$$F_\pi^2(T,\mu_\pi) = F_\pi^2 - 2\tilde{g}_1(M_0,T,\mu_\pi) + \mathcal{O}(M_0^4)\ , \tag{R.69}$$

con M_π y F_π los valores físicos para $T = \mu_\pi = 0$. Teniendo en cuenta ahora las correcciones al condensado de quarks al mismo orden, $\mathcal{O}(T^6)$, que está dado a partir de (R.67) y (R.61) usando (D.27):

$$\langle\bar{q}q\rangle(T,\mu_\pi) = \langle\bar{q}q\rangle(0,0)\left[1 - \frac{3}{2F_0^2}\tilde{g}_1(M_0,T,\mu_\pi)\right] + \mathcal{O}(T^8)\ , \tag{R.70}$$

obtenemos que la relación de Gell-Mann-Oakes-Renner (GOR) [GM68] se cumple también para $\mu_\pi \neq 0$ a este orden (un lazo en ChPT):

$$\frac{F_\pi^2(T,\mu_\pi)M_\pi^2(T,\mu_\pi)}{\langle\bar{q}q\rangle(T,\mu_\pi)} = \frac{F_\pi^2(0,0)M_\pi^2(0,0)}{\langle\bar{q}q\rangle(0,0)} = -m_{\rm q}\ . \tag{R.71}$$

Otra observación importante es que el cambio (R.68) en la masa a este orden, del mismo modo que en el caso $\mu_\pi = 0$ [Sch93], puede escribirse en términos de la amplitud de dispersión hacia adelante a partir de (D.23):

$$M_\pi^2(T,\mu_\pi) - M_\pi^2 = -\int \frac{\mathrm{d}^3\boldsymbol{p}}{(2\pi)^3}\ \frac{1}{2E_p}\frac{1}{\mathrm{e}^{\beta(E_p-\mu_\pi)}-1}\,\mathrm{Re}\left[T_{\pi\pi}^{\rm f}(s=(E_p+M_\pi)^2-|\boldsymbol{p}|^2)\right]\ , \tag{R.72}$$

donde $E_p^2 = M_\pi^2 + |\boldsymbol{p}|^2$ y $T_{\pi\pi}^{\rm f}(s)$ es la amplitud de dispersión hacia adelante promediada en isospín, que al orden más bajo $\mathcal{O}(p^2)$ viene dada por:

$$\begin{aligned} T_{\pi\pi}^{\rm f}(s) \equiv T_{\pi\pi}(s,0,u) &= \frac{1}{3}\sum_{I=0}^{2}(2I+1)T_I(s,0,u) = \frac{32\pi}{3}\sum_{I=0}^{2}\sum_{J=0}^{\infty}(2I+1)(2J+1)t_{IJ}(s) \\ &\simeq \frac{32\pi}{3}\left[t_{00}(s) + 9t_{11}(s) + 5t_{20}(s)\right] = -\frac{M_0^2}{F_0^2} + \mathcal{O}(s^2, M_0^4)\ . \end{aligned} \tag{R.73}$$

Aquí, $T_I(s,t,u)$ es la proyección de la amplitud de dispersión con isospín bien definido I, y s,t,u son las variables de Mandelstam. El resultado en (R.72) es la generalización a $\mu_\pi \neq 0$ de la fórmula relacionando el cambio en la auto-energía con la densidad de estados en la amplitud de dispersión a orden más bajo en la densidad [Sch93]. Un aspecto muy interesante consiste en que admite una extensión natural [Sch93] considerando (en el régimen de gas diluido) no sólo la amplitud perturbativa $\mathcal{O}(p^2)$, sino también órdenes más altos, incluyendo amplitudes unitarizadas.

En la Figura R.36 mostramos nuestros resultados para la masa térmica, considerando amplitudes a orden $\mathcal{O}(p^2)$, y unitarizadas con el IAM a orden $\mathcal{O}(p^4)$ en (R.72). Nuestros resultados muestran que el orden dominante, dado por el diagrama "tadpole" de la Figura R.35(a), produce una masa térmica que aumenta ligeramente con la temperatura y el potencial químico. Sin embargo, incluyendo en la amplitud las correcciones a orden $\mathcal{O}(p^4)$ o las unitarizadas, la masa tiende a decrecer significativamente con la temperatura y μ_π. Esto sugiere un escenario interesante: el sistema de piones podría experimentar condensación de Bose-Einstein (BE) debida a la reducción de la masa térmica por las interacciones. La condensación del número de piones y sus posibles consecuencias fenomenológicas en colisiones de iones pesados han sido extensivamente estudiadas en la literatura [Zim79, Gre93, Led00, Beg07]. Entre las posibles consecuencias observables se encuentra el aumento anómalo del espectro de piones a bajo $p_{\rm T}$.

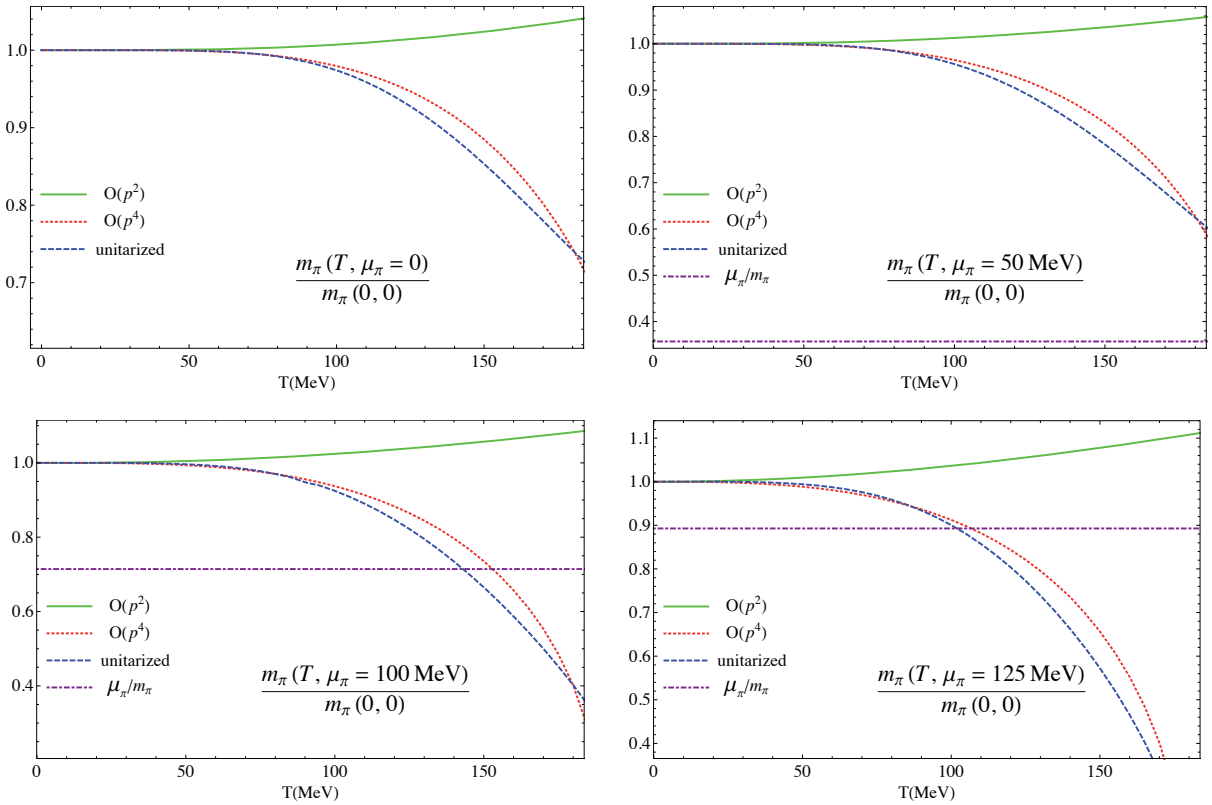

Figura R.36: Resultados para la dependencia de la masa térmica con la temperatura y el potencial químico, considerando diferentes órdenes en la amplitud de dispersión en (R.72).

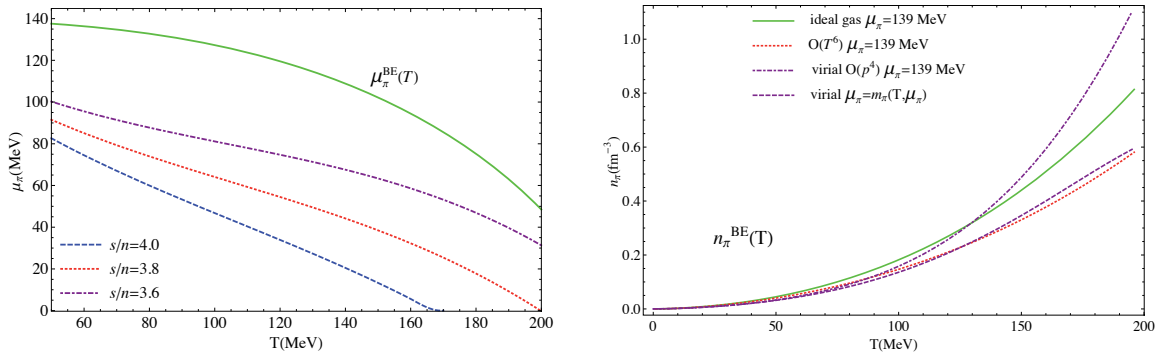

Figura R.37: Curvas de condensación de Bose-Einstein. Izquierda: la curva $\mu_\pi^{\rm BE} = M_\pi(T,\mu_\pi)$ con masa térmica calculada con la amplitudes a orden $\mathcal{O}(p^4)$, comparada con las curvas de expansión isentrópica para el caso del virial al mismo orden y para diferentes valores de s/n. Derecha: densidad de piones frente a la temperatura en el límite de condensación de BE $\mu_\pi \to M_\pi^-$ para diferentes órdenes en la interacción, comparado con el gas ideal y con el caso del virial con masa térmica.

Con nuestro método podemos describir las correcciones a la condensación de BE debidas a la interacción entre piones. En la Figura R.37 (izquierda) se representa la curva $\mu_\pi^{\rm BE}(T) = M_\pi(T,\mu_\pi^{\rm BE}(T))$ y se compara con las curvas isentrópicas correspondientes a diferentes valores de s/n. Vemos que la curva BE así definida no permanece muy alejada del resultado isentrópico y los valores fenomenológicos esperados. Esas curvas corresponden a las amplitudes $\mathcal{O}(p^4)$. En la Figura R.37 (derecha) mostramos también las curvas de densidad-temperatura correspondientes a $\mu_\pi \to M_\pi^-$ para distintos órdenes en la interacción. También mostramos la curva correspondiente al límite de BE. En cualquier caso, las correcciones debidas a las interacciones son pequeñas cerca del "freeze-out" térmico.

Finalmente, calculamos el orden dominante de la parte imaginaria de la auto-energía del pión, dada en ChPT por el diagrama (b) en la Figura R.35. Éste corresponde a la contribución dominante a la anchura térmica Γ_p dada por (R.16). Como hemos comentado, el resultado vendrá dado en términos del correlador retardado en RTF, aplicando las reglas de [Kob90], se llega a la expresión final

$$\Gamma_p(T,\mu_\pi) = \frac{1}{8E_p}\frac{1}{1+n_{\rm B}(E_p-\mu_\pi)}\int\left(\prod_{i=1}^{3}\frac{{\rm d}^3\boldsymbol{k}_i}{(2\pi)^3 2E_i}\right) n_{\rm B}(E_1-\mu_\pi)\,[1+n_{\rm B}(E_2-\mu_\pi)] \\ \times\,[1+n_{\rm B}(E_3-\mu_\pi)]\,|T_{\pi\pi}(s,t)|^2(2\pi)^4\delta^{(4)}(p+k_1-k_2-k_3)\ , \qquad \text{(R.74)}$$

donde $T_{\pi\pi}$ es la amplitud de colisión $\pi\pi$ promediada en isospín, con $s=(E_p+E_1)^2-|\boldsymbol{p}+\boldsymbol{k}_1|^2$, $t=(E_p-E_2)^2-|\boldsymbol{p}-\boldsymbol{k}_2|^2$. Considerando ahora el régimen de gas diluido en esta expresión, se obtiene la extensión de la fórmula de Luscher para la parte imaginaria de la auto-energía en términos de la amplitud de dispersión hacia adelante:

$$\Gamma_p^{\rm DG}(T,\mu_\pi) = \frac{1}{2E_p}\int\frac{{\rm d}^3\boldsymbol{k}}{(2\pi)^3}\ n_{\rm B}(E_k-\mu_\pi)\frac{\sqrt{s(s-4M_\pi^2)}}{2E_k}\,\sigma_{\pi\pi}(s) \\ = \frac{1}{2E_p}\int\frac{{\rm d}^3\boldsymbol{k}}{(2\pi)^3 2E_k}\ n_{\rm B}(E_k-\mu_\pi)\,{\rm Im}\,T^{\rm f}_{\pi\pi}(s)\ , \qquad \text{(R.75)}$$

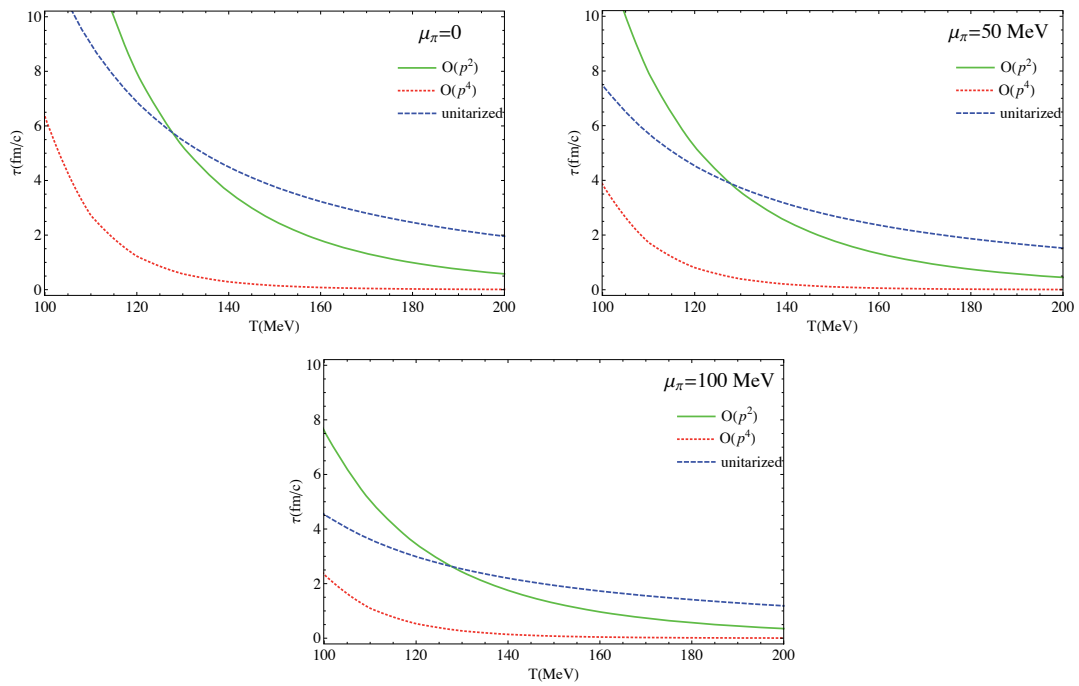

Figura R.38: Tiempo medio de colisión en el límite elástico y diluido, considerando diferentes órdenes para la amplitud de dispersión de piones y varios valores del potencial químico piónico.

donde hemos re-etiquetado $k_1 \mapsto k$, y $\sigma_{\pi\pi}$ es la sección eficaz $\pi\pi$

$$\sigma_{\pi\pi}(s) = \frac{32\pi}{3s}\sum_{IJ}(2I+1)(2J+1)|t_{IJ}(s)|^2 = \frac{1}{\sqrt{s(s-4M_\pi^2)}}\,\mathrm{Im}\,T^{\mathrm{f}}_{\pi\pi}(s)\ , \tag{R.76}$$

donde la última igualdad es el teorema óptico, derivado a partir de la unitariedad.

La anchura térmica es de especial relevancia fenomenológica puesto que, como hemos visto anteriormente, entra directamente en el cálculo de coeficientes de transporte en el gas de mesones. El tiempo medio de colisión definido para partículas ultra-relativistas como $\tau = 2/\bar{\Gamma}$ [Goi89, Son97, Hun98], con la anchura promediada

$$\bar{\Gamma}(T,\mu_\pi) = \frac{\displaystyle\int \mathrm{d}^3\boldsymbol{p}\ \Gamma_p(T,\mu_\pi) n_{\mathrm{B}}(E_p-\mu_\pi)}{\displaystyle\int \mathrm{d}^3\boldsymbol{p}\ n_{\mathrm{B}}(E_p-\mu_\pi)}\ , \tag{R.77}$$

proporciona información directa sobre relajación térmica. En la Figura R.38 representamos τ en el régimen diluido, usando la amplitud de dispersión para distintos órdenes.

Las curvas unitarizadas presentan importantes diferencias con respecto a las perturbativas en el rango de temperaturas mostrado. Hemos analizado este efecto exhaustivamente en la sección de coeficientes de transporte. Otro efecto claro que observamos es la reducción del tiempo libre medio con el potencial químico piónico, lo cual indica que las colisiones elásticas predominan sobre las inelásticas al aumentar el potencial químico, como comentamos anteriormente, y esta es la causa de que el equilibrio químico eventualmente se pierda durante la expansión del gas hadrónico.

R.5 Conclusiones

En esta tesis hemos estudiado, en el contexto de Teoría de Perturbaciones Quiral unitarizada, las propiedades espectrales de resonancias en el medio, coeficientes de transporte, y efectos de conservación del número de partículas para un gas de mesones ligeros. La mayoría de los cálculos han sido particularizados para el caso de un gas de piones junto con sus resonancias, $\rho(770)$ y $f_0(600)/\sigma$, aunque la extensión al caso más general de tres sabores es directa.

En primer lugar, hemos presentado un análisis del comportamiento de las amplitudes de dispersión $\pi\pi$ en Teoría de Perturbaciones Quiral unitarizada teniendo en cuenta efectos del medio incorporados de varias formas. En particular, nos hemos centrado en el comportamiento con la temperatura y la densidad nuclear de las resonancias $\rho(770)$ y $f_0(600)$, que generamos dinámicamente con el Método de la Amplitud Inversa. En el canal de la σ, hemos estudiado también efectos de densidad nuclear finita empleando un método de muchos cuerpos y unitarizando mediante la ecuación de Bethe-Salpeter.

Considerando sólo efectos térmicos en las amplitudes de dispersión obtenidas con el IAM, la ρ muestra un ensanchamiento considerable mientras que su masa experimenta una pequeña disminución a medida que la temperatura aumenta. En cuanto a la σ, principalmente experimenta un decrecimiento en su masa, como señal efectiva de restauración de la simetría quiral, aunque se mantiene como una resonancia ancha incluso cerca de la temperatura de transición de fase. El ensanchamiento obtenido con nuestro método a temperatura finita para la ρ es compatible con el análisis de la función espectral realizado recientemente a partir del espectro de dileptones por la colaboración experimental NA60. La evolución de la masa de la ρ con la temperatura no escalea como el condensado de quarks, lo que indica un desacuerdo cuantitativo entre nuestros resultados y el escenario de escaleo de Brown-Rho. El hecho de que, teniendo en cuenta únicamente efectos de temperatura, el polo de la σ permanezca alejado del eje real incluso cuando se encuentra situado en el umbral de dos piones implica que las correspondientes amplitudes de dispersión no experimentan aumento en el umbral; lo cual, según trabajos previos, supondría un efecto precursor de la restauración de la simetría quiral. Tampoco observamos en este caso un escaleo de la masa de la σ según el condensado de quarks, lo cual indica que la resonancia $f_0(600)/\sigma$ que generamos dinámicamente con nuestro método de unitarización tiene una componente no-$\bar{q}q$ que es relevante cerca de la transición de fase.

Al introducir efectos de densidad nuclear finita, la imagen cambia drásticamente. En una primera aproximación, hemos incorporado de modo efectivo los efectos de un medio nuclear mediante la disminución de F_π de acuerdo con la relación de GOR a orden lineal en la densidad. Para valores suficientemente bajos de F_π (altos en densidad), los polos de la ρ y la σ colapsan en el eje real de energías a la energía del umbral de dos piones, lo cual es precedido por un aumento significativo en el umbral de las amplitudes de dispersión. Hemos analizado estos efectos en el contexto de los resultados recientes sobre producción de resonancias en núcleos finitos y nuestros resultados están en consonancia con las observaciones experimentales. Un análisis detallado revela que cuando el polo correspondiente a la resonancia se encuentra cerca del eje real, se divide en dos estados en diferentes hojas de Riemann. Las propiedades de estos polos dobles nos permiten

clasificar la resonancia σ de acuerdo con su estructura interna: exhibe un comportamiento "molecular" (uno de los polos permanece cerca del umbral, bien separado del otro que evoluciona hacia energías inferiores para volverse degenerado con el pión). Por otra parte, de acuerdo con estos argumentos, la ρ correspondería a un estado $\bar{q}q$ no-molecular. Sin embargo, este criterio de clasificación sólo es aplicable en principio a resonancias escalares. De todos modos, la naturaleza $\bar{q}q$ de la ρ ha sido defendida en otros trabajos por medio de diversos argumentos, como por ejemplo el escaleo con N_c grande [Pel04, Pel06]. El escaleo de la masa del polo de la σ y el de la ρ con $F_\pi(\rho)$ sigue la evolución del condensado de quarks y por lo tanto es compatible con el escenario de escaleo de Brown-Rho, aunque uno debe tener en cuenta que algunos mecanismos relevantes de densidad nuclear finita han sido ignorados con esta aproximación.

Hemos también mejorado nuestra implementación de los efectos de densidad nuclear finita (y temperatura) utilizando un cálculo diagramático para la dispersión de piones en el medio nuclear. Hemos escogido un esquema de unitarización distinto para las amplitudes de dispersión $\pi\pi$, esto es, resolvemos la ecuación de Bethe-Salpeter para la interacción entre piones al orden más bajo de ChPT. A pesar de diferencias en las amplitudes al orden $\mathcal{O}(p^4)$, este método proporciona esencialmente los mismos resultados que el IAM y permite un análisis sistemático y la resumación de una clase relevante de mecanismos de interacción de piones con el medio nuclear. Las interacciones de los piones con el medio se encuentran codificadas en la auto-energía del pión, que tiene en cuenta las excitaciones en onda p partícula-agujero y Delta-agujero, así como correlaciones de corta distancia debidas a las interacciones nucleón-nucleón y Delta-nucleón. La apertura de canales bariónicos por encima de $\sigma \to \pi\pi$ a densidad finita extiende el espacio de fases disponible a energías más bajas y por tanto la amplitud de dispersión $\pi\pi$ exhibe un aumento de intensidad en y por debajo del umbral de dos piones, lo cual es incrementado a temperatura finita como consecuencia de los factores de Bose presentes en los modos de baja energía de los estados intermedios de $\pi\pi$. Se ha descubierto que dicho efecto proporciona una descripción satisfactoria de los datos de reacciones de foto-producción de dos piones en núcleos cuando se compara el espectro de masas en el canal pión-neutro frente al cargado para diferentes núcleos [Roc02, Mes02], donde densidades nucleares del orden de ρ_0 e inferiores son exploradas. En nuestro análisis, hemos considerado ambas, temperatura y densidad nuclear finitas, extendiendo así la aplicabilidad del presente método a otros posibles escenarios tales como el próximo programa de colisiones de iones pesados en FAIR. Comparado con el cálculo puramente térmico, los mecanismos de interacción atractiva del pión a densidad nuclear finita aceleran la migración del polo de la σ hacia el umbral de dos piones. El aumento en el umbral observado en la amplitud $\pi\pi$ está correlacionado con la evolución del polo de la σ hacia (y por debajo) $2M_\pi$. Sin embargo, de modo distinto al resultado obtenido reduciendo F_π, el polo de la σ permanece lejos del eje real, manteniendo una anchura de desintegración significativa a densidades tan altas como $2\rho_0$ y temperaturas cercanas a la de la transición de fase.

En segundo lugar, hemos presentado un método para calcular diferentes coeficientes de transporte (la conductividades eléctrica DC y térmica, y las viscosidades de cizalla y volumen) en un gas de mesones a temperaturas bajas en el contexto de la Teoría de Perturbaciones Quiral y la Teoría de Respuesta Lineal. El análisis ha sido particularizado para el

caso de un gas de piones, incluyendo también las resonancias $f_0(600)$ y $\rho(770)$ generadas dinámicamente a través de unitarización con el IAM. La naturaleza no-perturbativa de los coeficientes de transporte se refleja en la necesidad de incluir la anchura térmica del pión en los cálculos, con el objetivo de poder evitar singularidades del tipo "pinching pole". Físicamente, esto permite tener en cuenta las colisiones de piones relevantes en el medio térmico y da lugar a la contribución dominante en potencias del inverso de la anchura consistente con teoría cinética. Hemos mostrado que, tras una modificación adecuada del contaje estándar de ChPT e incluyendo correcciones de unitariedad en las amplitudes de dispersión con el objetivo de mejorar su comportamiento a altas energías, uno obtiene una descripción razonable para los coeficientes de transporte a temperaturas por debajo de la transición de fase quiral. A muy bajas temperaturas, nuestro método concuerda con las predicciones de teoría cinética no-relativista, mientras que a temperaturas más altas conseguimos el comportamiento de los coeficientes de transporte adecuado cuando comparamos con otros estudios basados en teoría cinética relativista. Para obtener estos resultados, hemos considerado el diagrama a un lazo que proporciona la contribución dominante, usando dispersión unitarizada en la anchura térmica correspondiente a las líneas internas de piones.

Un aspecto muy importante de nuestro análisis ha sido estudiar el papel de diagramas de orden superior que, aunque aparentemente suprimidos, su contribución es en principio incrementada por potencias adicionales del inverso de la anchura. Como ocurre en otras teorías, los diagramas dominantes son los del tipo "escalera", que en nuestro caso pueden ser interpretados en términos de dispersión de los piones correspondientes a las líneas internas. Una evaluación cuidadosa de los diagramas de escalera muestra que su contribución puede seguir siendo considerada perturbativa en ChPT a temperaturas bajas. Esto es particularmente importante a temperaturas muy bajas, $T \ll M_\pi$, donde las contribuciones aparentemente no-perturbativas son mayores. En ese régimen, hemos podido mostrar explícitamente que los diagramas de escalera son perturbativos, de modo que simplemente renormalizan el coeficiente numérico de la contribución del diagrama dominante mediante una corrección subdominante de orden superior en ChPT. Aunque ampliada colinealmente, nuestro análisis muestra que la contribución del orden siguiente al dominante supone una corrección del 5 % aproximadamente. A medida que la temperatura aumenta, los diagramas de escalera se vuelven relevantes, con la contribución más importante debida a escaleras con vértices derivativos. Por lo tanto, a temperaturas cerca de la transición de fase, no está claro que los diagramas de escalera puedan ser ignorados (por otra parte, estrictamente, ChPT no es aplicable en ese régimen). De hecho, es de esperar que otros efectos sean también relevantes a esas temperaturas, tales como la presencia de grados de libertad kaónicos y otras resonancias.

Como hemos mencionado anteriormente, la unitariedad juega un papel esencial en el cálculo de coeficientes de transporte. Hemos mostrado que el comportamiento con la temperatura de los diferentes coeficientes de transporte cambia cualitativamente al implementar unitariedad en las ondas parciales que entran en la anchura térmica del pión. Esto proporciona una imagen más física en relación con el comportamiento de las amplitudes de dispersión con la energía y la presencia de resonancias en el medio térmico ($f_0(600)/\sigma$ y $\rho(770)$). La conductividad eléctrica DC, tras ser unitarizada aumenta suavemente con la temperatura, lo cual es consistente con otros estudios analíticos y en el retículo para

temperaturas altas (muy por encima de la transición de fase). La conductividad térmica y la viscosidad de cizalla también experimentan un comportamiento creciente con la temperatura debido a la unitariedad. Por otra parte, el máximo en la viscosidad de volumen que obtenemos para temperaturas cercanas a la crítica es amplificado por el mismo efecto. Complementariamente, hemos analizado predicciones fenomenológicas para el espectro de fotones de muy baja energía y el cociente entre la viscosidad de cizalla y la densidad de entropía, que están en buen acuerdo con los datos experimentales. Por un lado, nuestro análisis implica que debería haber efectos significativos en la producción hadrónica de fotones a muy bajas energías y este resultado es consistente con otros análisis teóricos a bajas energía recientes y compatible con extrapolaciones directas de los datos experimentales. Por otro lado, hemos visto que el cociente η/s para el gas de piones respeta la cota inferior propuesta a partir de un cálculo de Kovtun y colaboradores en AdS/CFT. Nuestros resultados apuntan también a la posible existencia de un mínimo de η/s en la transición de fase de QCD. Además, nuestra estimación de η/s, que entra directamente en la longitud de atenuación del sonido, está en buen acuerdo con análisis previos de flujo elíptico en colisiones de iones pesados. Sin embargo, la falta de un conocimiento preciso tanto experimental como por parte de los resultados del retículo para el límite de frecuencia cero en densidades espectrales, junto con las propias limitaciones de nuestro método, no nos permiten extraer conclusiones muy cuantitativas.

Con respecto a la viscosidad de volumen, hemos mostrado que el gas de piones masivos desarrolla una fuerte correlación entre la viscosidad de volumen y la anomalía conforme, como ha sido sugerido por trabajos previos. Ambas cantidades muestran un pico a bajas temperaturas que corresponde a la ruptura explícita de la simetría de escala debida a la masa no-nula de los quarks, y otro pico cerca de la temperatura crítica que permanece prácticamente inalterado en el límite quiral, dominado pues por la contribución del condensado de gluones y no relacionado con la restauración de la simetría quiral. En teoría de perturbaciones, es necesario calcular la función de partición a orden $\mathcal{O}(T^8)$ el contaje de ChPT para poder obtener el pico anómalo en la anomalía de traza. Hemos visto que este pico puede ser obtenido también usando la Aproximación del Gas del Virial usando las amplitudes de dispersión de ChPT calculadas a orden $\mathcal{O}(p^4)$. Las resonancias ligeras σ y ρ, que generamos dinámicamente, son esenciales para obtener efectos apreciables cerca de la transición de fase. En el cálculo de la anomalía de la traza, hemos comparado también con los resultados de la aproximación del Gas de Resonancias Hadrónicas, en la cual se incluyen un gran número de resonancias como estados libres dando lugar a un buen acuerdo con los resultados del retículo. Sin embargo, puesto que en la aproximación HRG las resonancias no interaccionan entre sí, no es posible reproducir un máximo en la anomalía de traza con este método, a diferencia del cálculo en ChPT. Varias estimaciones indican que estados más pesados podrían dar lugar a una viscosidad de volumen mayor cerca de la transición, produciendo efectos observables en colisiones de iones pesados.

Hemos estudiado también el límite de gran N_c de los coeficientes de transporte obtenidos con nuestro método. La dependencia paramétrica con N_c es consistente con nuestro análisis previo y proporciona una descripción cualitativa del comportamiento de las viscosidades de cizalla y de volumen cuando se aproximan a la región crítica.

Finalmente, hemos desarrollado un formalismo diagramático basado en integrales de

camino holomorfas para poder analizar efectos de no-equilibrio químico en teorías de campos escalares neutros, en el régimen donde el número de partículas es aproximadamente conservado. Hemos derivado las correspondientes reglas de Feynman a temperatura finita incluyendo un potencial químico no nulo μ asociado al número total de partículas, cuya validez está restringida al régimen de temperaturas donde se pueden ignorar los procesos que cambian el número de partículas.

Hemos analizado sutilezas relacionadas con la elección del contorno en tiempos complejos, dando lugar a la extensión de los formalismos de tiempo real e imaginario al caso $\mu \neq 0$. Hemos mostrado que la formulación consistente es la de tiempo real, en acuerdo con otras formulaciones de no-equilibrio. El formalismo de tiempo imaginario puede dar lugar a contribuciones espurias, relacionadas con la pérdida de la periodicidad o, equivalentemente, la relación de KMS global. Estos problemas no están presentes en el formalismo de tiempo real, una vez que la representación adecuada del propagador en términos de la energía es escogida, de acuerdo con la elección estándar para $\mu \equiv 0$. Además, siguiendo estudios previos en la literatura para $\mu \equiv 0$, hemos podido construir las combinaciones de los diagramas en tiempo real que dan lugar a los correladores retardados y a los diagramas cerrados que contribuyen a la energía libre.

Hemos aplicado este formalismo a un gas de piones, caso relevante en colisiones relativistas de iones pesados en el rango de temperaturas comprendido entre los "freeze-out" térmico y químico con potencial químico μ_π no nulo asociado al número total de piones. El esquema diagramático relevante para temperaturas por debajo de la transición de fase es Teoría de Perturbaciones Quiral. Con nuestro método, hemos calculado las correcciones dominantes en la interacción quiral al gas ideal. Al orden dominante $\mathcal{O}(T^6)$, las correcciones a la presión pueden expresarse en términos de diagramas de tipo "tadpole" y son bastante pequeñas numéricamente hasta T_c. Al siguiente orden, $\mathcal{O}(T^8)$, los diagramas cerrados que contribuyen a la energía libre pueden ser obtenidos a partir de procesos que cambian el número de partículas, lo cual indica que la aproximación de número conservado de partículas comienza a fallar. Sin embargo, dado que μ_π es pequeño para temperaturas donde esas correcciones de ChPT se vuelven importantes, estas pueden ser calculadas fiablemente. De hecho, los resultados a ese orden están en acuerdo razonable con el análisis del VGA. Nuestros resultados para observables termodinámicos muestran que ambos efectos, las interacciones quirales y μ_π, tienden a incrementar la presión. La temperatura crítica de restauración de la simetría quiral disminuye al aumentar μ_π, lo cual sería de relevancia sólo si la restauración quiral ocurriera a temperaturas inferiores a la de "freeze-out" químico. Hemos calculado también la curva $\mu_\pi(T)$ a entropía constante para diferentes órdenes en las interacciones. Las correcciones al gas ideal muestran una reducción significativa de la temperatura de "freeze-out" químico.

Nuestro método permite también obtener correcciones térmicas a la auto-energía del pión para $\mu_\pi \neq 0$ a partir de los diagramas dominantes en ChPT en ambas partes, real e imaginaria, del correlador retardado. La parte imaginaria proviene de un diagrama a dos lazos, y en este caso el uso de las reglas del RTF para la construcción de la función retardada es crucial. Tras una evaluación detallada, nuestro resultado diagramático coincide con la expresión esperada de teoría cinética. La parte real proporciona la masa térmica que, junto con el condensado y la constante de desintegración del pión al mismo orden, satisfacen la extensión a $\mu_\pi \neq 0$ de la relación de Gell-Mann-Oakes-Renner. Además ambas,

la parte real y la imaginaria, satisfacen una relación del tipo Luscher en términos de la amplitud de dispersión del pión hacia adelante. Esta relación permite calcular en el régimen diluido las correcciones a la auto-energía para órdenes superiores en las amplitudes de ChPT, incluyendo amplitudes unitarizadas, que tienen el comportamiento físicamente esperado en energías y reproducen los estados resonantes más ligeros. Los resultados para la masa térmica muestran un claro decrecimiento con T y μ_π para las amplitudes a $\mathcal{O}(p^4)$ y para las unitarizadas. Esto sugiere la interesante posibilidad de lograr condensación de Bose-Einstein cuando el valor de la masa térmica efectiva se aproxima al del potencial químico. Hemos analizado esta posibilidad, que es un efecto debido puramente a la interacción, considerando una evolución isentrópica del plasma y comparando la densidad del gas de piones con la obtenida considerando un gas ideal en el límite de condensación de BE $\mu \to M_\pi^-$, donde M_π es la masa en vacío. Nuestra curva para la masa no está lejos de las isentrópicas aunque todavía por encima para valores razonables de "freeze-out" químico. Finalmente, usando también las amplitudes de dispersión, hemos evaluado las correcciones al tiempo medio de colisión para $\mu_\pi \neq 0$. El tiempo medio decrece con T y μ_π para todos los órdenes en la interacción, lo que implica una reducción apreciable para la temperatura de "freeze-out" térmico, estimada como aquella para la que τ se equipara al tiempo de vida típico del plasma, dentro de la aproximación isentrópica.

Por último, quisiéramos mencionar que como posibles futuras líneas de investigación consideramos extender nuestro estudio de resonancias mesónicas en el medio con el objetivo de analizar el caso de número de sabores igual a tres, e investigar la relación entre otras resonancias y la restauración de la simetría quiral, a temperaturas y densidades nucleares finitas con ambos métodos, el IAM y la ecuación de Bethe-Salpeter. También está prevista una investigación más detallada de los efectos de doblado de polos en el tratamiento con la ecuación de Bethe-Salpeter. Otra posible continuación consistiría en extender a su vez el análisis de coeficientes de transporte al sector con extrañeza (que incluye kaones, etas, y sus correspondientes resonancias), junto con la introducción de los correspondientes efectos adicionales de conservación aproximada del número de kaones y etas. Esto resultaría especialmente relevante para temperaturas cercanas a la transición de fase, donde los nuevos grados de libertad dejan de estar suprimidos en densidades por factores de Bose-Einstein, y es de esperar que jueguen un papel importante en ese régimen. El análisis sobre la resumación de diagramas de escalera y las posibles cancelaciones de términos puede ser también revelador, especialmente para la viscosidad de volumen que, calculada en equilibrio químico completo, involucra peldaños con procesos inelásticos.

Contents

Chapter 1

Introduction

This thesis is constituted by three main lines of research: resonances, transport coefficients, and chemical non-equilibrium in the meson gas. In Chapters 2, 3, and 4 each of these topics are thoroughly discussed. The treatment presented is in principle valid for a gas of mesons composed by several species (pions, kaons, etas, and their resonances), but our exposition will be particularized to the simpler case of a gas of pions, sigmas ($f_0(600)$), and rhos ($\rho(770)$) only[1]. Our analysis will be carried out within Chiral Perturbation Theory (ChPT), which is an effective field theory of QCD for low energies and temperatures (below the chiral phase transition).

In first place, we review in this chapter part of the material needed as a background to understand the results presented in the consecutive chapters. Special emphasis is made in finite-temperature field theory (Section 1.4), as well as in transport coefficients, being this latter point described from both the kinetic theory and the field theory points of view (Sections 1.5 and 1.6 respectively).

In Chapter 2 we present our analysis for thermal resonances in the meson gas. We discuss there the need of unitarizing the Chiral Perturbation Theory scattering amplitudes in order to correctly reproduce resonances. The behavior of the resonances present in the pion gas (the sigma and rho resonances) with temperature and nuclear density is analyzed. In order to incorporate nuclear density, two methods are used: scaling F_π (the pion decay constant), and a more accurate many-body approach based on the Bethe-Salpeter equation. We also discuss the "molecular" nature of these resonances, as well as the relation of their in-medium evolution with the restoration of chiral symmetry. Comparison with experimental results on threshold enhancement, and other phenomenological applications like dilepton production are also provided.

In Chapter 3 we develop a diagrammatic approach to transport coefficients in the context of Chiral Perturbation Theory. We start reviewing previous results for the calculation of transport coefficients in kinetic theory, scalar field theories, and gauge theories at high temperature, and we establish the connection with our diagrammatic approach for the meson gas at low temperatures. Next, in Section 3.3, we present the general analysis

[1] The three-flavor case is technically more involved, but it is also more interesting from the phenomenological point of view for temperatures close to the chiral phase transition, where all the light mesons play an important role. For low enough temperatures, the pion gas should be a good approximation.

of diagrams in ChPT for transport coefficients, which will allow us to calculate in the next sections the leading order contribution for the DC electrical conductivity, thermal conductivity, shear viscosity, and bulk viscosity. Several phenomenological and theoretical applications of the results obtained for transport coefficients are also discussed, like the connection between the DC conductivity and the soft-photon spectrum, the verification of the lower bound for η/s, the relation between the trace anomaly and the bulk viscosity, and a large-N_c analysis which provides a consistency check of our calculations.

Finally, in Chapter 4, the regime of chemical non-equilibrium for the meson gas is analyzed. It is assumed that the number of mesons is conserved so a chemical potential associated to this (approximate) conserved charge must be introduced. This approximation is valid for instance in the context of a relativistic heavy-ion collision, where chemical equilibrium is lost (at the chemical freeze-out temperature T_{CFO}) for the gas of hadrons before thermal freeze-out happens (at $T_{\mathrm{TFO}} < T_{\mathrm{CFO}}$), so the number of mesons is approximately conserved during that interval of temperatures. Since mesons (pions in our case) correspond to neutral scalar fields, it is necessary to modify the standard finite-temperature Feynman rules in order to deal with this out-of-equilibrium situation. This is discussed in Section 4.2, in terms of the holomorphic path-integral formalism. Once the Feynman rules are obtained, in Section 4.3 some interesting quantities are calculated out of chemical equilibrium for the pion gas: the partition function (and some other thermodynamic quantities derived from it like the pressure and the quark condensate), and the self-energy (thermal mass and width).

There is a section at the end of each of Chapters 2, 3, and 4 where the corresponding main conclusions are summarized. In addition, after Chapter 4, a section reviewing the main points of this thesis and future lines of work is provided. Finally, some complementary formulas, further technical details, notation, and a list of abbreviations are included in four appendixes.

The analyses and results presented in this thesis have been collected in almost their totality in the papers [FF06, GN07, FF07c, FF07a, FF07b, Cab08, FF09b, FF09c, FF09a].

1.1 QCD

Quantum Chromodynamics (QCD) is the field theory that describes the strong interaction taking place in the nuclei of atoms. The basic degrees of freedom (elementary particles) are quarks, which are fermions with spin 1/2, and gluons, massless gauge bosons with spin 1. The introduction of quarks by Gell-Mann and Zweig in 1964 was able to explain the symmetry under the zoo of strong-interacting particles known at that time.

The first evident (approximate) symmetry of the nuclear force was the so called *isospin symmetry* [Kra87, Hal84], with symmetry group SU(2), which transforms protons into neutrons due to their very similar masses[2]. The strong interaction is also approximately invariant under C (charge conjugation) and P (parity) [Kra87, Str64]. After the discovery in 1947 of the pion, the nucleon lost its central role in particle physics, and subsequently

[2]In this way, proton and neutron would be two different states of the same particle (the *nucleon*) with third component of isospin $I_3 = +\frac{1}{2}$ and $I_3 = -\frac{1}{2}$ respectively.

many other strong-interacting particles were found. The surprisingly low-rate for some reactions like $\Sigma^- \to n\pi^-$ in comparison with the typical scale of the strong interactions led to the introduction of an extra additive quantum number (besides I_3), the *strangeness* S, with possible values $S = -1, 0, 1$ (antiparticles have strangeness $-S$ with respect to the corresponding particles). Reactions involving strong and electromagnetic interactions only must conserve strangeness[3]. After the introduction of strangeness it was natural to try to accommodate the known spectrum of strong interacting particles into a symmetry group larger than SU(2). In 1961, SU(3) was proposed as the symmetry group of isospin and strangeness. But in 1964, with the introduction of the quark model, a much simpler picture was provided: any strong-interacting particle would be made of more elementary entities called *quarks*. Initially three types (*flavors*) of quarks were proposed: the quarks *up*, *down*, and *strange*, transforming in the fundamental representation of the (approximate) symmetry group SU(3) of flavor.

According to the quark model, all the hadrons could be classified by combining representations of the flavor group. Mesons, which are $\bar{q}q$ states, would then fit into the representations of SU(3): $3 \otimes \bar{3} = 8 \oplus 1$ (octet and singlet) [Geo99]. In the same way, baryons, which are qqq states, would fit into the representations $3 \otimes 3 \otimes 3 = 10 \oplus 8 \oplus 8 \oplus 1$. In Figure 1.1 we represent the ground-state mesons and baryons classified according to their values of I_3 and S. This graphical classification can be obtained by combining the graphical representation of the fundamental representation for quarks (top of the figure) [Hal84, Clo79, Geo99].

However, the symmetry of the ground-state baryons posed some problems, for instance, Δ^{++} is described with the symmetric wave function $u \uparrow u \uparrow u \uparrow$, whereas it must be antisymmetric under the exchange of identical quarks. In order to solve this problem, a new degree of freedom for quarks was introduced, the *color*, which is believed to be an exact symmetry of the strong interactions (unlike flavor symmetry, which is only approximate). Color can take three possible values: red, green or blue, and it is postulated that all hadrons are colorless (singlets of color).

Later on, three more quarks were discovered: the quark *charm* (predicted in 1964, observed in 1974), the quark *bottom* (observed in 1977), and the quark *top* (observed in 1995). The corresponding additive quantum numbers were introduced (charmness, bottomness, and topness, respectively), and the symmetry group enhanced. These quarks are much heavier than the (u, d, s) quarks (see Table 1.1 of quark properties[4]) and, by the decoupling theorem [App75], they can be ignored when one analyzes the low-energy dynamics of light hadrons, as it is the case in this thesis.

As we said above, quarks have another degree of freedom called color, so a quark of definite flavor f is at the same time a triplet of color (they transform under the

[3] $\Sigma^- \to n\pi^-$ decays slowly by weak interactions because it is forbidden by not conserving strangeness.

[4] Due to asymptotic freedom (see below) quarks are confined at low energies, so the definition of the mass of the quark involves some arbitrariness. The masses used for the light quarks (u, d and s) in the Table are the so called *current quark masses*.

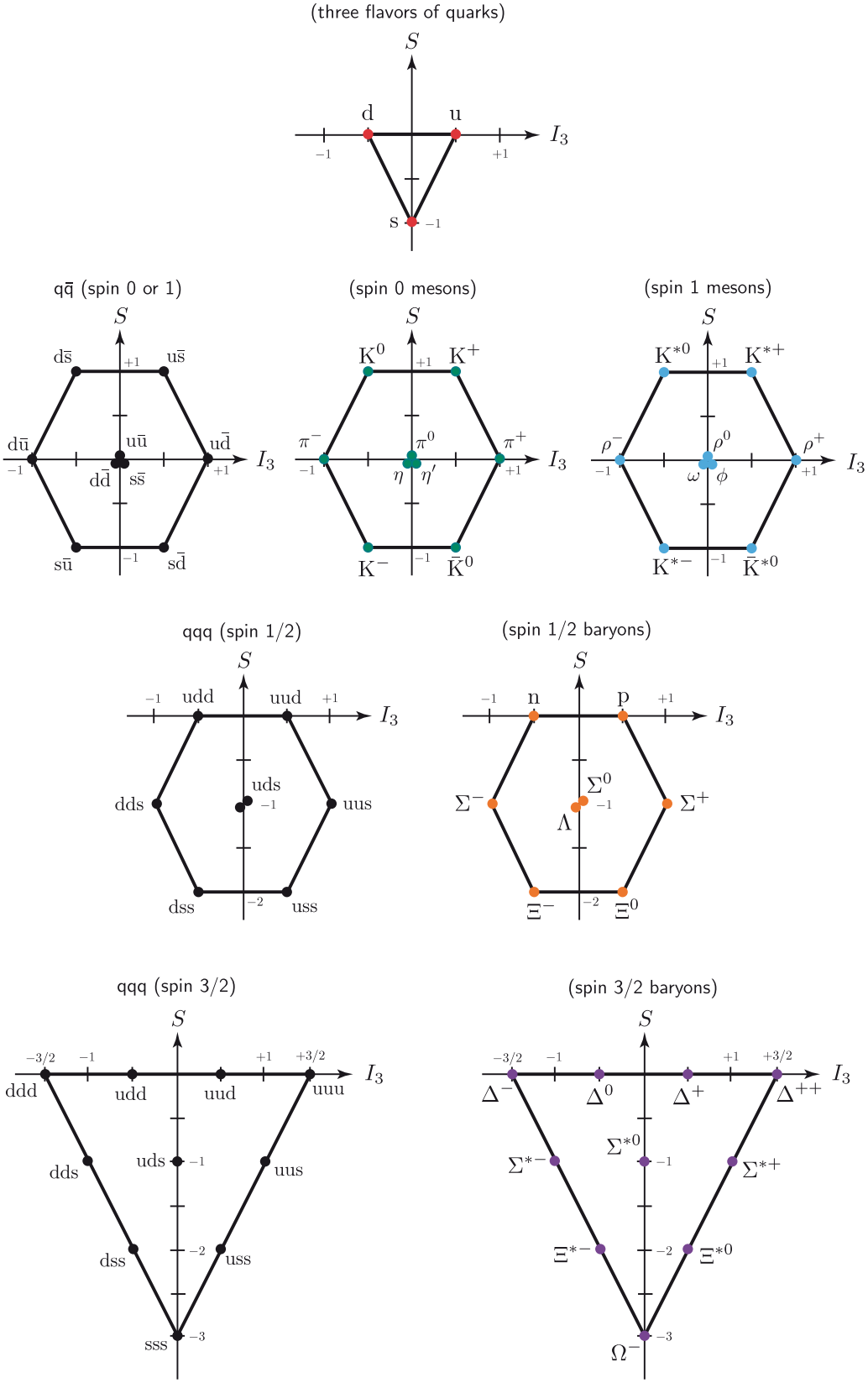

Figure 1.1: Classification of the ground-state mesons and baryons in terms of their third component of isospin and strangeness. The graphical classification for mesons and quarks can be obtained by combining the representation for quarks (top of the figure). Each meson with $S = 0$ is given by some combination of the states $\{u\bar{u}, d\bar{d}, s\bar{s}\}$.

Flavor	u (up)	d (down)	s (strange)	c (charm)	b (bottom)	t (top)
Charge	2/3	-1/3	-1/3	2/3	-1/3	2/3
Mass	$1.5 - 3.3$ MeV	$3.5 - 6.0$ MeV	104^{+26}_{-34} MeV	$1.27^{+0.07}_{-0.11}$ GeV	$4.20^{+0.17}_{-0.07}$ GeV	171.2 ± 2.1 GeV
I_3	1/2	-1/2	0	0	0	0
S	0	0	-1	0	0	0
C	0	0	0	1	0	0
B	0	0	0	0	-1	0
T	0	0	0	0	0	1

Table 1.1: Quark properties. Charges are given in units of the electron charge, e. Values for the masses correspond to the ones given in [Ams08]. I_3 is the third component of isospin, S is strangeness, C is charm, B denotes bottomness, and T is topness. All quarks have positive parity.

fundamental representation of the color group):

$$q_f = \begin{pmatrix} q_f^{\mathrm{R}} \\ q_f^{\mathrm{G}} \\ q_f^{\mathrm{B}} \end{pmatrix} \ .$$

Therefore, the lagrangian corresponding to free quarks is invariant under the global $\mathrm{SU(3)_c}$ color group. Analogously to what happens in Quantum Electrodynamics (QED) where photons and their interactions with electrons appear by gauging the corresponding U(1) group, in QCD we obtain the interaction between quarks and *gluons* by gauging the $\mathrm{SU(3)_c}$ group, with gluons being the corresponding gauge bosons. The QCD lagrangian then has the form [Sch03]:

$$\mathcal{L}_{\mathrm{QCD}} = \sum_{f=\substack{\mathrm{u,\,d,\,s}\\ \mathrm{c,\,b,\,t}}} \bar{q}_f(\mathrm{i}\not{D} - m_f)q_f - \frac{1}{4}F^a_{\mu\nu}F_a^{\mu\nu} \ , \tag{1.1}$$

where the field strength tensor is given in terms of the gluon fields and the gauge coupling g by:

$$F^a_{\mu\nu} = \partial_\mu A^a_\nu - \partial_\nu A^a_\mu + g f_{abc} A^b_\mu A^c_\nu \ . \tag{1.2}$$

And the covariant derivative is

$$D_\mu \equiv \partial_\mu - \mathrm{i}g \sum_{a=1}^{8} \frac{\lambda_a}{2} A^a_\mu \ , \tag{1.3}$$

where λ_a are the Gell-Mann matrices associated to the generators of the $\mathrm{SU(3)_c}$ group (see Appendix B). We note that the interaction between quarks and gluons is then independent of the flavor. We also see that as a consequence of the non-abelian character of gauge group $\mathrm{SU(3)_c}$, there appear self-interactions of gauge bosons with vertices involving 3 and 4 gluons.

From the point of view of gauge invariance, the lagrangian could also include a term of the form

$$\mathcal{L}_\theta = \frac{g^2\bar{\theta}}{64\pi^2}\epsilon^{\mu\nu\rho\sigma}F^a_{\mu\nu}F^a_{\rho\sigma} \ , \tag{1.4}$$

which implies an explicit P and CP violation of the strong interactions, but the experimental upper bounds for CP violation are very small and this term will be neglected in what follows.

In order to study the low-energy dynamics of hadrons, it is very useful to notice a clear separation in the orders of the masses of the three lightest and the three heaviest quarks,

$$\left.\begin{array}{l} m_{\rm u} \sim 2.4 \text{ MeV} \\ m_{\rm d} \sim 4.8 \text{ MeV} \\ m_{\rm s} \sim 100 \text{ MeV} \end{array}\right\} \ll 1 \text{ GeV} \leq \left\{\begin{array}{l} m_{\rm c} \sim 1.25 \text{ GeV} \\ m_{\rm b} \sim 4.25 \text{ GeV} \\ m_{\rm t} \sim 171 \text{ GeV} \end{array}\right. ,$$

where 1 GeV $\sim 4\pi F_\pi$ is the typical scale of mass for the lightest hadrons that are not Goldstone bosons (see below). In practice we will approximate the QCD lagrangian by its version with only the three lightest flavors. Also, due to the smallness of $m_{\rm u}$, $m_{\rm d}$, and m_s in comparison to 1 GeV, we will consider the QCD lagrangian in the *chiral limit*:

$$\mathcal{L}^0_{\rm QCD} = \sum_{f={\rm u,d,s}} \bar{q}_f \ {\rm i}\not{D}\, q_f - \frac{1}{4}F^a_{\mu\nu}F_a^{\mu\nu} \ . \tag{1.5}$$

1.1.1 Symmetries of the QCD lagrangian

Besides the above mentioned symmetries of the strong interactions, there are two symmetries of the lagrangian (1.5), which are actually broken at the quantum level, that are specially relevant in order to study the dynamics of QCD: *chiral symmetry* and *scale symmetry*.

Chiral symmetry

The lagrangian (1.5) is invariant under the global *chiral transformations* on the left- and right-handed components of the quark fields:

$$q_{\rm L} \overset{\chi}{\mapsto} \exp\left(-{\rm i}\theta^{\rm L}_a\frac{\lambda_a}{2}\right) q_{\rm L} \ , \tag{1.6}$$

$$q_{\rm R} \overset{\chi}{\mapsto} \exp\left(-{\rm i}\theta^{\rm R}_a\frac{\lambda_a}{2}\right) q_{\rm R} \ , \tag{1.7}$$

where $q_{\rm L} \equiv \dfrac{1-\gamma_5}{2}q$, and $q_{\rm R} \equiv \dfrac{1+\gamma_5}{2}q$. We denote the *chiral group* by $\chi \equiv {\rm SU(3)_L} \times {\rm SU(3)_R}$. These symmetries of the lagrangian give rise to the following conserved currents respectively:

$$L^{\mu,a} = \bar{q}_{\rm L}\gamma^\mu\frac{\lambda^a}{2}q_{\rm L} \ , \quad R^{\mu,a} = \bar{q}_{\rm R}\gamma^\mu\frac{\lambda^a}{2}q_{\rm R} \ . \tag{1.8}$$

From them we can define the *vector* and *axial-vector* currents:

$$V^{\mu,a} \equiv R^{\mu,a} + L^{\mu,a} = \bar{q}\gamma^{\mu}\frac{\lambda^a}{2}q \ , \quad A^{\mu,a} \equiv R^{\mu,a} - L^{\mu,a} = \bar{q}\gamma^{\mu}\gamma_5\frac{\lambda^a}{2}q \ . \tag{1.9}$$

By performing chiral transformations with the same and opposite phases, we can also obtain singlet vector and singlet axial-vector currents respectively:

$$V^{\mu} = \bar{q}\gamma^{\mu}q \ , \quad A^{\mu} = \bar{q}\gamma^{\mu}\gamma_5 q \ . \tag{1.10}$$

At the quantum level, chiral symmetry is spontaneously broken with the breaking pattern:

$$\mathrm{SU(3)_L} \times \mathrm{SU(3)_R} \equiv \mathrm{SU(3)_V} \times \mathrm{SU(3)_A} \longrightarrow \mathrm{SU(3)_V} \ , \tag{1.11}$$

where the subindices V and A refer to the vector and axial generators respectively. The fact that the vector part of the chiral group should remain unbroken was proved by Vafa and Witten in [Vaf84], but the reason for the breaking of the axial part remains unknown. The order parameter associated to the breaking of chiral symmetry is the quark condensate $\langle\bar{q}q\rangle = \langle\bar{u}u + \bar{d}d + \bar{s}s\rangle$ ($\neq 0$ in vacuum). On the other hand, the single axial-vector current involves an anomaly,

$$\partial_\mu A^\mu = \frac{3g^2}{32\pi^2}\epsilon_{\mu\nu\rho\sigma}F_a^{\mu\nu}F_a^{\sigma\rho} \ . \tag{1.12}$$

As a consequence, the difference between left-handed and right-handed quark numbers, according to (1.9), is not a constant of the motion [Sch03].

Scale symmetry, the trace anomaly, and asymptotic freedom

The lagrangian (1.5) is invariant at the classical level under the scale transformations [Itz05, Col85]:

$$x \mapsto \lambda x \ , \quad q \mapsto \lambda^{3/2}q \ , \quad A_\mu \mapsto \lambda A_\mu \ . \tag{1.13}$$

However, the scale invariance of the QCD lagrangian is broken explicitly by the quark mass, and by the running of the strong coupling constant at the quantum level [Col77]:

$$\partial_\mu s^\mu = T^\mu{}_\mu = \frac{\beta(g)}{2g}F^a_{\mu\nu}F_a^{\mu\nu} + \{1+\gamma(g)\}m\bar{q}q \ , \tag{1.14}$$

where we have considered the case of two flavors with $m \equiv m_{\mathrm{u}} \simeq m_{\mathrm{d}}$, $s^\mu = T^{\mu\nu}x_\nu$ is the dilation current, $\gamma(g)$ is the anomalous dimension of the quark mass, and the QCD β-function is given at the one-loop order by [Gro73, Pol73, Pes95]:

$$\beta(g) = \mu\frac{\partial g}{\partial \mu} = -\frac{g^3}{(4\pi)^2}\left(\frac{11}{3}N_{\mathrm{c}} - \frac{2}{3}N_{\mathrm{f}}\right) + \mathcal{O}(g^5) \ . \tag{1.15}$$

The fact that for $N_{\mathrm{c}} = 3$ and $N_{\mathrm{f}} \leq 16$ the β-function is negative has a major importance, because it essentially represents the rate of change of the coupling constant (running) with the scale. The direct consequence of this is known as *asymptotic freedom*, which

means that the strong interaction is weaker as the energy is increased, so quarks and gluons become free states at high enough momenta, whereas they interact strongly at low energies (where they become confined into hadrons).

As we will see in Section 3.4.4, there is a relation between the trace anomaly at finite temperature and the bulk viscosity. The equation (1.14) in the chiral limit ($m = 0$) is also suggestive to think that the condensate $\langle F^a_{\mu\nu} F^{\mu\nu}_a \rangle$ could be related somehow to confinement[5]. However, this relation between confinement and the gluon condensate is not clear for the moment[6].

1.1.2 Large-N_c limit of QCD

By studying the large-N_c limit of the QCD lagrangian one can obtain very useful qualitative information about non-perturbative phenomena [Man99, tH74a, tH74b, Wit79] since, in principle, one could think that this limit may not differ much from the original theory [Col85]. We are interested in analyzing that limit for correlation functions in QCD, in order to obtain the counting with N_c for transport coefficients (see Section 3.4.5), which can provide insight on possible phase transitions. We consider a non-abelian gauge theory with gauge group SU(N_c), and with N_f flavors of fermions (N_f fixed) in the fundamental representation of the color group. We will write the gauge coupling constant as

$$g \equiv \frac{\tilde{g}}{N_c} \tag{1.16}$$

in order to obtain a theory with a non-trivial large-N_c limit. Here the new coupling $\tilde{g}$ does not depend on the number of colors. We consider correlators that are vacuum expectation values of gauge invariant operators constructed out of quark and gluon fields. The operators need not to be local, but we require that we cannot split them into several color singlets. Allowed combinations are for instance $\bar{q}q$ or $F_{\mu\nu}F^{\mu\nu}$ but not $(\bar{q}q)^2$ [Man99].

It is also convenient to rescale the quark and gluon fields as:

$$\tilde{A}_\mu \equiv \tilde{g}\frac{A_\mu}{\sqrt{N_c}} \ , \quad \tilde{q} \equiv \frac{q}{\sqrt{N_c}} \ . \tag{1.17}$$

In terms of these rescaled fields, the lagrangian (1.1) takes now the form:

$$\tilde{\mathcal{L}} = N_c \left[-\frac{1}{4\tilde{g}^2}\tilde{F}_{\mu\nu}\tilde{F}^{\mu\nu} + \sum_f \bar{\tilde{q}}_f (\mathrm{i}\not{D} - m_f)\tilde{q}_f \right] \ . \tag{1.18}$$

The lagrangian has an overall N_c factor, but the theory does not reduce to a classical theory of quarks and gluons in the limit $N_c \to \infty$, because the number of components of $\tilde{q}_f$ and $\tilde{A}_\mu$ grows with N_c. From (1.18) we see that every vertex has a factor of N_c, every

[5] Confinement and asymptotic freedom are related to the appearance of a non-perturbative scale Λ_{QCD} generated by dimensional transmutation, so the static potential between a quark and an anti-quark is $V_{\bar{q}q}(r \to 0^+) \sim -(4/3)\alpha_s(r)/r$, $V_{\bar{q}q}(r \to \infty) \sim \sigma r$ ($\alpha_s \equiv g^2/4\pi$, and σ is the string tension) [Fis77, Pol87].

[6] The gluon condensate cannot be an order parameter (unlike the quark condensate in the case of spontaneous chiral symmetry breaking) because it does not vanish at high temperatures. The actual order parameter associated to confinement is the Polyakov loop [Pol78, Sus79, Pol87].

propagator has a factor of $1/N_\mathrm{c}$, and every color index loop gives a factor of N_c. Thus, using the notation for Feynman diagrams where gluon lines are double lines [Man99] and the diagram itself is a set of polygons with V vertices, E edges, and F faces, a connected vacuum diagram is then of order

$$\mathcal{O}(\text{diagram}) = N_\mathrm{c}^{V-E+F} \ . \tag{1.19}$$

If $\tilde{O}_i$ is a generic color-singlet operator given in terms of the rescaled fields, a connected correlation function of it can be obtained by differentiating $W[J]$ (generating functional, i.e., sum of connected vacuum diagrams):

$$\langle \tilde{O}_1 \tilde{O}_2 \dots \tilde{O}_r \rangle_\mathrm{c} = \frac{1}{\mathrm{i}N_\mathrm{c}} \frac{\delta}{\delta J_1} \dots \frac{1}{\mathrm{i}N_\mathrm{c}} \frac{\delta}{\delta J_r} W[J] \ , \tag{1.20}$$

where a source term $N_\mathrm{c}\tilde{O}_i J_i$ needs to be added to (1.18) in order to construct $W[J]$. Therefore, according to (1.20) and (1.19), pure-gluon r-point correlation functions are of order N_c^{2-r}. On the other hand, pure-quark r-point correlation functions are of order N_c^{1-r}. In the case of combination of quark and gluon states, if $\tilde{H}_i$ denotes a quark singlet, and $\tilde{G}_l$ denotes a gluon singlet, then the correlator $\langle \tilde{H}_1 \dots \tilde{H}_s \tilde{G}_1 \dots \tilde{G}_r \rangle$ will be of order N_c^{1-r-s}. This N_c counting was obtained for correlation functions involving the rescaled fields $\tilde{A}_\mu$ and $\tilde{q}$, so in order to obtain the counting for the original correlation functions we just have to multiply by the suitable factor according to (1.17). For instance, $\langle \bar{q}q \rangle = \mathcal{O}(N_\mathrm{c})$, and $\langle F_{\mu\nu} F^{\mu\nu} \rangle = \mathcal{O}(N_\mathrm{c}^2)$. A result that we will use in Section 3.4.5 is the behavior of the pion decay constant F_π with N_c. From its definition

$$\langle 0 | \bar{q} \gamma^\mu \gamma_5 T^a q | \pi^b(p) \rangle = \mathrm{i} F_\pi p^\mu \delta^{ab} \ , \tag{1.21}$$

where T^a is a SU(N) generator and $|\pi^b\rangle$ is a one-pion state, it is not difficult to obtain that $F_\pi = \mathcal{O}(\sqrt{N_\mathrm{c}})$, since $|\pi^a\rangle$ is essentially a quark bilinear acting on the vacuum [Man99]. This result for the pion decay constant means that, in the large-N_c limit, the meson-meson interactions are suppressed because they are proportional to inverse powers of F_π (see for instance Eq. (2.3)).

1.2 Some aspects on heavy-ion collisions

A quark-gluon plasma (QGP) phase is expected to be obtained by either heating or compressing hadronic matter [Paj07, Yag05]. Relativistic heavy ion collisions could in principle provide each of these situations. At energies between a few and a few tens of GeV per nucleon, the colliding ions stop each other and high baryon densities can be obtained. For much higher energies, the two ions pass through each other and the collision region acquires a high temperature but low baryon density.

The main objective of these experiments is to explore the QCD phase diagram (see Figure 1.2), which represents the different states of QCD matter as a function of the temperature and the quark chemical potential [Shu09]. The three most remarkable characteristics of this diagram are: confinement, chiral symmetry breaking, and color superconductivity. At low temperatures and chemical potentials we find the hadronic phase, characterized

by being confined and where chiral symmetry is broken. The color superconducting phase corresponds to low temperatures and high densities, and it is probably present in the core of some neutron stars. On the other hand, the QGP phase corresponds to very high temperatures, or both temperature and densities simultaneously. In the intermediate regions we can have several situations, e.g. there can coexist chiral and color-superconducting condensates. The Relativistic Heavy-Ion Collider (RHIC), in New York, has been exploring the high-temperature and low-density region of the phase diagram in order to obtain signals from a formed QGP, with the result of obtaining "the most perfect liquid on Earth", due to the low viscosity of the matter created [Ars05, Bac05, Ada05, Adc05]. Several experiments of the LHC at CERN will also analyze this region of the phase diagram but at higher temperatures. Other facilities, like FAIR in Darmstadt will probe the region of finite densities (see Fig. 1.2).

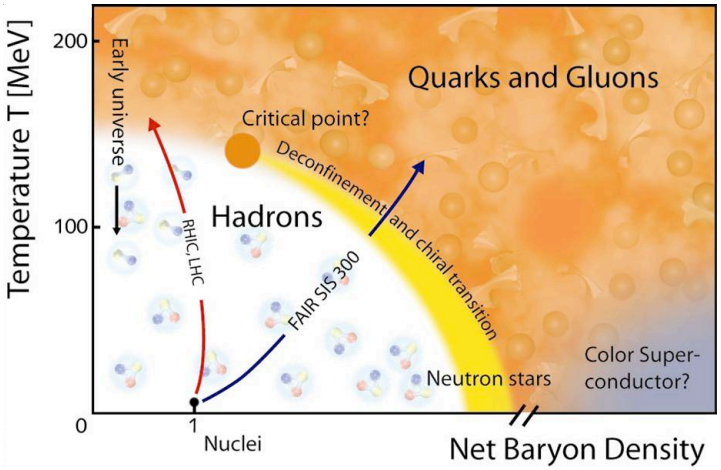

Figure 1.2: Phase diagram of QCD.

The space-time evolution of a relativistic heavy-ion collision can be divided into three main stages: The moment of the collision, the thermalization and evolution of the fireball, and hadronization followed by freeze-out. During the first stage, a large number of partons is produced and this determines the initial conditions for the subsequent development of the parton plasma. This stage is not well understood yet, and several models and descriptions have been proposed, among them, the Color Glass Condensate (CGC) description [McL02, Ian04], color-string percolation [Arm96, Paj05], or perturbative QCD models [Yag05].

During the second stage, it is expected that thermal equilibrium is reached and a hydrodynamical description of the evolution of the plasma can be applicable. In a non-central collision, the region where the two nuclei overlap, which will form a dense/hot matter, has an almond shape (see Fig. 1.3). The emission pattern of the particles coming out from this region strongly depends on the relation between the mean-free path λ and the size of the system R. When $\lambda \gtrsim R$, this emission pattern corresponds essentially to the superposition of many nucleon-nucleon collisions, and thus it is isotropic in the transverse plane. On the other hand, if $\lambda \ll R$ (where the hydrodynamical description

is applicable), the emission pattern is affected by the shape of the system. As we shall see in Section 1.5.2, in the hydrodynamical picture, according to Eq. (1.122), a gradient in pressure generates collective flow. In a peripheral collision ($b \neq 0$), the gradient of pressure is generated mainly in the X-direction (see Fig. 1.3), and thus the collective flow will be also produced in this direction. Therefore, the particle spectrum will have an elliptical shape in the transverse direction. Since the gradient of pressure is closely related to the equation of state (EOS), it is important to measure the elliptic flow in order to detect the existence of QGP in the early stages of the collision.

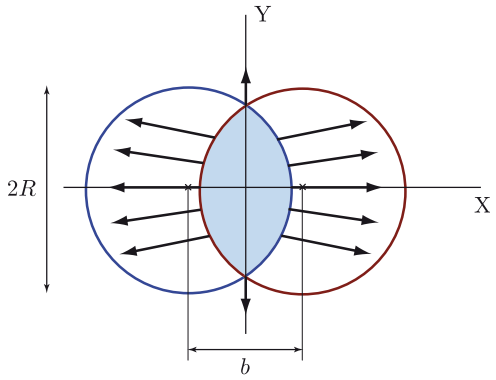

Figure 1.3: A peripheral collision projected over the transverse plane. The gradient of pressure is generated mainly along the X-axis.

Experimentally, the distribution of particles in azimuthal angle (angle measured in the transverse plane with respect to the axis X) is analyzed in the laboratory frame using the Fourier expansion

$$E\frac{\mathrm{d}^3N}{\mathrm{d}^3\boldsymbol{p}} = \frac{\mathrm{d}^2N}{2\pi p_{\mathrm{T}}\mathrm{d}p_{\mathrm{T}}\mathrm{d}y}\left(1+\sum_{n=1}^{\infty}2v_n\cos[n(\phi-\Phi_{\mathrm{r}})]\right)\ , \tag{1.22}$$

where the first two coefficients in this decomposition, v_1 and v_2, are called directed and elliptic flows respectively and they measure the strength of the corresponding type of flow, and Φ_{r} is the azimuthal angle of the reaction plane[7]. Consequently, from (1.22),

$$v_2(p_{\mathrm{T}}) = \langle\cos(2\phi)\rangle_{p_{\mathrm{T}}} \equiv \frac{\displaystyle\int_{-\pi}^{\pi}\mathrm{d}\phi\ \cos(2\phi)\frac{\mathrm{d}^2N}{p_{\mathrm{T}}\mathrm{d}p_{\mathrm{T}}\mathrm{d}y\mathrm{d}\phi}}{\displaystyle\int_{-\pi}^{\pi}\mathrm{d}\phi\ \frac{\mathrm{d}^2N}{p_{\mathrm{T}}\mathrm{d}p_{\mathrm{T}}\mathrm{d}y\mathrm{d}\phi}}\ , \tag{1.23}$$

where the angle ϕ is here measured relative to the reaction plane. To first order, the effect of viscosity on the distribution function (see Section 1.5) is given by [Tea03]:

$$\delta f = \frac{3}{4}\frac{\Gamma_{\mathrm{s}}}{T^2}f_0(1+f_0)p^\mu p^\nu\nabla_\mu\overset{\circ}{U}_\nu\ , \tag{1.24}$$

[7]The reaction plane is defined by the direction of collision, i.e. Z-axis, and the straight line joining the center of the two nuclei. Φ_{r} is not known a priory and has to be determined by analyzing the spectrum of the particles produced [Yag05].

where $\Gamma_s \equiv [(4/3)\eta + \zeta]/(\epsilon + P))$ is the sound attenuation length (the rest of the notation is explained in Section 1.5). Therefore, viscous effects could be important in order to describe properly elliptic flow results [Paj07]. In Figure 1.4 we show the plots from the work [Rom07], where data on elliptic flow are compared with several hydrodynamical calculations taking into account viscous effects[8]. We see that a non-zero viscosity is necessary in order to fit better the experimental data.

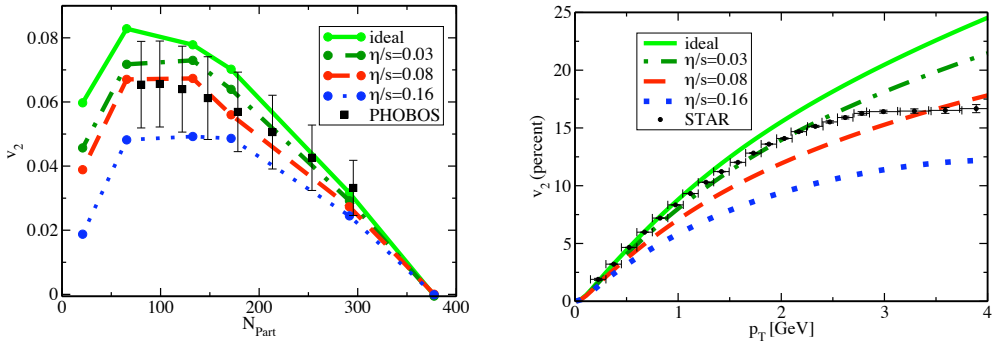

Figure 1.4: Elliptic flow measured by the PHOBOS collaboration as a function of the number of participants (left), and measured by the STAR collaboration as a function of the transverse momentum (right). Several curves corresponding to the perfect fluid case, and viscous corrections from a non-zero shear viscosity are also depicted.

1.3 Chiral Perturbation Theory

In order to describe the dynamics of the light mesons (pions, kaons and the eta) we will use Chiral Perturbation Theory (ChPT), which is an effective field theory of QCD for the low-energy regime [Sch03]. It is based on the spontaneous symmetry breaking pattern (1.11) of the chiral symmetry of the QCD lagrangian (for massless quarks), where the axial generators of the chiral algebra are broken leaving only the vector ones. As the result of this symmetry breaking, there must appear a number of Goldstone bosons equal to the number of broken generators (Goldstone theorem), and they are physically identified with the pions, kaons and eta. In order to construct an effective lagrangian, it is necessary to obtain the transformation rules of the Goldstone bosons, ϕ_a, under the original chiral group. It can be shown [Sch03] that they transform non-linearly, so if we use the exponential parameterization for the Goldstone bosons we have

$$U(x) \overset{\chi}{\mapsto} RU(x)L^\dagger \quad , \text{ with } U(x) \equiv \exp\left(\mathrm{i}\frac{\phi(x)}{F_0}\right) \quad , \text{ and } \phi(x) \equiv \sum_a \phi_a(x)\lambda_a \ , \qquad (1.25)$$

where $R \in \mathrm{SU}(N_\mathrm{f})$, $L \in \mathrm{SU}(N_\mathrm{f})$, λ_a are proportional to the broken generators, and F_0 coincides with the Goldstone boson decay constant to lowest order in the chiral expansion

[8]The bulk viscosity contribution has been traditionally neglected, but recently it has been proposed that it could be large near the phase transition (see Section 3.4.4). For a recent analysis of the effects on elliptic flow due to the bulk viscosity see [Den09].

(see below and [Sch03]). This non-linear transformation on $U(x)$ implies the following transformations for the Goldstone bosons separately under the vector and axial charges:

$$[Q_a^{\mathrm{V}}, \phi_b] = \mathrm{i} f_{abc}\phi_c \ , \quad [Q_a^{\mathrm{A}}, \phi_b] = g_{ab}(\boldsymbol{\phi}) \ , \tag{1.26}$$

where $g_{ab}(\boldsymbol{\phi})$ is some non-linear function. So we see that under the unbroken group the Goldstone bosons transform linearly but they do it non-linearly under the axial charges corresponding to the broken generators. Once one knows the transformation rules for the Goldstone bosons it is possible to construct a lagrangian which describes their dynamics as the most general expansion in terms of derivatives of the $U(x)$ field that respects all the symmetries of QCD:

$$\mathcal{L}_{\mathrm{ChPT}} = \mathcal{L}_2 + \mathcal{L}_4 + \mathcal{L}_6 + \dots \ , \tag{1.27}$$

where the subindex indicates the number of derivatives of the field $U(x)$.

For future convenience, we consider the QCD lagrangian with massless quarks coupled to some external fields [Sch03]:

$$\mathcal{L} = \mathcal{L}^0_{\mathrm{QCD}} + \bar{q}\gamma_\mu(v^\mu + \frac{1}{3}v^\mu_{(\mathrm{s})} + \gamma_5 a^\mu)q - \bar{q}(s - \gamma_5 p)q \ , \tag{1.28}$$

where $\mathcal{L}^0_{\mathrm{QCD}}$ is the QCD lagrangian with massless quarks and v^μ, $v^\mu_{(\mathrm{s})}$, a^μ, s, and p are some external (and color-neutral) iso-vector, iso-scalar vector, axial vector, scalar and pseudo-scalar fields respectively[9]. The usual QCD lagrangian with N_{f} massive flavors is recovered by setting $v^\mu = v^\mu_{(\mathrm{s})} = a^\mu = p = 0$, and $s = \mathrm{diag}(m_1, \dots, m_{N_{\mathrm{f}}})$.

In this thesis we will deal mainly with gases of pions, sigmas and rhos (these latter states not included as explicit degrees of freedom in our approach), although the general analysis can be directly extended to include kaons, etas and the corresponding meson resonances ($f_0(600)$, $\rho(770)$, $\mathrm{K}^*(892)$, κ, $f_0(980)$, $a_0(980)$ and the octet ω_8 [GN02a]). Therefore, we will consider the two-flavor case, so the asymptotic degrees of freedom will be pions, whereas the resonances $f_0(600)/\sigma$ and $\rho(770)$ will be generated dynamically by unitarization methods (see Chapter 2).

In practice, we will deal only with $\mathcal{L}_2$ and $\mathcal{L}_4$. In the chiral limit, these lagrangians must be invariant (locally with external sources) under $\mathrm{SU(2)_L \times SU(2)_R \times U(1)_V}$, while the ground state (vacuum) is invariant only under $\mathrm{SU(2)_V \times U(1)_V}$. To lowest order, $\mathcal{L}_2$, these symmetries are satisfied by the lagrangian given explicitly by the expression:

$$\mathcal{L}_2 = \frac{F_0^2}{4}\,\mathrm{Tr}\{\nabla_\mu U^\dagger \nabla^\mu U\} + \frac{F_0^2}{4}\,\mathrm{Tr}\{\chi U^\dagger + U\chi^\dagger\} \ , \tag{1.30}$$

[9] These external fields also have a matrix structure. For instance, in the $N_{\mathrm{f}} = 3$ case,

$$v^\mu = \sum_{k=1}^{8} \frac{\lambda_k}{2} v^\mu_k \ , \quad a^\mu = \sum_{k=1}^{8} \frac{\lambda_k}{2} a^\mu_k \ , \quad s = \sum_{k=0}^{8} \lambda_k s_k \ , \quad p = \sum_{k=0}^{8} \lambda_k p_k \ , \tag{1.29}$$

where $\{\lambda_a\}_{a=1}^8$ are the Gell-Mann matrices associated to the flavor group $\mathrm{SU(3)_f}$ (see Appendix B), $\lambda_0 \equiv \sqrt{2/3}\,\mathrm{diag}(1,1,1)$, and the singlet vector current $v^\mu_{(\mathrm{s})}$ is proportional to λ_0.

where

$$\chi \equiv 2B_0(s+\mathrm{i}p)\ ,\ \nabla_\mu U \equiv \partial_\mu U - \mathrm{i}r_\mu U + \mathrm{i}U l_\mu\ , \tag{1.31}$$

$$v_\mu \equiv \frac{1}{2}(r_\mu + l_\mu)\ ,\quad a_\mu \equiv \frac{1}{2}(r_\mu - l_\mu)\ . \tag{1.32}$$

By expanding $\mathcal{L}_2 = \mathcal{L}_2^{0\pi} + \mathcal{L}_2^{2\pi} + \mathcal{L}_2^{4\pi} + \mathcal{L}_2^{6\pi} + \ldots$ in powers of the pion field, considering the isospin-symmetric case $\chi = 2B_0 m \mathbf{1}_{2\times 2} \equiv M_0^2 \mathbf{1}_{2\times 2}$ and $l_\mu = r_\mu = 0$ ($m \equiv m_\mathrm{u} \simeq m_\mathrm{d}$ is the quark mass, and M_0 coincides to lowest order with the mass of the pion squared), and using the properties of the Pauli matrices (see Appendix B), we obtain the following terms

$$\mathcal{L}_2^{0\pi} = F_0^2 M_0^2\ , \tag{1.33}$$

$$\mathcal{L}_2^{2\pi} = \frac{1}{2}\partial_\mu \boldsymbol{\pi}\cdot\partial^\mu\boldsymbol{\pi} - \frac{1}{2}M_0^2\boldsymbol{\pi}^2\ , \tag{1.34}$$

$$\mathcal{L}_2^{4\pi} = \frac{1}{6F_0^2}\left[(\partial_\mu\boldsymbol{\pi}\cdot\boldsymbol{\pi})^2 - (\partial_\mu\boldsymbol{\pi}\cdot\partial^\mu\boldsymbol{\pi})\boldsymbol{\pi}^2 + \frac{M_0^2}{4}(\boldsymbol{\pi}^2)^2\right]\ , \tag{1.35}$$

$$\mathcal{L}_2^{6\pi} = \frac{1}{45F_0^4}\left[(\partial_\mu\boldsymbol{\pi}\cdot\partial^\mu\boldsymbol{\pi})(\boldsymbol{\pi}^2)^2 - (\partial_\mu\boldsymbol{\pi}\cdot\boldsymbol{\pi})^2\boldsymbol{\pi}^2 - \frac{M_0^2}{16}(\boldsymbol{\pi}^2)^3\right]\ . \tag{1.36}$$

The next-to-leading lagrangian is given by (it is the lagrangian of [Gas84] in the exponential parametrization [Sch03]):

$$\begin{aligned}
\mathcal{L}_4 = {} & \frac{l_1}{4}\left(\mathrm{Tr}\{(\nabla_\mu U)(\nabla^\mu U)^\dagger\}\right)^2 + \frac{l_2}{4}\,\mathrm{Tr}\{(\nabla_\mu U)(\nabla_\nu U)^\dagger\}\,\mathrm{Tr}\{(\nabla^\mu U)(\nabla^\nu U)^\dagger\} \\
& + \frac{l_3}{16}(\mathrm{Tr}\{\chi U^\dagger + U\chi^\dagger\})^2 + \frac{l_4}{4}\,\mathrm{Tr}\{(\nabla_\mu U)(\nabla^\mu\chi)^\dagger + (\nabla_\mu\chi)(\nabla^\mu U)^\dagger\} \\
& + l_5(\mathrm{Tr}\{f_{\mu\nu}^\mathrm{R} U f_\mathrm{L}^{\mu\nu} U^\dagger\} - \frac{1}{2}\,\mathrm{Tr}\{f_{\mu\nu}^\mathrm{L} f_\mathrm{L}^{\mu\nu} + f_{\mu\nu}^\mathrm{R} f_\mathrm{R}^{\mu\nu}\}) + \mathrm{i}\frac{l_6}{2}\,\mathrm{Tr}\{f_{\mu\nu}^\mathrm{R}(\nabla^\mu U)(\nabla^\nu U)^\dagger \\
& + f_{\mu\nu}^\mathrm{L}(\nabla^\mu U)^\dagger(\nabla^\nu U)\} - \frac{l_7}{16}\left(\mathrm{Tr}\{\chi U^\dagger - U\chi^\dagger\}\right)^2 + \frac{h_1+h_3}{4}\,\mathrm{Tr}\{\chi\chi^\dagger\} \\
& + \frac{h_1-h_3}{16}\left[(\mathrm{Tr}\{\chi U^\dagger + U\chi^\dagger\})^2 + (\mathrm{Tr}\{\chi U^\dagger - U\chi^\dagger\})^2\right. \\
& \left. -2\,\mathrm{Tr}\{\chi U^\dagger\chi U^\dagger + U\chi^\dagger U\chi^\dagger\}\right] - 2h_2\,\mathrm{Tr}\{f_{\mu\nu}^\mathrm{L} f_\mathrm{L}^{\mu\nu} + f_{\mu\nu}^\mathrm{R} f_\mathrm{R}^{\mu\nu}\}\ .
\end{aligned} \tag{1.37}$$

Expanding in powers of the pion field, and considering $f_{\mu\nu}^\mathrm{R} = f_{\mu\nu}^\mathrm{L} = 0$, we get the terms:

$$\mathcal{L}_4^{0\pi} = (l_3 + h_1)M_0^4\ , \tag{1.38}$$

$$\mathcal{L}_4^{2\pi} = -l_3 M_0^4 \frac{\boldsymbol{\pi}^2}{F_0^2}\ , \tag{1.39}$$

$$\mathcal{L}_4^{4\pi} = l_1\frac{(\partial_\mu\boldsymbol{\pi}\cdot\partial^\mu\boldsymbol{\pi})^2}{F_0^4} + l_2\frac{(\partial_\mu\boldsymbol{\pi}\cdot\partial_\nu\boldsymbol{\pi})^2}{F_0^4} + \frac{4l_3 + h_1 - h_3}{12}M_0^4\frac{(\boldsymbol{\pi}^2)^2}{F_0^4}\ . \tag{1.40}$$

The coupling constants F_0, B_0, l_i and h_i are called the *low-energy constants*, and are energy and temperature-independent by construction at the lagrangian level.

For the sake of completeness, we now give the expression of the lagrangian $\mathcal{L}_4$ for the case of $N_\mathrm{f} = 3$, where more independent terms appear (the lagrangian $\mathcal{L}_2$ takes the same form as in (1.30) but with the Pauli matrices replaced by the Gell-Mann matrices):

$$\begin{aligned}\mathcal{L}_4 = {} & L_1 \left(\mathrm{Tr}\{(\nabla_\mu U)(\nabla^\mu U)^\dagger\}\right)^2 + L_2 \,\mathrm{Tr}\{(\nabla_\mu U)(\nabla_\nu U)^\dagger\}\,\mathrm{Tr}\{(\nabla^\mu U)(\nabla^\nu U)^\dagger\} \\ & + L_3 \,\mathrm{Tr}\{(\nabla_\mu U)(\nabla^\mu U)^\dagger(\nabla_\nu U)(\nabla^\nu U)^\dagger\} + L_4 \,\mathrm{Tr}\{(\nabla_\mu U)(\nabla^\mu U)^\dagger\}\,\mathrm{Tr}\{\chi U^\dagger + U\chi^\dagger\} \\ & + L_5 \,\mathrm{Tr}\{(\nabla_\mu U)(\nabla^\mu U)^\dagger(\chi U^\dagger + U\chi^\dagger)\} + L_6 \left(\mathrm{Tr}\{\chi U^\dagger + U\chi^\dagger\}\right)^2 \\ & + L_7 \left(\mathrm{Tr}\{\chi U^\dagger - U\chi^\dagger\}\right)^2 + L_8 \,\mathrm{Tr}\{U\chi^\dagger U\chi^\dagger + \chi U^\dagger \chi U^\dagger\} \\ & - \mathrm{i}L_9 \,\mathrm{Tr}\{f_{\mu\nu}^\mathrm{R}(\nabla^\mu U)(\nabla^\nu U)^\dagger + f_{\mu\nu}^\mathrm{L}(\nabla^\mu U)^\dagger(\nabla^\nu U)\} + L_{10} \,\mathrm{Tr}\{U f_{\mu\nu}^\mathrm{L} U^\dagger f_\mathrm{R}^{\mu\nu}\} \\ & + H_1 \,\mathrm{Tr}\{f_{\mu\nu}^\mathrm{R} f_\mathrm{R}^{\mu\nu} + f_{\mu\nu}^\mathrm{L} f_\mathrm{L}^{\mu\nu}\} + H_2 \,\mathrm{Tr}\{\chi\chi^\dagger\} \,, \end{aligned} \tag{1.41}$$

where the low-energy constants L_i and H_i are different from the ones in (1.37) for the SU(2) case.

In order to deal with the infinite lagrangian $\mathcal{L}_\mathrm{ChPT}$ we need a way of estimating the contribution from the Feynman diagrams of interest, because we do not have an explicit coupling constant. Given a particular scattering amplitude $\mathcal{M}(m_\mathrm{q}, p_i)$, where m_q is the mass of the quarks and p_i the meson external momenta, the dimension D of the diagram is defined by rescaling these parameters in the following way:

$$\mathcal{M}(tp_i, t^2 m_\mathrm{q}) \equiv t^D \mathcal{M}(p_i, m_\mathrm{q}) \,. \tag{1.42}$$

Then, the dimension of a particular diagram can be easily computed (**Weinberg's Theorem** [Wei79]):

$$D = 2 + \sum_n N_n(n-2) + 2L \,, \tag{1.43}$$

where L is the number of loops in the diagram, and N_n the number of vertices coming from the lagrangian $\mathcal{L}_n$. This dimension so defined actually tells us that the contribution from a given diagram is $\mathcal{O}((p/\Lambda)^D)$, where p represents an energy, momentum, meson mass or temperature. The scale Λ will be of order $\Lambda_E \sim 4\pi F_\pi \simeq 1.2$ GeV for energies, momenta or meson masses[10], and of order $\Lambda_T \sim 300$ MeV for temperatures[11]. Therefore, the chiral expansion will be more reliable as we go down in energies and temperatures.

1.4 Finite-temperature field theory

In this section we will review the different formalisms used to extend the formulation of QFT for a single neutral scalar field from vacuum to finite temperatures [LB96, Lan87,

[10] It can be estimated as the momentum at which the contribution from a one-loop diagram with vertices of $\mathcal{L}_2$ that contributes to meson-meson scattering equals the tree level contribution from $\mathcal{L}_4$ [Geo09]. It can also be estimated as the energy of the lowest resonance, $\Lambda_E \sim$ 770 MeV, from where ChPT is expected to fail (see Section 2.1).

[11] It can be estimated as the temperature corresponding to an average energy equal to Λ_E, or as the critical temperature corresponding to the chiral phase transition.

Kap06]. The natural construction of thermal expectation values for quantum field operators is based on the definition of the *partition function* in QFT, which is the same as in QM[12]:

$$Z_\beta \equiv \mathrm{Tr}\{\mathrm{e}^{-\beta\hat{H}}\} \ , \tag{1.44}$$

where $\beta \equiv 1/T$ is the inverse of the temperature, and $\hat{H}$ is the hamiltonian operator of the system. Then, the thermal expectation value for an arbitrary field operator $\hat{\mathcal{O}}(x)$ is defined as

$$\langle\hat{\mathcal{O}}(x)\rangle_T \equiv \frac{1}{Z_\beta}\,\mathrm{Tr}\{\mathrm{e}^{-\beta\hat{H}}\hat{\mathcal{O}}(x)\} \ . \tag{1.45}$$

The *thermal propagator* in real time (RT) is then naturally defined as:

$$G(t,\boldsymbol{x}) \equiv \langle\hat{T}\hat{\phi}(t,\boldsymbol{x})\hat{\phi}(0,\boldsymbol{0})\rangle_T = \theta(t)G^{>}(t,\boldsymbol{x}) + \theta(-t)G^{<}(t,\boldsymbol{x}) \ , \tag{1.46}$$

where $\hat{T}$ is the time-ordering operator, $\hat{\phi}(t) = \mathrm{e}^{\mathrm{i}\hat{H}t}\hat{\phi}(0)\mathrm{e}^{-\mathrm{i}\hat{H}t}$ is the field operator in the Heisenberg's picture, and

$$G^{>}(t,\boldsymbol{x}) \equiv \langle\hat{\phi}(t,\boldsymbol{x})\hat{\phi}(0,\boldsymbol{0})\rangle_T \ , \quad G^{<}(t,\boldsymbol{x}) \equiv \langle\hat{\phi}(0,\boldsymbol{0})\hat{\phi}(t,\boldsymbol{x})\rangle_T = G^{>}(-t,-\boldsymbol{x}) \ . \tag{1.47}$$

By inserting a complete set of eigenstates of $\hat{H}$ we can express $G^{>}(t,\boldsymbol{x})$ as

$$G^{>}(t,\boldsymbol{x}) = \frac{1}{Z_\beta}\sum_{n,m}\mathrm{e}^{-\beta E_n}\mathrm{e}^{\mathrm{i}(E_n-E_m)t}|\langle n|\hat{\phi}(0,\boldsymbol{x})|m\rangle|^2 \ . \tag{1.48}$$

For (1.48) to be convergent it is necessary that

$$-\beta \leq \mathrm{Im}\, t \leq 0 \ . \tag{1.49}$$

Analogously, the corresponding convergence condition for $G^{<}$ is

$$\beta \geq \mathrm{Im}\, t \geq 0 \ . \tag{1.50}$$

Now, considering $\mathrm{e}^{-\beta\hat{H}}$ as an evolution operator in imaginary time (IT), we derive the following relation:

$$G^{>}(t,\boldsymbol{x}) = G^{<}(t+\mathrm{i}\beta,\boldsymbol{x}) \ . \tag{1.51}$$

This is known as the Kubo-Martin-Schwinger (KMS) relation. In momentum space the KMS relation takes the form

$$G^{<}(k_0) = G^{>}(-k_0) = \mathrm{e}^{-\beta k_0}G^{>}(k_0) \ . \tag{1.52}$$

The *spectral function* is defined as

$$\rho(k_0) \equiv G^{>}(k_0) - G^{<}(k_0) = \int_{-\infty}^{\infty}\mathrm{d}t\ \mathrm{e}^{\mathrm{i}k_0 t}\ \langle[\hat{\phi}(t),\hat{\phi}(0)]\rangle_T \ . \tag{1.53}$$

[12]We here assume no further conserved charges in the system besides the energy. See Chapter 4 for the more general case.

Using the representation (1.48) and the KMS condition we can obtain the following expression for the spectral density:

$$\rho(k_0) = \frac{2\pi}{Z}\sum_{n,m} \mathrm{e}^{-\beta E_n}[\delta(k_0 + E_n - E_m) - \delta(k_0 + E_m - E_n)]|\langle n|\hat{\phi}(0)|m\rangle|^2 \ . \tag{1.54}$$

From this expression we see that the spectral density is an odd real function of k_0, and it also verifies $\mathrm{sgn}(k_0)\rho(k_0) > 0$. For a free field, in vacuum or at finite temperature, the spectral density is easily calculated and is given by:

$$\rho_0(k_0) = 2\pi\,\mathrm{sgn}(k_0)\delta(k_0^2 - E_k^2) \ , \tag{1.55}$$

where $E_k \equiv (m^2 + |\boldsymbol{k}|^2)^{1/2}$, with m the mass of the field. In terms of the spectral function we can express the two-point functions $G^>$ and $G^<$ as:

$$G^>(k_0) = (1 + n_\mathrm{B}(k_0))\rho(k_0) \ , \quad G^<(k_0) = n_\mathrm{B}(k_0)\rho(k_0) \ , \tag{1.56}$$

where

$$n_\mathrm{B}(k_0) \equiv \frac{1}{\mathrm{e}^{\beta k_0} - 1} \tag{1.57}$$

is the Bose-Einstein distribution function.

1.4.1 Imaginary Time Formalism

Taking into account the convergence conditions (1.49) and (1.50) we now define the *propagator in imaginary time* (IT) by analytical continuation $t \mapsto -\mathrm{i}\tau$:

$$\Delta(\tau) \equiv \langle \hat{T}\{\hat{\phi}(\tau)\hat{\phi}(0)\}\rangle_T \ , \tag{1.58}$$

where for short we write $\hat{\phi}(\tau) = \mathrm{e}^{\hat{H}\tau}\hat{\phi}(0)\mathrm{e}^{-\hat{H}\tau}$ instead of $\hat{\phi}(-\mathrm{i}\tau)$, and the time-ordering operator acts in imaginary time:

$$\hat{T}\{\hat{\phi}(\tau_1)\hat{\phi}(\tau_2)\} = \begin{cases} \hat{\phi}(\tau_1)\hat{\phi}(\tau_2) \ , & \text{if } \tau_1 > \tau_2 \\ \hat{\phi}(\tau_2)\hat{\phi}(\tau_1) \ , & \text{if } \tau_2 > \tau_1 \end{cases} \ . \tag{1.59}$$

Because of the KMS relation, this propagator verifies for any $\tau \in [0, \beta]$ the periodicity property:

$$\Delta(\tau - \beta) = \Delta(\tau) \ . \tag{1.60}$$

Due to this periodicity property, and since the imaginary-time propagator is defined only in the time interval $[-\beta, \beta]$, we can define its Fourier transform as:

$$\Delta(\mathrm{i}\omega_n) \equiv \int_0^\beta \mathrm{d}\tau \ \mathrm{e}^{\mathrm{i}\tau\omega_n}\Delta(\tau) \ , \quad \Delta(\tau) = T\sum_n \mathrm{e}^{-\mathrm{i}\omega_n\tau}\Delta(\mathrm{i}\omega_n) \ , \tag{1.61}$$

where we have written $\Delta(\mathrm{i}\omega_n)$ instead of $\Delta(\omega_n)$ for future convenience when we perform analytical continuations. Because the Fourier transform is taken over a finite interval, the frequencies ω_n are discrete (called *Matsubara frequencies*):

$$\omega_n = \frac{2\pi n}{\beta} \ , \quad n \in \mathbb{Z} \ . \tag{1.62}$$

The propagator in IT is also called *Matsubara propagator*. In terms of the spectral density, the IT propagator is written as:

$$\Delta(\mathrm{i}\omega_n) = \int_{-\infty}^{\infty} \frac{\mathrm{d}k_0}{2\pi} \, \frac{\rho(k_0)}{k_0 - \mathrm{i}\omega_n} \ . \tag{1.63}$$

For a free field,

$$\Delta_0(\mathrm{i}\omega_n) = \frac{1}{\omega_n^2 + E_k^2} \ . \tag{1.64}$$

Other propagators that will appear in this thesis (for instance in the calculation of transport coefficients in LRT, see Section 1.6) are the *retarded* and *advanced* propagators, defined as:

$$G_{\mathrm{R}}(t) \equiv \theta(t)\langle[\hat{\phi}(t), \hat{\phi}(0)]\rangle_T \ , \quad G_{\mathrm{A}}(t) \equiv \theta(-t)\langle[\hat{\phi}(0), \hat{\phi}(t)]\rangle_T \ , \tag{1.65}$$

for $t \in \mathbb{R}$. Now, using the representation for the θ-function

$$\theta(t) = \mathrm{i} \int_{-\infty}^{\infty} \frac{\mathrm{d}k_0}{2\pi} \, \frac{\mathrm{e}^{-\mathrm{i}k_0 t}}{k_0 + \mathrm{i}0^+} \ , \tag{1.66}$$

we can express the Fourier transform of the retarded and advanced propagators by:

$$G_{\mathrm{R}}(k_0) = \mathrm{i} \int_{-\infty}^{\infty} \frac{\mathrm{d}k_0'}{2\pi} \, \frac{\rho(k_0')}{k_0 - k_0' + \mathrm{i}0^+} \ , \quad G_{\mathrm{A}}(k_0) = -\mathrm{i} \int_{-\infty}^{\infty} \frac{\mathrm{d}k_0'}{2\pi} \, \frac{\rho(k_0')}{k_0 - k_0' - \mathrm{i}0^+} \ . \tag{1.67}$$

Therefore, we can relate the IT propagator to the retarded and advanced ones by analytical continuation:

$$G_{\mathrm{R}}(k_0) = -\mathrm{i}\Delta(k_0 + \mathrm{i}0^+) \ , \quad G_{\mathrm{A}}(k_0) = \mathrm{i}\Delta(k_0 - \mathrm{i}0^+) \ . \tag{1.68}$$

For a scalar field theory with the lagrangian

$$\mathcal{L} = \frac{1}{2}\partial_\mu\phi\partial^\mu\phi - \frac{1}{2}m^2\phi^2 - \mathcal{V}(\phi) \ , \tag{1.69}$$

and considering $\mathrm{e}^{-\tau\hat{H}}$, with $\tau \in [0, \beta]$, as an evolution operator in IT, we can construct a path-integral representation for the generating functional of n-point correlation functions as usual [LB96, Lan87, Kap06]. It takes the form:

$$Z[j] = \mathcal{N} \exp\left(- \int_0^\beta \mathrm{d}^4 z \ \mathcal{V}\left(\frac{\delta}{\delta j(z)}\right)\right) \exp\left(\frac{1}{2}\int_0^\beta \mathrm{d}^4 x \ \mathrm{d}^4 y \ j(x)\Delta_0(x-y)j(y)\right) \ , \tag{1.70}$$

where $\mathcal{N}$ is some normalization constant. We can see that this form of the generating functional is very similar to the one used to derive Feynman rules at $T = 0$ in euclidean space; the only differences are the replacement of the Feynman propagator by the Matsubara one, $D_{\mathrm{F}} \mapsto \Delta_0$, and the integration range for the time variable that in ITF goes

from 0 to β. Therefore, Feynman rules in position space are the same in euclidean space at $T = 0$ and at finite T except for the mentioned replacements. In momentum space, the Feynman rules are obtained by replacing

$$D_{\mathrm{F}}(\boldsymbol{p}, p_4) \mapsto \Delta_0(\mathrm{i}\omega_n, \boldsymbol{p}) \ , \quad \int \frac{\mathrm{d}^4 p}{(2\pi)^4} \mapsto T \sum_n \int \frac{\mathrm{d}^3 \boldsymbol{p}}{(2\pi)^3} \ , \tag{1.71}$$

for propagators and loop integrals respectively, and the delta function corresponding to energy conservation at each vertex is replaced by a Kronecker delta involving the corresponding Matsubara frequencies: $\delta(\sum_i p_i^0) \mapsto \beta \delta_{\mathrm{K}}(\sum_i \omega_i)$. Also, there will be an overall factor $\beta(2\pi)^3 \delta^{(3)}(\mathbf{0}) = \beta V$ (V is the 3-dimensional volume).

As we have seen, when obtaining Feynman diagrams at finite temperature we will have to deal with sums over functions of Matsubara frequencies, called *Matsubara sums*. A useful technique to compute these sums is based on the Cauchy's Theorem by using a convenient contour of integration. If we have some complex function $f(z)$ with poles and cuts in the z-plane, and that goes to zero fast enough as $|z| \to \infty$, then [VB02, LB96, Kap06]:

$$T \sum_n f(\mathrm{i}\omega_n) = - \sum_{i(\mathrm{poles})} n_{\mathrm{B}}(z_i) \, \mathrm{Res}(f; z = z_i) + \sum_{i(\mathrm{cuts})} \int_{-\infty}^{\infty} \frac{\mathrm{d}\xi}{2\pi \mathrm{i}} \, n_{\mathrm{B}}(\xi) \, \mathrm{Disc}_i \, f \ . \tag{1.72}$$

In Figure 1.5 we represent a typical structure of poles and cuts of the product of two propagators. In order to perform the Matsubara sum, we start from a contour C_0 surrounding the poles corresponding to the Matsubara frequencies, then we deform it into the contour C and take the radius to infinity, leading to the formula (1.72).

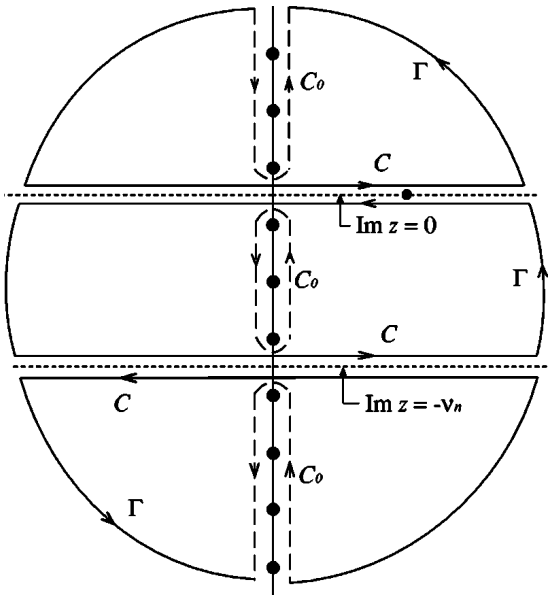

Figure 1.5: General contour of integration for calculating Matsubara sums, where we have several poles and cuts. C_0 is the original contour around the poles. C is the deformed contour. The contribution from the arcs Γ vanishes when the radius goes to infinity.

The *self-energy* in IT is defined as

$$\Delta(\mathrm{i}\omega_n, \boldsymbol{k}) = \Delta_0(\mathrm{i}\omega_n, \boldsymbol{k}) + \Delta_0(\mathrm{i}\omega_n, \boldsymbol{k})(-\Pi(\mathrm{i}\omega_n, \boldsymbol{k}))\Delta(\mathrm{i}\omega_n, \boldsymbol{k}) \ . \tag{1.73}$$

Analogously, retarded and advanced self-energies are given by:

$$\Pi_{\mathrm{R}}(k_0) \equiv -\mathrm{i}\Pi(\mathrm{i}\omega_n \mapsto k_0 + \mathrm{i}0^+) \ , \quad \Pi_{\mathrm{A}}(k_0) \equiv \mathrm{i}\Pi(\mathrm{i}\omega_n \mapsto k_0 - \mathrm{i}0^+) \ . \tag{1.74}$$

1.4.2 Real Time Formalism

We are now interested in a generating functional for n-point functions with real-time arguments, i.e.

$$G_C(x_1, \ldots, x_n) = \frac{1}{Z} \left. \frac{\delta^n Z_C[j]}{\mathrm{i}\delta j(x_1) \cdot \ldots \cdot \mathrm{i}\delta j(x_n)} \right|_{j=0} \ , \tag{1.75}$$

where $Z = Z_C[j=0]$, and

$$Z_C[j] = \mathrm{Tr}\left[\mathrm{e}^{-\beta\hat{H}} \hat{T}_C \exp\left(\mathrm{i} \int_C \mathrm{d}^4x \ j(x)\hat{\phi}(x) \right) \right] \ . \tag{1.76}$$

Here, the time-ordering operator $\hat{T}_C$ acts along a curve C that must contain the real axis. Furthermore, since we can write the generating functional in the form

$$Z_C = \int \mathrm{d}\phi'(\boldsymbol{x}) \ \langle \phi'(\boldsymbol{x}); t_{\mathrm{i}} - \mathrm{i}\beta | \hat{T}_C \exp\left(\mathrm{i} \int \mathrm{d}^4x \ j(x)\hat{\phi}(x) \right) | \phi'(\boldsymbol{x}); t_{\mathrm{i}} \rangle \ , \tag{1.77}$$

then, given a real starting point t_{i} for the path C, it must end at $t_{\mathrm{i}} - \mathrm{i}\beta$. The usual choice for the path C is shown in Figure 1.6, where $C = C_1 \cup C_2 \cup C_3 \cup C_4$. The perturbative

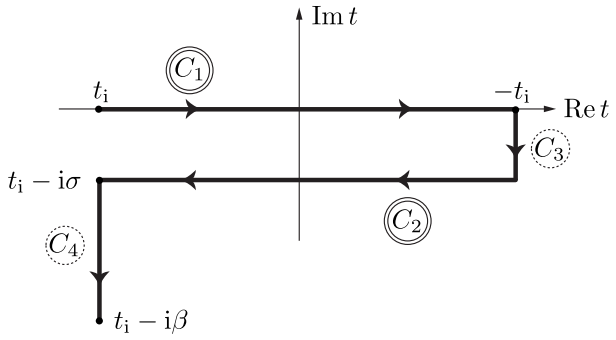

Figure 1.6: Path of integration in RTF. Only the segments C_1 and C_2 are physically relevant independently of the value of σ.

expansion is derived from

$$Z_C[j] = \exp\left(-\mathrm{i} \int_C \mathrm{d}^4z \ \mathcal{V}\left(\frac{\delta}{\mathrm{i}\delta j(z)} \right) \right) Z_C^0[j] \ , \tag{1.78}$$

where the free generating functional is given by

$$Z_C^0[j] = \mathcal{N} \exp\left(-\frac{1}{2} \int_C \mathrm{d}^4x \; \mathrm{d}^4y \; j(x) G_C^0(x-y) j(y) \right) \; . \tag{1.79}$$

And the free propagator for times on the curve C is defined as:

$$G_C^0(x-x') \equiv \theta_C(t-t') G_0^>(x-x') + \theta_C(t'-t) G_0^<(x-x') \; . \tag{1.80}$$

It can be shown [Lan87] that the generating functional can be factorized in the limit $t_\mathrm{i} \to -\infty$:

$$Z_C^0[j] = \mathcal{N}_1 Z_{C_{12}}^0[j] Z_{C_{34}}^0[j] \; , \tag{1.81}$$

with $C_{ab} \equiv C_a \cup C_b$. Therefore, the physical Green functions can be obtained from $Z_{C_{12}}$ only[13], which can be written as [LB96]

$$Z_{C_{12}}^0[j] = \mathcal{N}_2 \exp\left(-\frac{1}{2} \int_{-\infty}^{\infty} \mathrm{d}^4x \int_{-\infty}^{\infty} \mathrm{d}^4x' \; j_a(x) G_{ab}^0(x-x') j_b(x') \right) \; , \tag{1.82}$$

where a, b take the values 1 or 2 and indicate the segment of the path to which belong the real argument of the corresponding function. Since the segments C_3 and C_4 are not relevant, we can take $\sigma = 0$, then:

$$G_{11}^0(t) = [G_{22}^0(t)]^* = G_0(t) \; , \quad G_{12}^0(t) = G_{21}^0(-t) = G_0^<(t) \; , \tag{1.83}$$

$$G_{11}^0(k_0) = [G_{22}^0(k_0)]^* = \frac{\mathrm{i}}{k^2 - m^2 + \mathrm{i}0^+} + n_\mathrm{B}(|k_0|) 2\pi\delta(k^2 - m^2) \; , \tag{1.84}$$

$$G_{12}^0(k_0) = G_{21}^0(-k_0) = \left(\theta(-k_0) + n_\mathrm{B}(|k_0|)\right) 2\pi\delta(k^2 - m^2) \; . \tag{1.85}$$

The external vertices in a diagram must be of type 1, which are the physical ones, while vertices of type 2 are always internal. We can see it as a doubling in the number of degrees of freedom, where "fields of type 2" act as ghost fields that can never manifest as asymptotic states. The Feynman rules in RTF are the same as in vacuum except we now have two different types of vertices 1 and 2, and the rule for vertices of the second type is the conjugate of the one for vertices of type 1. Vertices are joint by propagators G_{ab}^0 where a and b take the values 1 or 2 depending on the vertices the propagator joins.

The *self-energy* in RT is defined as:

$$G_{ab}(k) = G_{ab}^0(k) + G_{ac}^0(k)(-\mathrm{i}\Pi_{cd}(k)) G_{db}^0(k) \; . \tag{1.86}$$

By diagonalizing the self-energy, i.e.

$$-\mathrm{i}\Pi_{ab}(k) = U_{ac}^{-1}(k) \begin{pmatrix} -\mathrm{i}\bar{\Pi}(k) & 0 \\ 0 & (-\mathrm{i}\bar{\Pi}(k))^* \end{pmatrix}_{cd} U_{db}^{-1}(k) \; , \tag{1.87}$$

[13]However there are some exceptions where the vertical part of the contour does not decouple [Kra04], see comments after Eq. (4.63).

with

$$U(k) = \begin{pmatrix} \sqrt{1+n_{\rm B}(k_0)} & \sqrt{n_{\rm B}(k_0)} \\ \sqrt{n_{\rm B}(k_0)} & \sqrt{1+n_{\rm B}(k_0)} \end{pmatrix} . \tag{1.88}$$

Then, we can express the rest of the components of the self-energy in terms of the quantity $\bar{\Pi}(k)$:

$$\mathrm{Re}\,\Pi_{11}(k) = \mathrm{Re}\,\bar{\Pi}(k) \ , \quad \mathrm{Im}\,\Pi_{11}(k) = \mathrm{sgn}(k_0)(1+2n_{\rm B}(k_0))\,\mathrm{Im}\,\bar{\Pi}(k) \ , \tag{1.89}$$

$$\Pi_{12}(k) = \frac{-\mathrm{i}}{\sinh(\beta|k_0|/2)}\ \mathrm{Im}\,\bar{\Pi}(k) \ . \tag{1.90}$$

From this we can also obtain a relation between the ITF-self-energy and the RT one [LB96]:

$$\bar{\Pi}(k) = \Pi(k_0(1+\mathrm{i}0^+), \boldsymbol{k}) \ . \tag{1.91}$$

In Chapter 4, we will need to calculate retarded Green functions in RTF, whereas the Feynman rules given above for the RT-case correspond to time-ordered correlators. According to [Kob90], retarded green functions can be obtained in the RTF by means of summing over all the possible ways of "circling" the vertices of a given diagram (except the one with the largest time argument). These "circled" vertices and the propagators attached to them have their own Feynman rules associated. The resulting function has the required causal retarded properties, namely that satisfies that one of the outgoing lines of the corresponding diagram has the largest time component. It was then shown in [Kob90] by several examples that this function coincides with the analytic continuation of the ITF correlator.

On the other hand, we can also calculate thermodynamic quantities within the RTF, i.e., the partition function or the free energy density, which are given in terms of vacuum diagrams. In principle, due to the factorization of the imaginary-leg commented above, the contribution to vacuum graphs when summing over fields of type 1 and 2 vanishes identically. However, it was shown in [Fuj84, Mat85] that fixing one of the vertices of a vacuum diagram to be "external" of type 1 and summing over the remaining internal vertices with an overall β factor reproduces the free-energy result and coincides with the ITF.

1.5 Hydrodynamics

A fluid is a many-particle system whose main characteristic is the easiness for it to be deformed. A solid, for instance, has a definite shape and this shape changes only when the external conditions change. On the other hand, a fluid does not have a preferred shape, and for an homogeneous one, the different parts of it can be rearranged without changing the macroscopic properties of the fluid. However, there are several examples of systems where there is a no clear distinction between the solid and the fluid behavior, i.e. they present a dual behavior.

We can give a first (not rigorous) definition of a *simple solid*, as one whose shape changes very little when a small external force acts on it. On the other hand, a *simple fluid* would be one whose shape would significantly change under a small external force

[Bat67]. Jelly or paint, for instance, present this dual character; they behave like an elastic solid after allowing to stand for a time, but recover a liquid behavior after intense shaking or brushing. But most common substances like air or water behave like simple fluids. As a simple fluid we will also consider one which cannot withstand the tendency by the external forces to modify its volume. There is a natural classification for fluids: *liquid* or *gas*. This classification is even less rigorous than that for fluids and solids. Usually, the density of a liquid is larger than of a gas, but the real distinction comes from their compressibilities: a gas can be compressed much more easily than a liquid (a big deformation in the volume of a gas does not imply a large variation of pressure). But also, there are circumstances where, in the motion of a fluid, there are small variations of pressures so liquids and gases behave very similar. In a normal gas (air, for instance), the mean distance between molecules is about 10 times larger than the mean distance in a liquid (water, for instance) or a solid (in both the distance is of the same order).

The term *perfect, or ideal, gas* is usually referred to a fluid for which the mean distance between the particles is so large that the interaction can be neglected in a first approximation (of course, the particles of the gas eventually collide, but the rest of the time they propagate freely). So we can understand a gas, in general, as a system where the distance between particles is so large that the interaction is very small, or also as a system where the interaction is small although the distance between particles may be small too. For both, liquids and solids, the interaction between particles is not small. Usually, the change of phase produced by melting implies only a change in density by several percent (the case of water is exceptional). In the liquid phase there can still be some ordering in the molecules of particles. The mean free path, λ, for particles in a liquid is of the same order as the radius of the interaction forces, r_0, and the description of it implies both quantum and classical approaches. For a gas instead, $\lambda \gg r_0$, and a classical description is sufficient (except for describing collisions).

On the other hand, the term *perfect fluid* is referred to a fluid for which no dissipation processes (like viscosities) take place. In general, a fluid (liquid or gas) will be a many-particle system[14] with a typical size L much larger than the mean distance $\bar{d}$ between particles, so it can be considered as a continuous medium. Moreover, in a fluid, the mean free path is much smaller than the typical dimensions of the system, $\lambda \ll L$, but long enough to keep local thermal equilibrium (or small deviations from it), which requires collisions to be maintained.

1.5.1 Relativistic formulation

Distribution function

The macroscopic properties of a dilute enough fluid (so the quasi-particle picture is valid) are completely described by knowing the *distribution function*, $f(x,p)$ (p^0 will be on-shell from now on, i.e., $p^0 = \sqrt{\boldsymbol{p}^2 + m^2} \equiv E_p$), defined so that $f(x,p)\Delta^3\boldsymbol{x}\Delta^3\boldsymbol{p}$ is the number of particles at the instant of time t in the element of fluid with momentum in the range $(\boldsymbol{p}, \boldsymbol{p}+\Delta\boldsymbol{p})$ and position in the 3-dimensional box $(\boldsymbol{x}, \boldsymbol{x}+\Delta\boldsymbol{x})$. It can be shown that the

[14] If the interaction is strong-enough, the quasi-particle picture of a liquid breaks down and we are left with the dynamics of quantum fields, but it is still a liquid.

distribution function is a Lorentz-scalar quantity [Gro80]. From the distribution function we can obtain the macroscopic properties of the fluid.

On the other hand, the macroscopic state of the fluid is also completely described by knowing the density of particles, $n(t, \boldsymbol{x})$, the hydrodynamic velocity $U^\mu(t, \boldsymbol{x})$, and the energy density, $\epsilon(t, \boldsymbol{x})$ (this is analogous to the mechanical description of a many-particle system, where we need to know the position of all the particles at a given time, their velocities at that time, and their interaction laws). For instance, the particle density (number of particle per unit volume) is given in terms of the distribution function by:

$$n(t, \boldsymbol{x}) \equiv \int \mathrm{d}^3\boldsymbol{p}\ f(x, p)\ . \tag{1.92}$$

We can also introduce the particle flow (number of particles per unit time and unit area) as:

$$\boldsymbol{j}(x) \equiv \int \mathrm{d}^3\boldsymbol{p}\ \boldsymbol{v} f(x, p)\ , \tag{1.93}$$

where $\boldsymbol{v} = \boldsymbol{p}/p^0$ is the velocity of one particle with momentum $\boldsymbol{p}$ (remember that $p^\mu \equiv \gamma m v^\mu$, with the Lorentz factor $\gamma \equiv (1 - v^2)^{-1/2}$). We will denote by v^μ the four-velocity of one particle, and by $U^\mu(x)$ the four-velocity of an element of the fluid (to be defined later). Therefore, we can define a particle four-flow as:

$$N^\mu(x) \equiv \int \frac{\mathrm{d}^3\boldsymbol{p}}{p^0}\ p^\mu f(x, p)\ . \tag{1.94}$$

The energy-momentum tensor is given by:

$$T^{\mu\nu}(x) \equiv \int \frac{\mathrm{d}^3\boldsymbol{p}}{p^0}\ p^\mu p^\nu\ f(x, p)\ . \tag{1.95}$$

In (1.95) have assumed that the fluid is dilute in the sense that the interaction energy of the particles is small in comparison to their kinetic energy. The 00 component corresponds to the energy density, the $0i$ component corresponds to the energy flow (energy per unit time and area in the direction i), and the ij component to the i-momentum flow (i-component of momentum per unit area and time in the direction j). We can also define the entropy four-flow as:

$$S^\mu(x) = -\int \frac{\mathrm{d}^3\boldsymbol{p}}{p^0}\ p^\mu f(x, p)\left[\ln f(x, p) - 1\right]\ . \tag{1.96}$$

So S^0 corresponds to the entropy density (remember that in statistical physics the entropy is usually defined as $S = \ln \Delta\Gamma$, with $\Delta\Gamma$ the statistical weight, such that $f(x, p)\Delta\Gamma = 1$ [Lan80]), and S^i to the entropy flow (the extra term with -1 is not physically relevant and it is introduced for convenience).

Hydrodynamic velocity

We now consider a non-perfect fluid, for which dissipation of energy occurs. The hydrodynamic velocity $U^\mu(x)$ of the fluid is defined in general as a time-like four-vector normalized as [Gro80, Wei72]:

$$U^\mu(x) U_\mu(x) = 1\ . \tag{1.97}$$

The *local rest frame* (LRF) is defined as the reference frame for which $\tilde{U}^0(x) \equiv 1$, and $\tilde{U}^i(x) \equiv 0$ (we shall denote quantities measured in this frame with tildes). Using the hydrodynamic velocity, we can also define the projector:

$$\Delta^{\mu\nu}(x) \equiv \eta^{\mu\nu} - U^\mu(x)U^\nu(x) \ . \tag{1.98}$$

It annihilates the part of a vector parallel to U^μ, i.e., $\Delta^{\mu\nu}U_\nu = 0$. The two most used conventions for the hydrodynamic velocity are:

- Eckart's choice:
$$U^\mu_{(\mathrm{E})}(x) \equiv \frac{N^\mu(x)}{\sqrt{N^\nu(x)N_\nu(x)}} \ . \tag{1.99}$$
So according to this choice, since $\tilde{N}^i_{(\mathrm{E})} = 0$, U^μ measures the mean particle velocity. Obviously, it is necessary that there is some conserved current N^μ in the system (besides $T^{\mu\nu}$) in order to choose the hydrodynamic velocity in this way.

- Landau's choice:
$$U^\mu_{(\mathrm{L})}(x) \equiv \frac{T^{\mu\nu}U_\nu}{\sqrt{U_\nu T^{\nu\sigma}T_{\sigma\rho}U^\rho}} \ . \tag{1.100}$$
In this case, since $\tilde{T}^{i0}_{(\mathrm{L})} = 0$, U^μ measures the velocity of momentum density or energy flow.

Physical quantities

Using the hydrodynamic velocity, we can now express macroscopic quantities in a covariant way. For instance, the particle density n (or any other density of charge) is explicitly defined as an scalar quantity by

$$n \equiv N^\mu U_\mu \ , \tag{1.101}$$

so we see, in the LRF, that it is actually the density of particles. Similarly, we define the *energy density* ϵ by

$$\epsilon \equiv T^{\mu\nu}U_\mu U_\nu \ . \tag{1.102}$$

We now define the *heat flow* I^μ_{q} as the difference between the energy flow and the flow of enthalpy carried by the particles:

$$I^\mu_{\mathrm{q}} \equiv (T^{\nu\sigma}U_\sigma - hN^\nu)\Delta^\mu{}_\nu \ , \tag{1.103}$$

where the *enthalpy* or *heat function per particle* is given by $h = (\epsilon + P)/n$ (P is the hydrostatic pressure, to be specified later). The form of the heat flow in the Eckart's and Landau's choices is respectively:

$$I^{\mu(\mathrm{E})}_{\mathrm{q}} = U_\rho T^{\rho\sigma}\Delta^\mu{}_\sigma \ , \quad I^{\mu(\mathrm{L})}_{\mathrm{q}} = -h\Delta^{\mu\nu}N_\nu \ . \tag{1.104}$$

We see that $\tilde{I}^0_{\mathrm{q}} = 0$, and $\tilde{I}^i_{\mathrm{q}} = \tilde{T}^{0i} - h\tilde{N}^i$. According to the definition in [Lan80], pag. 47, the heat function is $W \equiv E + PV$, where E is the internal energy, so $h \equiv W/N$ (with N the number of particles). According to the First Principle of Thermodynamics, $\mathrm{d}Q = \mathrm{d}E + P\mathrm{d}V$, so if the pressure of the system is constant: $\mathrm{d}Q = \mathrm{d}W$ (do not confuse

W with the work). In the Eckart's choice we obtain in the LRF the intuitive result for a heat flow, i.e. $\tilde{I}^i_{q(\mathrm{E})} = -h\tilde{N}^i$, since h somehow represents the "heat carried by the particle" (note that we here follow the conventions of [Lan80] for the signs of work and heat: if the work is done on the system it is positive, and if the heat is gained by the system it is positive).

Another quantity, the *pressure tensor* $P^{\mu\nu}$, is defined as:

$$P^{\mu\nu} \equiv T^{\sigma\rho}\Delta^{\mu}{}_{\sigma}\Delta^{\nu}{}_{\rho} \ . \tag{1.105}$$

Therefore, $\tilde{P}^{00} = 0$, $\tilde{P}^{i0} = 0$, and $\tilde{P}^{ij} = \tilde{T}^{ij}$, so we see that indeed it represents pressures (forces per unit area or equivalently flux of momentum, i.e. momentum per unit area and time). The *reversible* and *irreversible* parts of the pressure tensor, and the *hydrostatic pressure* are defined as:

$$P^{\mu\nu} \equiv -P\Delta^{\mu\nu} + \Pi^{\mu\nu} \ , \tag{1.106}$$

where the tensor $\Pi^{\mu\nu}$ is called the *viscous pressure tensor*. Finally, the entropy density s is defined as:

$$s \equiv S^{\mu}U_{\mu} \ . \tag{1.107}$$

Decomposition of the energy-momentum tensor

Taking into account the above definitions, we can also decompose the energy-momentum tensor into a reversible and an irreversible parts:

$$T^{\mu\nu} \equiv T^{\mu\nu}_{\mathrm{R}} + T^{\mu\nu}_{\mathrm{I}} \ , \tag{1.108}$$

where the reversible part is given by[15]

$$T^{\mu\nu}_{\mathrm{R}} \equiv \epsilon U^{\mu}U^{\nu} - P\Delta^{\mu\nu} \ , \tag{1.109}$$

and the irreversible part is

$$T^{\mu\nu}_{\mathrm{I}} \equiv \left[(I^{\mu}_{\mathrm{q}} + h\Delta^{\mu\sigma}N_{\sigma})U^{\nu} + (I^{\nu}_{\mathrm{q}} + h\Delta^{\nu\sigma}N_{\sigma})U^{\mu}\right] + \Pi^{\mu\nu} \ . \tag{1.110}$$

According to the Eckart's and Landau's choices:

$$T^{\mu\nu}_{\mathrm{I(E)}} = (I^{\mu}_{\mathrm{q}}U^{\nu} + I^{\nu}_{\mathrm{q}}U^{\mu}) + \Pi^{\mu\nu} \ , \quad T^{\mu\nu}_{\mathrm{I(L)}} = \Pi^{\mu\nu} \ . \tag{1.111}$$

1.5.2 Fluid equations

The equations of fluid dynamics follow directly from the conservation laws of the total particle number and momentum:

$$\partial_{\mu}N^{\mu} = 0 \ , \tag{1.112}$$

$$\partial_{\mu}T^{\mu\nu} = 0 \ . \tag{1.113}$$

[15]This part, by definition, corresponds to the energy-momentum tensor of a perfect fluid, more frequently written in the form $T^{\mu\nu}_{\mathrm{R}} = (\epsilon + P)U^{\mu}U^{\mu} - P\eta^{\mu\nu}$.

The hydrodynamic equations (HE) give the rate of change of the particle density, the hydrodynamical velocity, and the energy density. The resulting equations will depend on the choice for the hydrodynamical velocity (Eckart's or Landau's choice). These equations, together with the equation of state, determine the dynamics of the fluid completely. In order to derive the HE we separate the space-time derivative into a time-like and a space-like part, i.e.,

$$\partial^\mu \equiv U^\mu D + \nabla^\mu \ , \tag{1.114}$$

with:

$$D \equiv U^\mu \partial_\mu \ , \quad \nabla^\mu \equiv \Delta^{\mu\nu}\partial_\nu \ . \tag{1.115}$$

The operator D is called the *convective derivative*. In the LRF, $\tilde{D} = \partial/\partial\tilde{t}$, and $\tilde{\nabla}^0 = 0$, $\tilde{\nabla}^i = -\tilde{\partial}_i$ (we denote by $\tilde{t}$ and $\tilde{x}^i$ the temporal and spatial coordinates, respectively, in this particular reference frame), so they are co-moving time and spatial derivatives respectively. Since, in general, the hydrodynamical velocity does not correspond to the motion of the particles, it is also introduced the *substantial time derivative* $\mathcal{D} \equiv N^\mu \partial_\mu$. It has units of number of particle per unit volume per unit time, and it gives the change as seen when traveling along the particle flow.

Equation of continuity

We first split the particle flow N^μ into a part carried by the hydrodynamic velocity, and a dissipative part V^μ:

$$N^\mu \equiv nU^\mu + V^\mu \ . \tag{1.116}$$

Now, by introducing the decomposition (1.114) for the derivative, and this decomposition for the particle flow into (1.112) and manipulating it a little, we arrive to the equation:

$$Dn = -n\nabla_\mu U^\mu - \nabla_\mu V^\mu + V_\mu DU^\mu \ . \tag{1.117}$$

This is called the *equation of continuity*. If we can neglect the transport contributions I_q^μ and V^μ then we have a so called *perfect fluid*. In this case (1.117) transforms into the *relativistic Euler's equation*:

$$Dn = -n\nabla_\mu U^\mu \ . \tag{1.118}$$

The criterium for neglecting the transport contributions will be clear later, and it is based on the Chapman-Enskog method. There, the transport quantities I_q^μ and V^μ turn out to be of first order in the gradients, while the thermodynamical quantities are zeroth-order. With the substantial time derivative, the equation of continuity can be rewritten more concisely:

$$n^{-2}\mathcal{D}n = -\partial_\mu U^\mu - \partial_\mu(n^{-1}V^\mu) \ . \tag{1.119}$$

Equation of motion

From (1.113), contracting with $\Delta^\mu{}_\nu$, and using the forms (1.109) and (1.110) for the energy-momentum tensor, we obtain the *equation of motion*:

$$hnDU^\mu = \nabla^\mu P - \Delta^\mu{}_\nu \nabla_\sigma \Pi^{\nu\sigma} + (\Pi^{\mu\nu} DU_\nu - \Delta^\mu{}_\nu DW^\nu - W^\mu \nabla_\nu U^\nu - W^\nu \nabla_\nu U^\mu) \ , \tag{1.120}$$

where we have introduced:

$$W^\mu \equiv U^\sigma T_{\sigma\rho}\Delta^{\rho\mu} = I_{\rm q}^\mu + hV^\mu \ . \tag{1.121}$$

For a perfect fluid (we neglect the transport contributions $\Pi^{\mu\nu}$ and W^μ), we have:

$$DU^\mu = \frac{1}{hn}\nabla^\mu P \ . \tag{1.122}$$

Equation of energy

We now contract (1.113) with U_μ, and using again the forms (1.109) and (1.110), we get the *equation of energy*:

$$D\epsilon = -hn\nabla_\mu U^\mu + \Pi^{\mu\nu}\nabla_\nu U_\mu - \nabla_\mu W^\mu + 2W^\mu DU_\mu \ . \tag{1.123}$$

Thus, the energy density can variate because of the viscous pressure contribution or due to a purely relativistic contribution from the acceleration. For a perfect fluid:

$$D\epsilon = -hn\nabla_\mu U^\mu \ . \tag{1.124}$$

This is called the *relativistic Euler's equation of energy*.

1.5.3 Transport equation

Classical dynamics: the Boltzmann equation

It is an equation for the space-time behavior of the one-particle distribution function. There are several assumptions made to construct it:

- Only binary collisions are considered, so the gas must be dilute enough.
- The change of the distribution function on microscopic scales of space-time is negligibly small.
- *Hypothesis of molecular chaos*: absence of particle correlations before *each* collision (with the quantum formulation it will be only necessary to assume lack of correlation at one single instant of time, rather than repeatedly during the evolution). This means that the number of binary collisions is proportional to the product of the distribution functions of the two colliding particles and to the transition rate.

Consider the number of world-lines crossing the 3-surface $\Delta^3\sigma$ and having momentum in the range $\Delta^3\boldsymbol{p}$, i.e.,

$$\int\limits_{\Delta^3\sigma}\int\limits_{\Delta^3\boldsymbol{p}} \mathrm{d}^3\sigma_\mu \ \frac{\mathrm{d}^3\boldsymbol{p}}{p^0} \ p^\mu f(x,p) \ .$$

We see that in the LRF this quantity corresponds to the number of particles in the volume $\Delta^3\boldsymbol{x}$ (since $\mathrm{d}^3\sigma_\mu = (\mathrm{d}^3\boldsymbol{x}, 0, 0, 0)$) with momentum in the range $\Delta^3\boldsymbol{p}$. The surface $\Delta^3\sigma$ must be space-like (all its points have the same time coordinate), and therefore its

normal vector $\mathrm{d}^3\sigma_\mu$ must be time-like. We now construct a tube of flux from two space-like surfaces like above, containing a four-volume $\Delta^4 x$. Then, the net number of particles passing through the surface of this tube will be:

$$\int\limits_{\Delta^3\sigma}\int\limits_{\Delta^3\boldsymbol{p}} \mathrm{d}^3\sigma_\mu \, \frac{\mathrm{d}^3\boldsymbol{p}}{p^0} \, p^\mu f(x,p) = \int\limits_{\Delta^4 x}\int\limits_{\Delta^3\boldsymbol{p}} \mathrm{d}^4 x \, \frac{\mathrm{d}^3\boldsymbol{p}}{p^0} \, p^\mu \partial_\mu f(x,p) = \Delta^4 x \, \frac{\Delta^3\boldsymbol{p}}{p^0} \, C(x,p) \ . \quad (1.125)$$

The quantity in the right hand side represents the change in the number of particles in the tube characterized by a volume $\Delta^4 x$ and an interval of momentum $\Delta^3\boldsymbol{p}$. Note that if there is no collision between the particles, this quantity is zero. Finally, since the volumes $\Delta^4 x$ and $\Delta^3\boldsymbol{p}$ are arbitrary, it must be verified:

$$p^\mu \partial_\mu f(x,p) = C(x,p) \ . \quad (1.126)$$

The left-hand side of this equation is called the *streaming term*, and the right-hand side the *collision term*. We now consider a collision between two particles of momenta $\boldsymbol{p}_1$ and $\boldsymbol{p}_2$, giving particles with momenta $\boldsymbol{p}'_1$ and $\boldsymbol{p}'_2$ respectively. The quantity in the right-hand side of (1.125), according to the Hypothesis of Molecular Chaos, will be proportional to the number of particles of "type 1" per unit volume with momentum in the interval ($\boldsymbol{p}_1$,$\boldsymbol{p}_1 + \Delta\boldsymbol{p}_1$), i.e., to $\Delta^3\boldsymbol{p}_1 f(x,p_1)$. Analogously, it must be also proportional to $\Delta^3\boldsymbol{p}_2 f(x,p_2)$ and to the volumes $\Delta^4 x$, $\Delta^3\boldsymbol{p}'_1$, and $\Delta^3\boldsymbol{p}'_2$. The proportionality factor will be denoted by $w(p_1,p_2;p'_1,p'_2) \equiv W(p_1,p_2;p'_1,p'_2)/p_1^0 p_2^0 p_1'^0 p_2'^0$, where $W(p_1,p_2;p'_1,p'_2)$ is called the *transition rate*. Accordingly, the number of particles with momentum in the range ($\boldsymbol{p}_1$,$\boldsymbol{p}_1 + \Delta\boldsymbol{p}_1$) *lost* due to collisions is given by:

$$\frac{1}{2}\Delta^4 x \frac{\Delta^3\boldsymbol{p}_1}{p_1^0} \int \frac{\mathrm{d}^3\boldsymbol{p}_2}{p_2^0}\frac{\mathrm{d}^3\boldsymbol{p}'_1}{p_1'^0}\frac{\mathrm{d}^3\boldsymbol{p}'_2}{p_2'^0} \ f(x,p_1) f(x,p_2) W(p_1,p_2;p'_1,p'_2) \ .$$

The 1/2 factor is introduced because we cannot distinguish between the two final states. Thus, we see that the quantity $w(p_1,p_2;p'_1,p'_2)\Delta^3\boldsymbol{p}'_1\Delta^3\boldsymbol{p}'_2$ is the transition probability per unit volume and unit time for two particles of momenta $\boldsymbol{p}_1$ and $\boldsymbol{p}_2$ to be scattered in the range of outgoing momenta ($\boldsymbol{p}'_1, \boldsymbol{p}'_1 + \Delta\boldsymbol{p}'_1$) and ($\boldsymbol{p}'_2, \boldsymbol{p}'_2 + \Delta\boldsymbol{p}'_2$) respectively. In the same way, the gain of particles in the range $\Delta^4 x$ and ($\boldsymbol{p}_1$,$\boldsymbol{p}_1 + \Delta\boldsymbol{p}_1$) from collisions with initial momenta p'_1 and p'_2 is:

$$\frac{1}{2}\Delta^4 x \frac{\Delta^3\boldsymbol{p}_1}{p_1^0} \int \frac{\mathrm{d}^3\boldsymbol{p}_2}{p_2^0}\frac{\mathrm{d}^3\boldsymbol{p}'_1}{p_1'^0}\frac{\mathrm{d}^3\boldsymbol{p}'_2}{p_2'^0} \ f(x,p'_1) f(x,p'_2) W(p'_1,p'_2;p_1,p_2) \ .$$

Therefore, the collision term will be given by:

$$\begin{aligned} C(x,p_1) = \frac{1}{2}\int \frac{\mathrm{d}^3\boldsymbol{p}_2}{p_2^0}\frac{\mathrm{d}^3\boldsymbol{p}'_1}{p_1'^0}\frac{\mathrm{d}^3\boldsymbol{p}'_2}{p_2'^0} \ & [f(x,p'_1) f(x,p'_2) W(p'_1,p'_2;p_1,p_2) \\ & - f(x,p_1) f(x,p_2) W(p_1,p_2;p'_1,p'_2)] \ . \end{aligned} \quad (1.127)$$

We now want to relate the transition rate W with the scattering cross section σ. The differential cross section $\mathrm{d}\sigma/\mathrm{d}\Omega$ is defined as the number n_Ω of outgoing particles produced

in the solid angle Ω after the collision of a flux f_a (number of particles per unit time and area) with a density of particles σ_b in a differential of surface:

$$\frac{\mathrm{d}\sigma}{\mathrm{d}\Omega} = \frac{n_\Omega}{f_a \sigma_b} \ . \tag{1.128}$$

So according to our definition of the transition rate, the cross section will be obtained by dividing $w(p_1, p_2; p_1', p_2')\Delta^3\boldsymbol{p}_1'\Delta^3\boldsymbol{p}_2'$ by the relative velocity

$$\left| \frac{\boldsymbol{p}_1}{p_1^0} - \frac{\boldsymbol{p}_2}{p_2^0} \right| = \frac{F}{p_1^0 p_2^0} \ , \tag{1.129}$$

where $F \equiv \sqrt{(p_1 \cdot p_2)^2 - m^4} = \frac{1}{2}\sqrt{s(s-4m^2)}$ is called the invariant flux. Thus,

$$\mathrm{d}\sigma = \frac{1}{F} W(p_1, p_2; p_1', p_2') \frac{\mathrm{d}^3\boldsymbol{p}_1'}{{p_1'}^0} \frac{\mathrm{d}^3\boldsymbol{p}_2'}{{p_2'}^0} \ . \tag{1.130}$$

Since $W(p_1, p_2; p_1', p_2')$ is a Lorentz scalar and momentum is conserved in the collision, then it must verify the *detailed balance condition*:

$$W(p_1, p_2; p_1', p_2') = W(p_1', p_2'; p_1, p_2) \ . \tag{1.131}$$

Once we now this, we can express the transport equation in terms of the cross section:

$$p_1^\mu \partial_\mu f(x, p_1) = \frac{1}{2} \int \frac{\mathrm{d}^3\boldsymbol{p}_2}{p_2^0} \, \mathrm{d}\Omega \, (f_1' f_2' - f_1 f_2) F \frac{\mathrm{d}\sigma}{\mathrm{d}\Omega} \ . \tag{1.132}$$

An expression for the transport equation in presence of an external force F^μ (useful for instance, in its quantum version, to calculate the DC conductivity of the QGP, see Section 1.5.5) can be also obtained [Gro80], taking into account that at the second surface of the flux tube the particle momentum is now $p^\mu + F^\mu \Delta\tau$. The proper time τ is given by:

$$\Delta^4 x = \Delta\tau \frac{p^\mu}{m} \int_{\Delta^3\sigma} \mathrm{d}^3\sigma_\mu \ . \tag{1.133}$$

Then, this new transport equation takes the form:

$$p^\mu \partial_\mu f(x, p) + m F^\mu \frac{\partial}{\partial p^\mu} f(x, p) = C(x, p) \ . \tag{1.134}$$

In the derivation of this equation is assumed that the external force causes a small deviation of the particle trajectories, so they approach each other in rectilinear paths right before each collision. Hence, the external force does not modify the collision term.

Equilibrium state

If we assume that the distribution function tends to a definite limit as time progresses, then the system reaches an *equilibrium state*. Therefore, the entropy attains its maximum value, and the entropy production, $\Delta S \equiv \partial_\mu S^\mu$, vanishes at every point in the system.

This, along with the condition that the distribution function must be a solution of the transport equation, suffices to completely determine $f(x,p)$. The equilibrium distribution function contains the density, the global four-velocity, and the temperature as parameters. It can be shown [Gro80] that temperature is a Lorentz invariant quantity. All other thermodynamical quantities can be determined in therms of these parameters. It can also be shown [Gro80] that

$$\Delta S(x) = 0 \quad \Leftrightarrow \quad f(x,p_1)f(x,p_2) = f(x,p_1')f(x,p_2') \ , \tag{1.135}$$

where the momenta verify $p_1^\mu + p_2^\mu = p_1'^\mu + p_2'^\mu$. This condition essentially says that the inverse reaction is equally likely. A distribution function that verifies (1.135) is called a *local equilibrium* distribution function, and we denote it by $f^{(0)}(x,p)$. The most general form for a distribution function like this is:

$$\ln f^{(0)}(x,p) = a(x) + b_\mu(x)p^\mu(x) \ . \tag{1.136}$$

It is important to note that a local distribution function causes the collision term in the transport equation to vanish, i.e., $C[f^{(0)}] = 0$. But in general, (1.136) is not a solution of the transport equation. A distribution function of the form (1.136) that verifies the transport equation is called a *global equilibrium* distribution function (since it describes a state of global equilibrium), and we denote it by $f_{\rm eq}$. It can be shown that $b^\mu(x) = -U^\mu(x)/T(x)$, and that the most general motion for a system in global equilibrium is a translation and a rigid rotation. The identification of T with the temperature will come when we calculate the equation of state for the perfect gas, and by seeing that the rest of usual thermodynamical relations are correctly reproduced with this identification. The identification of U^μ with the hydrodynamic velocity comes from the calculation of N^μ [Gro80]. If we exclude the rigid rotation, then U^μ and T do not depend on x. In global equilibrium a also does not depend on x, so if we write $a = \mu/T$ we finally have:

$$f_{\rm eq}(x,p) = \frac{1}{(2\pi\hbar)^3} \exp\left(\frac{\mu - p_\nu U^\nu}{T}\right) \ , \tag{1.137}$$

where μ is identified as the chemical potential.

Transport equation for quantum fields

There is the quantum analog of the classical distribution function, and it is called the *Wigner function*. Its main feature is that quantum mechanical averages can be written as phase-space integrals rather than as traces of operators. The derivation of the quantum version of the Boltzmann equation is more subtle and we refer the reader to [Gro80] for a nice exposition. The following assumptions are considered in this case:

- The system is dilute enough, so initial correlations between colliding particles can be neglected.
- Only binary collisions are considered.
- The Wigner functions are sufficiently smooth.

The relativistic transport equation in the quantum case is:

$$p^\mu \partial_\mu f(x,p) = \frac{1}{2}\int \frac{\mathrm{d}^3\boldsymbol{p}_2}{p_2^0}\frac{\mathrm{d}^3\boldsymbol{p}_1'}{p_1'^0}\frac{\mathrm{d}^3\boldsymbol{p}_2'}{p_2'^0}\,[f(x,p_1')f(x,p_2')W(p_1',p_2';p_1,p_2) \\ -f(x,p_1)f(x,p_2)W(p_1,p_2;p_1',p_2')]\ , \tag{1.138}$$

where $f(x,p)$ is the one-particle Wigner function, which formally coincides with the one-particle distribution function. We see that the form of this equation is essentially the same as in the classical case[16]. The transition rate is now ($\hat{S} = 1 + \mathrm{i}\hat{T}$, with $\hat{S}$ the scattering matrix)

$$W(p_1,p_2;p_1',p_2') = \delta^{(4)}(p_1+p_2-p_1'-p_2')\ |\langle p_2',p_1'|\hat{T}|p_1,p_2\rangle|^2\ . \tag{1.139}$$

The relation with the scattering cross section remains unaltered. In the quantum case, in general, the detailed balance condition is not fulfilled:

$$W(p_1,p_2;p_1',p_2') \neq W(p_1',p_2';p_1,p_2)\ .$$

Its validity to an arbitrary order in perturbation theory will depend on the type of particles and interactions. However, it still remains valid for a large number of cases (in particular to lowest order in perturbation theory), and so we shall assume detailed balance in what follows.

The relativistic distribution function corresponding to the state of equilibrium in the quantum case depends on the type of fields we consider (bosonic or fermionic):

$$f^{\mathrm{eq}}_{\mathrm{B,F}}(x,p) = \frac{1}{(2\pi\hbar)^3}\,\frac{1}{\exp\beta(p_\nu U^\nu - \mu) \mp 1}\ . \tag{1.140}$$

It is also usual to denote the Bose-Einstein and Fermi-Dirac distribution functions by

$$n_{\mathrm{B,F}}(p) \equiv (2\pi)^3 f^{\mathrm{eq}}_{\mathrm{B,F}}(x,p)\ . \tag{1.141}$$

Finally, the *Uehling-Uhlenbeck* equation takes into account quantum degeneracy in the gas and constitutes an extended version of the transport equation (1.138) [Ueh33, Isr72, Lib03] (see also the comments in [dB55]):

$$p^\mu \partial_\mu f_1 = \frac{1}{2}\int \frac{\mathrm{d}^3\boldsymbol{p}_2}{p_2^0}\frac{\mathrm{d}^3\boldsymbol{p}_1'}{p_1'^0}\frac{\mathrm{d}^3\boldsymbol{p}_2'}{p_2'^0}\,[f_1'f_2'(1+\alpha f_1)(1+\alpha f_2) - f_1 f_2(1+\alpha f_1')(1+\alpha f_2')] \\ \times W(p_1,p_2;p_1',p_2')\ , \tag{1.142}$$

where, for brevity, we have denoted $f_i \equiv f(x,p_i)$ and $f_i' \equiv f(x,p_i')$, and $\alpha = \pm(2\pi)^3$ depending on whether the particle is a boson or a fermion respectively. The extra factors involving the distribution function that appear in this equation incorporate quantum degeneracy to the initial and final states, reducing or enhancing the phase space of the available states depending on whether the particle is a fermion or a boson respectively (there is an statistical affinity that identical bosons tend to be in a common domain

[16] In the case of massive spin-1/2 fermions, the collision term can be brought to the form (1.138) by locally diagonalizing the Wigner function (see Chapter IV of [Gro80]).

[Hua87]). The equations (1.138) and (1.142) are not only valid for quantum fields but also in the QM case. Finally, from (1.142), the equilibrium distribution function has the following property:

$$f'_{1,\mathrm{eq}} f'_{2,\mathrm{eq}} (1 + \alpha f_{1,\mathrm{eq}})(1 + \alpha f_{2,\mathrm{eq}}) = f_{1,\mathrm{eq}} f_{2,\mathrm{eq}} (1 + \alpha f'_{1,\mathrm{eq}})(1 + \alpha f'_{2,\mathrm{eq}}) \ , \tag{1.143}$$

for momenta which verify $p_1^\mu + p_2^\mu = p_1'^\mu + p_2'^\mu$.

1.5.4 Thermodynamic forces and fluxes: transport coefficients

The description of irreversible phenomena taking place in out-of-equilibrium systems is dominated by two kinds of concepts: thermodynamic forces and flows. The latter tend to smooth out the non-uniformities characterized by the former. As a result, an isolated system relaxes to its equilibrium state in the course of time. Transport coefficients are defined as the coefficients for a series expansion of the fluxes in terms of the thermodynamic forces. Phenomenologically, one finds that the linear approximation in this expansion is usually enough. Transport coefficients depend on the kind of system and on the local thermodynamic variables, but they are independent of the local variations of these quantities.

We define *thermodynamic forces* as those quantities which consist of gradients of thermodynamic quantities (temperature, hydrodynamic velocity, or the particle density). These thermodynamic forces produce *fluxes* which try to restore equilibrium in the system. Previously, we have considered in particular the flows:

$$I_{\mathrm{q}}^\mu \equiv (U_\nu T^{\nu\sigma} - hN^\sigma)\Delta^\mu{}_\sigma \ , \quad \Pi^{\mu\nu} \equiv \bar{\Pi}^{\mu\nu} - \Pi\Delta^{\mu\nu} \ , \tag{1.144}$$

where we have split $\Pi^{\mu\nu}$ into a traceless part, $\bar{\Pi}^{\mu\nu}$, and a remainder ($\Pi = -\Pi^\mu{}_\mu/3$). We now define the thermodynamic forces (generalization of the definitions in the non-relativistic theory):

$$X \equiv -\nabla^\mu U_\mu \ , \tag{1.145}$$

$$X_{\mathrm{q}}^\mu \equiv \frac{\nabla^\mu T}{T} - \frac{\nabla^\mu P}{hn} \ , \tag{1.146}$$

$$\bar{X}^{\mu\nu} \equiv \left[\frac{1}{2}(\Delta^\mu{}_\sigma \Delta^\nu{}_\tau + \Delta^\nu{}_\sigma \Delta^\mu{}_\tau) - \frac{1}{3}\Delta^{\mu\nu}\Delta_{\sigma\tau}\right] \nabla^\sigma U^\tau \ . \tag{1.147}$$

In the first Chapman-Enskog approximation[17] [Gro80], thermodynamic forces and fluxes are linearly related:

$$\Pi = \zeta X \ , \tag{1.148}$$

$$I_{\mathrm{q}}^\mu = \kappa T X_{\mathrm{q}}^\mu \ , \tag{1.149}$$

$$\bar{\Pi}^{\mu\nu} = 2\eta \bar{X}^{\mu\nu} \ . \tag{1.150}$$

[17] It means that the distribution function is expanded in terms of the mean free path over the dimension of the system. To lowest order in spatial gradients, it coincides with the equilibrium distribution function. The next order is the first Chapman-Enskog approximation (linear is spatial gradients).

The coefficients ζ, κ, and η are called *bulk viscosity*, *thermal conductivity*, and *shear viscosity* respectively, and they are all positive [Gro80].

It is convenient to pass to the LRF and recover the more familiar expressions for transport coefficients. In the LRF, $\tilde{U}^\mu = (1, \mathbf{0})$, $\tilde{\Pi}^{00} = 0$ (from the definition), and then we have:

$$\tilde{T}_{ij} = P\delta_{ij} + \eta\left(\partial_i\tilde{U}_j + \partial_j\tilde{U}_i + \frac{2}{3}\delta_{ij}\partial_k\tilde{U}^k\right) - \zeta\delta_{ij}\partial_k\tilde{U}^k \ . \tag{1.151}$$

And for the case of the thermal conductivity:

$$\tilde{T}^{i0} - h\tilde{N}^i = -\kappa T\left(\frac{\tilde{\partial}_i T}{T} - \frac{\tilde{\partial}_i P}{hn}\right) \ . \tag{1.152}$$

Now, using the relativistic Gibbs-Duhem relation

$$\frac{1}{n}\nabla^\mu P = h\frac{\nabla^\mu T}{T} + T\nabla^\mu\left(\frac{\mu}{T}\right) \ , \tag{1.153}$$

we can rewrite (1.152) as

$$\tilde{T}^{i0} - h\tilde{N}^i = \kappa\frac{T^2}{h}\,\tilde{\partial}_i\left(\frac{\mu}{T}\right) \ . \tag{1.154}$$

Therefore we see that for a system without any conserved current (besides the energy-momentum tensor) the thermal conductivity is zero[18] [Dan85]. It is also convenient to write the defining equation for the thermal conductivity in both the Landau's and Eckart's choices of the hydrodynamical velocity [Gro80]:

$$\tilde{N}^i_{(\mathrm{L})} = -\kappa\frac{T^2}{h^2}\,\tilde{\partial}_i\left(\frac{\mu}{T}\right) \ , \tag{1.155}$$

$$\tilde{T}^{i0}_{(\mathrm{E})} = \kappa\frac{T^2}{h}\,\tilde{\partial}_i\left(\frac{\mu}{T}\right) \ . \tag{1.156}$$

In the non-relativistic limit, we can neglect the second term in the right hand side of (1.152) and we recover, for the Eckart's choice, the familiar Fourier's Law $\tilde{T}^{0i}_{(\mathrm{E})} = -\kappa\tilde{\partial}_i T$. It is important to remark here that these Landau's and Eckart's conventions apply to macroscopic averages of the currents $T^{\mu\nu}$ and N^μ over a fluid element, and not to the microscopic currents themselves. The microscopic quantities will be relevant in Section 1.6, where we obtain the expressions for transport coefficients in Linear Response Theory.

Finally, for the *DC conductivity*, an electric current is induced in the gas by a external electric field which is constant in space and time, $J^i = \sigma^i{}_j E^j_{\mathrm{ext}}$. In general, the DC conductivity will be a tensor, but we will consider here the isotropic case so $\sigma_{ij} = \sigma\eta_{ij}$ (see Section 1.6.2).

[18] In this case $N^i \equiv 0$ and $\mu \equiv 0$, so there cannot be gradients of chemical potential, the Eckart choice is not possible, and $\tilde{T}^{0i}_{(\mathrm{L})} = 0$.

Relativistic Navier-Stokes equations

The relativistic version of the Navier-Stokes equations form a self-consistent set of partial differential equations which completely describe the time evolution of a relativistic fluid, provided that appropriate initial and boundary conditions are imposed. They are obtained by linearizing with respect to thermodynamic forces the equation of continuity (1.117), the equation of motion (1.120), and the equation of energy (1.123). They differ from the equations for a perfect fluid by terms that are proportional to the transport coefficients, which represent the dissipative effects in the system. They take the following form both in the Eckart's and Landau's choices[19] [Gro80]:

- Eckart's choice:

$$\text{Eq. of continuity:} \quad Dn = -n\nabla_\mu U^\mu \ , \tag{1.157}$$

$$\text{Eq. of motion:} \quad hnDU^\mu = \nabla^\mu P - 2\eta\nabla_\nu \nabla^{\overline{\mu}} \overset{\circ}{U^{\nu}} - \zeta\nabla^\mu\nabla_\nu U^\nu - DI_q^\mu \ , \tag{1.158}$$

$$\text{Eq. of energy:} \quad DI_q^\mu = \xi\nabla^\mu\nabla_\nu U^\nu \ , \quad \xi \equiv \frac{\kappa T}{h}[(1-\gamma)h + \gamma T] \ . \tag{1.159}$$

- Landau's choice:

$$\text{Eq. of continuity:} \quad Dn = -n\nabla_\mu U^\mu + \frac{\kappa}{h}\left(\nabla^2 T - \frac{T}{hn}\nabla^2 P\right) \ , \tag{1.160}$$

$$\text{Eq. of motion:} \quad hnDU^\mu = \nabla^\mu P - 2\eta\nabla_\nu \nabla^{\overline{\mu}} \overset{\circ}{U^{\nu}} - \zeta\nabla^\mu\nabla_\nu U^\nu \ , \tag{1.161}$$

$$\text{Eq. of energy:} \quad \frac{DT}{T} = (1-\gamma)\left[\nabla_\mu U^\mu + \frac{\kappa}{P}\left(1 - \frac{T}{h}\right)\left(\nabla^2 T - \frac{T}{hn}\nabla^2 P\right)\right] \ . \tag{1.162}$$

The Navier-Stokes equations are differential equations of the parabolic type. Such equations allow solutions with an infinite propagation velocity. Within the framework of the Chapman-Enskog procedure, however, this paradox is easily resolved, since it is assumed that the macroscopic wave lengths are much greater than the mean free path, which precludes propagation velocities faster than the thermal velocity of the particles. Difficulties arise in numerical calculations where short wavelength modes are also taken into account, or if one tries to extend the theory to the transition regime where the mean free path is no longer negligible as compared to the length scale of the non-uniformities.

A possible solution to the problem of causality is known as the Müller-Israel-Stewart theory, where for each transport coefficient a relaxation time is introduced which controls the speed of propagation of the superluminal modes. The resulting set of equations are of the hyperbolic type, precluding the superluminal solutions. In this theory, the bulk and shear stresses, as well as the heat flux, are modified in the following way for the Landau's

[19] $A^{\overline{\mu\nu}} \equiv \frac{1}{2}(\Delta^\mu{}_\sigma\Delta^\nu{}_\tau + \Delta^\nu{}_\sigma\Delta^\mu{}_\tau)A^{\sigma\tau}$, and $A^{\overset{\circ}{\overline{\mu\nu}}} \equiv A^{\overline{\mu\nu}} - \frac{1}{3}\Delta^{\mu\nu}\Delta_{\sigma\tau}A^{\sigma\tau}$.

choice[20] [Isr79]:

$$\Pi = -\frac{1}{3}\zeta_{\rm V}(u^{\mu}{}_{;\mu} + \beta_0\dot{\Pi} - \alpha_0 q^{\mu}{}_{\mu}) \ , \tag{1.163}$$

$$\tau_{\mu\nu} = -2\zeta_{\rm S}(u_{\langle\mu;\nu\rangle} + \beta_2\dot{\pi}_{\mu\nu} - \alpha_1 q_{\langle\mu;\nu\rangle}) \ , \tag{1.164}$$

$$q^{\mu} = \kappa T\Delta^{\mu\nu}[(\partial_\mu\alpha)nT/(\rho+P) - \beta_1\dot{q}_\nu + \alpha_0\partial_\nu\Pi + \alpha_1\pi^{\lambda}_{\nu;\lambda}] \ . \tag{1.165}$$

We see that it introduces five additional transport coefficients: α_0, α_1, β_0, β_1 and β_2. For low momentum modes (i.e., to first order in thermodynamic forces), the Müller-Israel-Stewart theory coincides with the Navier-Stokes formulation. There are other possible formulations, and additional transport coefficients can be introduced. However, it has been recently analyzed in the context of Relativistic Heavy-Ion Collisions the effect of these higher-order terms in the hydrodynamics equations, and it seems that they can be neglected in a first approximation [Bai08, Luz08, Dus08, Hei09] (what means that the system is not far from equilibrium). We will not consider these additional transport coefficients in this thesis, so we will limit ourselves to the Navier-Stokes formulation.

1.5.5 Calculation of transport coefficients in kinetic theory

We now consider a system with the energy-momentum tensor $T^{\mu\nu}$ and some vector field N^μ as the the only conserved currents, with the latter current given by

$$N^\mu = \int \frac{{\rm d}^3\boldsymbol{p}}{p^0}\ p^\mu q f(x,p) \ , \tag{1.166}$$

where q is the conserved charge per particle (the particle four-flow corresponds to $q \equiv 1$). According to (1.95) and (1.166), both currents are determined by knowing the distribution function $f(x,p)$. If the system is slightly out of equilibrium, we can split the distribution function as

$$f(x,p) = f_{\rm eq}(x,p) + f_{\rm out}(x,p) \ , \tag{1.167}$$

with $f_{\rm out}(x,p)$ small in the sense $|f_{\rm out}(x,p)| \sim \lambda|\nabla f_{\rm eq}(x,p)| \ll |f_{\rm eq}(x,p)|$, with λ the mean free path. It turns out to be convenient to write:

$$f_{\rm out}(x,p) \equiv f_{\rm eq}(x,p)[1+\alpha f_{\rm eq}(x,p)]\phi(x,p) \ .$$

Whereas ϕ plays no role for local densities, it does enter into the expressions of the flows[21]:

$$I^\mu_q = (U_\sigma T^{\nu\sigma} - hN^\nu)\Delta^\mu{}_\nu = \int \frac{{\rm d}^3\boldsymbol{p}}{p^0}\ [p_\nu U^\nu - qh]p_\sigma\Delta^{\sigma\mu} f_{\rm eq}(1+\alpha f_{\rm eq})\phi \ , \tag{1.168}$$

$$T^{\mu\nu} = T^{\mu\nu}_{\rm R} + \int \frac{{\rm d}^3\boldsymbol{p}}{p^0}\ p^\mu p^\nu f_{\rm eq}(1+\alpha f_{\rm eq})\phi \ , \tag{1.169}$$

[20] Their notation is different from ours, e.g. the hydrodynamic velocity is normalized as $u^\mu u_\mu = -1$. α is here the thermal potential. They also consider an arbitrary metric. See [Isr79] for details.

[21] The term in $I^\mu_{\rm q}$ corresponding to the equilibrium part of $f(x,p)$ vanishes because of the form of $f_{\rm eq}$ (see [Gro80]).

Therefore, by comparing Eqs. (1.168) and (1.169) with (1.152) and (1.151) respectively, we see that the calculation of transport coefficients reduces to the determination of ϕ. In order to obtain ϕ we need to solve the transport equation (1.142). Linearizing the collision term in ϕ (i.e., first order in gradients), the transport equation takes the form [Ueh33]:

$$\left(p_1^\mu \partial_\mu + mF^\mu \frac{\partial}{\partial p_1^\mu}\right) f_{1,\mathrm{eq}} = \frac{1}{2} f_{1,\mathrm{eq}} \int \frac{\mathrm{d}^3\boldsymbol{p}_2}{p_2^0} \frac{\mathrm{d}^3\boldsymbol{p}_1'}{p_1'^0} \frac{\mathrm{d}^3\boldsymbol{p}_2'}{p_2'^0} \; f_{2,\mathrm{eq}}(1+\alpha f_{1,\mathrm{eq}}')(1+\alpha f_{2,\mathrm{eq}}') \\ \times [\phi_1' + \phi_2' - \phi_1 - \phi_2] W(p_1, p_2; p_1', p_2') \equiv f_{1,\mathrm{eq}} \mathcal{I}[\phi] \;, \quad (1.170)$$

where we have used the condition (1.143), and we have introduced an external force in the left-hand side according to (1.134). To linear order in gradients, the left-hand side of (1.170) can be written as [Gro80, Dav96]:

$$\left(p^\mu \partial_\mu + mF^\mu \frac{\partial}{\partial p^\mu}\right) f_{\mathrm{eq}} \bigg|_{\mathrm{lin}} = -\frac{1}{T}[QX - (p_\mu U^\mu - qh) p_\nu X_{\mathrm{q}}^\nu + p_\mu p_\nu \bar{X}^{\mu\nu} - q p_\mu E^\mu] f_{\mathrm{eq}}(1+\alpha f_{\mathrm{eq}}) \;, \quad (1.171)$$

with

$$Q \equiv -\frac{1}{3} m^2 + (p_\mu U^\mu)^2 \left(\frac{4}{3} - \gamma\right) + \left[T^2(1-\gamma) \frac{\partial}{\partial T}\left(\frac{\mu}{T}\right) - \rho \frac{\partial \mu}{\partial \rho}\right] p_\mu U^\mu \;, \quad (1.172)$$

where $\rho = qn$ is the density of charge, and $\gamma - 1 = 1/\bar{c}_{\mathrm{v}}$ with $\bar{c}_{\mathrm{v}} = \partial(\epsilon/n)/\partial T|_V$ the heat capacity per particle at constant volume. Since we also want to obtain an expression for the DC electrical conductivity, we have particularized here for the Lorentz force $F^\mu = -(q/m) F^{\mu\nu} p_\nu$, with $F^{\mu\nu}$ the electromagnetic strength tensor, so $F^{0i} = E^i$, $F^{ij} = \epsilon^{ijk} B^k$, and $E^\mu = -F^{\mu\nu} U_\nu$. The quantities γ, $\partial(\mu/T)/\partial T$, and $\partial\mu/\partial\rho$ in (1.172) are calculated in the ideal gas approximation from the equilibrium distribution function (1.140) and the definitions (1.95) and (1.166) [Gro80, Dav96]. In Sections 3.4.2 and 3.4.4 we will see that within the diagrammatic approach to the calculation of transport coefficients, the thermodynamic quantities that enter into the corresponding expressions must be calculated beyond the ideal gas approximation, changing this the qualitative behavior of transport coefficients with respect to the KT calculation at higher temperatures. Because of Curie's principle[22], ϕ must have the following form [Gro80]:

$$\phi = AX - B_\mu X_{\mathrm{q}}^\mu + C_{\mu\nu} \bar{X}^{\mu\nu} - D_\mu E^\mu \;. \quad (1.173)$$

[22]It essentially claims that flows and thermodynamic forces of different tensor rank do not couple [Gro80].

Then, the expressions for transport coefficients in KT read[23]:

$$\zeta = \frac{1}{3}\int \frac{\mathrm{d}^3\boldsymbol{p}}{p^0}\ |\boldsymbol{p}|^2 A f_{\mathrm{eq}}(1+\alpha f_{\mathrm{eq}})\ , \tag{1.174}$$

$$\kappa = \frac{1}{3T^2}\int \frac{\mathrm{d}^3\boldsymbol{p}}{p^0}\ |\boldsymbol{p}|^2 B(E_p - qh) f_{\mathrm{eq}}(1+\alpha f_{\mathrm{eq}})\ , \tag{1.175}$$

$$\eta = \frac{1}{15T^2}\int \frac{\mathrm{d}^3\boldsymbol{p}}{p^0}\ |\boldsymbol{p}|^4 C f_{\mathrm{eq}}(1+\alpha f_{\mathrm{eq}})\ , \tag{1.176}$$

$$\sigma = \frac{q}{3T^2}\int \frac{\mathrm{d}^3\boldsymbol{p}}{p^0}\ |\boldsymbol{p}|^2 D f_{\mathrm{eq}}(1+\alpha f_{\mathrm{eq}})\ , \tag{1.177}$$

with A, $B_\mu \equiv B\Delta_{\mu\nu}p^\nu/T$, $C_{\mu\nu} \equiv C p\overset{\circ}{\mu}\overset{\circ}{p_\nu}/T^2$, and $D_\mu \equiv D\Delta_{\mu\nu}p^\nu/T$ the solutions of

$$\mathcal{I}[A] = -\frac{Q}{T}(1+\alpha f_{\mathrm{eq}})\ , \tag{1.178}$$

$$\mathcal{I}[B\Delta_{\mu\nu}p^\nu] = -(p_\sigma U^\sigma - qh)\Delta_{\mu\nu}p^\nu(1+\alpha f_{\mathrm{eq}})\ , \tag{1.179}$$

$$\mathcal{I}[C p\overset{\circ}{\mu}\overset{\circ}{p_\nu}] = -T p\overset{\circ}{\mu}\overset{\circ}{p_\nu}(1+\alpha f_{\mathrm{eq}})\ , \tag{1.180}$$

$$\mathcal{I}[D\Delta_{\mu\nu}p^\nu] = -q\Delta_{\mu\nu}p^\nu(1+\alpha f_{\mathrm{eq}})\ . \tag{1.181}$$

Two standard methods are usually employed for solving the integral equations (1.178–1.181) in order to calculate transport coefficients in QCD: variational [Dav96, Arn00, Arn06b], or expanding the solutions in terms of a convenient basis [Gro80, Pra93, Dob04]. Finally, it is interesting to remark the similarity between the above expressions for σ, κ, η, ζ and the results (3.22), (3.42), (3.46), (3.53) respectively, obtained in Chapter 3 using Linear Response Theory for the case of a pion gas.

1.6 Kubo's formulae for transport coefficients

1.6.1 Linear Response Theory

Let be a system described by a hamiltonian $\hat{H}_0$ (independent of time) to which we add a perturbation $\hat{V}(t)$, such that $\hat{V}(t) = 0$ for $t \leq 0$. Linear Response Theory (LRT) consists in taking into account only the linear effects produced by the perturbation on the magnitudes of the system. For this to be a good approximation it is necessary that $\hat{V}(t)$ be small in the sense that the eigenvalues E_α of $\hat{H}(t) \equiv \hat{H}_0 + \hat{V}(t)$ and the eigenvalues $E_\alpha^{(0)}$ of $\hat{H}_0$ verify $|E_\alpha - E_\alpha^{(0)}|/E_\alpha^{(0)} \ll 1$. Then, it can be shown [LB96] that if $\hat{O}(t)$ is a certain operator in the Schrödinger's picture, the variation of the mean value of the

[23]For the case of the bulk viscosity it has been standard within the KT framework to consider only number-conserving collisions in the collision integral (1.170) at low temperatures. However, it was pointed out in [Jeo95, Jeo96], and more recently in [Arn06b], that number-changing processes actually give the dominant contribution in a massive system which reaches full thermodynamic equilibrium (thermal + chemical). In Sections 3.1.1, 3.1.2 and 3.4.4 we will comment further on this point. For the moment we keep only number-conserving processes even for the calculation of the bulk viscosity.

operator produced when the perturbation is introduced is given (to linear order in the perturbation) by:

$$\begin{aligned}\delta\langle\hat{O}(t)\rangle &\equiv \langle\Psi(t)|\hat{O}(t)|\Psi(t)\rangle - \langle\Psi^{(0)}(t)|\hat{O}(t)|\Psi^{(0)}(t)\rangle \\ &= -\mathrm{i}\int_0^\infty \mathrm{d}t'\ \langle\Psi^{(0)}(0)|\theta(t-t')[\hat{O}_{\mathrm{H}}(t),\hat{V}_{\mathrm{H}}(t')]|\Psi^{(0)}(0)\rangle\ , \end{aligned} \tag{1.182}$$

where $|\Psi^{(0)}(0)\rangle$ represents the state of the system at $t=0$, $|\Psi^{(0)}(t)\rangle \equiv \mathrm{e}^{-\mathrm{i}\hat{H}_0 t}|\Psi^{(0)}(0)\rangle$, $|\Psi(t)\rangle \equiv \mathrm{e}^{-\mathrm{i}\hat{H}t}|\Psi^{(0)}(0)\rangle$, and $\hat{O}_{\mathrm{H}}(t) \equiv \mathrm{e}^{\mathrm{i}\hat{H}_0 t}\hat{O}(t)\mathrm{e}^{-\mathrm{i}\hat{H}_0 t}$ (Heisenberg's picture). The result (1.182) is also valid if instead of mean values we deal with thermal averages $\langle\ \cdot\ \rangle_T$ and then we want to study small deviations from thermal equilibrium. Note that in this case, according to (1.182), we calculate these deviations by evaluating the expectation value of the commutator at equilibrium.

Now, by applying some small perturbation to our system in order to take it slightly out of equilibrium and using LRT, we can obtain the expressions for transport coefficients in terms of correlators.

1.6.2 DC conductivity

Consider that we have a free charged particle and that we couple to it an external electromagnetic field (*external* means that the particle does not modify the electromagnetic field). The lagrangian of the particle is [Itz05]:

$$L = -m\frac{\mathrm{d}\tau}{\mathrm{d}t}\ + L_{\mathrm{int}}\ ,$$

being τ the *proper time* of the particle, and

$$L_{\mathrm{int}} = -\int \mathrm{d}^3\boldsymbol{x}\ j_\mu(t,\boldsymbol{x})A^\mu_{\mathrm{ext}}(t,\boldsymbol{x})\ .$$

The current density four-vector for one particle is:

$$j^\mu = \rho(1,\boldsymbol{v})\ ,$$

being $\boldsymbol{v} \equiv \mathrm{d}\boldsymbol{r}/\mathrm{d}t$ the velocity vector of the particle and ρ the density of charge given by:

$$\rho(t,\boldsymbol{x}) = q\delta^{(3)}(\boldsymbol{x}-\boldsymbol{r}(t))\ .$$

Therefore,

$$L = -m\sqrt{1-\boldsymbol{v}^2} + q(\boldsymbol{A}\cdot\boldsymbol{v} - A^0)\ .$$

Then, the classical hamiltonian of the particle is:

$$H = \boldsymbol{v}\cdot\boldsymbol{p} - L = \frac{m}{\sqrt{1-\boldsymbol{v}^2}} + qA^0 = [m^2 + (\boldsymbol{p}-q\boldsymbol{A})^2]^{1/2} + qA^0\ , \tag{1.183}$$

being $\boldsymbol{p}$ the *conjugate momentum*, given by:

$$\boldsymbol{p} \equiv \frac{\partial L}{\partial \boldsymbol{v}} = \frac{m\boldsymbol{v}}{\sqrt{1-\boldsymbol{v}^2}} + q\boldsymbol{A} \ .$$

Now if we consider a small vector potential $\boldsymbol{A}$, we can approximate (1.183) as:

$$H \simeq [m^2 + \boldsymbol{p}^2]^{1/2} - \frac{q}{m}\boldsymbol{p}\cdot\boldsymbol{A} + qA^0 \ ,$$

with

$$\boldsymbol{p} \simeq m\gamma\boldsymbol{v} \ .$$

So we can write:

$$H(t) \simeq H_0 + V(t) \ ,$$

with $H_0 \equiv [m^2 + \boldsymbol{p}^2]^{1/2}$, and

$$V(t) \equiv \int \mathrm{d}^3\boldsymbol{x} \ j_\mu(t,\boldsymbol{x}) A^\mu_{\mathrm{ext}}(t,\boldsymbol{x}) \ .$$

In general, if L_{int} is small (a perturbation characterized by a dimensionless parameter $\alpha \ll 1$, if $\alpha = 0$, $L_{\mathrm{int}} = 0$), we can always write

$$H = H_0 - L_{\mathrm{int}} \ ,$$

where H_0 is the unperturbed hamiltonian. This is because the conjugate momentum $\boldsymbol{p}$ in presence of the perturbation is:

$$\boldsymbol{p} = \frac{\partial L_0}{\partial \boldsymbol{v}} + \frac{\partial L_{\mathrm{int}}}{\partial \boldsymbol{v}} \ . \tag{1.184}$$

And the hamiltonian is:

$$H = \boldsymbol{p}\cdot\boldsymbol{v} - L_0 - L_{\mathrm{int}}.$$

Now, expanding $\boldsymbol{v}(\alpha)$ around $\alpha = 0$ and only keeping the linear terms, by virtue of (1.184):

$$\begin{aligned} H &\simeq \boldsymbol{p}\cdot\boldsymbol{v}_0 + \alpha\boldsymbol{p}\cdot\boldsymbol{v}_0' - L_0(\boldsymbol{x},\boldsymbol{v}_0,t) - \alpha\frac{\partial L_0(\boldsymbol{x},\boldsymbol{v}_0,t)}{\partial\boldsymbol{v}}\cdot\boldsymbol{v}_0' \\ &\quad - L_{\mathrm{int}}(\boldsymbol{x},\boldsymbol{v}_0,t) - \alpha\frac{\partial L_{\mathrm{int}}(\boldsymbol{x},\boldsymbol{v}_0,t)}{\partial\boldsymbol{v}}\cdot\boldsymbol{v}_0' \\ &\simeq \boldsymbol{p}_0\cdot\boldsymbol{v}_0 - L_0(\boldsymbol{x},\boldsymbol{v}_0,t) - L_{\mathrm{int}}(\boldsymbol{x},\boldsymbol{v}_0,t) = H_0 - L_{\mathrm{int}} \ , \end{aligned}$$

where $\boldsymbol{v}_0$ is the solution of (1.184) when $\alpha = 0$, and $\boldsymbol{p}_0 \equiv \partial L_0/\partial\boldsymbol{v} = \boldsymbol{p} + \mathcal{O}(\alpha)$. Therefore, any perturbation in the lagrangian produces the same pertubation (but with opposite sign) in the hamiltonian.

Now we consider the case of a gas of charged quantum particles coupled to an external classical (weak) electromagnetic field. The perturbation is given by:

$$\hat{V}(t) = \int \mathrm{d}^3\boldsymbol{x} \ \hat{J}_\mu(t,\boldsymbol{x}) A^\mu_{\mathrm{ext}}(\boldsymbol{x}) \ ,$$

where $\hat{J}$ is the current operator. Therefore, by (1.182), the induced current is:

$$\begin{aligned} J_\mu(x) \equiv \delta\langle \hat{J}_\mu(x)\rangle_T &= -\mathrm{i}\int \mathrm{d}^4x'\ \theta(t-t')\langle[\hat{J}_\mu(x),\hat{J}_\nu(x')]\rangle_T A^\nu_{\mathrm{ext}}(x') \\ &= -\mathrm{i}\int \mathrm{d}^4x'\ G^{\mathrm{R}}_{\mu\nu}(x-x')A^\nu_{\mathrm{ext}}(x')\ , \end{aligned} \tag{1.185}$$

being $G^{\mathrm{R}}_{\mu\nu}$ the retarded thermal correlator of currents.

In order to obtain the DC conductivity, we perturb the system by coupling it to an external classical electromagnetic field:

$$\hat{V}(t) = \int \mathrm{d}^3\boldsymbol{x}\ \hat{J}_\mu(x)A^\mu_{\mathrm{ext}}(x)\ . \tag{1.186}$$

Therefore, the induced current is

$$\delta\langle \hat{J}_\mu(x)\rangle = -\mathrm{i}\int \mathrm{d}^4x'\ G^{\mathrm{R}}_{\mu\nu}(x-x')A^\nu_{\mathrm{ext}}(x')\ , \tag{1.187}$$

where $G^{\mathrm{R}}_{\mu\nu}(x) \equiv \theta(t)\langle[\hat{J}_\mu(x),\hat{J}_\nu(0)]\rangle$ is the *retarded* current-current correlator. Now, using the gauge $A^0_{\mathrm{ext}} = 0$, we get $E^i_{\mathrm{ext}} = -\partial_0 A^i_{\mathrm{ext}}$. And therefore, in momentum space,

$$J^i(\omega,\boldsymbol{p}) = -\frac{(G^{\mathrm{R}})^i{}_j}{\omega}E^j_{\mathrm{ext}}(\omega,\boldsymbol{p}) \equiv \sigma^i{}_j(\omega,\boldsymbol{p})E^j_{\mathrm{ext}}(\omega,\boldsymbol{p})\ . \tag{1.188}$$

Now, since the DC conductivity corresponds to the action of a *constant* electric field, and taking the real part in (1.188), and assuming spatial isotropy, we finally obtain:

$$\sigma = -\frac{1}{3}\lim_{\omega\to0^+}\lim_{|\boldsymbol{p}|\to0^+}\frac{\mathrm{Im}\,\mathrm{i}(G^{\mathrm{R}})^i{}_i(\omega,\boldsymbol{p})}{\omega} = -\frac{1}{6}\lim_{\omega\to0^+}\lim_{|\boldsymbol{p}|\to0^+}\frac{\rho_\sigma(\omega,|\boldsymbol{p}|)}{\omega}\ , \tag{1.189}$$

where $\rho_\sigma = 2\,\mathrm{Im}\,\mathrm{i}(G^{\mathrm{R}})^i{}_i$ is the spectral function of the current-current correlator. The order in which the limit is taken is important, since the opposite one would correspond to a field constant in time and slightly not constant in space what would produce a rearrangement of the static charges giving a vanishing electric current. This is called a Kubo formula for the DC conductivity, and we can express it in another useful form in terms of a Wightman function $G^>$ by using the KMS relation $G^<(p) = \mathrm{e}^{-\beta p^0}G^>(p)$ and $\rho = G^> - G^<$ [Jeo95, LB96]:

$$\begin{aligned} \sigma &= -\frac{1}{6}\lim_{\omega\to0^+}\lim_{|\boldsymbol{p}|\to0^+}\frac{\partial}{\partial\omega}\int \mathrm{d}^4x\ \mathrm{e}^{\mathrm{i}p\cdot x}\langle[\hat{J}^i(x),\hat{J}_i(0)]\rangle \\ &= -\frac{\beta}{3}\lim_{\omega\to0^+}\lim_{|\boldsymbol{p}|\to0^+}\int \mathrm{d}^4x\ \mathrm{e}^{\mathrm{i}p\cdot x}\ \langle\hat{J}^i(x)\hat{J}_i(0)\rangle\ , \end{aligned} \tag{1.190}$$

where $\beta \equiv 1/T$, and we implicitly assume thermal averages. As we show in Chapter 3, in the perturbative evaluation of transport coefficients, the spatial momentum can be taken equal to zero from the beginning if the particle width is properly accounted for.

We are now going to show the relation between the current-current correlator $\Delta^{\mu\nu}$ and the photon self-energy $\Pi^{\mu\nu}$ (either retarded or not). This will be specially useful in Section 3.4.1, where we will discuss the soft-photon spectrum. Firstly, we consider the current-current correlator:

$$\Delta^{\mu\nu}(x-y) = \langle 0|\hat{T}\{\hat{J}^{\mu}(x)\hat{J}^{\nu}(y)\}|0\rangle \ .$$

From Maxwell's equations and using the Lorentz gauge $\partial_\mu A^\mu = 0$ (cf. [Jac99]), we have:

$$\Box A^{\mu} = J^{\mu} \ .$$

Therefore,

$$\Delta^{\mu\nu}(x-y) = \langle 0|\hat{T}\{\Box_x \hat{A}^{\mu}(x)\Box_y \hat{A}^{\nu}(y)\}|0\rangle \ .$$

Now, taking into account that

$$\frac{\partial}{\partial x^0}\hat{T}\{\hat{A}^{\mu}(x)\hat{A}^{\nu}(y)\} = \hat{T}\{\partial_0\hat{A}^{\mu}(x)\hat{A}^{\nu}(y)\} + \delta(x^0-y^0)[\hat{A}^{\mu}(x),\hat{A}^{\nu}(y)] \ ,$$

and using $[\hat{A}^{\mu}(x),\hat{A}^{\nu}(y)] = [\hat{A}^{\mu}_{\rm int}(x),\hat{A}^{\nu}_{\rm int}(y)]$, where $\hat{A}^{\mu}_{\rm int}$ is the electromagnetic field operator in the interaction picture, and knowing that $\Box A^{\mu}_{\rm int} = 0$, we obtain:

$$\begin{aligned}\Delta^{\mu\nu}(x-y) &= \Box_x\Box_y[\langle 0|\hat{T}\{\hat{A}^{\mu}(x)\hat{A}^{\nu}(y)\}|0\rangle - \langle\hat{0}|\hat{T}\{\hat{A}^{\mu}_{\rm int}(x)\hat{A}^{\nu}_{\rm int}(y)\}|\hat{0}\rangle] \\ &= \Box_x\Box_y[G^{\mu\nu}(x-y) - G_0^{\mu\nu}(x-y)] \ ,\end{aligned}$$

where $\hat{0}$ denotes the non-interacting vacuum, $G^{\mu\nu}$ is the full photon propagator, and $G_0^{\mu\nu}$ is the free photon propagator.

Now, in the Lorentz gauge, $-\mathrm{i}\eta_{\mu\nu}\Box_x$ is the inverse of the free propagator, in the sense:

$$\eta_{\mu\lambda}\Box_x G_0^{\lambda\nu}(x-y) = \mathrm{i}\delta_{\mu}{}^{\nu}\delta^{(4)}(x-y) \ ,$$

and we denote it by $G^{-1}_{0x\mu\nu}$. Thus:

$$\Delta_{\mu\nu}(x-y) = -G^{-1}_{0x\mu\lambda}G^{-1}_{0y\nu\rho}[G^{\lambda\rho}(x-y) - G_0^{\lambda\rho}(x-y)] \ .$$

Therefore, in momentum space and ommiting indices:

$$\Delta = -G_0^{-1}G_0^{-1}[G - G_0] \ .$$

Now, introducing the self-energy:

$$\mathrm{i}\Pi \equiv G^{-1} - G_0^{-1} \ ,$$

we finally obtain:

$$-\mathrm{i}\Delta = \Pi G G_0^{-1} \ .$$

Therefore, to the lowest order in the electron charge,

$$-\mathrm{i}\Delta = \Pi \ . \tag{1.191}$$

1.6.3 Shear and bulk viscosities

As we have seen, viscosities are related to gradients of the hydrodynamical velocity in the fluid. Since we will evaluate the correlators at thermal equilibrium, we can choose a global reference frame which is at rest with the fluid. We will give here a simple derivation of the Kubo formulae for the viscosities and the thermal conductivity (for a more rigorous discussion see [Zub74]). By performing a boost that depends on the point, we can simulate gradients of the velocity, so the fluid velocity around some point x_0 becomes $U^i(x) \simeq x^j \partial_j U^i(x_0)$. Then, this boost implies the change in the energy density $\delta\mathcal{H} = -\boldsymbol{U}\cdot\boldsymbol{p}$ where $\boldsymbol{p}$ is the density of momentum in the fluid. Therefore, this corresponds to the perturbation in the hamiltonian density:

$$\mathcal{V}(x) = -T^{0i} x^j \partial_j U^i \ . \tag{1.192}$$

Under this perturbation, the variation in the expectation value of the energy-momentum tensor is

$$\delta\langle \hat{T}^{ij} \rangle = \mathrm{i} \int \mathrm{d}^4x' \ t' \, \theta(t-t') \langle [\hat{T}^{ij}(x), \hat{T}^{kl}(x')] \rangle \partial_k U_l \ , \tag{1.193}$$

where we have integrated by parts and used $\partial_\mu T^{\mu\nu} = 0$. If we now particularize for the case $\partial_k U^k = 0$, and compare with the expression (1.151), we then obtain:

$$\eta = \frac{\mathrm{i}}{12} \int \mathrm{d}^4x \ t \, \theta(t) \langle [\hat{T}_{ij}(x), \hat{T}^{ij}(0)] \rangle \ . \tag{1.194}$$

In momentum space, we can write it as

$$\eta = \frac{1}{20} \lim_{\omega\to 0^+} \lim_{|\boldsymbol{p}|\to 0^+} \frac{\rho_\eta(\omega, |\boldsymbol{p}|)}{\omega} \ , \tag{1.195}$$

with

$$\rho_\eta(\omega, |\boldsymbol{p}|) = \int \mathrm{d}^4x \ \mathrm{e}^{\mathrm{i}p\cdot x} \langle [\hat{\pi}_{ij}(x), \hat{\pi}^{ij}(0)] \rangle \ , \tag{1.196}$$

and $\pi_{ij} \equiv T_{ij} - g_{ij} T^k_{\ k}/3$. In order to obtain the bulk viscosity we consider instead $\partial_i U_j = (1/3)\delta_{ij}\partial_k U^k$, and we have:

$$\delta\Pi = \delta\langle \hat{\mathcal{P}} \rangle = \mathrm{i} \int \mathrm{d}^4x' \ t' \, \theta(t-t') \langle [\hat{\mathcal{P}}(x), \hat{\mathcal{P}}(x')] \rangle \partial_k U^k \ , \tag{1.197}$$

with $\mathcal{P} \equiv -T^k_{\ k}/3$. And comparing with (1.151), we get:

$$\zeta = \mathrm{i} \int \mathrm{d}^4x \ t \, \theta(t) \langle [\hat{\mathcal{P}}(x), \hat{\mathcal{P}}(0)] \rangle \ . \tag{1.198}$$

In momentum space we can express it as

$$\zeta = \frac{1}{2} \lim_{\omega\to 0^+} \lim_{|\boldsymbol{p}|\to 0^+} \frac{\rho_\zeta(\omega, |\boldsymbol{p}|)}{\omega} \ , \tag{1.199}$$

with

$$\rho_\zeta(\omega,|\boldsymbol{p}|)=\int \mathrm{d}^4x\ \mathrm{e}^{\mathrm{i}p\cdot x}\langle[\hat{\mathcal{P}}(x),\hat{\mathcal{P}}(0)]\rangle\ . \tag{1.200}$$

In other more rigorous derivations of the Kubo formulas [Zub74, Hos84, Hor87], where energy-momentum conservation in the correlators is not used, the expression of the bulk viscosity involves the operator

$$\hat{\mathcal{P}}\equiv-\hat{T}^k{}_k/3-c_\mathrm{s}^2\hat{T}^{00}-\mu\hat{N}^0\ , \tag{1.201}$$

where c_s is the speed of sound in the plasma and μ the chemical potential. This operator will give the same result as $\mathcal{P}=-T^k{}_k/3$ for the bulk viscosity if it is calculated exactly (non-perturbatively). This is a consequence of the following property of Wightman functions involving a conserved current N^μ (so $\partial_\mu N^\mu=0$): for any operator $\hat{\mathcal{O}}(x)$, and frequency $\omega\neq0$, it is verified

$$\int \mathrm{d}^4x\ \mathrm{e}^{\mathrm{i}\omega t}\langle\hat{N}^0(x)\hat{\mathcal{O}}(0)\rangle=0\ . \tag{1.202}$$

However, in our calculations we will use (1.201) to obtain the bulk viscosity, because we are interested in a *perturbative* calculation using propagators with a non-zero width, so the conservation of the energy-momentum tensor in correlators will not be exact within the level of approximation we will use. As we will see in Chapter 3, the extra c_s^2 term in (1.201) will be crucial in our approach.

1.6.4 Thermal conductivity

As we have seen, it is necessary to have some conserved current in the system (besides $T^{\mu\nu}$) for the thermal conductivity to be non-zero. According to Eq. (1.154), heat conduction can be produced by a gradient in the chemical potential. In order to create such a gradient, we couple an external gauge field A^μ_ext to the conserved current N^μ (A^0_ext plays the role of an effective chemical potential, cf. Section 4.1), so the perturbation in the hamiltonian density is:

$$\mathcal{V}(x)=N_\mu A^\mu_\mathrm{ext}\ . \tag{1.203}$$

By choosing $A^i_\mathrm{ext}=0$, integrating by parts, and using $\partial_\mu N^\mu=0$ we obtain:

$$\delta I^i_q=\delta\langle\hat{T}^{i0}-h\hat{N}^i\rangle(x)=\mathrm{i}\int \mathrm{d}^4x'\ t'\,\theta(t-t')\langle[\hat{\mathcal{T}}^i(x),N^j(x')]\rangle\partial_j A^0_\mathrm{ext}(x')\ , \tag{1.204}$$

with $\mathcal{T}^i\equiv T^{0i}-hN^i$. Thus, by comparing with Eq. (1.154), taking $\partial_j A^0_\mathrm{ext}$ constant, and assuming spatial isotropy, we have that the Kubo formula for κ is:

$$\kappa=-\frac{\beta}{6}\lim_{\omega\to0^+}\lim_{|\boldsymbol{p}|\to0^+}\frac{\rho_\kappa(\omega,|\boldsymbol{p}|)}{\omega}\ , \tag{1.205}$$

with

$$\rho_\kappa(\omega, |\boldsymbol{p}|) = \int \mathrm{d}^4x \; \mathrm{e}^{\mathrm{i}p\cdot x} \langle [\hat{\mathcal{T}}^i(x), \hat{\mathcal{T}}_i(0)] \rangle \; , \tag{1.206}$$

where we have used (1.202). From the expression for ρ_κ we explicitly see that if there is no conserved current in the system (besides $T^{\mu\nu}$), then the thermal conductivity is zero. We will use $\mathcal{T}^i \equiv T^{0i} - hN^i$ (instead of only $-hN^i$) in the calculation of the thermal conductivity, because of the same reason explained previously in the case of the bulk viscosity.

Chapter 2

Spectral properties of thermal resonances and chiral symmetry

The lightest meson resonances, the $\rho(770)$ and the $f_0(600)$ or σ, play a crucial role in different phenomena pertaining to the hot and/or dense medium created both in Relativistic Heavy Ion Collisions and in Nuclear Matter experiments. The modifications of the spectral function of the ρ resonance in medium are crucial to understand correctly the dilepton yield emerged from Heavy Ion Collisions [Aga05, Arn06a]. The two main theoretical scenarios currently proposed in the literature can be classified into resonance mass shifting and broadening, according to the resulting dominant effect. Mass shifting models are inspired by the Brown-Rho (BR) scaling hypothesis [Bro91], which predicted that vector meson masses should scale with the quark condensate and therefore the main spectral modification of the resonance would be dictated by chiral symmetry restoration. This scenario is supported also by the so called hidden local symmetry approach [Har06]. The broadening-dominated scenario is supported by different theoretical analyses [Her92, Pis95, Pet98, Rap97, Rap00] including recent Unitarized Chiral approaches [Cab02, Dob02]. The most recent experimental dimuon data from the NA60 Collaboration [Arn06a] clearly favor a broadening situation with negligible mass shift, whereas the earlier CERES results [Aga05] were reasonably explained by both descriptions. It is worth mentioning also the results of the STAR Collaboration at RHIC [Ada04b], which has reported a sizable mass reduction by medium effects measured in $\rho^0 \rightarrow \pi^+\pi^-$ instead of dileptons. The modifications of the ρ properties have also been measured in cold nuclear matter experiments. The E325-KEK collaboration [Nar06] has reported a measurable shift in the masses of vector mesons compatible with theoretical predictions based on Brown-Rho scaling [Bro02] and QCD sum rules [Hat95]. On the other hand, the JLab-CLAS experiment [Nas07] has obtained results compatible with vanishing mass shift, as predicted by most of in-medium hadronic many-body analyses where broadening is the dominant effect [Her92, Pet98, Urb98, Cab02].

The possible modification of the $f_0(600)/\sigma$ in hot and dense matter is interesting because this is a state with the same quantum numbers as the vacuum and therefore it might be sensitive to chiral symmetry restoration. In this sense, an early proposal [Hat85] suggested that the σ could induce a measurable threshold enhancement of the $\pi\pi$ cross section, which would be interpreted as a precursor of chiral symmetry restoration.

The argument was that the mass of the σ state should decrease by medium effects, since it is proportional to its vacuum expectation value in the chiral limit. Such a decrease would eventually shrink the available two-pion phase space when the σ mass reaches the two-pion threshold, producing a bump in the imaginary part of the scattering amplitude, due to the proximity of the pole to the real axis. It is important to remark that in this original argument, it is implicitly assumed that i) the σ is dominated by its $\bar{q}q$ component so that its expectation value behaves like the quark condensate and ii) that the σ is narrow enough so that its width (imaginary part of the pole) vanishes when its mass (real part) approaches the threshold. None of these assumptions seem to be supported by the physical (vacuum) $f_0(600)$ state quoted by the Particle Data Group [Ams08], which is a very broad state measured in $\pi\pi$ scattering. Although it is commonly accepted that this state is a member of the scalar nonet, its $\bar{q}q$ nature has been criticized on the basis of lattice [Alf00] and large-N_c [Pel04] analyses. The physical state is likely to have important non-$\bar{q}q$ component such as tetraquark, glueball or meson-meson, this last one commonly referred to as a "molecular" state ($\pi\pi$ bound state). Nevertheless, threshold enhancement is indeed observed in nuclear matter experiments, both in $\pi A \to \pi\pi A'$ [Bon00, Sta00] and in $\gamma A \to \pi\pi A'$ [Mes02] reactions. Although the size of the effect is still under debate, a clear signal is seen in the scalar channel for increasing nuclear density as compared with the vector channel and this is in fair agreement with most theoretical analyses at finite nuclear density [Chi98a, Dav00, Jid01, Roc02, Pat03, Cab05]. In contrast, finite temperature analyses show that this state remains broad even near the chiral phase transition despite the proximity of the pole to the two-pion threshold [Pat03, Hid04], which in practice does not produce any sizable enhancement in the scattering amplitude or cross section. A striking possibility to be explored is that by increasing further the medium strength, the σ could become a $\pi\pi$ bound state, as suggested earlier in [Sch88] and confirmed recently in [Pat03, Hid04].

The content of this chapter reviews the work presented in the papers [FF07c, Cab08], where we investigated further about these issues, within the context of unitarized chiral approaches. The main goal has been to establish to what extent chiral symmetry dictates the in-medium properties of the light meson resonances. The most general framework to account for all the interactions compatible with chiral symmetry is the effective chiral lagrangian approach. The most prominent example is Chiral Perturbation Theory for the meson sector [Wei79, Gas84], but it can be equally applied to the meson-baryon one [Ber95]. Since these effective theories are built basically as expansions in derivatives or energies, they cannot account for resonances, because the chiral expansion violates the unitarity bounds. This has been traditionally solved by introducing unitarization methods, giving rise to the so called chiral unitary approaches, which have proved to be very successful in vacuum to describe meson-meson and meson-baryon interactions and generate dynamically low lying resonances [Dob90, Dob93, Dob97, Oll98, Nie99, GN00, Nie00, Oll01, GN02a]. Furthermore, as commented above, the unitarization program has been extended to account for finite temperature and density effects [Ram00, Cab02, Dob02, Roc02, Cab05, Tol08]. In the study of the $\rho(770)$ and $f_0(600)$ resonances we have payed special attention to their nature and their role in chiral symmetry restoration. In Section 2.1 we will present the formalism and results for the evolution of resonances with temperature within the framework of the Inverse Amplitude Method (IAM). In the same

section we analyze the need of extending the IAM definition for the scattering amplitude near the threshold in order to avoid unphysical spurious poles. In Section 2.2 we will introduce nuclear density effects only by rescaling properly the pion decay constant at $T = 0$ within the IAM. In that section, we provide in particular an interpretation of our results in terms of molecular classification and a numerical comparison with experimental results from dilepton decays in resonance production in finite nuclei. Finally, in Section 2.3 we present an analysis of the combined effects of temperature and nuclear density for the σ meson based on a Lippmann-Schwinger (or Bethe-Salpeter) equation approach accounting for many-body pion dynamics versus a simplified F_π-scaling scenario, and we compare with the simpler approach of rescaling F_π.

2.1 Finite temperature resonances with the IAM

One of the simplest and most powerful unitarization methods for chiral theories is the so called Inverse Amplitude Method [Dob90, Dob93, Dob97]. Its name comes from the simple observation that unitarity implies that the inverse of a given partial wave amplitude t_{IJ} in $\pi\pi \to \pi\pi$ scattering should satisfy:

$$\hat{S}^\dagger \hat{S} = 1 \quad \Rightarrow \quad \mathrm{Im}\, t_{IJ}(s) = \sigma_0(s)|t_{IJ}(s)|^2 \quad \Rightarrow \quad \mathrm{Im}\, \frac{1}{t_{IJ}(s)} = -\sigma_0(s) \ , \tag{2.1}$$

for $s > 4M_\pi^2$, where s is the center of mass energy squared and $\sigma_0(s) = \sqrt{1 - 4M_\pi^2/s}$ is the two-pion phase space.

Consider now the ChPT expansion of partial wave amplitudes:

$$t_{IJ}(s) = t_{IJ}^{(2)}(s) + t_{IJ}^{(4)}(s) + \mathcal{O}(p^6) \ . \tag{2.2}$$

Here, I denotes isospin, J denotes orbital angular momentum, p denotes generically a meson momentum, mass or temperature (p is to be compared with the characteristic chiral scale $\Lambda_\chi \sim 1$ GeV, whereas T is meant to be below the critical temperature $T_c \sim$ 200 MeV), and $t_{IJ}^{(k)}$ is the $\mathcal{O}(p^k)$ contribution. For the energies and temperatures of interest here, only the partial waves involving $J \leq 1$ are relevant. According to the standard ChPT power counting [Wei79, Gas84] (see also Section 1.3), $t^{(2)}$ accounts for tree level diagrams from the lowest order lagrangian $\mathcal{L}_2$ (the non-linear sigma model). This lowest-order amplitude is temperature-independent, gives Weinberg's low-energy theorem [Wei66], and has the following form:

$$t_{IJ}^{(2)}(s) = A_{IJ}(s - s_2^{IJ}) \ , \tag{2.3}$$

IJ	$16\pi F_\pi^2 A_{IJ}$	s_2^{IJ}/M_π^2
00	1	1/2
11	1/6	4
20	−1/2	2

where s_2 is the so called Adler zero (the point where the amplitude vanishes) to second order. For the relevant partial waves in pion scattering, the values of the A_{IJ} and s_2 constants are given in Table 2.3. Note that, to this order, the amplitudes depend only

on the pion mass $M_\pi \simeq 140$ MeV and the pion decay constant $F_\pi \simeq 93$ MeV. The order $t^{(4)}$ includes the one-loop diagrams from $\mathcal{L}_2$ plus the tree level $\mathcal{L}_4$ terms needed for renormalization. The $\mathcal{L}_4$ low-energy constants entering the pion scattering amplitude, when it is expressed in terms of the physical M_π, F_π, are denoted $\bar{l}_1 - \bar{l}_4$ in the convention of [Gas84][1].

The chiral expansion (2.2) satisfies only a perturbative version of the unitarity relation (2.1), namely:

$$\mathrm{Im}\, t_{IJ}^{(4)}(s) = \sigma_0(s)|t_{IJ}^{(2)}(s)|^2 \ , \tag{2.4}$$

and so on for higher orders, which eventually means that chiral expansions are not compatible with the bounds on partial waves implied by unitarity. In other words, they grow arbitrarily with energy and, in particular, these partial waves cannot reproduce resonances. Unitarization methods allow to construct chiral amplitudes that are exactly unitary. In particular, the IAM amplitudes are built by demanding i) exact unitarity and ii) that at low energies they match the ChPT series to a given order. These conditions lead to the IAM result, which is formally justified by the use of dispersion relations [Dob90, Dob93, Dob97]. According to the IAM, the unitarized partial waves to order $\mathcal{O}(p^4)$ are given by:

$$t_{IJ}^{\mathrm{U}}(s) = \frac{\left[t_{IJ}^{(2)}(s)\right]^2}{t_{IJ}^{(2)}(s) - t_{IJ}^{(4)}(s)} \ . \tag{2.5}$$

In addition to appearing as peaks in the scattering cross section, resonances can also be identified as poles in the scattering amplitude after continued to the second Riemann sheet (SRS). The amplitude (2.5) is analytical on the complex plane off the real axis, it has the right unitarity cut starting at the two-pion threshold $s = 4M_\pi^2$ and a left cut for $s < 0$ coming from diagrams in the $t - u$ channels [Dob02]. From these analytical properties, one can immediately define the amplitude on the SRS which continuously connects with the imaginary part of the first Riemann sheet (FRS) amplitude across the right cut. If $t^{(\mathrm{I})}$ denotes the analytical continuation of the scattering amplitude off the real axis (FRS), then the scattering amplitude on the SRS, $t^{(\mathrm{II})}$, is defined by $\mathrm{Im}\, t^{(\mathrm{II})}(s - \mathrm{i}0^+) = \mathrm{Im}\, t^{(\mathrm{I})}(s + \mathrm{i}0^+)$, for $s > 4M_\pi^2$. Therefore one has

$$t^{(\mathrm{II})}(s) = \frac{t^{(\mathrm{I})}(s)}{1 - \mathrm{i}2\sigma_0(s)t^{(\mathrm{I})}(s)} \ . \tag{2.6}$$

It can be shown [New02, Tay06] that the mass and width of a Breit-Wigner-like resonance are related to the pole of $t^{(\mathrm{II})}$ in the lower half complex plane by $s_{\mathrm{pole}} = (M_{\mathrm{R}} - \mathrm{i}\Gamma_{\mathrm{R}}/2)^2$ [Ams08]. We shall use this relation as a definition of the mass and width of the resonances we obtain in unitarized $\pi\pi$ scattering, although for the case of the $f_0(600)$ the width is not small. Since we work in the center of mass reference frame, the mass and width obtained correspond to a resonance at rest.

There is however a further, more technical requirement, which is that the IAM partial-wave amplitudes should vanish at the same values of the energy and with the same power

[1] These are the low-energy constants l_i of Section 1.3 renormalized at the scale M_0 (so they are renormalization-scale independent, but they depend on the pion mass).

as the perturbative amplitudes. These values are the so called Adler zeros and lie below threshold. Since a zero of the amplitude is a pole of its inverse, this affects the analytic structure of $1/t$. A detailed discussion can be found in [GN08] where the proper correction to the IAM is derived using dispersion relations and it is shown that these additional terms produce a negligible effect in the physical region. However, as we will see below (Section 2.1.1), taking into account this correction is important when dealing with medium effects that can drive the poles to the real axis, as it is the case here, since otherwise there would be spurious poles both in the first and second Riemann sheets below threshold.

The IAM can be extended at finite temperature by including the thermal corrections to the scattering amplitude, which have been calculated in [GN02b] to one loop in ChPT. Since temperature enters only in the loops, $t^{(2)}$ is T-independent. For $t^{(4)}(s,T)$ one gets a perturbative unitarity relation exactly like (2.2) but with the phase space replaced by:

$$\sigma_T(s) = \sigma_0(s)[1 + 2n_{\rm B}(\sqrt{s}/2)] \ , \tag{2.7}$$

with $n_{\rm B}(x) \equiv [\exp(x/T) - 1]^{-1}$ the Bose-Einstein distribution function. The function $\sigma_T(s)$ is the thermal phase space, which is increased with respect to the $T = 0$ one by the difference $[1 + n_{\rm B}(E_1)]\,[1 + n_{\rm B}(E_2)] - n_{\rm B}(E_1)n_{\rm B}(E_2) = 1 + n_{\rm B}(E_1) + n_{\rm B}(E_2)$, where $E_{1,2}$ are the energies of the two colliding pions, corresponding to the difference between enhancement due to the increase of two-pion outgoing states and absorption due to collisions of the incoming pions with the thermal bath ones. In the center of mass frame, where partial waves are defined, $E_1 = E_2 = \sqrt{s}/2$ and the thermal phase space reduces to (2.7). One can then use the same $T = 0$ IAM requirements, replacing $\sigma_0 \mapsto \sigma_T$ and the partial waves by the finite-T ones, provided that only intermediate two-pion states are relevant in the thermal bath, as expected in a dilute gas regime at low and moderate temperatures. Finally, one arrives to the thermal IAM formula for a given partial wave (see Section 2.1.1 for the details of the derivation):

$$\begin{aligned} t^{\rm IAM} &= \frac{(t^{(2)}(s))^2}{t^{(2)}(s) - t^{(4)}(s,T) + A(s,T)} \ , \\ \text{with} \quad A(s,T) &\equiv t^{(4)}(s_2,T) - \frac{(s_2 - s_4)(s - s_2)}{s - s_4}\left[t^{(2)\prime}(s_2) - t^{(4)\prime}(s_2,T)\right] \ , \end{aligned} \tag{2.8}$$

where the A function is the Adler zero contribution discussed above, s_k denoting the Adler zero (T-dependent for $k > 2$) to order $\mathcal{O}(p^k)$, with $s_4 = s_2 - t^{(4)}(s_2,T)/t^{(2)\prime}(s_2)$.

Performing the conventional extension of the amplitude to the second Riemann sheet, one finds poles in the $I = J = 0$ and $I = J = 1$ channels which are identified as the $f_0(600)$ and the $\rho(770)$. We show in Figure 2.1 the results for the pole position $s_{\rm pole} = (M_{\rm p} - {\rm i}\Gamma_{\rm p}/2)^2$ for different temperatures. The $\bar{l}_i$ values we have used are $\bar{l}_1 = -0.3$, $\bar{l}_2 = 5.6$, $\bar{l}_3 = 3.4$ and $\bar{l}_4 = 4.3$, which give for the mass and width of the $\rho(770)$ at $T = 0$ $M_{\rm p} \simeq 756$ MeV and $\Gamma_{\rm p} \simeq 151$ MeV. For the $f_0(600)/\sigma$ at $T = 0$ we find $M_{\rm p} \simeq 441$ MeV and $\Gamma_{\rm p} \simeq 464$ MeV. The general features we observe are that the thermal ρ pole shows a predominant and increasing broadening behavior, while for the σ an important mass decrease takes place, presumably due to chiral restoration (see Section 2.1.3), while the width increases for low temperatures but decreases for temperatures of $T \simeq 100$ MeV and beyond. From Section 2.1.2 on, we will discuss in more detail these different behaviors in connection with the phenomenological issues commented in the introduction.

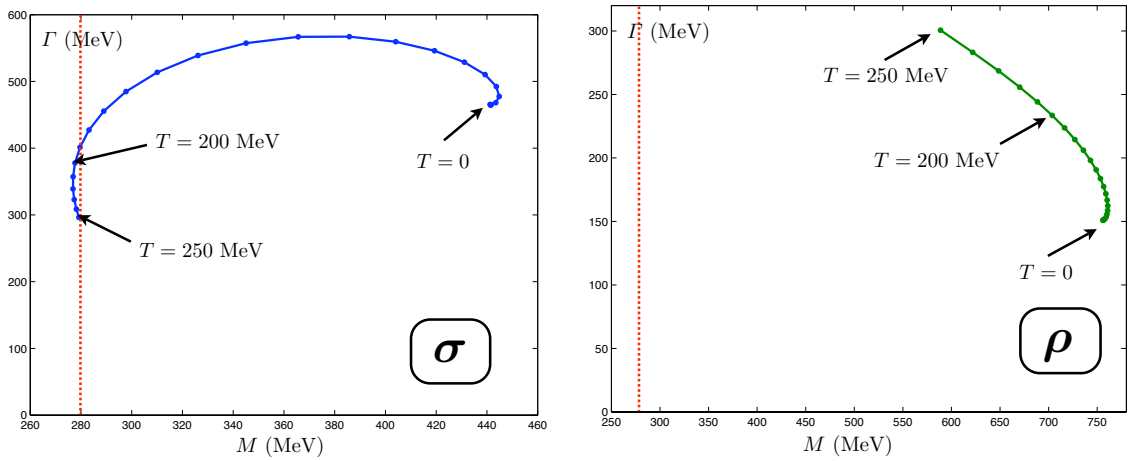

Figure 2.1: Temperature dependence of the $f_0(600)$ and ρ complex poles unitarized by the IAM. The points are obtained by varying the temperature in 10 MeV intervals.

2.1.1 Real axis poles and Adler zeros

The analysis of poles near the real axis below threshold is relevant for the chiral restoring behavior, as discussed above. As we will show here, the unitarized IAM amplitude below threshold has to be extended in order to account properly for the Adler zeros and remove spurious poles. For clarity, we will discuss the $T = 0$ case first.

$T = 0$ extended amplitude

Consider the IAM unitarized amplitude (2.5). Near threshold, $t^{\rm IAM} \sim t^{(2)} + t^{(4)}$ and $t^{(4)}$ is perturbatively small compared to $t^{(2)}$. On the other hand, the perturbative amplitude must have an Adler zero, i.e, a point where it vanishes, as a consequence of Weinberg's low-energy theorem [Wei66], which predicts that the pion scattering amplitude vanishes in the chiral limit at $s = 0$. Both $t^{(2)}$ and $t^{(2)} + t^{(4)}$ have this property and is natural to expect that $t^{\rm IAM}$ has a zero not far from the perturbative one. The zero of $t^{(2)}$ is given by s_2 in (2.3) and we will call s_4 the zero of $t^{(2)} + t^{(4)}$. Note that the IAM expression (2.5) vanishes exactly at s_2, although the order of the zero is not necessarily the same: if $t^{(4)}(s_2) \neq 0$, $t^{\rm IAM} \sim (s - s_2)^2$, while $t^{(2)}$ has a zero of order one. In addition, note that if $t^{(2)}$ and $t^{(4)}$ have the same sign and $t^{(4)}(s_2) \neq 0$, there is a point $\tilde{s} > s_2$ where the denominator of (2.5) vanishes. If that point exists for a given channel, it produces a spurious pole in the first Riemann sheet, since it would predict a not-observed $T = 0$ $\pi\pi$ bound state. That pole does exist in the $I = J = 0$ channel at $\tilde{s} \simeq (89\ \text{MeV})^2$ and at $\tilde{s} \simeq (197.4\ \text{MeV})^2$ for $I = 2, J = 0$. In the $I = J = 1$ channel there is no such problem, since the scattering length has to vanish by parity so that $s_2 = s_4 = 4M_\pi^2$ and at that point both $t^{(2)}$ and $t^{(4)}$ vanish, so that (2.5) is not divergent. The position of s_2, s_4 and $\tilde{s}$ (all of them below threshold) for the 00 channel are shown in Figure 2.2. The contribution of the possible amplitude zeros was already mentioned in early IAM papers [Dob93, Dob97], although it was not taken into account since its effect is negligible in the physical region, as we will show below. The existence of the non-physical pole has also

been noticed in [Bug03], where it is also linked to the presence of the Adler zero.

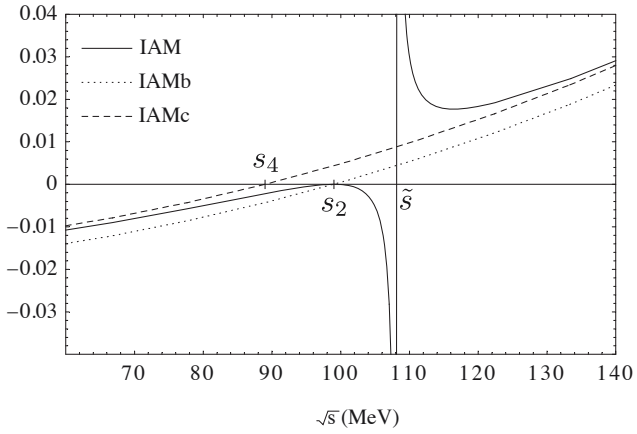

Figure 2.2: Unitarized amplitudes at $T = 0$ in the $I = J = 0$ channel, where s_2 and s_4 are, respectively, the Adler zeros of second and fourth order and $\tilde{s}$ is the point where the IAM diverges.

Therefore, the IAM definition (2.5) is affected with two related problems below threshold: the wrong order of the Adler zero and the presence of spurious poles. We will see now a simple way to cure both without spoiling the essential properties of chiral symmetry and unitarity of the IAM. For that purpose, we note that if we extend the inverse amplitude as:

$$\frac{1}{t^{\mathrm{IAM}}(s)} \mapsto \frac{1}{t^{\mathrm{IAM}}(s)} + g(s) \ , \tag{2.9}$$

with g an analytic function off the real axis, real for $s \in \mathbb{R}$, the unitarity condition (2.1) remains unaltered and so does the analytic structure of the amplitude. The choice of g is in principle arbitrary. Therefore, since having a double zero in the amplitude means having a double pole in the inverse amplitude, if we choose $g_b(s) = -R/(s - s_2)^2$ with R the residue of $1/t^{\mathrm{IAM}}$ at the double pole s_2, we get an amplitude with an Adler zero of order one at $s = s_2$. In fact, note that, taking into account (2.3), the expansion of the inverse amplitude near s_2 reads:

$$\frac{1}{t^{\mathrm{IAM}}(s)} = -\frac{t^{(4)}(s_2)}{A^2(s - s_2)^2} + \frac{A - t^{(4)\prime}(s_2)}{A^2(s - s_2)} + \dots \ , \tag{2.10}$$

where the dots stand for terms which do not diverge as $s \to s_2$.

Therefore, $R = -t^{(4)}(s_2)/A^2$ and the extended amplitude with this choice of g becomes simply:

$$t^{\mathrm{IAM},b}(s) = \frac{\left[t^{(2)}(s)\right]^2}{t^{(2)}(s) - t^{(4)}(s) + t^{(4)}(s_2)} \ . \tag{2.11}$$

The expression (2.11) has a simple Adler zero at $s = s_2$ as long as $t^{(4)\prime}(s_2) \neq 0$. But in addition, if $t^{(2)}(s) - t^{(4)}(s)$ is an increasing function of s from $s = 0$ to threshold, the IAM pole disappears, since in that case, s_2 is the only point where the denominator of (2.11) vanishes. This is what happens in the 00 channel, as shown in Figure 2.2.

We can improve further the unitarized amplitude, by demanding also that it matches the ChPT series near threshold. Note that this condition does not hold for (2.11), which can easily be seen by re-expanding it in powers of F_π^{-2}. Since $t^{(4)}(s_2) = \mathcal{O}(F_\pi^{-4})$, we get $t(s) \simeq t^{(2)}(s) + t^{(4)}(s) - t^{(4)}(s_2)$ instead of the $t^{(2)} + t^{(4)}$ of ChPT. That is, it only matches correctly the first $O(F_\pi^{-2})$ order $t^{(2)}$. If we want the amplitude to match $t^{(2)} + t^{(4)}$, then, as we will show below, it is sufficient to demand that both have the Adler zero at the same point, i.e, at $s = s_4$. Therefore, in order that $1/t$ has a simple pole at that point and according to (2.10) we must subtract now the s_2 pole and add the s_4 one, i.e, we choose:

$$g_c(s) = \frac{1}{A^2}\left[\frac{t^{(4)}(s_2)}{(s-s_2)^2} - \frac{A - t^{(4)\prime}(s_2)}{s-s_2} + \frac{c}{s-s_4}\right] , \tag{2.12}$$

where c is an undetermined constant that we will fix by demanding the perturbative matching with the ChPT series to fourth order. Adding (2.12) to $1/t^{\rm IAM}$ we get:

$$t^{{\rm IAM},c}(s) = \frac{A^2(s-s_2)^2(s-s_4)}{c(s-s_2)^2 - (s-s_4)\left[t^{(4)}(s) - t^{(4)}(s_2) - (s-s_2)t^{(4)\prime}(s_2)\right]} . \tag{2.13}$$

Let us expand the previous expression in powers of F_π^{-2}. Recall that $A = \mathcal{O}(F_\pi^{-2})$, $t^{(4)} = \mathcal{O}(F_\pi^{-4})$ and $s_4 = s_2 + \mathcal{O}(F_\pi^{-2})$, so that the leading order is $t^{{\rm IAM},c} = (A^2/c)(s-s_2)$ and therefore $c = A + \mathcal{O}(F_\pi^{-4})$. Expanding now the expression $t^{(2)}(s_4) + t^{(4)}(s_4) = 0$ around s_2 we find:

$$s_4 = s_2 - t^{(4)}(s_2)/A + \mathcal{O}(F_\pi^{-4}) . \tag{2.14}$$

Using this in the expansion of (2.13) to fourth order, we have $t^{{\rm IAM},c}(s) = t^{(2)}(s) + t^{(4)}(s) - (s-s_2)(c - A + t^{(4)\prime}(s_2)) + \mathcal{O}(F_\pi^{-6})$. Therefore, by taking:

$$c = A - t^{(4)\prime}(s_2) , \tag{2.15}$$

in (2.13), the unitarized amplitude matches the chiral expansion up to fourth order and has the Adler zero at the same position and with the same order as the perturbative amplitude. Note also that with c in (2.15), (2.13) reduces to (2.11) when $s_4 \to s_2$, as it should. In fact, since the difference between s_4 and s_2 is perturbatively small, we expect this extended amplitude to behave very similarly as the simplest version (2.11), and in particular to remove the spurious pole while being numerically closer to the original IAM amplitude. That is indeed the case, as it can clearly be seen in Figure 2.2. The same situation takes place in the $I = 2, J = 0$ channel. The extended amplitudes are expected to differ little from $t^{\rm IAM}$ away from s_2 or s_4, since the $g_{b,c}$ functions vanish for $s \gg s_2, s_4$. For that reason, in Figure 2.2 we have only shown the region around the spurious pole and the Adler zero. Away from that region, either in the real axis or in the complex plane, there is practically no difference between the IAM or its extended versions discussed here.

It is interesting to note that if we had not redefined the amplitude, there would be also a non-physical pole in the second Riemann sheet just below the real axis and below threshold. The IAM in the second Riemann sheet for $T = 0$ reads, from (2.5) and (2.6):

$$t^{\rm IAM,II} = \frac{(t^{(2)})^2}{t^{(2)} - t^{(4)} - 2\tilde{\sigma}(t^{(2)})^2} , \tag{2.16}$$

where we have defined $\tilde{\sigma}(s) \equiv \mathrm{i}\sigma_0(s - \mathrm{i}0^+) = \sqrt{4M_\pi^2/s - 1}$ for $0 < s < 4M_\pi^2$. Thus, the denominator of (2.16) is positive near threshold for an attractive channel (dominated by $t^{(2)} \geq 0$) like the 00 one and diverges to minus infinity as $s \to 0^+$, so that it must have an odd number of zeros. Since the denominator is not zero at $s = s_2$, that means that there would be at least one such real pole for the IAM in the second sheet. Consider however the extended amplitude, for instance (2.11). Now,

$$t^{\mathrm{IAM},b,\mathrm{II}} = \frac{(t^{(2)})^2}{t^{(2)} - t^{(4)} + t^{(4)}(s_2) - 2\tilde{\sigma}(t^{(2)})^2} \ , \tag{2.17}$$

which is not necessarily singular below threshold since both the denominator and the numerator vanish at $s = s_2$. A similar argument holds for $t^{\mathrm{IAM},c,\mathrm{II}}$, whose denominator is now positive both at threshold (provided again that the $\mathcal{O}(F_\pi^2)$ terms dominate there) and at $s = 0$. The conclusion is then that for the extended amplitudes, there are no real poles in the second Riemann sheet below threshold, or an even number of them. We have checked that there are no such real poles at $T = 0$. It is unclear whether the real second sheet pole found in [Hid03, Hid04] (for the σ self-energy) is also spurious, in the sense discussed here.

Finally, we have checked that the $\rho(770)$ and $f_0(600)$ poles remain at the same place at $T = 0$ with the second Riemann sheet extensions of the extended amplitudes, as expected from our previous arguments. We also note that the above extended amplitudes can also be obtained by using dispersion relations [GN08], as it was also done in early derivations of the IAM [Dob93, Dob97], which provides a more formal justification of the results shown here.

$T \neq 0$ corrections

Once we have extended the $T = 0$ amplitude to ensure the correct behavior below threshold, we obtain the extended $T \neq 0$ amplitudes by including the thermal corrections in $t^{(4)}(s, T)$. Therefore, the values of s_4 and $\tilde{s}$ become temperature dependent. With this extended amplitude, we do not find any spurious pole in the first Riemann sheet, as it happened for $T = 0$, up to temperatures close to the phase transition, nor any additional pole in the second sheet apart from the standard $f_0(600)$ pole. The results are shown in Figure 2.3 with the extended amplitude $t^{\mathrm{IAM},c}(s, T)$. We remark that this is consistent with the fact that the $f_0(600)$ pole shown in Figure 2.1 remains far from the real axis near the phase transition. Our result in this respect is different from that in [Hid03, Hid04], where an additional pole in the second sheet is found for all temperatures, although we agree with [Hid03] in that finite-T threshold effect are not seen. We also agree with [Pat02], where the additional pole does not appear for low and moderate T.

An important remark is that temperature effects make $t^{(4)}(s, T)$ grow with respect to $t^{(2)}(s)$ so that some of our previous $T = 0$ conclusions could change. For instance, regarding the number of poles, the denominator of (2.11) or (2.13) could become now negative at threshold, so that we would have an odd number of real poles in the second Riemann sheet and also in the first one, which would correspond to $\pi\pi$ bound states.

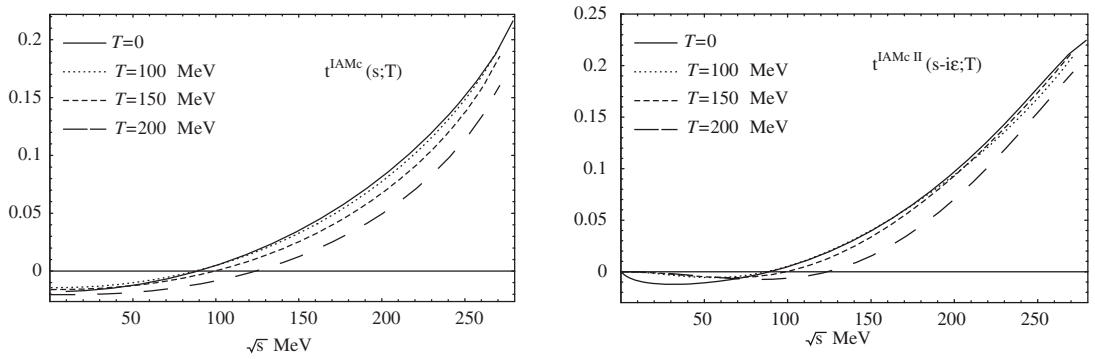

Figure 2.3: Extended unitarized amplitude at finite temperature (channel $IJ = 00$), in the first and second Riemann sheets. No real pole is observed for temperatures up to $T \simeq 200$ MeV.

Although this is not the case at finite temperature, we will see in Section 2.2 that it is possible that other chirally restoring effects, such as nuclear density, may cause the appearance of new poles in both sheets, as those obtained for instance in [Pat02] and consistently with threshold enhancement nuclear effects.

2.1.2 The thermal ρ meson: broadening versus mass scaling in $\pi\pi$ scattering and dilepton probes

The ρ pole obtained in our IAM thermal approach undergoes a significant broadening at finite temperature. The main source of thermal broadening is the Bose-Einstein increase of phase space given in (2.7). However, it is not the only one. In fact, using the Breit-Wigner ($\Gamma_{\rm p} \ll M_{\rm p}$) parametrization for the ρ exchange in $\pi\pi \to \rho \to \pi\pi$, one gets [Dob02]:

$$\frac{\Gamma_T}{\Gamma_0} = [1 + 2n_{\rm B}(M_T/2)]\ \frac{g_T^2 M_T}{g_0^2 M_0}\ , \tag{2.18}$$

where g is the effective $\rho\pi\pi$ vertex.

In Figure 2.4 (left) we show in detail the dependence of the mass, width and effective vertex and is clearly seen that the width increases roughly as the phase space up to $T \simeq 100$ MeV and then further broadening arises due to the increasing effective $\rho\pi\pi$ vertex. The broadening we have obtained is also present in the electromagnetic pion form factor [GN05], which enters directly into the dilepton yield (for back to back dileptons in our case) arising from $\pi^+\pi^- \to l^+l^-$. Our result is therefore compatible with the broadening scenario observed clearly in NA60 [Arn06a] (see the discussion in the introduction). The mass of the pole barely changes with temperature in our approach. This seems to be in contradiction with the dropping-mass scenario obtained in scaling models, which predict that the mass should scale roughly with the quark condensate $M_T/M_0 \simeq \langle\bar{q}q\rangle_T/\langle\bar{q}q\rangle_0$ [Bro91, Bro05b]. However, it is worth mentioning that more recent analyses based on the same scaling hypothesis [Har06, Bro05a, Bro05b] suggest that the mass dropping might be really effective only very close to the transition temperature, which in practice would mean that those predictions are not strictly incompatible with the dilepton data.

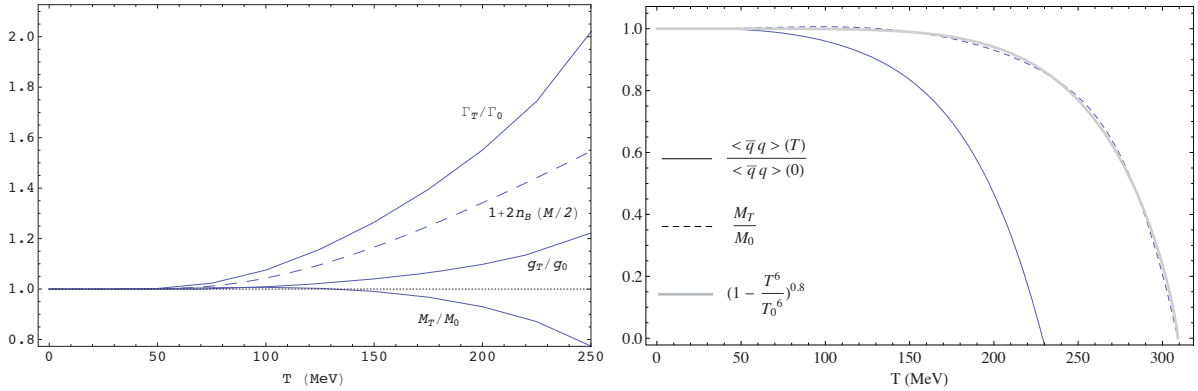

Figure 2.4: Thermal width and mass of the ρ as extracted from its IAM pole. In the left plot we also show the T-dependence of the effective $\rho\pi\pi$ vertex. In the right plot we compare the mass with the quark condensate. The mass vanishes at $T_0 \simeq 310$ MeV.

In order to clarify our results on this matter, we have plotted in Figure 2.4 (right) the pole mass and the quark condensate calculated from a virial expansion [Dob99] using the $\mathcal{O}(p^4)$ pion scattering amplitudes, which gives a critical temperature $T_c \simeq 230$ MeV. The results are extrapolated up to the temperature T_0 where the mass vanishes, although our ChPT-based approach is not meant to be valid there. We see that the mass drops rather abruptly, with a T^6 power, while, as said before, it remains almost constant for T below the chiral transition. We do not see a scaling pattern when compared to the condensate and, besides, $T_0 \simeq 310$ MeV lies far from the critical value where the condensate vanishes. On the other hand, in BR-like scaling models, the effective vertex decreases [Har06] and, as commented before, there is no significant broadening. In conclusion, although we obtain a dropping mass qualitatively compatible with BR-like models, our dominant broadening effect, the increase of the effective vertex and the departure from the condensate are in conflict (at finite temperature) with that scenario.

2.1.3 The thermal $f_0(600)/\sigma$ meson: threshold behavior and $\bar{q}q$ nature

As mentioned in the introduction, the interest in the σ pole concerns mainly its role as a precursor of the phase transition. The temperature dependence we obtain in Figure 2.1 shows that mass decreasing is a prominent feature in this channel, thus signaling chiral restoration. In fact, this is the dominant effect here over phase space increase for $T \simeq 100$ MeV and beyond. However, and this is crucial as far as observable effects are concerned, the pole remains broad even when its real part has reached the two-pion threshold.

Let us now provide a qualitative description of the above results. Consider the prop-

agator and spectral function of the resonance under consideration at rest:

$$D(s) = \frac{1}{s - M^2(s) + iM(s)\Gamma(s)} \ , \tag{2.19}$$

$$\rho(s) = -2\,\mathrm{Im}\,D = \frac{2M(s)\Gamma(s)}{\left[s - M^2(s)\right]^2 + \left[M(s)\Gamma(s)\right]^2} \ . \tag{2.20}$$

Recall that (2.20) reduces to $\rho = 2\pi\delta(s - M^2)$ when $\Gamma \to 0^+$, as it corresponds to a free particle of mass M and positive energy. Here we are denoting by $M^2(s)$ and $-M(s)\Gamma(s)$ the real and imaginary parts of the resonance self-energy respectively, with both M and Γ real functions of s in the general case. In the complex s plane, the pole of the propagator is the solution of $s_{\rm pole} = M^2(s_{\rm pole}) - \mathrm{i}M(s_{\rm pole})\Gamma(s_{\rm pole})$. Thus, with our convention for the poles, we have:

$$M^2(s_{\rm pole}) = M_{\rm p}^2 - \frac{\Gamma_{\rm p}^2}{4} \ , \quad \Gamma^2(s_{\rm pole}) = \frac{M_{\rm p}^2\Gamma_{\rm p}^2}{M_{\rm p}^2 - \Gamma_{\rm p}^2/4} \ . \tag{2.21}$$

Consider now the contribution to the $\pi\pi$ scattering amplitude of the exchange of a resonance "R" in s-channel with propagator (2.19) and the same quantum numbers as the corresponding IJ channel:

$$t^{\rm ex}(s) = \frac{-M(s)\alpha(s)}{s - M^2(s) + \mathrm{i}M(s)\Gamma(s)} \ , \tag{2.22}$$

where $M\alpha$ is the effective $\pi\pi R$ vertex squared. The parametrization (2.22) of the partial waves can be made unitary by demanding (2.1) in (2.22), which gives $\Gamma(s) = \sigma_0(s)\alpha(s)$ for $s \in \mathbb{R}$ and $s > 4M_\pi^2$. This parametrization is therefore compatible with chiral symmetry and unitarity, although a correct description of the 00 channel in the real axis would also need the addition of background contributions [Ams04], which does not change our qualitative arguments here. As far as we do not make any claim about the relative size of Γ and M nor about their behavior with s, the parametrization (2.22) can be viewed as a generalized Breit-Wigner form on the real axis above threshold.

It is instructive at this point to remind the narrow resonance limit behavior. If $\Gamma_{\rm p} \ll M_{\rm p}$, the pole is close to the real axis, so that the amplitude on the real axis is peaked around $s = M^2 \simeq M_{\rm p}^2$ and the width $\Gamma_{\rm p} \simeq \Gamma(M^2) = \alpha(M^2)\sigma_0(M^2)\theta(M^2 - 4M_\pi^2)$. If $M \to 2M_\pi$, driven for instance by chiral restoration in the 00 channel, the spectral function (2.20) and $\mathrm{Im}\,t$ are then enhanced for s near threshold as:

$$\rho(s) \sim \frac{\theta\left(s - 4M_\pi^2\right)}{\alpha\sqrt{s - 4M_\pi^2}} \ , \quad \mathrm{Im}\,t(s) \sim \frac{2M_\pi\theta\left(s - 4M_\pi^2\right)}{\sqrt{s - 4M_\pi^2}} \ . \tag{2.23}$$

This is the typical threshold enhancement produced by phase space squeezing [Chi98b, Hat99] which consequently implies an enhancement in the $\pi\pi$ cross section, as explained before. On the other hand, if medium effects do not change M and α much, as it happens for the ρ, the only temperature modification is the replacement of the phase space $\sigma_0 \mapsto \sigma_T$, which leads to $\Gamma_T/\Gamma_0 = \sigma_T/\sigma_0$, as announced above.

Let us now show how the previous arguments change when the resonant state is not narrow, i.e, when the pole position values $\Gamma_{\rm p}$ and $M_{\rm p}$ are of the same order. For that purpose, we will consider, as a working example, a BW-like form (2.22) for the amplitude.

First, in the broad resonance case, the dependence of the functions M, α, Γ with s may be important. For instance, if M is roughly constant and large compared to Γ, a formal s-expansion of (2.22) gives $t \sim \alpha/M$. Comparing this to the lowest ChPT order $t^{(2)}$ in (2.3) (required by chiral symmetry) would give $\alpha \sim AM(s-s_2)$ near threshold. If $s_2 \neq 4M_\pi^2$ as in the 00 channel, that behavior for α is compatible with the enhancement as $M \to 2M_\pi$, since near threshold the denominator of (2.22) is dominated by its imaginary part $\Gamma \sim \sigma_0$ as compared with the real part $(s - M^2) \sim \sigma_0^2$. However, this need not be the case if M as given by (2.21) is not large compared to $2M_\pi$ (for the $f_0(600)$, $M \sim 373.3$ MeV already at $T = 0$ and it gets further reduced at finite T). In that case, $t(s)$ in (2.22) near threshold can be made compatible with $t^{(2)}$ by taking $\alpha \sim -A(s-s_2)(s-M^2)/M$, so that $t(s) \sim (-M\alpha)/(s-M^2) \sim A(s-s_2)$ near threshold, even if $M \to 2M_\pi$ at a certain temperature, since now $\Gamma \sim \sigma_0^3$ so that the σ_0^2 in the real part of the denominator dominates. The result is now that $t(s)$ near threshold is roughly independent of M and therefore of T, with no threshold enhancement. This is consistent with what we see in Figure 2.8 (left), which means that the leading order ChPT expression (T-independent) basically dominates at all temperatures near threshold.

Second, the phase space vanishing of the width near threshold for narrow resonances relies heavily on the fact that the spectral function is peaked around $s \sim M^2$ or, in other words, that the pole is reasonably close to the real axis. However, for the $f_0(600)$, the spectral function is broadly distributed so that the phase space $\sigma_T(s)$ is not directly evaluated at $s = M^2$. An explicit way to see this is to consider the decay rate of the $\mathrm{R} \to \pi\pi$ process. In the narrow resonance limit, R can be considered a particle with four-momentum $P^2 = M_\mathrm{R}^2$ so that the differential decay rate in the rest frame is given by:

$$\mathrm{d}\Gamma_\mathrm{D} = \frac{1}{2}\frac{1}{2M_\mathrm{R}}|\langle \mathrm{R}|T|\pi\pi\rangle|^2 \, \mathrm{d}\Phi_{12} \, , \tag{2.24}$$

where

$$\mathrm{d}\Phi_{12} = \prod_{i=1,2} \frac{\mathrm{d}^3\boldsymbol{p}_i}{(2\pi)^3 2E_i} \, (2\pi)^4\delta^{(4)}(P - p_1 - p_2) \, , \tag{2.25}$$

is the two-particle differential phase space, $P = (M_\mathrm{R}, \mathbf{0})$, $E_i^2 = |\boldsymbol{p}_i|^2 + M_\pi^2$ and therefore $s = (p_1+p_2)^2 = P^2 = M_\mathrm{R}^2$. Replacing the $\mathrm{R} \to \pi\pi$ T-matrix element in (2.24) by $M\alpha$, which is assumed to depend only on the energy of the R state, and integrating the phase space $\int \mathrm{d}\Phi_{12} = \sigma_0(s)\theta(s-4M_\pi^2)/(8\pi)$ gives for the decay rate $\Gamma_\mathrm{D} = \sigma_0(M^2)\alpha(M^2)\theta(s-4M_\pi^2)/(32\pi) = \Gamma(M^2)/(32\pi) \simeq \Gamma_\mathrm{p}/(32\pi)$, yielding the standard relation between the width and the decay rate, which is also suppressed by phase space when the mass of the state approaches threshold.

If the spectral function of the resonance is not well approximated by a δ function, the differential decay width (2.24) is generalized by replacing $1/2M_\mathrm{R} \mapsto \int(\mathrm{d}\omega/2\pi)\ \rho(\omega)\theta(\omega)$ so that instead of Γ_D one has the number of decays per unit volume and per unit of four-momenta [Wel93], integrated over the energy ω distributed according to the spectral function of the resonant state. Accordingly, with the spectral function (2.20) and replacing M, Γ, σ_0, α by their T-dependent counterparts, the quantity

$$F_T = \int_{4M_\pi^2}^{\infty} \frac{\mathrm{d}s}{2\pi} \, \frac{M_T(s)\alpha_T(s)\sigma_T(s)}{2\sqrt{s}} \, \frac{2M_T(s)\Gamma_T(s)}{\left[s - M_T^2(s)\right]^2 + \left[M_T(s)\Gamma_T(s)\right]^2} \tag{2.26}$$

should behave qualitatively as a generalized decay rate and therefore we expect it to follow a similar pattern as the imaginary part of the pole position $\Gamma_{\rm p}(T)$. As a consistency check, in the narrow resonance limit $F_T = \alpha_T \sigma_T \theta(M_T^2 - 4M_\pi^2)$. In the general case though, when $M_T \to 2M_\pi$, there will be a non-vanishing contribution to the integral due to the broad spectral function.

Obviously, we cannot draw any conclusion about the evolution of F_T without specifying the T and s dependence of α_T, M_T, Γ_T. In order to check that this is a consistent description, let us choose for simplicity s-independent M_T and Γ_T, related to the pole position values by (2.21), with the values of $\Gamma_{\rm p}$ and $M_{\rm p}$ obtained in our full IAM calculation. We also take $\alpha_T = \Gamma_T$, which is consistent with the unitarity requirement away from threshold (the spectral function in the integrand is suppressed for s near threshold in the broad case, according to our previous arguments). We emphasize that this is a rough approximation, since the actual profile of the t_{00} partial wave does not resemble a BW-like form, even with large Γ [Ams04]. Nevertheless, it provides us with a simple model to explain a thermal resonance behavior similar to the one we obtain. With that simplification, F_T rises with T until $T \sim 100$ MeV ($F_{100}/F_0 \simeq 1.1$) due to phase space increasing in the numerator of (2.26) and then starts decreasing as the real part of the pole approaches threshold, reaching a value $F_{200}/F_0 \simeq 0.7$. Comparing with the evolution of $\Gamma_{\rm p}$ in Figure 2.1, where $\Gamma_{\rm p}(100\ {\rm MeV})/\Gamma_{\rm p}(0) \simeq 1.2$ and $\Gamma_{\rm p}(200\ {\rm MeV})/\Gamma_{\rm p}(0) \simeq 0.8$, we see that a broad resonant thermal state with a finite generalized decay rate near the two-pion threshold behaves in a qualitatively similar way as our thermal $f_0(600)$ state.

From the above discussion we conclude that for a broad state like the $f_0(600)$ at finite temperature there is always a balance between thermal phase space increasing, which has nothing to do with chiral symmetry restoration, and chiral restoring mass and width decreasing. Depending on how broad the resonance is when chiral restoring effects start being important, the pole may move towards the real axis more or less rapidly. There is no way to know a priori whether it can be close enough to be considered a narrow resonance before the chiral transition, so that observable effects such as threshold enhancement may take place. In our approach, this does not happen at finite T (the situation may change at finite density as we will see in Section 2.2) i.e., the $f_0(600)$ is still broad at the transition, in agreement with [Pat02] but not with previous approaches [Hat85, Chi98b]. We also agree with [Hid03, Hid04] as far as the complex broad $I = J = 0$ pole is concerned.

The role of the σ pole as a precursor of the transition is strongly linked to its $\bar{q}q$ nature, as discussed in the introduction. In Figure 2.5 we compare the mass of the pole with the root of the quark condensate, similarly as we did with the ρ in the previous section. Recall that, in a $O(4)$ model, $M_\sigma \sim \langle\sigma\rangle \sim F_\pi$ and, on the other hand, $F_\pi^2 = -m_{\rm q}\langle\bar{q}q\rangle/M_\pi^2$ from the Gell-Mann-Oakes Renner (GOR) relation [GM68]. We also plot the results near the chiral limit[2], where the condensate vanishes at a lower temperature and explicit chiral

[2]Here, a technical remark is in order. As commented above, we are expressing our amplitudes in terms of the scale-independent low-energy constants $\bar{l}_i$, with the same convention as in [Gas84]. Namely, they are related to the one-loop renormalized constants as $l_i^{\rm r}(\mu) = \gamma_i \left[\bar{l}_i + \ln\left(M_0^2/\mu^2\right)\right]/(32\pi^2)$ where γ_i are numerical factors and μ is the renormalization scale. Since the $l_i^{\rm r}(\mu)$ are mass-independent, when we change the pion mass from m_1 to m_2, we should also change $\bar{l}_i \mapsto \bar{l}_i + \ln\left(m_1^2/m_2^2\right)$ in the amplitudes when calculating the poles. The same observation applies to the numerical value of F_π we are using, which is also mass-dependent since to one loop, $F_\pi = F_0\left[1 + \bar{l}_4 M_0^2/(16\pi^2 F_0^2)\right]$ [Gas84], where $F_0 \simeq 87.6$ MeV is the pion decay constant in the chiral limit.

symmetry breaking effects are minimized. In any case, we do not see a scaling pattern, as expected from our result of a broad thermal state. Near the chiral limit, the pole mass does not even go to threshold near the critical temperature, since the width is notably increased due to the more available phase space. From our analysis of thermal effects one can also conclude that the non-$\bar{q}q$ component of the $f_0(600)$ must be of crucial importance. As discussed in the introduction, the same conclusion has been reached in vacuum studies [Alf00, Pel04]. The novelty here is the use of thermal arguments. We will see in Section 2.2 that finite density effects driving the resonance poles to the real axis below threshold allow also to extract interesting conclusions about their $\bar{q}q$ nature.

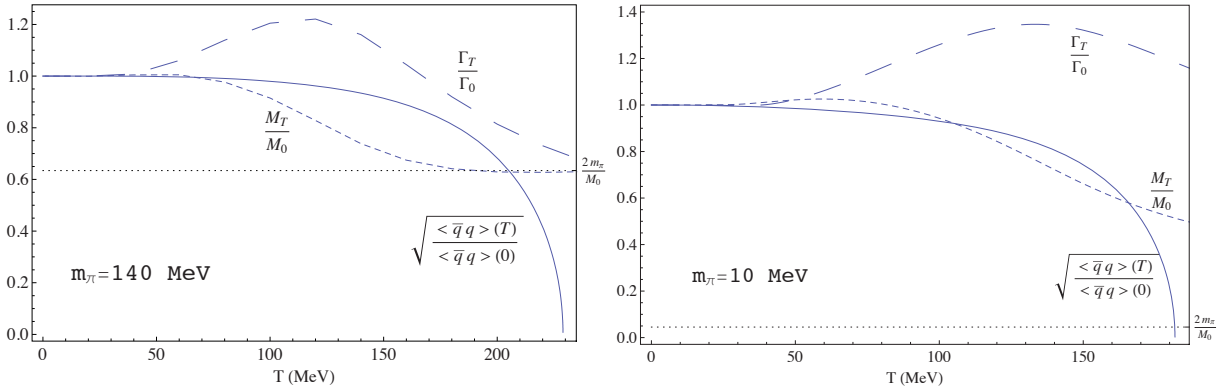

Figure 2.5: Comparison between the $\sigma/f_0(600)$ mass (extracted from the IAM pole) at finite temperature and the root of the condensate, for the physical pion mass and near the chiral limit.

2.2 Finite density chiral restoring effects at $T = 0$ through F_π scaling in the IAM

The simplest way to incorporate nuclear density effects at $T = 0$ in the unitarized chiral approach is to encode them only in the variation of the pion decay constant, to linear order in density, by means of the GOR relation at finite density [Tho95, Mei02][3]:

$$\frac{F_\pi^2(\rho)}{F_\pi^2(0)} \simeq \frac{\langle\bar{q}q\rangle(\rho)}{\langle\bar{q}q\rangle(0)} \simeq \left(1 - \frac{\sigma_{\pi N}}{M_\pi^2 F_\pi^2(0)}\rho\right) \simeq \left(1 - 0.35\frac{\rho}{\rho_0}\right) \ , \tag{2.27}$$

where ρ is the nuclear density, $\sigma_{\pi N} \simeq 45$ MeV is the pion-nucleon sigma term and $\rho_0 \simeq 0.17$ fm^{-3} is the normal or saturation nuclear matter density. Therefore, by varying F_π in our IAM approach, we mimic chiral restoring nuclear effects. This approach clearly ignores standard many-body corrections, like the coupling of pions to particle-hole (ph) and Delta-hole (Δh) excitations, considered for instance in [Rap97, Cab02, Chi98a, Cab05]. This approximation is meant to be more adequate for the σ than for the ρ since, as we have

[3]Strictly, it is only the timelike component of the pion decay constant which enters into the GOR relation at finite density [Tho95, Pis96], but for our purposes it is valid to consider a modification in the complete F_π.

seen at finite temperature, chiral restoration tends to dominate the σ pole behavior under medium effects. In fact, by changing only F_π, no medium broadening is produced, which is probably unrealistic for the ρ case, as emphasized in many-body works [Her92, Pet98, Cab02]. This must be borne in mind when interpreting our results for the ρ in terms of BR-scaling. In any case, in Section 2.3 we will consider a different unitarization scheme, which allows to introduce all the above mentioned nuclear many-body effects and compare with our simple "F_π scaling" considered here.

The results obtained by varying F_π in the IAM amplitudes are displayed in Figs. 2.6 and 2.7 for the pole trajectories in the complex plane and mass scaling, respectively, in the 00− and 11−channels. In Fig. 2.8 (right) we also show the effect on the scattering amplitude in the σ channel. As F_π decreases the σ pole becomes narrow enough so that chiral mass reduction brings it to the real axis, which produces threshold enhancement in the amplitude although at densities well above ρ_0. Regarding the mass dropping, it takes place now along with the condensate (see Fig. 2.7). In Fig. 2.9 we show $|t_{00}|^2$ considering simultaneously temperature and finite density according to Eq. (2.27) for F_π. We observe that the net effect of introducing temperature is, on one hand, an effective broadening in the scattering amplitudes, as expected by the phase space arguments commented before. On the other hand, for a given value of F_π (small enough), the temperature amplifies threshold enhancement, as the amplitude is notably softened at higher energies, by thermal broadening, what makes the low energy region relatively more important. Still, one has to keep in mind that (a) this effect is driven by the proximity of the σ pole to the real axis when decreasing F_π, (b) thermal effects alone do not generate threshold enhancement in the amplitude as discussed above, and (c) the $\pi\pi$ phase space is not open below $2M_\pi$ even at finite temperature. In Sect. 2.3 we will compare these results for the 00-channel with an implementation of nuclear density effects in a dynamical many-body calculation.

As for the ρ channel, the BR-like scaling pattern is now closely followed. In fact, our ρ-meson pole moves gradually from the $\langle\bar{q}q\rangle^{1/2}$ curve to the $\langle\bar{q}q\rangle$ one, as obtained in [Bro04]. However, one must be careful about this conclusion, since we are disregarding medium related broadening which might change the scaling picture observed here. Strictly speaking, our results indicate that if the relevant density effects amount *only* to a scaling of F_π, then one gets scaling in the pole mass, which is quite consistent with the BR idea.

There is an additional interesting feature of our results: when density is increased further, $\pi\pi$ bound states (first sheet poles) appear just below threshold in both channels. As we shall see in Sect. 2.2.2, this result allows for an interpretation in terms of a "molecular" classification of resonances, which is completely different in both channels. In fact, we note that in the σ channel the bound state is preceded by a doubling of poles in the second sheet. This will be further discussed in Sect. 2.2.2. The appearance of pole doubling and bound states has been also analyzed in other works [Pat03, Hid04, Sch88].

2.2.1 Comparison with nuclear matter experiments

As discussed above, apart from Heavy Ion Collisions, there are several dedicated experiments on production reactions in nuclei where our analysis can be useful, namely, those related to threshold enhancement in $\pi\pi$ production and the modification of dilepton spectra from ρ decays. The threshold enhancement observed in [Bon00, Sta00, Mes02] in the

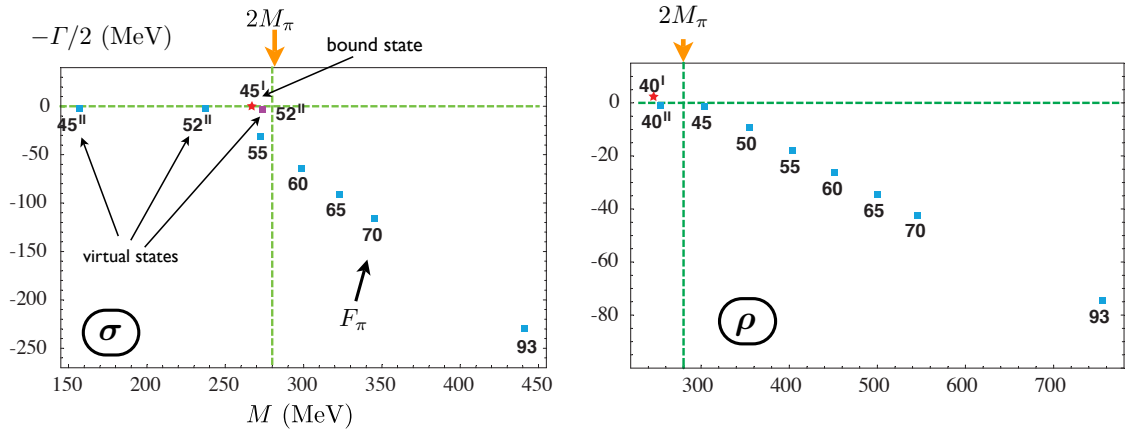

Figure 2.6: IAM poles with varying F_π. The numbers attached to the pole positions indicate $F_\pi(\rho)$ in MeV according to (2.27). The first-sheet and second-sheet poles are indicated.

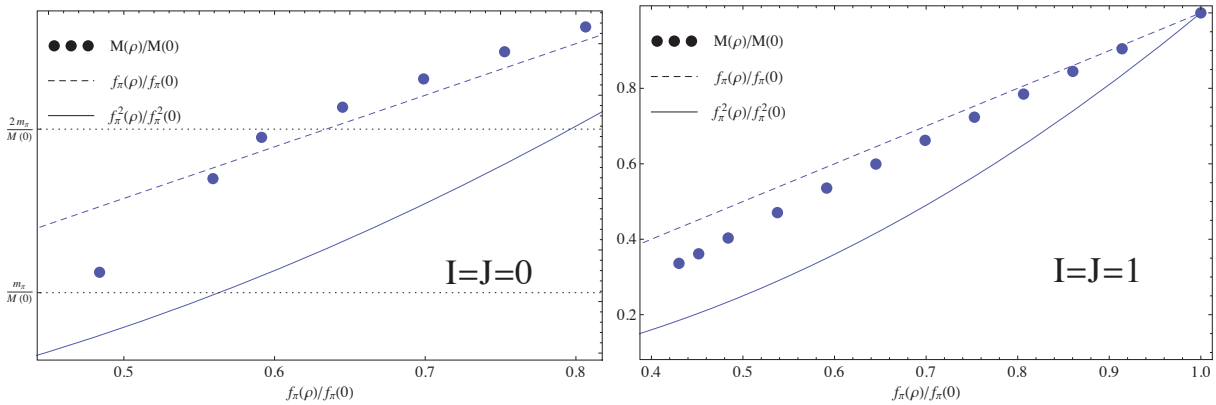

Figure 2.7: Scaling of the mass, compared with $F_\pi^2(\rho)/F_\pi^2(0) \sim \langle\bar{q}q\rangle(\rho)/\langle\bar{q}q\rangle(0)$ and with $F_\pi(\rho)/F_\pi(0)$. In the $I = J = 0$ case, the masses displayed correspond to the lowest masses of the second-sheet poles.

$I = J = 0$ channel is qualitatively reproduced in our "F_π scaling" approach for emulating finite nuclear density. Comparing with our finite-T analysis in the previous sections, our main conclusion is that, due to the broad nature of the σ at finite T, threshold enhancement is not visible at finite T and it can only take place if chiral restoring finite-density effects are strong enough, compared for instance with medium effects we have neglected which could also increase the σ width, preventing the pole from approaching the real axis, as in the finite-T case, and erasing the threshold effect. This does not seem to be the case when many-body interactions are properly accounted for [Chi98a, Roc02], which gives support to this simple approximation. In fact, the observed effect is in reasonable quantitative agreement with previous theoretical works [Dav00, Jid01, Pat03] and it is not very strong for densities $\rho \lesssim \rho_0$ (the range available experimentally) in line with the experimental results in [Sta00].

As for dileptons in nuclear matter, a parameter directly measurable in those experi-

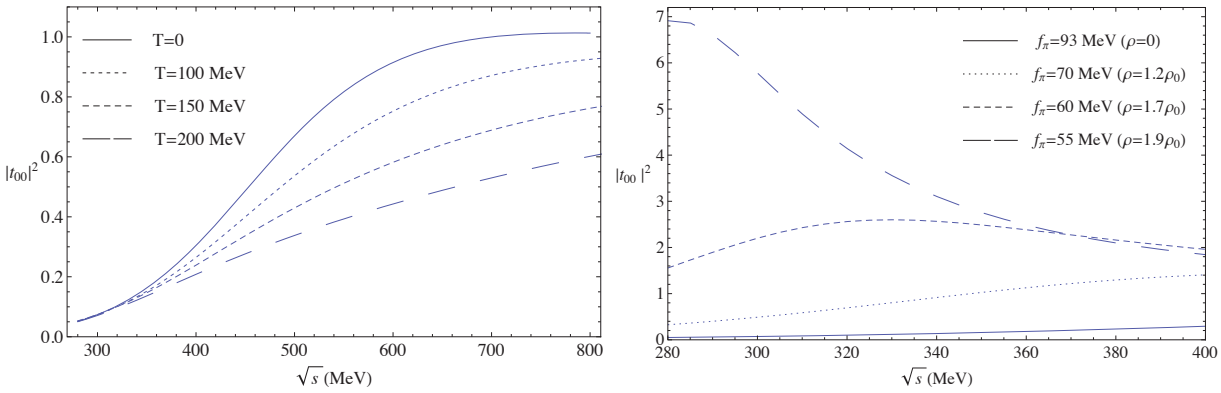

Figure 2.8: Squared modulus of the $I = J = 0$ partial wave at finite temperature (left) and at $T = 0$ and varying F_π (right) to simulate chiral restoration at finite density.

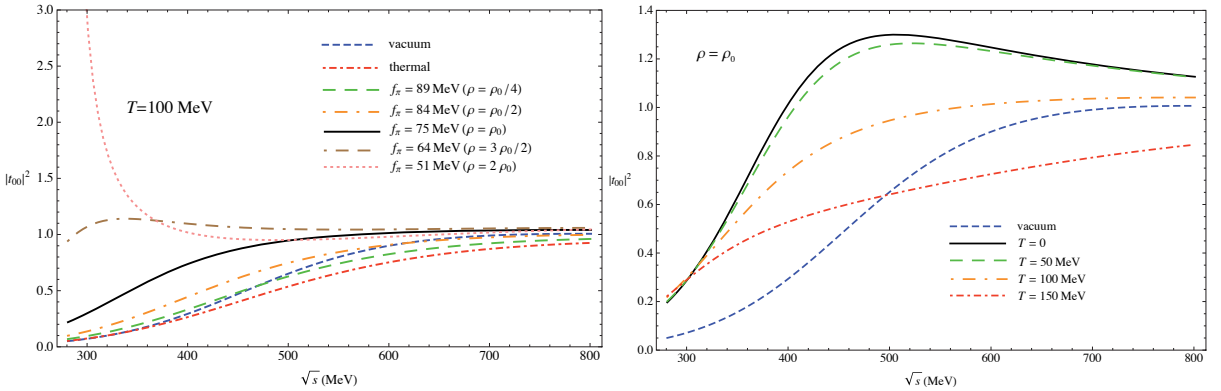

Figure 2.9: Squared modulus of the $I = J = 0$ partial wave at $T = 100$ MeV for several densities (left), and at nuclear matter density ($F_\pi = 75$ MeV) for several temperatures (right).

ments is the coefficient of the linear density term for the mass of the $\rho(770)$ meson:

$$\frac{M(\rho)}{M(0)} = 1 - \alpha \frac{\rho}{\rho_0} \ . \tag{2.28}$$

The experimental values available so far are $\alpha = 0.092 \pm 0.002$ obtained by the E325-KEK collaboration [Nar06] and $\alpha = 0.02 \pm 0.02$ measured by the JLab-CLAS experiment [Nas07]. We have performed a linear fit of our pole results in the $I = J = 1$ channel for $F_\pi = 93, 85, 80, 75$ MeV, i.e., up to $\rho \lesssim \rho_0$ to be closest to the experimental situation. Our fit gives $\alpha = 0.2$, which is closest to the result in [Nar06] than to [Nas07], although a bit above the experimental value. Our result is also in agreement with Brown-Rho scaling [Bro02] and QCD sum rules [Hat95] which predict $\alpha \simeq 0.1 - 0.2$. It is important to remark again that so far we ignore all medium broadening effects, which, unlike the case of the σ, may be crucial in this case, as emphasized in many-body treatments [Her92, Pet98, Cab02, Urb98]. In fact, in [Leu98] it was realized that QCD sum rules themselves do not provide a unique constraint for the in-medium mass and width variation, unless

additional model assumptions are made. In particular, it is shown that if one assumes that the width is not increased then automatically the mass drops. This is the scenario we have recovered in our present approach, which, as commented several times above, does not mean that this is the physically relevant case.

2.2.2 "Molecular" classification of resonances

One of the objectives of this thesis has been to analyze the $\bar{q}q$ structure of light meson resonances from a thermal and finite-density viewpoint. We have already discussed in Section 2.1.3 that our results for the thermal σ are not consistent with its pure $\bar{q}q$ nature. The situation changes qualitatively with the $T = 0$ finite-density dependence obtained in Section 2.2. We see in Figure 2.7 that the σ pole follows quite well the same pattern of a $O(4)$ σ-like $\bar{q}q$ state. One may then wonder about the implication of this for the $\bar{q}q$ nature of the in-medium σ. We want to point out here that actually one can gain very useful information about that by looking at the behavior of the poles near threshold. Our argument is supported by the classification of resonances lying near threshold given in [Mor91, Mor92] and based on the "effective range expansion"[4]. In those works it is stated that although generally it is difficult to extract properties about the "internal" nature of resonances from its decay products (scattering poles), when the pole lies near threshold, a general rule can be applied: *a "potential" or "molecular" resonance shows up as a single pole near threshold, while for a $\bar{q}q$-like state two poles near threshold appear very close to one another in different Riemann sheets.*

This classification was originally applied to states like the $f_0(980)$, which lies very close to the $\bar{\mathrm{K}}\mathrm{K}$ threshold. Our claim here is that this classification argument can equally be applied to light resonances if medium effects drive the poles to the real axis. This is exactly the situation when we include density effects only through Eq. (2.27), as it is clear from the results in Figure 2.6, although bearing in mind that the effective values of F_π for which the poles reaches the real axis are too small to trust entirely our ChPT-based approach. We see that the σ pole follows a clear molecular pattern, since the pole that remains close to threshold and eventually becomes a bound state is well separated from the second-sheet pole that lies below threshold. We interpret this as a coexistence of two states for high enough densities: a $\pi\pi$ "molecule" and a virtual state which behaves as a "chiral partner" of the pion, in the sense that it tends to become degenerate in mass with it (albeit with different quantum numbers) following the order parameter. Note that the pole we represent in Figure 2.7 is precisely this virtual state. This picture is in contrast with what we observe for the ρ channel, where two nearby poles remain below threshold, one of them moving to the first sheet and becoming a bound state. This would be a $\bar{q}q$, non-molecular scenario, according to the previously discussed classification, although the criterium is in principle only applicable to scalar resonances. Nevertheless, the $\bar{q}q$ nature of the ρ has been supported by other analyses based on large-N_c arguments [Pel04, Pel06]. We remark that a similar picture for the real axis poles has been obtained in [Pat03], where

[4]This method consists in writing the scattering amplitude T for c.m. momentum k in the opening channel as $T = [M - \mathrm{i}k]^{-1}$. Under a potential scattering regime, M can be expanded as $M = M^{(0)} + \frac{1}{2} r_{\mathrm{eff}} k^2 + \mathcal{O}(k^4)$, where $|r_{\mathrm{eff}}|$ is the range of the potential. Then, $M - \mathrm{i}k$ cannot have two distinct zeros with $|k|$ appreciable less than $|r_{\mathrm{eff}}|^{-1}$. A resonance having such a pair of associated poles is therefore not of molecular type.

the density dependence is also parametrized in F_π, and in vacuum [Han08], by increasing the quark mass in order to compare with lattice results (chiral extrapolation)[5].

2.3 Finite temperature and density in a many-body unitarized approach

In this section we extend our previous results in the $I = J = 0$ channel by incorporating finite nuclear density and temperature effects in a many-body description of pion dynamics. We follow the line of Refs. [Chi98a, Cab05] where the effective $\pi\pi$ scattering amplitude in cold nuclear matter was evaluated in a chiral unitary framework. For technical reasons which we discuss below, it is convenient to use a different unitarization scheme for the T-matrix, which however provides similar results in vacuum to those from the IAM, i.e., the light meson-meson resonances are dynamically generated in the scalar channel and many scattering observables are described in good agreement with experiment [Oll97, Oll98, Oll99b].

The idea is to solve the coupled-channel Bethe-Salpeter (BS) equation for the partial wave scattering amplitude T:

$$T = V + \overline{VGT} \ , \tag{2.29}$$

where we have used a short notation to write this integral equation: T, V, and G are matrices with indices corresponding to the different scattering channels, and the line over the product VGT represents a loop integration (see Figure 2.10).

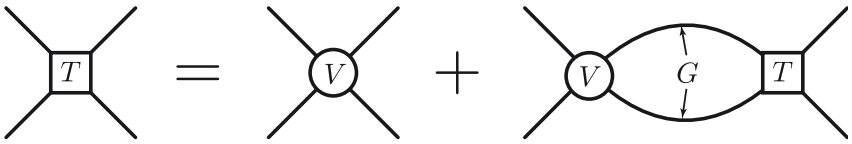

Figure 2.10: Diagrammatic representation of the Bethe-Salpeter equation.

The potential (kernel) V of the equation is provided by the lowest order tree level amplitude from the chiral lagrangian. In Eq. (2.29),

$$G_i(P) = \mathrm{i} \int \frac{\mathrm{d}^4 q}{(2\pi)^4} \, \frac{1}{(P^0 - q^0)^2 - \boldsymbol{q}^{\,2} - m_i^2 + \mathrm{i}0^+} \, \frac{1}{(q^0)^2 - \boldsymbol{q}^{\,2} - m_i^2 + \mathrm{i}0^+} \ , \tag{2.30}$$

stands for the intermediate two-particle meson-meson Green's function of channel i (G is diagonal), where $P = (P^0, \mathbf{0})$ is the total external momentum in the center of mass frame of the two pions (rest frame with respect to the nuclear medium), with $s = (P^0)^2$. In principle, both V and T enter off-shell under the momentum integration ($\overline{VGT}$ term) of the meson-meson loop. However, as it was shown in Ref. [Oll97], the (divergent) off-shell contributions of V and T in the s-wave interaction can be reabsorbed in a renormalization of the bare coupling constants and masses order by order. Therefore, both V and T can

[5]This latter method is also similar to ours in the sense that the interaction between pions is increased.

be factorized on-shell, leaving the four-momentum integration only in the two-particle meson-meson propagator, cf. Eq. (2.30). An alternative justification for solving the Bethe-Salpeter equation with on-shell amplitudes can be found in the framework of the N/D method, applied for meson-meson [Oll99a] and meson-baryon [Oll01] interactions. We are thus left with a set of linear algebraic equations with trivial solution,

$$T = [1 - VG]^{-1} V \ . \tag{2.31}$$

Since we are interested in the σ meson energy region (and particularly close to the two-pion threshold), for simplicity we shall work in a single-channel approach (the coupled $\bar{\mathrm{K}}\mathrm{K}$ channel lies far above in energy and has little effect at low energies). The conditions under which this unitarization procedure is equivalent to the IAM were discussed in [Oll98, Oll99b]. The main difference of the present approach as compared to the full IAM amplitude lies in the $\mathcal{O}(p^4)$ contribution (which here comes from the s-channel meson-meson loop and no tadpole or $\mathcal{L}_4$ tree-level terms are included) and the absence of t- and u-channel diagrams (or, in other words, the left-hand analytical cut is ignored). On the other hand, the renormalization procedure used here employs a cut-off as a regulator, unlike in IAM case, because it is not possible to use dimensional regularization due to the infinite number of diagrams we have to resummate. Still, the present scheme dynamically generates the σ pole with similar properties as in the IAM and the experimental phase shifts in $\pi\pi$ scattering are well reproduced [Oll97, Oll98, Oll99b]. Also note that Eqs. (2.1) and (2.7) are equally satisfied in this approach. We show in Fig. 2.11 a diagrammatic representation of the series of s-channel diagrams which is summed in the BS equation.

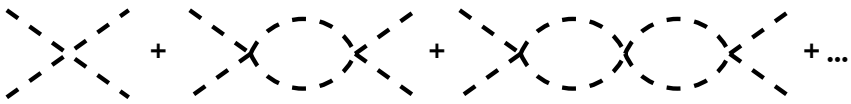

Figure 2.11: Diagrammatic representation of the Bethe-Salpeter equation for $\pi\pi$ scattering.

The calculation of the thermal amplitude proceeds by first reanalyzing the on-shell factorization of V and T in the BS equation. At finite temperature, the divergent contribution from off-shell terms in the one-loop scattering amplitude has the same structure as in vacuum, but a finite, temperature-dependent part survives which cannot be cast as a (vacuum) renormalization of F_π or M_π. This contribution can be accounted for as a temperature correction to the $\mathcal{O}(p^2)$ kernel that, once calculated in the ITF, has the form:

$$\delta V_{\mathrm{off}}^T(s) = \frac{4}{3F_\pi^2}\left(V_{\mathrm{on}}(s) + \frac{s}{3F_\pi^2}\right)\ I_0^T \ , \tag{2.32}$$

where $I_0^T \equiv (2\pi^2)^{-1}\int_0^\infty \mathrm{d}q\ \boldsymbol{q}^2\ n_{\mathrm{B}}(\omega_q)/\omega_q$ comes from the finite-temperature part of the one-loop integral J_0 (see Appendix C), $V_{\mathrm{on}}(s) = -(s - M_\pi^2/2)/F_\pi^2$ is the tree level amplitude, and $\omega_q^2 = \boldsymbol{q}^{\,2} + M_\pi^2$ (we follow in this section the normalization of partial waves given in [Oll97, Oll99b], which differs from the one in Section 2.1 by a factor 16π). In order to keep as close as possible to the physics described by the IAM amplitude, we

have also considered the finite-T contribution from tadpole terms, which becomes relevant as the σ meson pole is driven towards the two-pion threshold and its behavior is no longer dominated by the two-pion phase space [GN02b]. The corresponding diagrams are depicted in Fig. 2.12 and, to the lowest order in the chiral counting, they emerge from $\mathcal{O}(p^2)$ interaction terms with up to six meson fields. The finite-T correction to the tree level amplitude to account for these terms reads

$$\delta V_{\rm tad}^T(s) = \left[\frac{20}{9}\, s\, I_0^T - \frac{25}{6}\, I_2^T\right] / F_\pi^4 + V_{\rm on}(s) \frac{4}{3F_\pi^2}\, I_0^T \ , \tag{2.33}$$

where $I_2^T \equiv M_\pi^2\, I_0^T$ comes from the finite-temperature part of the one-loop integral J_2 in Appendix C.

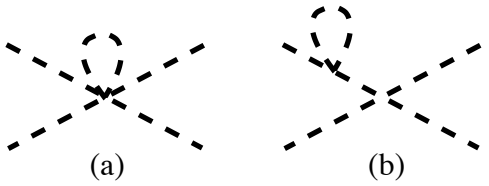

Figure 2.12: Pion tadpole diagrams in $\pi\pi$ scattering.

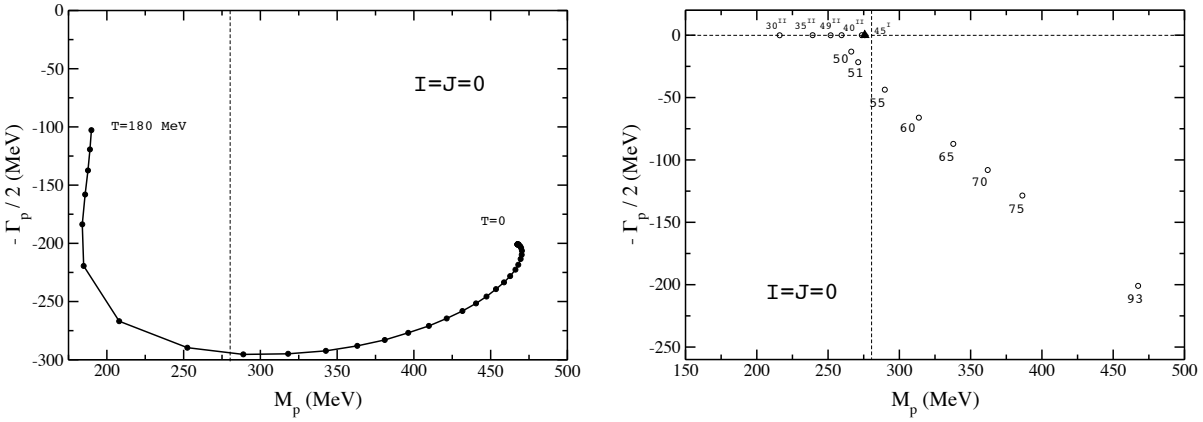

Figure 2.13: Left: Temperature dependence of the σ complex pole in the BS equation approach including thermal corrections to the $\mathcal{O}(p^2)$ kernel (the temperature interval between each point is 5 MeV). Right: Pole trajectory from F_π scaling. The numbers attached to each point indicate the value of F_π in MeV.

In Fig. 2.13 (left) we show the σ pole trajectory (see comments below on the analytical continuation to the SRS) for the thermal calculation in the BS equation approach with the $\mathcal{O}(p^2)$ kernel including the thermal corrections discussed above. As we can see, the evolution of the pole follows quite a similar pattern as in the IAM, although the position of the σ mass reaches values further below the two-pion threshold for high temperatures. As in the IAM, the σ pole stays far from the real axis, indicating a substantial width for

temperatures up to about 200 MeV, despite the low value of $M_{\rm p}$. The stronger attraction felt by the σ meson in this approach as compared to the IAM seems to reflect that missing thermal contributions from t- and u-channel dynamics are relevant in this energy region and provide a repulsive contribution. Nevertheless, we obtain a qualitatively similar physical behavior of the σ pole in both the BS equation approach and the IAM. Thus, we shall use the former as a starting point to incorporate finite density effects. As a further test, we have also calculated the σ pole trajectory in the effective "F_π scaling" scenario, which we depict in the right hand panel of Fig. 2.13. We obtain a similar result as in the IAM regarding the σ pole collapsing onto the real energy axis for F_π values below approximately 50 MeV. We also find a pole-doubling effect which follows the "molecular" pattern discussed in Sect. 2.2. Differences are observed at the numerical level as the close-to-threshold behavior of the σ pole is dictated by the relative weight of the $\mathcal{O}(p^2)$ and $\mathcal{O}(p^4)$ amplitudes, which are different for the two approaches discussed in this work. Finally, we have also studied threshold enhancement in the $\pi\pi$ amplitude for decreasing values of F_π, which we omit here as our results resemble very much those depicted in Figs. 2.8 and 2.9 for the IAM calculation.

The introduction of nuclear density effects on top of the temperature follows by a renormalization of the pion propagator in the hot and dense medium. In cold nuclear matter, the pion spectral function exhibits a mixture of the pion quasi-particle mode and p-wave particle-hole (ph), Delta-hole (Δh) excitations [Ose82]. The lowest order, irreducible p-wave pion self-energy due to ph and Δh excitations reads

$$\Pi^p_{\pi{\rm NN}^{-1}+\pi\Delta{\rm N}^{-1}}(q_0,\boldsymbol{q};T)=\left(\frac{F_{\rm N}}{M_\pi}\right)^2\boldsymbol{q}^2\left[U_{{\rm NN}^{-1}}(q_0,\boldsymbol{q};T)+U_{\Delta{\rm N}^{-1}}(q_0,\boldsymbol{q};T)\right]\ , \tag{2.34}$$

where U stands for the finite temperature Lindhard function, which we evaluate in Imaginary Time Formalism [Urb00, Tol08], and the density dependence enters U through the baryon chemical potential. We use phenomenological πNN and πNΔ coupling constants determined from analysis of pion nucleon and pion nucleus reactions, $F_{\rm N}/M_\pi = 0.007244$ MeV^{-1} and $F_\Delta/F_{\rm N}=2.13$. The strength of the considered collective modes is modified by repulsive, spin-isospin NN and NΔ short range correlations [Ose82], which we include in a phenomenological way with a single Landau-Migdal interaction parameter, $g'=0.7$. The RPA-summed (retarded) pion self-energy then reads:

$$\Pi^p_\pi(q_0,\boldsymbol{q};T)=\frac{\left(\frac{F_{\rm N}}{M_\pi}\right)^2 F_\pi(\boldsymbol{q}^2)\,\boldsymbol{q}^2\,\left[U_{{\rm NN}^{-1}}(q_0,\boldsymbol{q};T)+U_{\Delta{\rm N}^{-1}}(q_0,\boldsymbol{q};T)\right]}{1-\left(\frac{F_{\rm N}}{M_\pi}\right)^2 g'\,\left[U_{{\rm NN}^{-1}}(q_0,\boldsymbol{q};T)+U_{\Delta{\rm N}^{-1}}(q_0,\boldsymbol{q};T)\right]}\ , \tag{2.35}$$

where we have accounted for the finite size of πNN and πNΔ vertices with the hadronic monopole form factors $F_\pi(\boldsymbol{q}^2)=\Lambda_\pi^2/(\Lambda_\pi^2-\boldsymbol{q}^2)$, with $\Lambda_\pi=1300$ MeV.

The in-medium pion propagator modifies the analytical structure of the meson-meson loop function, G. At lowest order in a density expansion (number of baryon-hole irreducible insertions) the in-medium $\pi\pi$ amplitude at one loop includes diagram (a) in

Fig. 2.14, in which one of the intermediate pions excites a ph (or Δh) bubble (and similarly with the lower pion line), on top of the vacuum $\pi\pi$ loop (Fig. 2.14, second diagram). Again one is obliged to check whether the on-shell factorization of V and T is still valid in a nuclear medium. This is actually the case for $\pi\pi$ scattering in the scalar channel as it was shown in [Chi98a]. The argument is as follows: in addition to diagram (a), chiral symmetry requires a set of meson baryon contact terms, depicted as diagrams (b-d) (which can be seen as contributions to the $\pi\mathrm{N} \to \pi\pi\mathrm{N}$ amplitude by cutting simultaneously the ph bubble and the lower pion line in diagrams (a-d)). It turns out that the contribution from the off-shell part of V in diagram (a) exactly cancels with the sum of the amplitudes from diagrams (b-d), leaving us with diagram (a) with each of the $\pi\pi$ vertices factorized on-shell. Therefore, the algebraic solution of Eq. (2.29) is no altered and one only has to replace the vacuum pion propagators in G, cf. Eq. (2.30), by the in-medium ones, $D_\pi = [(q^0)^2 - \omega_q - \Pi_\pi]^{-1}$. The argument holds at finite temperature as we have checked explicitly, in ITF, that the same cancellation of off-shell terms takes place in the thermal amplitude.

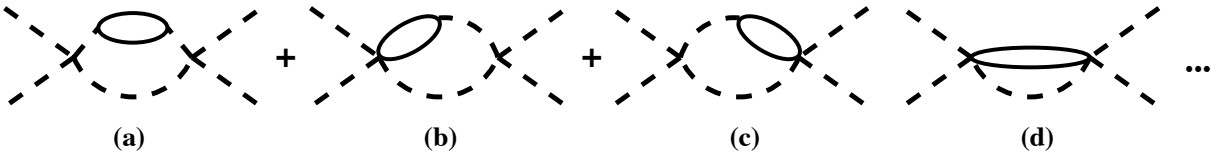

Figure 2.14: Lowest order baryon-hole insertions in the meson meson loop function including vertex corrections.

In order to re-evaluate G in the hot and dense medium we use the spectral (Lehmann) representation of the pion propagator. The final expression for G, once continued onto the real energy axis, reads

$$G(P;\rho,T) = \int_0^\infty \frac{\mathrm{d}\Omega}{2\pi} \left[\frac{1}{P^0 - \Omega + \mathrm{i}0^+} - \frac{1}{P^0 + \Omega + \mathrm{i}0^+}\right] F(\Omega) \ , \tag{2.36}$$

with

$$F(\Omega) \equiv \int \frac{\mathrm{d}^3\boldsymbol{q}}{(2\pi)^3} \int_{-\Omega}^{\Omega} \mathrm{d}u \ \pi \left[1 - n_\mathrm{B}(E_+) - n_\mathrm{B}(E_-)\right] S_\pi(E_+,\boldsymbol{q}) S_\pi(E_-,\boldsymbol{q}) \ , \tag{2.37}$$

where $S_\pi = -\pi^{-1}\,\mathrm{Im}\,D_\pi$ is the spectral function of the retarded pion propagator and $E_\pm \equiv (\Omega \pm u)/2$ (we have omitted here the contribution from diffusion poles which typically provides a small correction in the time-like region). Note that $\mathrm{Im}\,G(P^0) = -F(P^0)/2$ and thus F plays the role of a generalized in-medium two-pion phase space including both temperature and nuclear density effects. In the pure thermal case, $F(\sqrt{s}) = \sigma_T(s)\theta(s - 4M_\pi^2)/8\pi$, with σ_T the thermal phase-space in (2.7).

In Fig. 2.15 we show the phase space function, $F(P^0)$, at normal nuclear matter density ($\rho_0 \simeq 0.17$ fm^{-3}) and different temperatures in the range $T = 0 - 150$ MeV. We

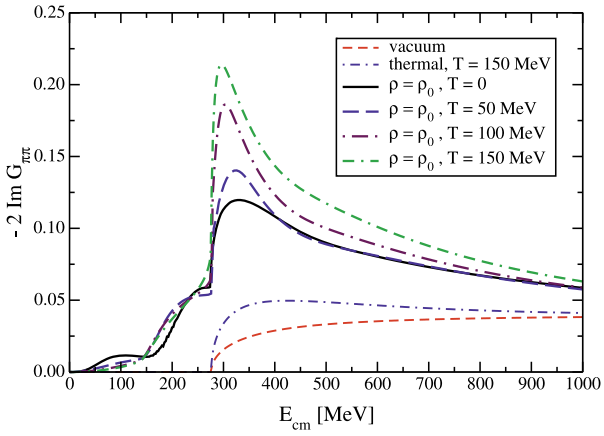

Figure 2.15: Two-pion phase-space function at finite nuclear density and temperature.

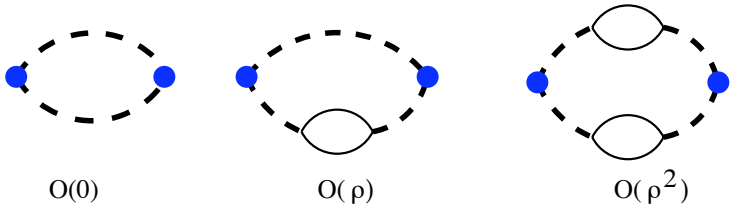

Figure 2.16: $\mathcal{O}(0, \rho, \rho^2)$ contributions to the meson meson loop function from irreducible pion self-energy insertions.

have also depicted the vacuum and thermal cases for comparison. The very first difference that one observes at finite nuclear density is the appearance of strength below the two-pion threshold, which is absent in the thermal case. It can be understood on the basis of the baryon-related interaction mechanisms of the pion discussed above. At small nuclear densities, one of the intermediate pions may excite a *ph* pair whereas the other is placed on the mass shell (see the second diagram in Fig. 2.16). This mechanism is responsible for the strength right below $2M_\pi$ and lowers the threshold down to M_π. For increasing density, the probability for the two pions to be absorbed by baryon-hole excitations sets in (third diagram in Fig. 2.16), which builds additional strength below M_π and shifts the threshold practically down to $P^0 = 0$ (note the smaller size of this $\mathcal{O}(\rho^2)$ contribution with respect to the excitation of one single *ph* bubble). For $P^0 > 2M_\pi$, $F(P^0)$ also exhibits a remarkable enhancement with respect to the vacuum and thermal cases, indicating an increased phase space for $\sigma \to \pi\pi$ decays. This reflects the widely spread structure of the pion spectral function in the medium and the considerable attraction experienced by the pion quasiparticle peak.

When the temperature is increased, the low energy region looses some strength, as the phase space for NN^{-1} excitations is smeared off by the thermal motion of the nucleons. Above $P^0 = M_\pi$, Bose enhancement is more effective as one of the pions is placed on-shell and one can appreciate some increase over the $T = 0$ result. The latter effect is strongly magnified right above the two-pion threshold, since (i) the pion spectral function

is populated at low energies and (ii) the pion quasiparticle peak is strongly attracted in the medium. Note that the rapid energy dependence of the p-wave pion self-energy is also responsible from the quick increase of phase space right beyond the opening of the $\pi\pi$ channel.

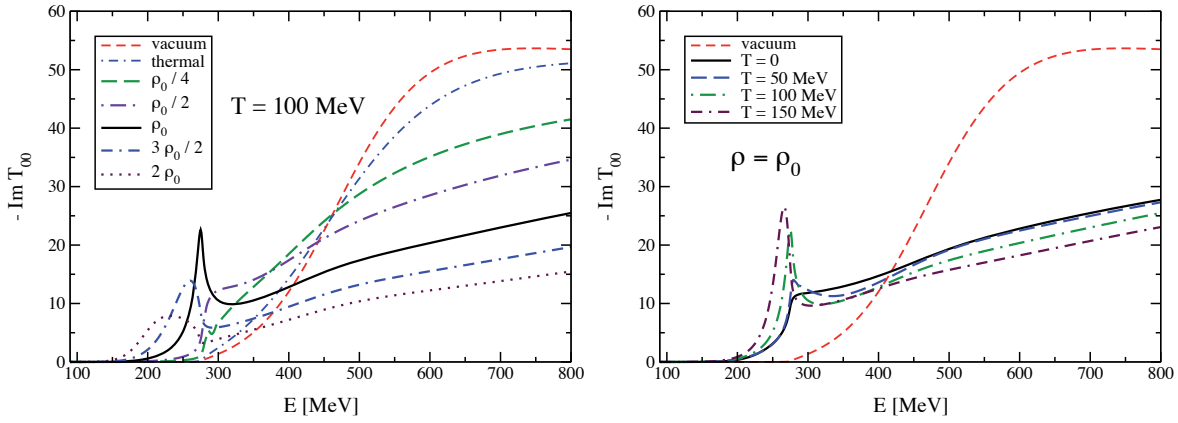

Figure 2.17: Imaginary part of the $\pi\pi$ amplitude in the $I = J = 0$ channel at finite temperature and nuclear density. We also include the result in free space for reference.

We finally show in Fig. 2.17 the imaginary part of the $\pi\pi$ amplitude for different densities and temperatures, which we can compare to the thermal calculation and the "F_π scaling" scenario in order to study threshold enhancement effects. We recall here that in the vacuum and thermal cases $\mathrm{Im}\, T$ vanishes below the two-pion threshold. Our result, from a dynamical calculation of many-body effects in the intermediate two-pion state, exhibits a sizable accumulation of strength at and below $P^0 = 2M_\pi$ already at nuclear matter density and zero temperature. On the other hand, the amplitude is strongly depleted beyond $\sqrt{s} = 400$ MeV as compared to the vacuum case, an effect that is not shared by the reduced-F_π calculation at the equivalent density (see Fig. 2.9, although note that the quantity plotted there is the squared modulus of the amplitude) which does not account for baryon-related σ-decay mechanisms. Only for much smaller values of F_π the strength focuses at the vacuum threshold, as the σ pole lies very close to the real energy axis; the resulting enhancement in the amplitude in that case is by far larger than obtained here, which is related to, but not fully driven by the σ pole behavior as we explain below. With respect to the thermal calculation, finite density additionally softens the amplitude at high energies and brings strength below the vacuum threshold, a feature which is linked to the presence of a baryonic medium and the excitation of pionic collective modes, as discussed above.

We have also studied the behavior of the σ pole at finite nuclear density. The analytic continuation of T in this case is not trivial because of the form of the dependence on Ω in (2.37) through the spectral functions and the limits of integration. Therefore, unlike in the IAM case where the analytic continuation was given by (2.6) with the replacement $\sigma_0 \mapsto \sigma_T$, we have used an approximated prescription in this case, namely to add to the evaluation of G in the 1st Riemann sheet the discontinuity on the real axis with

respect to the unphysical (2nd) sheet, $\mathrm{Disc}\, G(P^0) = -2\mathrm{i}\,\mathrm{Im}\, G(P^0)$. Still, this procedure provides the qualitative in-medium behavior of the σ pole [Roc02], although its absolute position in the complex plane carries some uncertainty (which we believe is superseded by other theoretical uncertainties in the evaluation of the pion self-energy). The combined effects of temperature and nuclear density accelerate the migration of the σ pole towards the $\pi\pi$ threshold. For instance, at $\rho = \rho_0/2$, the σ mass reaches $M_\mathrm{p} = 2M_\pi$ at about $T \simeq 150$ MeV, whereas at normal nuclear density $M_\mathrm{p} \simeq 300$ MeV already at $T = 0$ and it quickly reaches the two-pion threshold at about $T = 100$ MeV. This is correlated with the cusp structures observed in the amplitude at threshold, cf. Fig. 2.17; however, the strength observed at lower energies is linked to the many-body pion dynamics. In spite of this, the σ remains as a broad resonance at nuclear matter density and temperatures approaching the transition one, similarly to what happens in the thermal calculation (at comparatively higher temperatures) and at variance with the simplified "F_π scaling" approximation. In fact, if we keep increasing the density, at some point the σ pole crosses below $2M_\pi$ (one should not trust our implementation of medium effects far beyond $\rho = \rho_0$, but as an exercise it provides information about the phase-space behavior of the resonance). For instance, at $\rho = 2\rho_0$ and $T = 100$ MeV the σ mass from the pole lies about 70 MeV below the two-pion threshold but still we find $\Gamma_\mathrm{p} \simeq 150$ MeV.

2.4 Conclusions

We have presented in this chapter an analysis of the behavior of $\pi\pi$ scattering amplitudes in Unitarized Chiral Perturbation Theory with medium effects incorporated in several ways. In particular, we have been focused on the behavior with finite temperature and nuclear density of the $\rho(770)$ and $f_0(600)/\sigma$ resonances, which are generated dynamically within the Inverse Amplitude Method. In the channel of the σ, we have also studied nuclear-density effects using a many-body approach and unitarizing by means of the Bethe-Salpeter equation.

By considering only thermal effects on the IAM $\pi\pi$ amplitudes, the ρ exhibits a considerable broadening with a small mass decrease as temperature increases, whereas the σ mainly decreases its mass, effectively signaling chiral symmetry restoration, although it still remains as a broad resonance even at the transition temperature. The broadening obtained in our approach for the ρ meson at finite temperature is compatible with the spectral function analysis from dilepton spectra in the recent experiment by the NA60 Collaboration. The evolution of the ρ mass with temperature does not scale as the condensate, which renders our results in quantitative disagreement with the Brown-Rho scaling scenario. The fact that the σ pole remains far from the real axis even at the two-pion threshold when only temperature effects are considered implies no significant threshold enhancement for the scattering amplitude, which has been advocated as a precursor of chiral symmetry restoration. We neither observe a scaling of the σ mass with the quark condensate, which indicates that the $f_0(600)/\sigma$ resonance dynamically generated in our unitarized chiral approach has a non-$\bar{q}q$ component which is relevant near the phase transition.

By introducing finite nuclear density the picture changes dramatically. In a first

approximation, we have incorporated the effect of a nuclear medium by decreasing F_π according to the GOR relation to linear order in the density. At sufficiently low (high) values of F_π (density), the ρ and σ poles collapse onto the real energy axis at the threshold energy, which is preceded by a significant threshold enhancement in the scattering amplitudes. We have discussed these effects in the context of recent results from resonance production in finite nuclei and our results are in line with the experimental observations. A detailed analysis reveals that when the resonance pole is close to the real axis it splits into two states in separated Riemann sheets. The properties of these double poles allow us to classify the σ resonance according to its internal structure: it exhibits a "molecular" behavior (one of the poles stays close to threshold, well separated from the other one which evolves to lower energies to become degenerated with the pion). On the order hand, according to these arguments the ρ would correspond to a $\bar{q}q$, non-molecular, scenario. However, this criterium of classification is in principle only applicable to scalar resonances. Nevertheless, the $\bar{q}q$ nature of the ρ has been supported by other analyses based on different methods, such as large-N_c scaling [Pel04, Pel06]. The mass scaling from the σ and ρ pole with $F_\pi(\rho)$ follows the quark condensate evolution and therefore is compatible with a Brown-Rho scaling scenario, although one should keep in mind that relevant finite density mechanisms are neglected in this approximation.

Finally, we have improved our implementation of finite nuclear density (and temperature) effects by considering a microscopic calculation of many-body pion dynamics in $\pi\pi$ scattering. We have chosen a different unitarization scheme for the $\pi\pi$ scattering amplitude, namely to solve the Bethe-Salpeter equation for the lowest order ChPT interaction. Despite differences in the amplitudes at $\mathcal{O}(p^4)$, this scheme essentially provides the same results as the IAM and allows a systematic analysis and resummation of a relevant class of pion interaction mechanisms with the nuclear medium. The pion interactions with the medium are encoded in the single-particle pion self-energy, which accounts for the excitation of p-wave particle-hole and Delta-hole components as well as short distance correlation effects from nucleon-nucleon and Delta-nucleon interactions. The opening of baryon-related channels on top of $\sigma \to \pi\pi$ at finite density extends the available phase space to lower energies and therefore the $\pi\pi$ scattering amplitude exhibits an increased strength at and below the two-pion threshold, which is magnified at finite temperature as a consequence of Bose enhancement on the low energy modes of the $\pi\pi$ intermediate states. Such an effect has been found to provide a satisfactory description of the data from the two-pion photoproduction reaction in nuclei when comparing the mass spectrum in the neutral- vs charged-pion channels for different nuclei [Roc02, Mes02], where nuclear densities of the order of ρ_0 and below are explored. In our analysis we have considered both finite temperature and nuclear density, thus extending the applicability of the present approach to other experimental scenarios such as the forthcoming Heavy-Ion physics program at FAIR. As compared to the purely thermal calculation, the attractive interaction mechanisms of the pion at finite density accelerate the migration of the σ pole towards the two-pion threshold. The threshold enhancement observed in the $\pi\pi$ amplitude is correlated to the evolution of the σ pole towards (and below) $2M_\pi$. However, differently from the reduced-F_π result, the σ pole stays far from the real axis indicating a sizable decay width of the resonance at densities as high as $2\rho_0$ and temperatures close to the transition one.

Chapter 3

Transport coefficients in Chiral Perturbation Theory

The analysis of transport properties within the Heavy Ion Collision program has become a very interesting topic, with many phenomenological and theoretical implications. As we have seen in the Introduction, transport coefficients provide the linear response of the system to thermodynamic forces. Energy and momentum transport is encoded in the viscosity coefficients (shear and bulk) whereas charge and heat conduction produce electrical and thermal conductivities, respectively.

A prominent example of physical applications to Heavy Ions is found in viscosities. Although the matter produced after thermalization behaves as a nearly perfect fluid [Ada04a], there are measurable deviations, which are seen mainly in elliptic flow and can be reasonably explained with a small shear viscosity over entropy density ratio [Rom07]. In these analyses, bulk viscosity is customarily neglected, based on several theoretical studies made in both the high and low-temperature regimes [Arn06b, Pra93, Dav96]. However, it has been recently noted [Kha08, Kar08] that the bulk viscosity might be larger than expected near the QCD phase transition, by the effect of the conformal anomaly. On the other hand, shear viscosity over entropy density is believed to have a minimum in that region. If the two viscosity coefficients were comparable at the temperatures of interest, then there would be several physical consequences such as radial flow suppression, modifications of the hadronization mechanism [Kar08], or clustering at freeze-out [Tor08].

Lattice analyses of transport coefficients are cumbersome, since they involve the zero momentum and energy limit of spectral functions [Aar02, Mey08b, Hue08, Gup04], and no conclusive results are available at this moment. It is therefore very interesting and useful to consider regimes accessible to theoretical analysis in order to provide complementary information about transport coefficients. The theoretical analysis of transport coefficients has been traditionally carried out within two frameworks: kinetic theory and the diagrammatic approach. The kinetic theory approach involves linearized Boltzmann-like equations and has been successfully applied in high temperature QCD [Arn00, Arn03, Arn06b], in the meson sector [Pra93, Dav96, Dob04, Dob07a, Dob07b, Dob09], and in the color-flavor locked matter present in the core of dense neutron stars [Man05, Man07, Man08], whereas the diagrammatic method has been developed for scalar and high-T gauge theories [Jeo95, Jeo96, MR01, VB02, Aar02, Aar03, Aar04, Aar05]. In both formalisms, it

is crucial to include accurately the collisional width, identifying the dominant scattering processes in the plasma.

In this chapter it is described our recent diagrammatic study of transport coefficients within Chiral Perturbation Theory, pertinent for analyzing the meson sector at low energies and temperatures below the chiral phase transition [Ger89]. The results of this analysis have been previously collected in the papers [FF06, FF07a, FF07b, FF09a, FF09c], and we here present them as a whole along with further comments and clarifications. We start reviewing briefly previous works on transport coefficients in QCD, in order to establish as clear as possible the relation with our own approach. Also, the importance of dressing particle propagators when calculating transport coefficients is emphasized, and in Section 3.2 the calculation of the particle width is shown. Then, in Section 3.3, we describe in detail the diagrammatic analysis of transport coefficients in ChPT, pointing out the differences with respect to other quantum field theories, e.g. $\lambda\phi^4$. Later on, we proceed to the calculation of transport coefficients for a gas of pions. Our analysis is in principle applicable to a general gas of mesons, describable by SU(3) ChPT, but we have limited ourselves to the pion gas for simplicity. The pionic component dominates, at not very high temperatures, the hadron gas formed after a relativistic heavy-ion collision. The results corresponding to the DC conductivity, thermal conductivity, shear viscosity, and bulk viscosity have been separated in the respective sections, where some phenomenological applications and comparison with previous results are provided.

3.1 Transport coefficients in QCD

3.1.1 Kinetic theory approaches

These approaches consist in calculating transport coefficients according to the procedure we showed in Section 1.5.3, with different methods for solving the corresponding integral equations for the collision integral. The KT approach, as we saw in Sections 1.5.5, is in principle applicable to dilute systems where the mean free path λ is much larger than the Compton length λ_c associated to the particle excitations, and much smaller than the typical size L of the system, $\lambda \ll L$. However, it was shown not so long ago [Jeo95, Jeo96] that an *effective* kinetic theory description is also valid at high temperatures, where $\lambda \lesssim \lambda_c(T = 0)$. This effective kinetic theory approach has been successfully applied to the calculation of transport coefficients in QCD at very high temperatures [Arn00, Arn03, Arn06b]. On the other hand, at low temperatures $T < 150$ MeV, in the hadronic phase, the gas is dilute enough so the usual procedure has been to apply standard kinetic theory.

Hadronic phase

In Figure 3.1 we show the results obtained in [Dav96] for the thermal conductivity and the shear and bulk viscosities of a pion gas calculated in KT for several values of the chemical potential associated to the total number of pions. The continuous line in the plots of Fig. 3.1 corresponds to the result obtained in [Pra93] for $\mu = 0$ using the transport equation (1.138) without the Bose-Einstein enhancement factors of the Uehling-Uhlenbeck equation

(1.142). We see that the effect of these extra Bose-Einstein factors over the transport coefficients is smaller than a factor 2 for the temperatures considered.

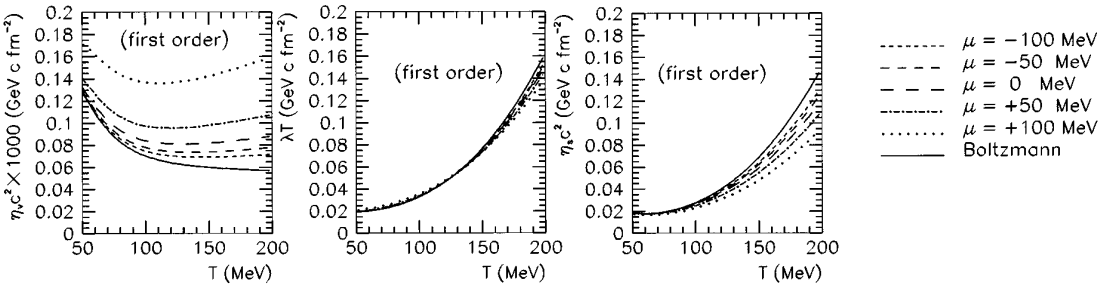

Figure 3.1: Thermal conductivity (denoted in the plot by λ), and the shear and bulk viscosities for a pion gas (denoted by η_s and η_v respectively), calculated in [Dav96] within KT using the Uehling-Uhlenbeck transport equation.

In Figure 3.2 (left) we show a plot from [Pra93] where the three transport coefficients for a pion gas are compared. In the same Figure (right) the enhancement produced by introducing kaons and nucleons is also shown (right). According to these results, the bulk viscosity is negligible in comparison with the shear viscosity for the temperatures considered.

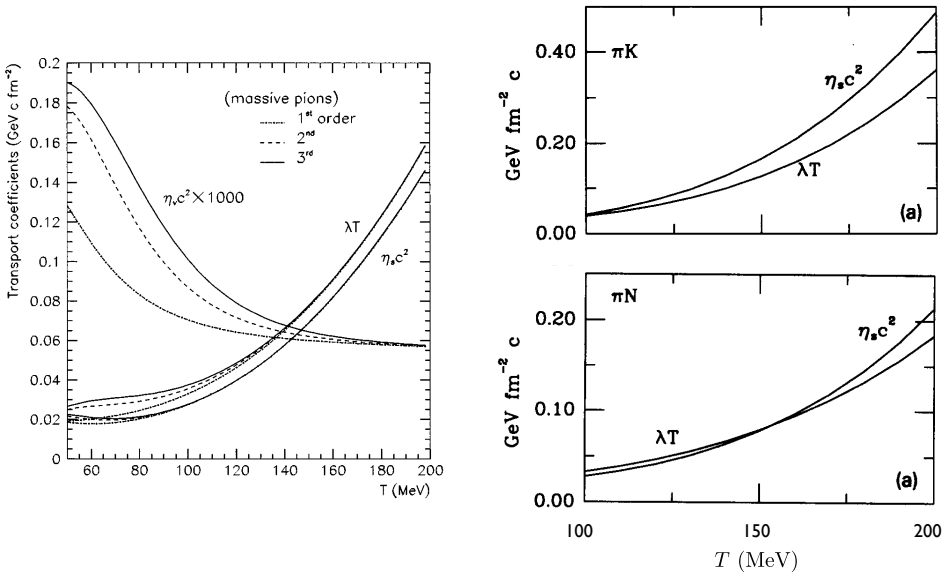

Figure 3.2: Left: Thermal conductivity (denoted in the plot by λ), shear viscosity, and bulk viscosity for a pion gas, calculated using KT in [Pra93]. Right: enhancement produced in the thermal conductivity and in the shear viscosity by introducing kaons and nucleons.

Finally, in Figure 3.3 we show the results for the shear viscosity calculated in [Dob04] within KT using the Uehling-Uhlenbeck transport equation, for a pion gas (left), for a gas of pions + kaons (upper right), and pions + etas (lower right). We here also see that the

effect of introducing kaons and the eta is to increase significantly the value of the shear viscosity.

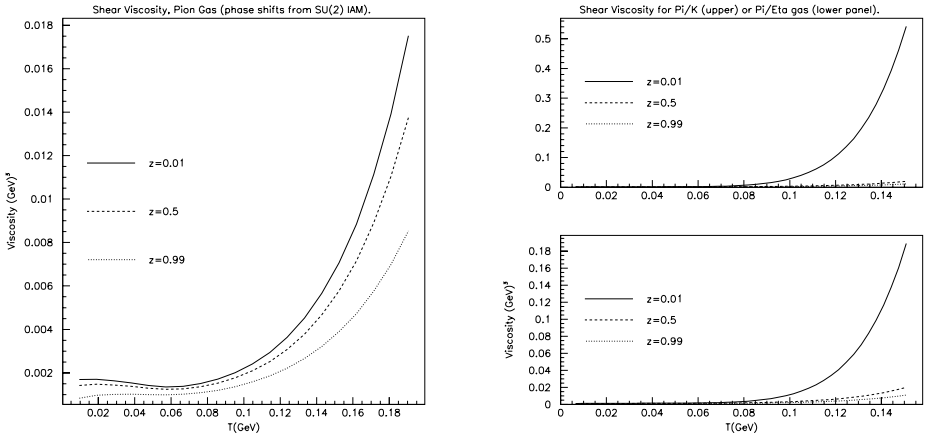

Figure 3.3: Shear viscosity calculated in [Dob04] within KT using the Uehling-Uhlenbeck transport equation for several fugacities $z \equiv \exp \beta(\mu - m)$.

Kinetic theory analyses in the hadron phase are perfectly applicable for low enough temperatures (dilute gas), but to solve the transport equation is technically involved and the final expressions for the transport coefficients are complicated. In contrast, as we shall see, the diagrammatic calculation within ChPT can provide simple analytical expressions to leading order for transport coefficients at low temperatures which can be extrapolated using unitarization methods and, in this way, it provides a way of analyzing qualitatively their behavior near the phase transition. In principle, the diagrammatic approach is also valid near the phase transition, where a KT analysis is not applicable. However, in this regime, the number of diagrams that we should take into account could be very large (potentially infinite).

Note that the previous calculations of the bulk viscosity in the hadron phase within KT consider collision terms with number-conserving interactions only, whereas the restoration of thermodynamic equilibrium under a uniform expansion is due to the change in the number of particles. Therefore, calculations considering only number-conserving interactions are valid for short periods of time so the plasma remains out of the chemical equilibrium (see discussion at the end of Section 3.1.2, Section 3.4.4 and Chapter 4).

QGP phase at high temperatures

As we mentioned above, at high temperatures ($T \gg T_{\rm c}, m_{\rm q}$) an effective kinetic theory treatment is applicable although $\lambda \lesssim \lambda_{\rm c}(T=0)$ [Jeo95, Jeo96, Arn00]. At those temperatures, the only relevant scale is the temperature itself, so every transport coefficient will be proportional to T^n with an appropriate power n depending on the corresponding dimension, and a proportionality factor equal to some function of the QCD gauge coupling. The results in the QGP phase for the shear and bulk viscosities to leading order in the

coupling constant are [Arn00, Arn06b]:

$$\eta = c_1 \frac{T^3}{\alpha_{\rm s}^2 \ln(1/\alpha_{\rm s})} \ , \quad \zeta = c_2 \frac{\alpha_{\rm s}^2 T^3}{\ln(1/\alpha_{\rm s})} \ , \tag{3.1}$$

where c_1 and c_2 are numeric factors which depends on the number of flavors, and $\alpha_{\rm s} \equiv g^2/4\pi$ with g the running gauge coupling constant. We here see that at high temperatures the bulk viscosity is also negligible parametrically in comparison to the shear viscosity. This is due to the restoration of scale symmetry in the limit of infinite temperature (see Section 3.4.4). For the calculation of the bulk viscosity in [Arn06b], the dominant contribution is due to elastic processes in the plasma, unlike what happens in a $\lambda\phi^4$ theory (cf. Sect. 3.1.2).

3.1.2 Diagramatic approach

The diagrammatic approach was thoroughly analyzed for renormalizable scalar theories in [Jeo95, Jeo96], with special emphasis in the high-temperature regime. The main conclusion was that in order to obtain the leading order contribution in perturbation theory of a certain transport coefficient, an infinite number of diagrams must be resummed at any temperature. Moreover, after performing this resummation, the result is an effective kinetic theory with a thermal mass instead of a vacuum mass[1]. Due to this equivalence between the diagrammatic and kinetic theory approaches, later calculations for transport coefficients in QCD at high temperatures were made using kinetic theory [Arn00, Arn03, Arn06b] (see Section 3.1.1), although there also was some diagrammatic analysis for gauge theories at high T [VB02].

We now review in some detail the analysis of [Jeo95, Jeo96] for a $\lambda\phi^4$ theory. As we have seen in Section 1.6, a transport coefficient is given in LRT by taking the limit when the external momentum goes to zero of the imaginary part (spectral density) of some correlator. This process of taking the limit of zero external momentum implies the appearance of the so called *pinching poles*, which are products of retarded and advanced propagators sharing the same four-momentum:

$$G_{\rm R}(p)G_{\rm A}(p) \simeq \frac{\pi}{4E_p^2 \Gamma_p} \left[\delta(p^0 - E_p) + \delta(p^0 + E_p)\right] \ , \quad \text{for} \quad \Gamma_p \ll E_p \ , \tag{3.2}$$

where the particle width (inverse of the collision time in the plasma) Γ_p is related to the particle self-energy[2] by

$$\Gamma_p = -\frac{\operatorname{Im} \Pi_{\rm R}(E_p, \boldsymbol{p})}{2E_p} \ . \tag{3.3}$$

Note that the product (3.2) is ill-defined when the particles propagate freely, i.e., when $\Gamma_p = 0$. A pinching pole would correspond to the contribution from two lines in a diagram which share the same four-momentum when the external frequency is zero. And as we see from Eq. (3.2) those lines are nearly on-shell in that limit, which is reasonable if the

[1] For low temperatures, the leading order result is exactly the same as the one obtained in standard KT, which is applicable at those temperatures.

[2] The self-energy modifies the dispersion relation of the particle in the way $p^2 = m^2 + \Pi(p;T)$.

collision time is long. For a $\lambda\phi^4$ theory, the first contribution to the particle width comes from the diagram of Figure 3.9, which is $\mathcal{O}(\lambda^2)$. Therefore, *ladder diagrams* as the one depicted in Figure 3.4 all count the same, $\mathcal{O}(1/\lambda^2)$, in the coupling constant and have to be resummed at any temperature.

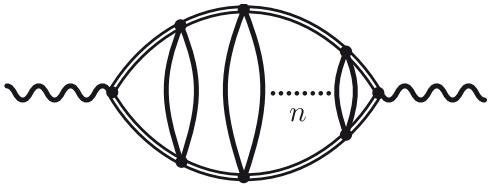

Figure 3.4: A ladder diagram with n rungs.

Another kind of diagrams, *bubble diagrams* (Fig. 3.5), in principle would give the dominant contribution increasing with the number of bubbles according to the counting scheme given above, so they would be naively $\mathcal{O}((1/\lambda^2)^n\lambda^{n-1}) = \mathcal{O}(1/\lambda^{n+1})$. But after some analysis [Jeo95] it can be shown that they can all be resummed giving a subdominant contribution (except for the bulk viscosity) with respect to the one-bubble diagram of Figure 3.10, i.e., they correspond to the graph of Figure 3.6 with $\Lambda_1 = \Lambda^{(0)} + \mathcal{O}(\lambda)$ and $\Lambda_2 = \Lambda^{(0)}$, with $\Lambda^{(0)}$ being the lowest-order vertex. Furthermore, it was shown in [Jeo95] that the dominant contribution for the bulk viscosity is given by ladder diagrams more complex than the ones shown in Fig. 3.4, with rungs involving number-changing processes (see discussion below).

Therefore it is interesting from the theoretical point of view to analyze what happens in ChPT, where there is no explicit coupling constant, in order to see whether a resummation is needed.

Figure 3.5: A bubble diagram with n bubbles.

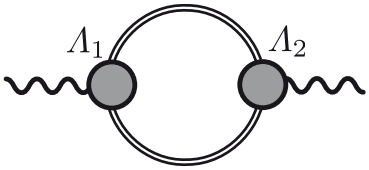

Figure 3.6: Generic representation of a ladder and/or bubble diagram in terms of two effective vertices, Λ_1 and Λ_2.

The role of number-changing processes in the bulk viscosity

Viscosities are typically determined by the slowest process which is required for relaxation to equilibrium from the corresponding perturbation [Arn06b]. In [Jeo95, Jeo96] it was

found that, under a uniform expansion or compression of the gas, the total number of particles in a massive $\lambda\phi^4$ theory equilibrates very slowly, and thus, processes which change the number of particles determine the bulk viscosity. In the case of the shear viscosity though, elastic processes suffice to randomize momenta and give the dominant contribution.

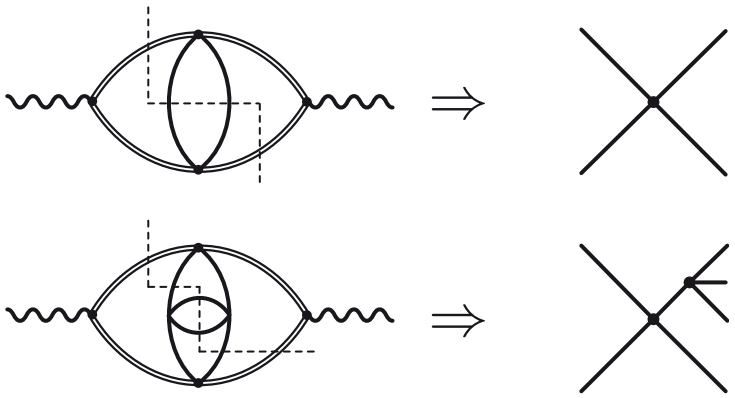

Figure 3.7: (Top) By cutting a ladder diagram with a simple rung we recover elastic processes. (Bottom) Rungs that include interactions correspond to number-changing interactions.

In the language of ladder diagrams, elastic and inelastic processes can be identified by cutting the corresponding rungs (see Figure 3.7). We see however that ladder diagrams corresponding to inelastic processes are in principle subdominant according to the counting in powers of the coupling constant. The need of introducing these diagrams can be formally seen by writing in the following form the integral equation corresponding to the resummation of ladder diagrams (see Fig. 3.8) [Jeo95]:

$$|\mathcal{V}\rangle = |\mathcal{V}_0\rangle + \hat{\mathcal{M}}\hat{\mathcal{G}}|\mathcal{V}\rangle \ , \tag{3.4}$$

where $\mathcal{M}$ represents one arbitrary rung in the ladder diagram, $\mathcal{V}_0$ is the zero-order vertex (the vertex corresponding to the insertion of the operator $\hat{\mathcal{P}}$ in the case of the bulk viscosity, cf. Section 1.6.3). The integral equation (3.4) will be solvable if any zero mode of the kernel $1 - \hat{\mathcal{K}}$, with $\hat{\mathcal{K}} \equiv \hat{\mathcal{M}}\hat{\mathcal{G}}$, is orthogonal to the inhomogeneous term $|\mathcal{V}_0\rangle$. If we now denote by $\hat{\mathcal{K}}_0$ the kernel corresponding to ladder diagrams with simple rungs (as the one depicted in Fig. 3.7 (top)), the change in the solution of (3.4) by making the substitution $\hat{\mathcal{K}} \mapsto \hat{\mathcal{K}}_0$ will be subdominant if both the zero modes of $\hat{\mathcal{K}}_0$ and $\hat{\mathcal{K}}$ are orthogonal to $|\mathcal{V}_0\rangle$, otherwise the new integral equation would be singular implying that the neglected part of $\mathcal{K}$ is not negligible. This issue with the zero modes does not arise when considering the contribution from an individual ladder diagram, but rather reflects the convergence (or lack thereof) of the infinite series of ladder diagrams.

It can be shown [Jeo95, Jeo96] that, in the case of a massive $\lambda\phi^4$ theory, there is a zero mode of $\hat{\mathcal{K}}_0$ which is not orthogonal to $|\mathcal{V}_0\rangle$, whereas by including number-changing processes in the rung the orthogonality condition is satisfied. This implies for instance that even for very low temperatures, in a massive $\lambda\phi^4$ theory, the bulk viscosity is determined by inelastic processes giving a behavior $\zeta \sim \exp(2m/T)/\lambda^4$ for $T \ll m$ [Jeo95]. However,

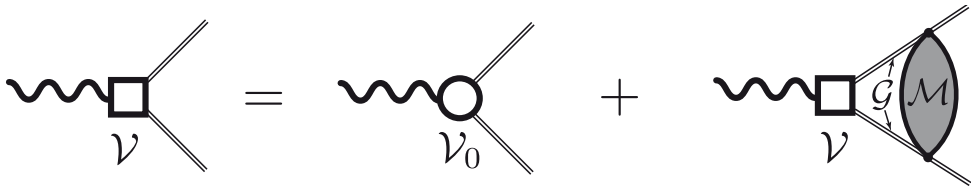

Figure 3.8: Recurrence relation for the effective vertex representing an arbitrary number of ladders or bubbles.

in our analysis of the bulk viscosity within ChPT in Section 3.4.4, we will not consider number-changing processes in the rungs, even though the massive pion gas at very low temperatures essentially behaves like a $\lambda\phi^4$ theory. The reason is that we will be interested in the (higher) temperatures typical of a heavy-ion environment between chemical freeze-out and thermal freeze-out (also more interesting from the phenomenological point of view), for which the number of particles is approximately conserved (cf. Chapter 4). Moreover, one of the main goals in Section 3.4.4 is to show the relation between the bulk viscosity and the trace anomaly, rather than obtaining an accurate estimation of the viscosity near the phase transition temperature in full statistical equilibrium (thermal + chemical).

3.2 Particle width

As we have mentioned in the previous section, it is crucial to have lines with a non-zero width in the generic diagram of Fig. 3.6 (double lines) in order to take into account the collisions between the particles of the fluid, as also dictated by kinetic theory. If the particle width were zero it would mean that particles would propagate without interaction, implying that the corresponding transport coefficient would be infinite. We can approximate the interaction between the particles in the bath by considering the following spectral density with a non-zero width Γ_p:

$$\rho(p^0, \boldsymbol{p}) = \frac{1}{E_p}\left[\frac{\Gamma_p}{(p^0 - E_p)^2 + \Gamma_p^2} - \frac{\Gamma_p}{(p^0 + E_p)^2 + \Gamma_p^2}\right] . \tag{3.5}$$

This approximation by a Lorentzian will be valid for a small-enough width. The width is generically calculated for two-body collisions by [Goi89]:

$$\Gamma(k_1) = \frac{\sinh(\beta E_1/2)}{4E_1}\int \mathrm{d}\nu_2\,\mathrm{d}\nu_3\,\mathrm{d}\nu_4\ (2\pi)^4\delta^{(4)}(k_1 + k_2 - k_3 - k_4)|T(s,t)|^2 , \tag{3.6}$$

with $\mathrm{d}\nu_i \equiv \mathrm{d}^3\boldsymbol{k}_i/[(2\pi)^3 4E_i \sinh(\beta E_i/2)]^{-1}$, $T(s,t)$ is the two-body scattering amplitude, and $s \equiv (k_1 + k_2)^2$ and $t \equiv (k_1 - k_3)^2$ the Mandelstam variables. In the case of the pion, its thermal width is also related to the imaginary parts of the the space-like and time-like components of the pion decay constant, and it determines the speed of propagation (refraction index) of pions in the medium [Pis96, MR98].

If the gas is dilute, i.e. $\beta E \gg 1$ (dilute gas approximation, DGA), the previous

expression reduces to:

$$\Gamma(k_1) \simeq \frac{1}{2}\int \frac{\mathrm{d}^3\boldsymbol{k}_2}{(2\pi)^3}\ \mathrm{e}^{-E_2/T}\ \sigma_{\mathrm{tot}}(s) v_{\mathrm{rel}}(1-\boldsymbol{v}_1\cdot\boldsymbol{v}_2)\ , \tag{3.7}$$

where σ_{tot} is the total scattering cross section, $\boldsymbol{v}_i$ the velocity of each the two colliding particles, and v_{rel} their relative speed. The leading order contribution to the pion width is represented by the diagram in Figure 3.9. Cutting this diagram in order to extract its imaginary part (the width) leads to the formula (3.6) with $T(s,t)$ being the pion-pion scattering amplitude. Up to energies of 1 GeV (enough for temperatures below T_{c}) it can be shown [GN02a] that for $\pi\pi$ scattering only the channels $IJ = 00, 11, 20$ of isospin-angular momentum are relevant and then we can make the approximation:

$$\sigma_{\mathrm{tot}}(s) = \frac{32\pi}{3s}\sum_{I,J}(2J+1)(2I+1)|t_{IJ}(s)|^2 \simeq \frac{32\pi}{3s}\left[|t_{00}(s)|^2 + 9|t_{11}(s)|^2 + 5|t_{20}(s)|^2\right]\ , \tag{3.8}$$

where $t_{IJ}(s)$ are the partial waves, so the total (isospin-averaged) scattering amplitude for $\pi\pi$ scattering is decomposed in terms of the isospin-projected scattering amplitude, T_I, and the partial waves as:

$$T(s,t) = \frac{1}{3}\sum_{I=0}^{2}(2I+1)|T_I(s,t)|^2\ , \tag{3.9}$$

$$\text{with}\quad T_I(s,t) \equiv 32\pi\sum_{J=0}^{\infty}(2J+1)t_{IJ}(s)P_J(\cos\theta)\ , \tag{3.10}$$

and P_J being Legendre polynomials. To lowest order in ChPT, $\mathcal{O}(p^2)$, according to (2.3):

$$t_{00}^{(2)}(s) = \frac{2s-M_0^2}{32\pi F_0^2}\ ,\quad t_{11}^{(2)}(s) = \frac{s-4M_0^2}{96\pi F_0^2}\ ,\quad t_{20}^{(2)}(s) = -\frac{s-2M_0^2}{32\pi F_0^2}\ . \tag{3.11}$$

Higher order expressions are more complicated [GN02a], and will not be explicitly displayed here. Furthermore, in the 00 and 11 channels there appear the $f_0(600)$ and $\rho(770)$ resonances respectively. In order to deal properly with these resonances within ChPT we will have to unitarize our scattering amplitudes (see Chapter 2).

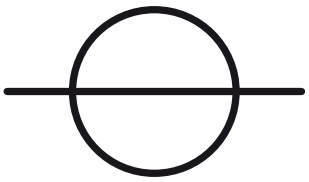

Figure 3.9: Leading-order contribution to the pion width.

For very low temperatures, $T \ll M_\pi$, we can approximate the scattering cross section

by a constant[3] since $s \simeq 4M_\pi^2$:

$$\sigma_{\rm tot} \simeq \frac{23M_\pi^2}{128\pi F_\pi^4} \ , \tag{3.12}$$

and then the expression (3.7) can be approximated by:

$$\Gamma(k) \simeq \frac{23M_\pi^3 T^2 {\rm e}^{-M_\pi/T}}{512\pi^3 F_\pi^4}\left[{\rm e}^{-k^2/2M_\pi T} + \pi^{1/2}\frac{{\rm erf}(k/\sqrt{2M_\pi T})}{\sqrt{2M_\pi T}}(k + M_\pi T/k)\right] \ . \tag{3.13}$$

In the chiral limit, i.e. $M_0 \equiv 0$, and very low temperatures, $T \ll F_\pi$, the cross section can be approximated by the lowest order result:

$$\sigma_{\rm tot}(s) \simeq \frac{5s}{48\pi F_0^4} \ . \tag{3.14}$$

But in this case we cannot apply (3.7) because the DGA is not valid even for very low temperatures (the gas is not dilute). We have to use instead the original expression (3.6) with the lowest order scattering amplitude:

$$|T|^2 = \frac{2(s^2+t^2+u^2)}{F_\pi^4} \ . \tag{3.15}$$

The final expression has not a simple form even for $T \ll F_\pi$ [Goi89]:

$$\Gamma(k_1) \simeq \frac{\sinh(k_1/2T)}{8k_1^2}\frac{\pi}{(4\pi F_\pi)^4}\int_0^\infty {\rm d}k_2 \int_0^{k_1+k_2} {\rm d}k_3 \ \frac{\theta(k_+-k_-)f_1 + 4\theta(q_+-q_-)f_2}{\sinh(k_2/2T)\sinh(k_3/2T)\sinh(k_4/2T)} \ , \tag{3.16}$$

$$\begin{aligned} f_1 &\equiv 2(k_+-k_-)(k_1+k_2)^4 - \frac{4}{3}(k_+^3-k_-^3)(k_1+k_2)^+\frac{2}{5}(k_+^5-k_-^5) \ , \\ f_2 &\equiv (q_+-q_-)(k_1-k_3)^4 - \frac{2}{3}(q_+^3-q_-^3)(k_1-k_3)^3 + \frac{1}{5}(q_+^5-q_-^5) \ , \\ k_+ &\equiv \min(k_1+k_2, k_3+k_4) \ , \\ k_- &\equiv \max(|k_1-k_2|, |k_3-k_4|) \ , \\ q_+ &\equiv \min(k_1+k_3, k_2+k_4) \ , \\ q_- &\equiv \max(|k_1-k_3|, |k_2-k_4|) \ . \end{aligned}$$

From this expression we see that the pion width becomes zero in the chiral limit for $k_1 \to 0^+$ while in the massive case it remains finite in that limit. This means that interactions between pions become arbitrarily weak in the massless case when momenta go to zero, as dictated by Weinberg's theorem [Wei79] (we can also see it in Eq. (3.11)).

[3]For the massive case at very low temperatures, the Bose-Einstein factors select small three-momenta so the average momentum is of order $\mathcal{O}(\sqrt{M_\pi T}) \ll M_\pi$. Therefore, in this limit it is enough to consider only the $\mathcal{O}(p^2)$ amplitudes in the cross section, which allows to perform a systematic T/M_π expansion for Γ_p and transport coefficients.

3.3 General analysis of diagrams for transport coefficients in ChPT

In the analysis of transport coefficients within ChPT, analogously to what happens in high-temperature quantum field theory, we also find non-perturbative contributions, $\propto 1/\Gamma$ (and $\Gamma = \mathcal{O}(p^5)$), due to the presence of pinching poles. This would indicate that the standard ChPT power counting, dictated by Weinberg's formula (1.43), has to be modified in some way because otherwise, naively, diagrams with a larger number of pinching poles would become more important as the temperature is lowered. We will show that for low temperatures, ladder diagrams are the most relevant, but still perturbatively small in comparison to the leading order given by the simple diagram of Fig. 3.10.

Figure 3.10: Leading-order contribution to transport coefficients for low temperatures in ChPT.

Again, the same topology arguments used in high-temperature theories are a priori applicable for the ChPT case, so we expect that the dominant contribution to transport coefficients come from ladder and bubble diagrams. Following closely the analysis of [VB02], we now derive the expression for the zero-frequency limit of the derivative of the spectral function corresponding to the generic diagram depicted in Figure 3.6. In the ITF, the self-energy of this diagram is[4]:

$$\Pi^{AA}(\mathrm{i}\nu_n, \mathbf{0}) = \theta T \sum_m \int \frac{\mathrm{d}^3\boldsymbol{p}}{(2\pi)^3}\, \Delta_\Gamma(\mathrm{i}\omega_m + \mathrm{i}\nu_n, \boldsymbol{p})\Delta_\Gamma(\mathrm{i}\omega_m, \boldsymbol{p}) \times \Lambda_1^A(\mathrm{i}\omega_m, \mathrm{i}\omega_m + \mathrm{i}\nu_n; \boldsymbol{p})\Lambda_2^A(\mathrm{i}\omega_m + \mathrm{i}\nu_n, \mathrm{i}\omega_m; \boldsymbol{p}) \ , \quad (3.17)$$

where ν_n is the external Matsubara frequency, ω_m is the corresponding to one of the two internal lines, θ is some combinatoric factor equal to either 1/2 or 1 depending on whether Δ_Γ correspond to a self-conjugate field or not, and we have also introduced the indices A that depend on the nature of the external lines (scalar, vectorial or tensorial). We consider here that the vertex $\Lambda_1^A(z + \mathrm{i}\nu_n, z; \boldsymbol{p})$ is real and has no singularities as a function of the complex variable z. The vertex $\Lambda_2^A(z + \mathrm{i}\nu_n, z; \boldsymbol{p})$ will be constructed out of Λ_1^A by means of a recurrence relation of the type depicted in Fig. 3.8. Then, the vertex $\Lambda_2^{(n)}$ corresponding to n ladders/bubbles is related to $\Lambda_2^{(n-1)}$ by:

$$\Lambda_2^{(n)}(\mathrm{i}\omega_m + \mathrm{i}\nu_n, \mathrm{i}\omega_m; \boldsymbol{p}) = T \sum_{\nu_q} \int \frac{\mathrm{d}^4 Q}{(2\pi)^4}\, \Delta_\Gamma(\mathrm{i}\omega_m + \mathrm{i}\nu_n + \mathrm{i}\nu_q, \boldsymbol{p} + \boldsymbol{q})\Delta_\Gamma(\mathrm{i}\omega_m + \mathrm{i}\nu_q, \boldsymbol{p} + \boldsymbol{q}) \times \frac{\rho(Q)}{q^0 - \mathrm{i}\nu_q}\Lambda_2^{(n-1)}(\mathrm{i}\omega_m + \mathrm{i}\nu_n + \mathrm{i}\nu_q, \mathrm{i}\omega_m + \mathrm{i}\nu_q; \boldsymbol{p} + \boldsymbol{q}) \ , \quad (3.18)$$

[4]For $\Gamma \neq 0$, the correlator is continuous in the zero-momentum limit at $\omega \neq 0$.

where $\rho(Q)$ is the spectral density of the ladder/bubble. For $n = 1$, (3.18) and (1.72) imply that $\mathit{\Lambda}_2^{(1)}$ has only the singularities of the product $\mathit{\Delta}_\Gamma \mathit{\Delta}_\Gamma$. By mathematical induction, it follows that $\mathit{\Lambda}_2^{(n)}$, and hence $\mathit{\Lambda}_2$, inherit the same property. Therefore, $\mathit{\Lambda}_2^A(z+\mathrm{i}\nu_n, z; \boldsymbol{p})$ has two branch cuts at $\mathrm{Im}(z+\mathrm{i}\nu_n) = 0$ and $\mathrm{Im}\, z = 0$. We now do the Matsubara sum in (3.17), perform the analytical continuation $\mathrm{i}\nu_n \mapsto \omega + \mathrm{i}0^+$, and keep only the terms containing products $G_\mathrm{A} G_\mathrm{R}$, which constitute the dominant contribution according to (3.2) due to pinching poles. The resulting expression is:

$$\begin{aligned}\mathit{\Pi}_\mathrm{R}^{AA}(\omega, \mathbf{0}) = & -\theta \int_{-\infty}^{\infty} \frac{\mathrm{d}\xi}{2\pi\mathrm{i}} \int \frac{\mathrm{d}^3\boldsymbol{p}}{(2\pi)^3}\, G_\mathrm{A}(\xi, \boldsymbol{p}) G_\mathrm{R}(\xi+\omega, \boldsymbol{p}) \mathit{\Lambda}_1^A(\xi - \mathrm{i}0^+, \xi + \omega + \mathrm{i}0^+) \\ & \times \mathit{\Lambda}_2^A(\xi + \omega + \mathrm{i}0^+, \xi - \mathrm{i}0^+)[n_\mathrm{B}(\xi) - n_\mathrm{B}(\xi+\omega)] \ . \end{aligned} \tag{3.19}$$

Since we assume that vertex $\mathit{\Lambda}_1^A$ is real, it follows from mathematical induction that $\mathit{\Lambda}_2^A$ is also real. Using this, we finally obtain the following result for the spectral density associated to the diagram of Fig. 3.6:

$$\begin{aligned}\lim_{\omega\to 0^+} \frac{\rho^{AA}(\omega, \mathbf{0})}{\omega} = & -\theta\beta \int \frac{\mathrm{d}^3\boldsymbol{p}}{(2\pi)^3} \int_{-\infty}^{\infty} \frac{\mathrm{d}\xi}{2\pi}\, n_\mathrm{B}(\xi)[1 + n_\mathrm{B}(\xi)] G_\mathrm{R}(\xi, \boldsymbol{p}) G_\mathrm{A}(\xi, \boldsymbol{p}) \\ & \times \mathit{\Lambda}_1^A(\xi - \mathrm{i}0^+, \xi + \mathrm{i}0^+; \boldsymbol{p}) \mathit{\Lambda}_2^A(\xi + \mathrm{i}0^+, \xi - \mathrm{i}0^+; \boldsymbol{p}) \ . \end{aligned} \tag{3.20}$$

As we have mentioned above, we expect the Weinberg's counting to be modified in order to take account of the non-perturbative contributions coming from pinching poles. In order to give a first and naive estimation of the contribution at low temperatures from every diagram, we assign a factor Y, that we expect to be non-perturbative, to each pair of lines sharing the same four-momentum, and a factor X, that we expect to be of order $X_1 \equiv [M_\pi/(4\pi F_\pi)]^2$ (since X_1 is the typical contribution from a chiral loop) for very low temperatures to any other "ordinary" loop. Therefore, according to this new counting, the contribution from a ladder diagram with n rungs would be of order

$$\mathcal{O}(X^n Y^{n+1}) \ , \tag{3.21}$$

so ladder diagrams could in principle become more important as we go down in temperatures, where ChPT is expected to work better, if Y is non-perturbative (see Section 3.3.1 for an specific example). Evidently, the contribution from the simple diagram in Fig. 3.10 would be of order $\mathcal{O}(Y)$ instead of the $\mathcal{O}(X)$ estimation given by Weinberg's power counting. In the following section, we are going to analyze in detail the counting (3.21) in the particular case of the DC electrical conductivity, although the results are applicable to the other transport coefficients. We shall see that for very low temperatures, ladder diagrams are perturbatively suppressed, whereas the bubble ones can be neglected. However, near the critical temperature, in principle the sum of these types of diagrams could be relevant.

3.3.1 Ladder and bubble diagrams

In this section we shall analyze ladder and bubble diagrams with the external vertices corresponding to insertions of electromagnetic currents, as it is necessary in order to study

the DC electrical conductivity. However, the analysis presented here is directly applicable to other transport coefficients by adequately modifying the external vertices[5].

Using (3.20), the contribution to the DC conductivity to low temperatures, corresponding to the diagram of Fig. 3.10, is given by

$$\sigma^{(0)} = \frac{e^2}{3T} \int \frac{\mathrm{d}^3\boldsymbol{p}}{(2\pi)^3} \, \frac{|\boldsymbol{p}|^2}{E_p^2 \Gamma_p} n_{\mathrm{B}}(E_p)[1 + n_{\mathrm{B}}(E_p)] \; , \tag{3.22}$$

where e is the charge of the electron and $E_p \equiv \sqrt{M_\pi^2 + |\boldsymbol{p}|^2}$. For very low temperatures ($T \ll M_\pi$), using (3.13), this expression takes the simple form:

$$\sigma^{(0)} \simeq 14 \, \frac{e^2 F_\pi^4}{T^{1/2} M_\pi^{5/2}} \; . \tag{3.23}$$

This behavior, $\lim_{\omega \to 0^+} \rho(\omega)/\omega \sim \sqrt{M_\pi/T} \sim Y$, for the spectral density at low temperatures indicates that there could be important non-perturbative contributions from higher-order diagrams (ladder diagrams with an arbitrary number of rungs) in this temperature regime. We analyze in detail this in what follows.

Ladder diagrams at very low temperatures ($T \ll M_\pi$)

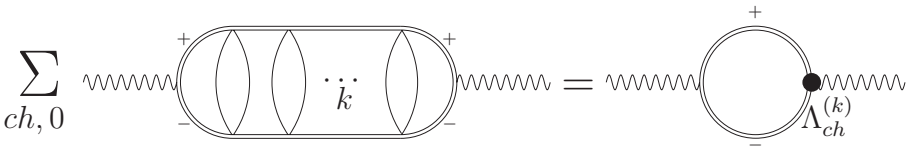

Figure 3.11: Ladder diagrams contributing to the electrical conductivity.

In the more general case of a ladder diagram with k rungs (see Fig. 3.11), its contribution in the ITF to the EM current-current correlator is:

$$\begin{aligned} \left[\Delta^{(k)}\right]_j^j (\mathrm{i}\nu_m, \boldsymbol{0}) = e^2 T \sum_{n=-\infty}^{\infty} \int \frac{\mathrm{d}^3\boldsymbol{p}_1}{(2\pi)^3} \; 2\boldsymbol{p}_1 \cdot \boldsymbol{\Lambda}_{\mathrm{ch}}^{(k)}(\mathrm{i}\omega_n + \mathrm{i}\nu_m, \mathrm{i}\omega_n, \boldsymbol{p}_1) \\ \times \Delta_\Gamma(\mathrm{i}\omega_n, |\boldsymbol{p}_1|) \Delta_\Gamma(\mathrm{i}\omega_n + \mathrm{i}\nu_m, |\boldsymbol{p}_1|) \; , \end{aligned} \tag{3.24}$$

where Δ_Γ denotes the Matsubara propagator of the pion lines with a non-zero width. $\boldsymbol{\Lambda}_{\mathrm{ch}}^{(k)}$ is the effective $\pi^+\pi^-\gamma$ vertex[6] made of k rungs, as depicted in Figure 3.11, where the sum is made over all possible ways of inserting internal lines and vertices corresponding to

[5]There will be some differences though, due to the particular character (scalar, vectorial, or tensorial) of the corresponding transport coefficient. But the main conclusions remain unaltered.

[6]The charge eigenstates of the pion, $\{\pi^+, \pi^-, \pi^0\}$, are expressed in terms of the eigenstates of the third component of isospin, $\{\pi^1, \pi^2, \pi^3\}$, as $\pi^+ = (\pi^1 - \mathrm{i}\pi^2)/2$, $\pi^- = (\pi^1 + \mathrm{i}\pi^2)/2$, and $\pi^0 = \pi^3$. The photon is coupled to the pion gas using the method of the external sources (see Section 1.3), by considering the external fields $r_\mu = l_\mu = -\frac{\sigma^3}{2} A_\mu^{\mathrm{ext}}$, $v_{\mathrm{s}}^\mu = -\frac{e}{2} A_{\mathrm{ext}}^\mu$ [Sch03]. The resulting $\gamma\pi\pi$ interaction term in the lagrangian is $\mathcal{L}_2^{\gamma\pi\pi} = -e\epsilon_{3ij}\pi_i \partial^\mu \pi_j A_\mu^{\mathrm{ext}}$.

charged and neutral pions, respecting charge conservation and including the corresponding combinatoric factors. Note that the two pairs of lines attached to the external lines are always charged, denoted in the figure by $+,-$ symbols. The lowest order effective vertex is $\boldsymbol{\Lambda}^{(0)}_{\rm ch} = 2\boldsymbol{p}_1$. Photons are coupled to pions by using the external sources method [Sch03], where the electric charge e is formally considered of order $\mathcal{O}(p)$ in the chiral counting.

The effective vertices satisfy a recurrence relation (cf. Fig. 3.8) which ultimately leads to integral equations corresponding to linearized Boltzmann equations [Jeo95, Jeo96, VB02]. The same results for the effective vertices are obtained in the real-time formalism [Wan99, Arn01]. In our present case, the integral equations become a little more involved due to the presence of neutral and charged particles, as well as derivative vertices[7]. However, for $T \ll M_\pi$ an important simplification takes place: the leading order of the sum in Figure 3.11 for a given number of rungs k is proportional to a single diagram where all vertices are replaced by constant vertices M_π^2/F_π^2 and therefore the spectral function of the rung integral is given by that of the loop correlator J_0 in (C.10), analyzed in Appendix C.

Let us justify our previous statement. We have seen in Section 3.1.2 that the presence of a pair of double lines forces its momentum to be on shell at $p_0 = \pm E_p$. Thus, consider the one-loop subgraph made of two "incoming" double lines and two "outgoing" ones. The two vertices contain different combinations of powers of two momenta or two masses in each vertex, where the momenta can be "external" (double lined) p_1, p_2 or "internal" k and $k + p_1 \pm p_2$ (see details below). In addition, as we will see below, the integrals over p_1 and p_2 contain Bose-Einstein factors that, according to our very low T counting, suppress powers of $\boldsymbol{p}_{1,2}/M_\pi$. Therefore, the leading contribution for $T \ll M_\pi$ in M_π^4 or $p_{1,2}^4$ vertices is proportional to $M_\pi^4 J_0(k)$, since $E_{1,2} \simeq M_\pi$. As for the powers involving "internal" momenta, using that $E_1 + E_2 \simeq 2M_\pi \gg |\boldsymbol{p_1} - \boldsymbol{p_2}| \gg E_1 - E_2 = \mathcal{O}(|\boldsymbol{p}|^2_{1,2}/M_\pi)$ and the relation among the different one-loop thermal integrals with momentum powers in the numerator discussed in Appendix A of [GN02b], we have checked explicitly that we are left, to leading order, only with $M_\pi^4 J_0$, $M_\pi^3 J_1$ or $M_\pi^2 J_2$ contributions to the imaginary part (spectral function) of the loops, which, as our analysis below will show, provides the relevant contributions to the ladder diagrams. The imaginary part of the J_α integrals is given in Appendix C. For $T \ll M_\pi$ we can replace the Bose-Einstein distributions by Boltzmann exponentials and the relevant integrals can be explicitly evaluated, with the result that both for the thermal and for the unitarity cuts (see Appendix C), the leading order of $\mathrm{Im}\, J^{\rm R}_\alpha$ are proportional to $M_\pi^\alpha \,\mathrm{Im}\, J^{\rm R}_0$ for $\alpha = 1, 2$.

Therefore, for $T \ll M_\pi$, we have

$$\boldsymbol{\Lambda}^{(k)}_{\rm ch} = \left(\frac{M_\pi}{F_\pi}\right)^{4k} \alpha^{(k)} \boldsymbol{\Lambda}^{(k)} \ , \tag{3.25}$$

[7] The effective vertex $\boldsymbol{\Lambda}^k_{\rm ch}$ is actually a matrix with indices corresponding to the different types of pion lines, thus implying coupled recurrence relations, although this is not relevant for any of the conclusions we obtain. See also comments after (3.32).

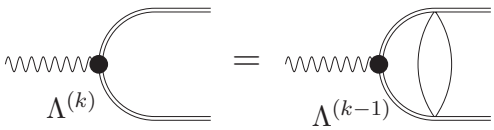

Figure 3.12: Recurrence relation between ladder vertices.

with $\alpha^{(k)}$ a purely numerical factor and

$$\boldsymbol{\Lambda}^{(k)}(\mathrm{i}\omega_m+\mathrm{i}\nu_m,\mathrm{i}\omega_m,\boldsymbol{p}_1)=\int\limits_{-\infty}^{\infty}\frac{\mathrm{d}\omega'}{2\pi}\int\frac{\mathrm{d}^3\boldsymbol{p}_2}{(2\pi)^3}\,\rho(\omega',|\boldsymbol{p}_2-\boldsymbol{p}_1|)$$
$$\times\,T\sum_{n=-\infty}^{\infty}\boldsymbol{\Lambda}^{(k-1)}(\mathrm{i}\omega_n+\mathrm{i}\nu_m,\mathrm{i}\omega_n,\boldsymbol{p}_2)\frac{\Delta_\Gamma(\mathrm{i}\omega_n,|\boldsymbol{p}_2|)\Delta_\Gamma(\mathrm{i}\omega_n+\mathrm{i}\nu_m,|\boldsymbol{p}_2|)}{\omega'-\mathrm{i}(\omega_n-\omega_m)}\;, \tag{3.26}$$

where $\rho(\omega,|\boldsymbol{q}|)=2\,\mathrm{Im}\,J_0^{\mathrm{R}}(\omega,|\boldsymbol{q}|)=2\,\mathrm{Im}\,I^{\mathrm{R}}(\omega,|\boldsymbol{q}|;0)$ according to our notation in the Appendix. The above recurrence relation is depicted in Figure 3.12 and allows us to proceed along similar steps as in [VB02]. By induction, we have that the only singularities of $\boldsymbol{\Lambda}^{(k)}(z+\mathrm{i}\nu_m,z,\boldsymbol{p})$ are the same two cuts as the propagator product in (3.26), i.e, at $\mathrm{Im}\,z=0$ and at $\mathrm{Im}\,z=-\nu_m$. This allows to perform the frequency sum in (3.24) in a similar manner as we did to derive (3.20) and also the sum in the equation for the effective vertex (3.26), where in the latter case we have to consider, in addition to the cuts contribution, the pole contribution at $z=\omega'+\mathrm{i}\omega_m$. As in [VB02], the previous arguments on the analytic structure of the effective vertex imply that the analytic continuation $\mathrm{i}\nu_m\to\omega+\mathrm{i}0^+$ is well defined. Altogether, we find for the low-T conductivity to leading order in $1/\Gamma$, using (3.2):

$$\sigma^{(k)}=\frac{e^2\alpha^{(k)}}{3T}\left(\frac{M_\pi}{F_\pi}\right)^{4k}\int\frac{\mathrm{d}^3\boldsymbol{p}_1}{(2\pi)^3}\frac{|\boldsymbol{p}_1|^2}{E_1^2\Gamma_1}\;n_{\mathrm{B}}(E_1)\,[1+n_{\mathrm{B}}(E_1)]\,A^{(k)}(|\boldsymbol{p}_1|)\;, \tag{3.27}$$

with

$$A^{(k)}(|\boldsymbol{p}_1|)\equiv\frac{1}{|\boldsymbol{p}_1|^2}\int\frac{\mathrm{d}^3\boldsymbol{p}_2}{(2\pi)^3}\,\frac{\boldsymbol{p}_1\cdot\boldsymbol{p}_2}{8E_2^2\Gamma_2}A^{(k-1)}(|\boldsymbol{p}_2|)\,\{[n_{\mathrm{B}}(E_2-E_1)-n_{\mathrm{B}}(E_2)]$$
$$\times\,\rho\,(E_2-E_1,|\boldsymbol{p}_2-\boldsymbol{p}_1|)-[n_{\mathrm{B}}(E_2+E_1)-n_{\mathrm{B}}(E_2)]\,\rho\,(E_2+E_1,|\boldsymbol{p}_2+\boldsymbol{p}_1|)\}\;, \tag{3.28}$$

where we have also used that $\rho(\omega')=-\rho(-\omega')$ and we have denoted for the effective vertex $\boldsymbol{\Lambda}^{(k)}(x+\mathrm{i}0^+,x-\mathrm{i}0^+,\boldsymbol{p})=2\boldsymbol{p}\tilde{A}^{(k)}(|\boldsymbol{p}|;x)$ and $A^{(k)}(|\boldsymbol{p}|)=(\tilde{A}^{(k)}(|\boldsymbol{p}|;E_p)+\tilde{A}^{(k)}(|\boldsymbol{p}|;-E_p))/2$ so that $A^{(0)}=1$. For simplicity, we have denoted $E_{1,2}\equiv E_{p_1,p_2}$ and so on for $\Gamma_{1,2}$ and omitted their explicit dependence with $|\boldsymbol{p}_1|,|\boldsymbol{p}_2|$.

Let us comment on the result (3.28). The two terms in the right hand side correspond to evaluate the imaginary part of the rung loop at $p_1\pm p_2$ for on-shell $p_{1,2}$ "external" momenta. That is, those contributions arise from the s,t channels of the $\pi\pi$ elastic scattering amplitude of the double lines in Figure 3.12 (right), to one loop. Here we call by convenience $\mathcal{S}\equiv(E_1+E_2,|\boldsymbol{p}_1+\boldsymbol{p}_2|)$ and $\mathcal{T}\equiv(E_1-E_2,|\boldsymbol{p}_1-\boldsymbol{p}_2|)$. This interpretation will be very useful in our analysis of the different ChPT diagrams. In fact, note that

the remaining u-channel contribution would be given by the contribution to the effective vertex of the bubble diagrams in Figure 3.14, since the loop integral of the bubble does not depend on p_1 and p_2, only on the external photon momentum q, i.e, we can identify $\mathcal{U} \equiv (\omega, \mathbf{0})$. Now we remark (see Appendix C) that the imaginary part $\rho(E, |\boldsymbol{Q}|)$ is non-zero both for $E^2 \geq |\boldsymbol{Q}|^2 + 4M_\pi^2$ ("unitarity" cut) and for $E^2 \leq |\boldsymbol{Q}|^2$ ("thermal" cut). Since $s = \mathcal{S}^2 \geq 2M_\pi^2$, the s-channel is given by the unitarity contribution in (C.4) with $E = E_1 + E_2, \boldsymbol{Q} = \boldsymbol{p}_1 + \boldsymbol{p}_2$, while $t = \mathcal{T}^2 \leq 2M_\pi^2$ and thus the t-channel is given by the thermal part in (C.7) with $E = E_1 - E_2, \boldsymbol{Q} = \boldsymbol{p}_1 - \boldsymbol{p}_2$. Note that a consequence of this analysis is that, as announced, the bubble diagrams in Figure 3.14 are indeed suppressed in the $\omega \to 0^+$ limit since $u = \mathcal{U}^2 = \omega^2$ does not fall within any of the two cuts. This will be confirmed below.

At very low T, there are further simplifications of the above equations, namely $n_{\rm B}^2(E_{1,2}), n_{\rm B}(E_1 + E_2) \ll n_{\rm B}(E_{1,2}) \simeq \exp(-E_{1,2})/T$. Consistently, in the $\mathcal{S}$-channel, we can neglect the T-dependent part in the unitarity contribution (C.4). In the $\mathcal{T}$ channel, we can approximate in (C.7) the logarithm in the right hand side by $e^{-y_0/T}\left(1 - e^{-|E_1 - E_2|}\right) = e^{-(y_0 + |E_1 - E_2|)/T}/n_{\rm B}(|E_1 - E_2|)$. Since $y_0 \geq M_\pi$, the leading contribution in that term comes from the $n_{\rm B}(E_2 - E_1)$ term in (3.28), giving a net $\mathcal{O}(e^{-2M_\pi/T})$ contribution, the same as in the $\mathcal{S}$-channel and in the $\Gamma_1\Gamma_2$ in the denominator. The latter approximations are valid in the dilute gas regime, which as commented previously, extends to $T \lesssim M_\pi$. In addition, for $T \ll M_\pi$ in the $\mathcal{S}$-channel, the product of the Bose-Einstein distributions $n_{\rm B}(E_1)n_{\rm B}(E_2)$ implies $E_{1,2} \simeq M_\pi + [|\boldsymbol{p}_{1,2}|^2/(2M_\pi)]$ and hence, the two-particle phase-space is $\sigma_{\rm 2p} \simeq |\boldsymbol{p}_1 - \boldsymbol{p}_2|/(2M_\pi)$. Finally, we have for $T \ll M_\pi$:

$$\sigma_{\rm LT}^{(k)} = e^2\alpha^{(k)}\frac{M_\pi}{3}\left(\frac{F_\pi}{M_\pi}\right)^4\sqrt{\frac{M_\pi}{T}}\int\frac{{\rm d}^3\boldsymbol{y}_1}{(2\pi)^3}\frac{y_1^2}{f(y_1)}A_{\rm LT}^{(k)}\left(\sqrt{M_\pi T}y_1\right)\exp\left(-\frac{y_1^2}{2}\right)\,, \tag{3.29}$$

$$A_{\rm LT}^{(k)}\left(\sqrt{M_\pi T}y_1\right) \equiv \frac{1}{32\pi y_1^2}\int\frac{{\rm d}^3\boldsymbol{y}_2}{(2\pi)^3}\frac{\boldsymbol{y}_1\cdot\boldsymbol{y}_2}{|\boldsymbol{y}_1 - \boldsymbol{y}_2|f(y_2)}A_{\rm LT}^{(k-1)}(\sqrt{M_\pi T}y_2)\exp\left(-\frac{y_2^2}{2}\right)$$

$$\times\left\{\frac{|\boldsymbol{y}_1 - \boldsymbol{y}_2|^2}{4} + \exp\left[\frac{1}{4}\left(y_1^2 + y_2^2 - \frac{1}{2}\frac{(y_1^2 - y_2^2)^2}{|\boldsymbol{y}_1 - \boldsymbol{y}_2|^2} - \frac{1}{2}|\boldsymbol{y}_1 - \boldsymbol{y}_2|^2\right)\right]\right\}\,, \tag{3.30}$$

for $k \geq 1$, where the function f is defined as:

$$f(x) \equiv \frac{23}{512\pi^3}\left[\exp(-x^2/2) + \sqrt{\frac{\pi}{2}}\frac{1 + x^2}{x}\,{\rm erf}(x/\sqrt{2})\right]\,, \tag{3.31}$$

and we have rescaled $\boldsymbol{p}_{1,2} = \sqrt{M_\pi T}\boldsymbol{y}_{1,2}$ ($y_{1,2} \equiv |\boldsymbol{y}_{1,2}|$).

From the previous equations (3.29)-(3.30) we can draw one of our main conclusions: the low-T effective vertex $A_{\rm LT}^{(k)}\left(\sqrt{M_\pi T}y_1\right)$ is T-independent and hence, from (3.29) the correct order for the contribution of the k-rung ladder to the conductivity in our power counting scheme is $\sigma_{\rm LT}^{(k)} = e^2 M_\pi \mathcal{O}(X^k\sqrt{M_\pi/T}) = e^2 M_\pi \mathcal{O}(X^k Y)$ rather than the $\mathcal{O}(X^k Y^{k+1})$ following from direct inspection, as discussed at the beginning of this section. The independence of the LT effective vertex on T follows from (3.30) by induction, since $A^0 = 1$. Then, the only dependence with T in $\sigma_{\rm LT}^{(k)}$ is the $1/\sqrt{T}$, the same as the lowest order

(3.23). We can also understand why the "direct" counting misses k inverse powers of Y. The reason is that the contribution from the spectral functions introduce an extra $\sqrt{T/M_\pi}$ factor inside the integrand in (3.30). These factors come from $\rho_{\mathcal{S}} \sim |\boldsymbol{p}_1 - \boldsymbol{p}_2|/M_\pi$ and $\rho_{\mathcal{T}} \sim T/|\boldsymbol{p}_1 - \boldsymbol{p}_2|$ before rescaling the integration variables. This reflects the fact that the imaginary parts are small at low T due to the presence of the Bose-Einstein factors and represents one of the main differences between our analysis and the standard one in a coupling constant perturbation theory. The remaining $\mathcal{O}(X^k)$ contribution comes from having k chiral loops. To check explicitly our conclusions, we have evaluated numerically the one-rung contribution $k = 1$ in (3.29)-(3.30) setting $\alpha^{(1)} = 1$. We obtain $\sigma^{(1)}_{\rm LT}/\sigma^{(0)}_{\rm LT} \simeq 0.06$. The reason why this gives a slightly higher value than expected by power counting is the presence of a collinear effect in the $\mathcal{T}$-channel, coming from the region $\boldsymbol{y}_1 \simeq \boldsymbol{y}_2$ in (3.30). The integral is convergent but that region enhances its value with respect to the $\mathcal{S}$ channel. In fact, for $k = 1$ the $\mathcal{T}$-channel contribution is about five times larger than the $\mathcal{S}$-channel one, which has the expected chiral reduction mentioned above. Collinear effects of this kind are characteristic of these analysis and play a crucial role in gauge theories [Moo04, Aur98]. In our case, this numerical enhancement does not spoil the perturbative nature of these contributions.

We can then conclude that the ladder diagrams at very low T, although representing the main contribution beyond leading order, are perturbative in the ChPT scheme. Moreover, following our previous arguments, it is not difficult to conclude that, as far as the ladder diagrams are perturbatively controlled in the chiral expansion, so are the same diagrams with vertices coming from the lagrangians $\mathcal{L}_d$ with $d > 2$ and also ladder diagrams with rung loops made with more than four pion vertices.

Ladder diagrams for $T \lesssim M_\pi$

Our previous analysis shows that the ladder diagrams are still chirally perturbative in the very low T region, even though we should not miss the fact that their correct counting gives a much larger contribution than their standard ChPT one, namely $\sigma^{(k)}/\sigma^{(0)} = \mathcal{O}(p^{2k})$ instead of the $\mathcal{O}(p^{4k})$ given by Weinberg's theorem (1.43). The reason is the presence of the non-perturbative Y factors, as we have seen. Following our chiral counting arguments for temperatures of the order of M_π, we realize first that now $Y \sim \mathcal{O}(1)$ around $T \sim M_\pi$. This means that we expect again $\sigma^{(k)}/\sigma^{(0)} = \mathcal{O}(p^{2k})$ for the k-ladder diagram, coming from the rung loops. It must be reminded though that for these temperatures, the simplification of reducing any ladder diagram to one with constant vertices does not hold. In fact, for higher temperatures we expect derivative vertices to become increasingly important, but as long as T remains within the ChPT applicability range (not much above the pion mass) we can consider all those diagrams perturbatively suppressed.

To check our previous comment we have evaluated numerically the ladder diagram with one rung and constant vertices, setting in (3.27)-(3.28) $k = 1$ and $\alpha^{(1)} = 1$ and performing only the dilute gas approximations mentioned in the previous section but not those specific of $T \ll M_\pi$. We have also considered, for comparison, the contribution of a ladder diagram with one rung but with one possible combination of derivative vertices, namely, that obtained by taking $k = 1$ in (3.27)-(3.28) but replacing the constant $(M_\pi/F_\pi)^4$ factor by $|\boldsymbol{p}_1|^4/F_\pi^4$ in the integrand. The results are shown in Figure 3.13, where we have also

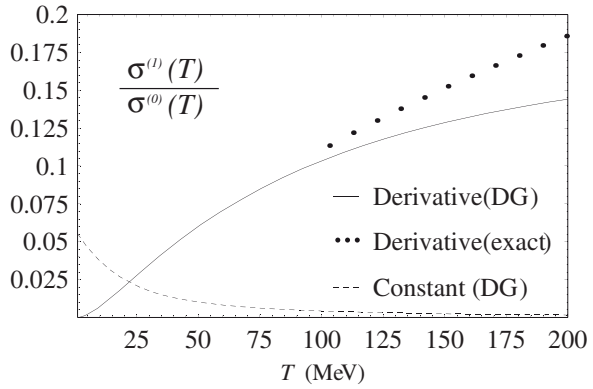

Figure 3.13: Estimation of the contribution of ladder diagrams for higher temperatures, with and without derivative vertices. The points correspond to the exact expressions without using the dilute gas approximation.

put for comparison some points calculated without using the dilute gas approximation. Clearly, the derivative vertices become the more important ones at moderate and high temperatures, showing that the sum of ladder diagrams is expected[8] to be more relevant at temperatures close to the phase transition, where the ChPT power counting fails anyway.

Bubble diagrams

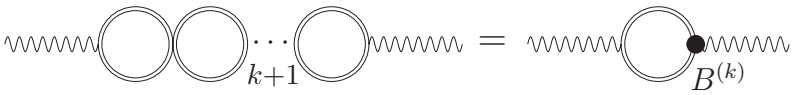

Figure 3.14: A generic bubble diagram with $k+1$ bubbles ($k \geq 1$).

In the case of the bubble diagram shown in Figure 3.14, which could in principle give non-perturbative contributions of $\mathcal{O}(Y^n)$, our previous discussion based on the scattering of internal lines has already suggested that these diagrams do not receive contributions of $\mathcal{O}(1/\Gamma)$ to the conductivity. Let us show this in more detail. First, we define a k-bubble effective vertex $\boldsymbol{B}^{(k)}$ with $k \geq 1$ (see Figure 3.14) exactly as we have done in (3.24) for the ladder vertices $\boldsymbol{\Lambda}^{(k)}$. Given the structure of the bubble vertices, one readily realizes that, unlike the ladder ones, $\boldsymbol{B}^{(k)}(\mathrm{i}\omega_n + \mathrm{i}\nu_m, \mathrm{i}\omega_n, \boldsymbol{p})$ is independent of the frequency and momentum of the external pion leg $(\mathrm{i}\omega_n, \boldsymbol{p})$ if only constant four-pion vertices are considered. Therefore, the contribution of those diagrams to the conductivity vanishes by parity, for instance by making $\boldsymbol{p}_1 \mapsto -\boldsymbol{p}_1$ in the integral analogous to (3.24). Thus, one needs derivative vertices to yield a non-vanishing contribution. In fact, following the parity argument, the only contributions of a $k+1$-bubble diagram which do not vanish by parity are those where all the four-pion vertices contain the factor $\boldsymbol{p}_i \cdot \boldsymbol{p}_{i+1}$ $(i = 1, \ldots, k)$ where p_i is the momentum running through the i-th bubble. We remark that we are

[8]However, there might be cancellations between subsets of ladder diagrams [Car98a, Car98b].

considering only pion vertices coming from $\mathcal{L}_2$, higher order vertices being suppressed by Weinberg's power counting and the same holds for bubbles made with more pion lines, say with vertices with more than four pions. Thus, the bubble effective vertices satisfy a recurrence relation of the form:

$$\boldsymbol{B}^{(k)}(\mathrm{i}\nu_m,\boldsymbol{p}) = \int \frac{\mathrm{d}^3\boldsymbol{p}_2}{(2\pi)^3}\,\frac{\boldsymbol{p}\cdot\boldsymbol{p}_2}{F_\pi^2}\,T\sum_{n=-\infty}^{\infty}\boldsymbol{B}^{(k-1)}(\mathrm{i}\nu_m,\boldsymbol{p}_2)\Delta_\Gamma(\mathrm{i}\omega_n,|\boldsymbol{p}_2|)\Delta_\Gamma(\mathrm{i}\omega_n+\mathrm{i}\nu_m,|\boldsymbol{p}_2|)\ . \tag{3.32}$$

In fact, we should take into account that here there can also be neutral pion loops in bubble diagrams with more than two bubbles, implying different vertex and combinatoric numerical factors in front of $\boldsymbol{p}_i\cdot\boldsymbol{p}_{i+1}$ for the $\pi^0\pi^0\pi^+\pi^-$, $\pi^+\pi^-\pi^+\pi^-$ and $(\pi^0)^4$ vertices. Thus, we really have to define two effective vertices $\gamma\pi^+\pi^-$ and $\gamma\pi^0\pi^0$, the latter starting with one bubble and one has then two coupled recurrence relations between those vertices, instead of the single one in (3.32). However, that merely complicates the calculation but does not change our main conclusion, namely that bubble diagrams are subdominant. Hence, for simplicity, let us show it for the case in which all 4π vertices contribute simply as $\boldsymbol{p}_i\cdot\boldsymbol{p}_{i+1}/F_\pi^2$ and all internal lines are charged. Proceeding then as we did in our analysis of ladder diagrams, we realize that the calculation is particularly simple now since the vertex (3.32) is still independent of the frequency of the external leg $\mathrm{i}\omega_m$ and therefore there is no pole contribution, unlike (3.26). After doing the Matsubara sum, and performing the analytic continuation $\mathrm{i}\nu_m\mapsto\omega+\mathrm{i}0^+$, we get to leading order in $1/\Gamma$ and $\omega\to 0^+$:

$$\boldsymbol{B}^{(k)}(\omega,\boldsymbol{p}) = \frac{\mathrm{i}\omega}{T}\int\frac{\mathrm{d}^3\boldsymbol{p}_2}{(2\pi)^3}\,\frac{\boldsymbol{p}\cdot\boldsymbol{p_2}}{F_\pi^2}\,\frac{n_{\mathrm{B}}(E_2)\left[1+n_{\mathrm{B}}(E_2)\right]}{4E_2^2\Gamma_2}\boldsymbol{B}^{(k-1)}(\omega,\boldsymbol{p}_2) \equiv \frac{\mathrm{i}\omega\boldsymbol{p}}{F_\pi^2}F^{(k-1)}(\omega;T)\ , \tag{3.33}$$

for $k\geq 1$, where the last equality holds by Euclidean covariance and defines the scalar function F, which satisfies then the recurrence relation:

$$F^{(k)}(\omega;T) = \frac{\mathrm{i}\omega I(T)}{F_\pi^2}F^{(k-1)}(\omega;T) = 2I(T)\left[\frac{\mathrm{i}\omega I(T)}{F_\pi^2}\right]^k\ , \tag{3.34}$$

where $I(T)$ is the integral appearing in the lowest order conductivity in (3.22), namely $\sigma^{(0)}=4e^2I(T)$ and we have used that $B_j^{(0)}=\Lambda_j^{(0)}=2p_j$ so that $F^{(0)}=2I(T)$.

From the above results, we note that the two main differences between the bubble effective vertices and the ladder ones are, first, that for small ω, the contribution of the $k+1$-bubble diagram to the conductivity is $\mathcal{O}(\omega^k)$ and, second, that the bubble effective vertices are not all real, $B^{(k)}$ is real for k even and purely imaginary for k odd, to leading order in $1/\Gamma$. This confirms our previous discussion about the role of the different diagrams as related to the "scattering" of the internal pion lines. The one-bubble diagram amounts to the tree level contribution to the scattering in ChPT which is always real. The first diagram giving a non-vanishing contribution to the scattering spectral function is the two-bubble one, but it vanishes as $\omega\to 0^+$ as corresponds to the $\mathcal{U}$ channel.

The simple form of the bubble vertices allows to perform explicitly their contribution to the conductivity, since they form basically a geometric series according to (3.34). The

fact that bubble diagrams can be summed is a well-established result and holds also in other analysis of transport coefficients [Jeo95]. In fact, we remark that in our case it is consistent to sum them, following our power counting arguments, since the bubble diagrams are neither reduced by chiral loops like the ladder ones (all lines are double) nor by higher order pion vertices if all pion vertices come from $\mathcal{L}_2$.

Thus, the contribution of the sum of the bubble diagrams to the conductivity is of the form:

$$\begin{aligned}\sigma_{\rm bub} &= \frac{e^2}{3}\lim_{\omega\to 0^+}\frac{1}{T}\int\frac{{\rm d}^3\boldsymbol{p}}{(2\pi)^3}\frac{n_{\rm B}(E_p)\,[1+n_{\rm B}(E_p)]}{4E_p^2\Gamma_p}\,{\rm Re}\sum_{k=1}^{\infty}2\boldsymbol{p}\cdot\boldsymbol{B}^{(k)}(\omega,\boldsymbol{p})\\ &= 2e^2\lim_{\omega\to 0^+}{\rm Re}\sum_{k=1}^{\infty}F^{(k)}(\omega)=\sigma^{(0)}(T)\lim_{\omega\to 0^+}{\rm Re}\,\frac{{\rm i}\omega I(T)/F_\pi^2}{1-{\rm i}\omega I(T)/F_\pi^2}\\ &= \mathcal{O}(\omega^2)\sigma^{(0)}(T)\ ,\end{aligned}\tag{3.35}$$

and the same conclusion, i.e., $\sigma_{\rm bub}=\mathcal{O}(\omega^2)\sigma^{(0)}(T)$ is reached when considering the full contributions of charged and neutral diagrams, as commented before. We wish to stress that the leading order in the bubble vertices comes from the "pinching poles" in products $G_{\rm R}G_{\rm A}$ and carries the $\mathcal{O}(\omega/\Gamma)$ contributions analyzed above. Taking the next-to-leading order could give a non-vanishing contribution as $\omega\to 0^+$ but with no $1/\Gamma$ terms (the $I(T)$ integrals above) and therefore suppressed by the ordinary chiral power counting of the loops so that, typically, the $\omega I(T)$ factors in the sum (3.35) would be replaced by an $\mathcal{O}(p^2)$ contribution. Therefore, our conclusion is that the bubble diagrams are subdominant for all temperatures within the validity range of ChPT.

3.4 Results for transport coefficients

3.4.1 Electrical conductivity

As we saw in Section 3.3.1, Eq. (3.22), the leading-order contribution to the DC conductivity to low temperatures, corresponding to the diagram 3.10, is given by

$$\sigma^{(0)}=\frac{e^2}{3T}\int\frac{{\rm d}^3\boldsymbol{p}}{(2\pi)^3}\,\frac{|\boldsymbol{p}|^2}{E_p^2\Gamma_p}n_{\rm B}(E_p)[1+n_{\rm B}(E_p)]\ ,$$

And for very low temperatures, $T\ll M_\pi$, we have:

$$\sigma^{(0)}\simeq 14\,\frac{e^2F_\pi^4}{T^{1/2}M_\pi^{5/2}}\ .$$

It is interesting to compare our result with the expected kinetic theory (KT) behavior. According to KT, $\sigma\sim e^2n_{\rm ch}\tau/M_\pi$ ($n_{\rm ch}$ is the density of charged particles, τ is the collision mean time, and e is the particle charge), and $\tau\sim 1/\Gamma$, $\Gamma\sim nv\sigma_{\pi\pi}$ (v is the mean speed of the particles). In the non-relativistic limit ($T\ll M_\pi$), $n\sim(\sqrt{M_\pi T})^3{\rm e}^{-M_\pi/T}$, $v\sim\sqrt{T/M_\pi}$, and $\sigma_{\pi\pi}$ is a constant, therefore $\sigma\sim 1/\sqrt{T}$. Thus, our result in ChPT is consistent with KT for $T\ll M_\pi$.

In Fig. 3.15 we plot the lowest order contribution to the DC conductivity as a function of temperature for different choices of the scattering amplitudes that enter into the pion width. We see that unitarization (resonances) makes the conductivity grow from certain temperature on, otherwise it would decrease to asymptotically zero with temperature. An increasing behavior for the DC conductivity is also obtained in lattice calculations [Gup04]. The dots in the plot correspond to unitarizing the scattering amplitudes at finite temperature, as we explained in Section 2.1. We see that the thermal evolution of the resonances does not affect much the conductivity. A more significant effect on the conductivity is produced when finite nuclear density is considered effectively by reducing F_π according to (2.27), but only at low temperatures (as we can see in Fig. 3.15, at high temperatures $\sigma^{(0)}$ is approximately constant, indicating that medium effects might be not important in that regime).

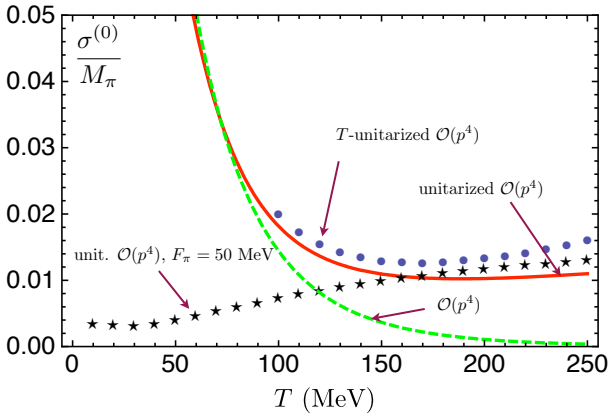

Figure 3.15: Lowest-order contribution to de DC conductivity as a function of the temperature. The dashed line corresponds to considering non-unitarized partial waves to $\mathcal{O}(p^4)$ in the pion width, the red line corresponds to the unitarized case to $\mathcal{O}(p^4)$, and the dots correspond to unitarize at $\mathcal{O}(p^4)$ at finite temperature. The stars correspond to unitarized partial waves to $\mathcal{O}(p^4)$ with $F_\pi = 50$ MeV ($\rho \simeq 2\rho_0$) simulating nuclear density according to (2.27).

Soft-photon spectrum

As a phenomenological application of the previous calculation of the electrical conductivity, we now consider the photon emissivity coming from the hadronic phase. The photon differential rate emerging from an equilibrated system is directly related with the EM current-current spectral function as [Ala01]:

$$\omega \frac{\mathrm{d}R_\gamma}{\mathrm{d}^3\boldsymbol{p}} = \frac{1}{8\pi^3} n_{\mathrm{B}}(\omega) \rho^\mu{}_\mu(\omega = |\boldsymbol{p}|) \ . \tag{3.36}$$

The Ward Identity $p^\mu \rho_{\mu\nu} = 0$ implies $\rho_{00}(\omega \neq 0, \boldsymbol{p} = 0) = 0$ so that the electrical conductivity provides direct information about the vanishing energy limit ($\omega \to 0^+$) in the static region [Gup04, Bla05] simply as $\omega \mathrm{d}R_\gamma/\mathrm{d}^3\boldsymbol{p}(\omega \to 0^+, \boldsymbol{p} = 0) = 3T\sigma(T)/(4\pi^3)$,

i.e, a non-zero conductivity implies a constant value for the photon yield near the origin[9].

With this motivation in mind, we will compare our results for the conductivity for temperatures physically relevant in a Relativistic Heavy Ion environment with some recent theoretical and experimental analysis of the low-energy hadronic photon spectrum. Among the theoretical works, one can find the virial expansion approach followed in [Ste96] with non-strange mesons only, extended in [Ste97] to include baryon density. More recent analysis follow the conventional kinetic theory approach, where all possible photon-producing reactions of the type $1 + 2 \to 3 + \gamma$ are evaluated, 1,2,3 being meson degrees of freedom $\pi, \rho, \mathrm{K}, ...$ parametrized in an effective lagrangian with explicit resonances included [Ala01, Rap99, Tur04]. Within the latter framework, the present experimental data are described remarkably well for $\omega > 200$ MeV when all the relevant processes are evaluated and finite density effects are accounted for [Tur04]. However, it is worth mentioning that recent analysis of the WA98 experiment [Agg04] at CERN have produced data at lower transverse momentum, showing a slight systematic enhancement with respect to theoretical predictions. At those low energies, the hadronic gas contribution seems to dominate over the QGP one.

The low-energy rate with non-strange mesons in [Ste96], which deals then with the same degrees of freedom as our approach, reaches a maximum value of approximately 3×10^{-5} GeV^{-2}fm^{-5} (for $T = 150$ MeV) at $\omega \sim 400$ MeV and then drops to zero at the origin. When including baryons in the same approach [Ste97] the behavior is the same but the maximum is at $\omega \sim 200$ MeV and grows up to about 4×10^{-4} GeV^{-2}fm^{-4}. The results in [Rap99] for the hadronic gas are similar to those in [Ste96, Ste97] except that the curve with baryon density decreases monotonically for $\omega \geq 200$ MeV (they do not analyze smaller frequencies). In [Tur04], more relevant channels have been included, the most interesting result being that there are meson contributions that do not vanish when approaching the origin, for instance those involving $\pi\rho a_1$ mesons. The latter contributions amount to almost twice more photons near the origin that in the earlier work [Rap99]. We remark that the prediction in [Tur04] is the one used in the experimental WA98 paper [Agg04] to compare with data and the rate thereof remains below the lowest energy experimental points (cf. Figure 3.16). Using the unitarized width, we get for the vanishing energy photon rate $3T\sigma/(4\pi^3) \simeq 3.7 \times 10^{-3}$ GeV^{-2}fm^{-4} at $T = 150$ MeV. Therefore, we predict a sizable value of the hadronic photon rate at the origin. A linear extrapolation of the low energy curve ($\omega \simeq 200$ MeV) in [Tur04] to the origin gives a value of about 2×10^{-3}GeV^{-2}fm^{-4} at $T = 150$ MeV. This is an indication that our prediction lies in the correct range.

We will now try to establish a more direct comparison with experimental data, bearing in mind that our approach only gives information about the value very close to the origin. One then has to integrate the photon rate in (3.36) over space-time and average over the photon rapidity [Tur04] in order to obtain the experimentally measured photon yield $\omega \mathrm{d}N_\gamma/\mathrm{d}^3\boldsymbol{p}$ as a function of p_T, the component of the photon momentum transverse to

[9]This result for the photon spectrum extrapolates smoothly from the time-like static region $(\omega, \mathbf{0})$ to the light-like one. Remember that the small energy and momentum limits of the thermal correlators may give different answers. We have checked explicitly that to leading order $G^\mathrm{R}_{00}(\omega \neq 0, \mathbf{0}) = 0$, according to the Ward Identity, when a tadpole diagram contributing to $\mathrm{Re}(\mathrm{i}G^\mathrm{R}_{00})$ is added to the diagram in Figure 3.10 with zero-width in the pion lines. However, from (C.10)-(C.12) we find that $\rho_{00}(\omega \to 0^+, |\boldsymbol{p}| \to 0^+)/\omega$ vanishes for slightly time-like photons but diverges for space-like ones, analogously to (3.7).

the collision axis in the laboratory frame. Obviously, the results depend heavily on the hydrodynamical space-time evolution for the conditions applicable to a particular experiment. We will just give here rough estimates and for that purpose we will neglect transverse flow and assume a simple Bjorken's hydrodynamical description [LB96, Pei02] so that $\omega = p_{\mathrm{T}} \cosh(y - \eta)$ with y and η the photon and fluid rapidities respectively. Therefore, our value at $\omega \to 0^+$ translates directly into the value of the yield at $p_{\mathrm{T}} \to 0^+$. As for the space-time integration, we use the typical value [LB96, Pei02] for the nuclear transverse radius $R_A \simeq 1.3$ fm $A^{1/3} \simeq 7.7$ fm for ^{208}Pb and change to proper time τ and rapidity η coordinates. In the Bjorken's limit and for $p_{\mathrm{T}} \to 0^+$, there is no dependence with rapidity so that we have simply to multiply by the expansion velocity [Pei02] $\Delta\eta_{\mathrm{nucl}} = 2\,\mathrm{arccosh}(\sqrt{s}/2A\ \mathrm{GeV}) \simeq 10.1$ for the WA98 collision energy $\sqrt{s} = 158A$ GeV. With these approximations, the photon yield at the origin is given by:

$$\omega \frac{\mathrm{d}N_\gamma}{\mathrm{d}^3\boldsymbol{p}}(p_{\mathrm{T}} \to 0^+) \simeq \pi R_A^2 \Delta\eta_{\mathrm{nucl}} \int_{\tau_{\mathrm{i}}}^{\tau_{\mathrm{f}}} \frac{3T(\tau)\sigma(T(\tau))}{4\pi^3}\, \tau \mathrm{d}\tau \ . \tag{3.37}$$

A crude estimate is obtained by assuming a purely thermal hadronic phase, i.e., a constant temperature. Taking proper time values $\tau_{\mathrm{i}} = 1$ fm/c and $\tau_{\mathrm{f}} = 13$ fm/c [Tur04] and $T = 150$ MeV, this gives $\mathrm{d}N_\gamma/\mathrm{d}^3\boldsymbol{p}(p_{\mathrm{T}} = 0) \simeq 5.8 \times 10^2$. A more realistic approximation is to take the cooling law of an ideal gas $T(\tau) = T_{\mathrm{i}}(\tau_{\mathrm{i}}/\tau)^{1/3}$ [LB96] which is probably still rather crude for mesons at moderate or high temperatures. Taking $\tau_{\mathrm{i}} = 3$ fm/c, more appropriate for the hadronic phase, $\tau_{\mathrm{f}} = 13$ fm/c and $T_{\mathrm{i}} = 170$ MeV, we get $T_{\mathrm{f}} = 104$ MeV which is of the order of the freeze-out temperature. Inserting this law in (3.37) with the unitarized conductivity in Fig. 3.15 we obtain $\mathrm{d}N_\gamma/\mathrm{d}^3\boldsymbol{p}(p_{\mathrm{T}} = 0) \simeq 5.6 \times 10^2$ (we indicate this value in the plot of Fig. 3.16) although this result is very sensitive to variations in temperature.

Taking the two points of smallest p_{T} in [Agg04] and simply extrapolating them to the origin with a straight line gives $\mathrm{d}N_\gamma/\mathrm{d}^3\boldsymbol{p}(p_{\mathrm{T}} = 0) \simeq 5 \times 10^2$. Therefore, our results are compatible with the recent data, in the sense of a naive linear extrapolation from the origin and not forgetting that we are bordering the applicability range of our approach, in addition to the many approximations performed to arrive to a number comparable with experiment. In any case, our analysis would suggest that purely thermal cuts in pion-pion annihilation (there is no $T = 0$ real photon production from $\pi\pi$ annihilation for energies below $2M_\pi$) with a non-zero pion thermal width may be a relevant effect[10]. In this sense, it should be borne in mind that the pion thermal width is not considered in [Ste96, Ste97, Ala01, Rap99, Tur04] since it does not play any role at the energies of interest for the photon yield considered in those works. For low energies the hadronic component is expected to dominate the spectrum, and it that regime a finite width in the particle propagator may be relevant due to the Landau-Pomeranchuk—Migdal (LPM) effect[11], which was not taken into account in those studies and would make the contribution to the spectrum finite at the origin [Liu07]. On the other hand, our approach could be too limited to describe correctly the effect of some resonances like the a_1. It is

[10] We would get a vanishing contribution to the $\omega \to 0^+$ photon spectrum with zero pion width and slightly time-like photons.

[11] The LPM effect consists in the suppression of bremsstrahlung due to multiple scatterings of the pion with particles in the medium, and it is closely related to the (non-zero) thermal width of the pion.

also unclear whether our prediction at small energies has simply to be added to previous hadronic ones, since we are extracting the photon rate from the self-energy and not from individual processes. What is more clear in this respect is that the contribution analyzed here does not come from baryonic sources.

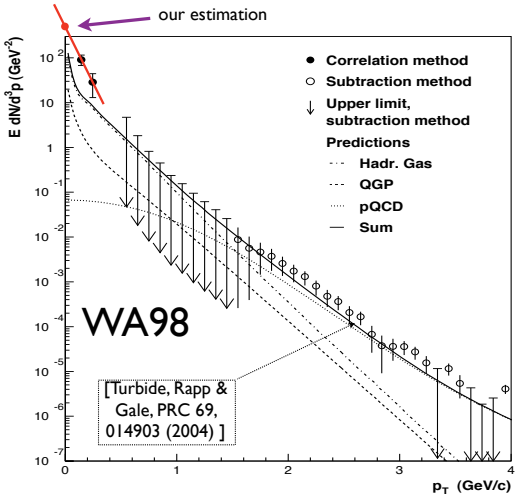

Figure 3.16: Photon spectrum obtained by the experiment WA98 [Agg04]. Our estimate at the origin is compatible with a linear extrapolation from the two lowest-energy points.

3.4.2 Thermal conductivity

Although in the pion gas the only strictly conserved quantity is the energy-momentum tensor, in the energy and temperature regime we are dealing with, it is a good approximation to assume that $2 \to 2$ collisions are the only relevant scattering processes in a Heavy-Ion Collision environment, which in practice means that the pion number is approximately conserved (see Chapter 4), yielding a non-zero thermal conductivity even when the pion chemical potential is very small [Gav85]. The thermal conductivity is given by[12]:

$$\kappa = -\frac{\beta}{6} \lim_{\omega \to 0^+} \lim_{|\boldsymbol{p}| \to 0^+} \frac{\rho_\kappa(\omega, |\boldsymbol{p}|)}{\omega} \ , \tag{3.38}$$

where

$$\rho_\kappa(\omega, |\boldsymbol{p}|) = \int \mathrm{d}^4x \ \mathrm{e}^{\mathrm{i}p\cdot x} \langle [\hat{\mathcal{T}}^i(x), \hat{\mathcal{T}}_i(0)] \rangle \ , \tag{3.39}$$

[12]Strictly, the limit of external frequency going to zero means that we take into account the scattering processes at any time scale. For an arbitrary long time interval, inelastic processes would compensate the elastic ones, giving a zero thermal conductivity. However, we can keep the limit of frequency going to zero provided inelastic processes are not included in the Feynman diagrams of the corresponding correlator (see also the discussion regarding inelastic processes in the calculation of the bulk viscosity, Section 3.4.4).

with $\mathcal{T}^i \equiv T^{i0} - hN^i$ [13]. But now, under this assumption, thermal averages would only imply sums over states of well-defined number of particles, $|N\rangle$. Then, since in the diagram of Fig. 3.10 the energy-momentum enters to lowest order (i.e. without interaction), and based on the KT theory expressions of Section 1.5.1 in equilibrium:

$$T^{i0} = \int \frac{\mathrm{d}^3\boldsymbol{p}}{(2\pi)^3}\ E_p v^i n_{\mathrm{B}}(E_p)\ , \tag{3.40}$$

$$N^i = \int \frac{\mathrm{d}^3\boldsymbol{p}}{(2\pi)^3}\ v^i n_{\mathrm{B}}(E_p)\ , \tag{3.41}$$

with $v^i = p^i/E_p$, we define the operator $\hat{N}^i$ through its Feynman rule for the vertex in momentum space heuristically as $N^i \equiv T^{i0}/E_p$ (the limit of external momentum equal to zero is understood). According to this, the lowest-order contribution is then given by:

$$\kappa^{(0)} = \frac{1}{8\pi^2 T^2}\int_0^\infty \mathrm{d}|\boldsymbol{p}|\ \frac{|\boldsymbol{p}|^4(E_p-h)^2}{E_p^2\Gamma_p} n_{\mathrm{B}}(E_p)[1+n_{\mathrm{B}}(E_p)]\ . \tag{3.42}$$

This expression is very similar to the one obtained in [Gav85] for the pion gas. As we have seen in the derivation of the Kubo formula for the thermal conductivity, here h represents the *exact* heat function per particle. However, we will approximate in our results $h \equiv (\epsilon + P)/n = Ts/n$ (s is the entropy density and n the density of particles) by the corresponding ideal gas expression, since we expect it to be reasonable for low temperatures[14]. For very low temperatures, $T \ll M_\pi$, we have:

$$\kappa^{(0)} \simeq 63\ \frac{T^{1/2}F_\pi^4}{M_\pi^{5/2}}\ . \tag{3.43}$$

By KT [Lif81], $\kappa \sim T^{-1}(\bar{e}-h)lv$ ($\bar{e}$ is the mean energy per particle and $l \sim 1/(\sigma_{\pi\pi}n)$ is the particle mean free path). In the non-relativistic limit, $\bar{e} \sim M_\pi$, $h \sim 5T/2 + M_\pi$, and then $\kappa \sim T^{1/2}$, so it is compatible with our result for low temperatures. In Fig. 3.17 we compare our results for κ with a KT analysis [Pra93]. Again, unitarity changes the behavior of the thermal conductivity with temperature, showing a minimum near $T = 140$ MeV. We now see that density effects modify significantly the thermal conductivity at high temperatures, as expected when introducing an additional conserved charge (the baryon number). Finally, we would like to remark that the contribution from the heat function is essential to determine the qualitative behavior of the thermal conductivity at low temperatures. In Figure 3.18 we plot $\kappa^{(0)}$ without the contribution from h and compare with the KT result from [Dob07b], where they do not include this term and also use scattering amplitudes obtained with the IAM. As we can see, the agreement between both results is very good, but the qualitative behavior at very low temperatures is different from the one in Fig. 3.17.

[13] Note that in [FF07b] we did not take into account the term with N^i, and therefore the result that we show here is qualitatively different at low temperatures.

[14] In the KT calculation of [Pra93, Dav96], h is consistently included in the ideal gas approximation (see comments in Section 1.5.5). On the other hand, within our diagrammatic approach, we do not expect that higher order contributions in h change much the qualitative behavior of $\kappa^{(0)}$ with the temperature, because the change in s/n with T when these corrections are included is small (see Chapter 4).

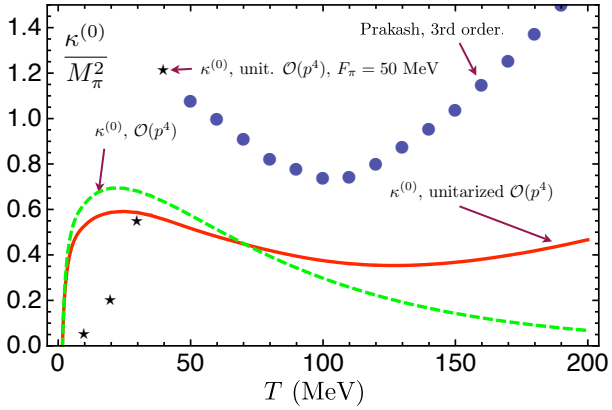

Figure 3.17: Lowest-order contribution to the thermal conductivity as a function of the temperature. We compare with the analysis of [Pra93], which is based on kinetic theory.

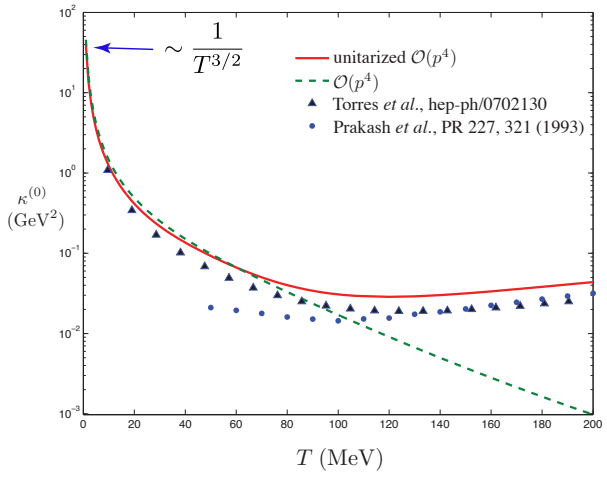

Figure 3.18: Lowest-order contribution to the thermal conductivity of a pion gas as a function of the temperature without the contribution from the heat function. We compare with the analysis of [Dob07b], which is based on kinetic theory and uses the IAM scattering amplitudes.

3.4.3 Shear viscosity

It is given in LRT by:

$$\eta = \frac{1}{20} \lim_{\omega \to 0^+} \lim_{|\boldsymbol{p}| \to 0^+} \frac{\rho_\eta(\omega, |\boldsymbol{p}|)}{\omega} \ , \tag{3.44}$$

with

$$\rho_\eta(\omega, |\boldsymbol{p}|) = \int \mathrm{d}^4x \ \mathrm{e}^{\mathrm{i}p\cdot x} \langle [\hat{\pi}^{ij}(x), \hat{\pi}_{ij}(0)] \rangle \ , \tag{3.45}$$

and $\pi^{ij} \equiv T^{ij} - g^{ij} T^k_{\ k}/3$. Then, the lowest-order contribution is:

$$\eta^{(0)} = \frac{1}{10\pi^2 T} \int_0^\infty \mathrm{d}|\boldsymbol{p}| \ \frac{|\boldsymbol{p}|^6}{E_p^2 \Gamma_p} n_{\mathrm{B}}(E_p)[1 + n_{\mathrm{B}}(E_p)] \ , \tag{3.46}$$

For very low temperatures, $T \ll M_\pi$, we have:

$$\eta^{(0)} \simeq 37 \frac{T^{1/2} F_\pi^4}{M_\pi^{3/2}} \ . \tag{3.47}$$

In Fig. 3.19 we compare our results for the shear viscosity with those obtained by Prakash *et al.* using a KT analysis [Pra93]. We also agree with a pion gas KT work by Dobado *et al.* [Dob04]. We see that nuclear density effects would only imply a significant change in the shear viscosity at low temperatures. By non-relativistic KT we expect the behavior $\eta, \zeta \sim M_\pi v n l$, thus $\eta, \zeta \sim \sqrt{T}$ and both viscosities should then be of the same order at very low temperatures[15].

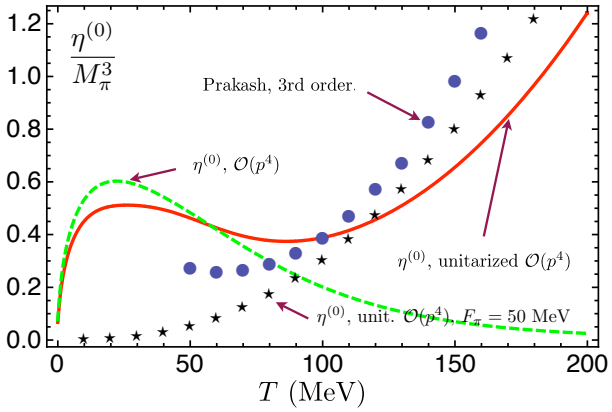

Figure 3.19: Lowest-order contribution to the shear viscosity as a function of temperature for several approximations in the scattering amplitudes. We also compare with the KT results of [Pra93] (dots).

Unitarity makes the quotient η/s (s is the entropy density) for the pion gas respect the bound $1/(4\pi)$ conjectured by Kovtun *et al.* for any type of matter [Kov05], as we can see in Fig. 3.20. Without unitarization, the Uncertainty Principle would be also violated eventually, since $\eta/s \sim \epsilon\tau/n \sim E\tau \gtrsim 1$. Furthermore, near T_c our value for η/s is not far from recent lattice and model estimates [Nak05]. Although we do not represent it in the figure, we do obtain a behavior for η/s growing very slowly with T for temperatures (unrealistic) > 550 MeV. A slowly increasing behavior is also obtained by high-temperature calculations from the quark gluon plasma (QGP) phase [Cse06]. It is also remarkable the fact that the AdS/CFT result $\eta/s = 1/(4\pi)$ is temperature independent [Kov05]. However, a recent analysis predicts a more pronounced increase of the shear viscosity near the phase transition, in the so-called semi-QGP phase [Hid08b, Hid08a]. It is well known that the quantity η/s for several common substances presents a minimum at the phase transition temperature [Cse06, Dob09], and therefore it is also expected that this minimum occurs in QCD at the critical temperature. In Section 3.4.5, we shall see that the large-N_c behavior of η/s below and above the critical temperature is also compatible with a minimum at the transition point.

[15]However, as we shall see in Section 3.4.4, and as we have discussed at the end of Section 3.1.2, the actual behavior of the bulk viscosity at very low temperatures is $\zeta \propto \exp(2M_\pi/T)$, being much larger than the shear viscosity in that regime.

As another check, we can compute the sound attenuation length, which is given by (neglecting the contribution from the bulk viscosity) $\Gamma_s \simeq 4\eta/(3sT)$, and is directly related to phenomenological effects such as *elliptic flow* or *HBT radii* (see Section 1.2). We get, at $T = 180$ MeV, the value $\Gamma_s \simeq 0.55$ fm, in agreement with the estimate by Teaney [Tea03].

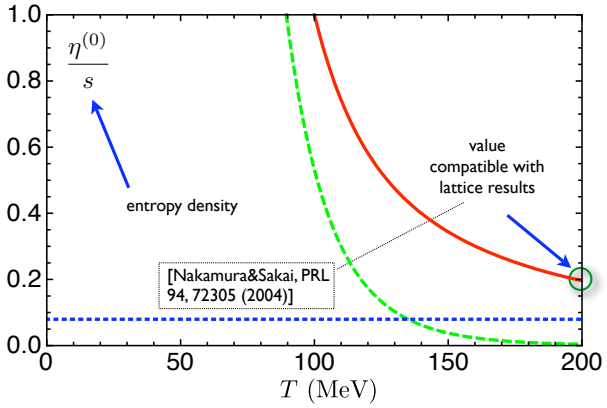

Figure 3.20: Shear viscosity over the entropy density as a function of temperature. The horizontal dashed line corresponds to the AdS/CFT bound $1/(4\pi)$.

In the chiral limit with only $\mathcal{O}(p^2)$, we get exactly $\eta = 18\pi\zeta(3)F_\pi^4/(25T)$ with the Riemann's zeta function $\zeta(3) \simeq 1.2$. This $1/T$ decreasing behavior, obtained for instance in [Che07], would imply that the AdS/CFT bound for η/s is violated at some point, departing also from the phenomenological estimates discussed above. This highlights the importance of reproducing correctly the high energy features of particle scattering, as we do within our unitarized approach.

3.4.4 Bulk viscosity and the trace anomaly

As we mentioned in the introduction, it has been recently proposed [Kar08] that ζ might be large near the QCD phase transition. The argument is that, by using the QCD sum rule [Ell98, Shu99]

$$\left(T\frac{\partial}{\partial T} - d\right)^n \langle\hat{\mathcal{O}}\rangle = \int \mathrm{d}\tau_n \int \mathrm{d}^3\boldsymbol{x}_n \cdots \int \mathrm{d}\tau_1 \int \mathrm{d}^3\boldsymbol{x}_1 \, \langle \hat{T}^\mu_\mu(\tau_n, \boldsymbol{x}_n) \cdots \hat{T}^\mu_\mu(\tau_1, \boldsymbol{x}_1)\hat{\mathcal{O}}(0,\boldsymbol{0})\rangle_c \ , \tag{3.48}$$

where $\hat{\mathcal{O}}$ is an arbitrary renormalization-group invariant operator of dimension d, and $T^\mu_\mu \equiv \theta$ is the trace of the QCD energy-momentum, one can write the following equation for the correlator involving the trace of the energy-momentum tensor [Kar08, Kha08]:

$$\int_{-\infty}^{\infty} \mathrm{d}\omega \, \frac{\rho_{\theta\theta}(\omega,0)}{\omega} = -\left(4 - T\frac{\partial}{\partial T}\right)\langle\theta\rangle_T = T^5\frac{\partial}{\partial T}\frac{(\epsilon - 3P)^*}{T^4} + 16|\epsilon_v| \ , \tag{3.49}$$

where $(\cdot)^* \equiv (\cdot)_T - (\cdot)_0$ is what is measured on the lattice, $\langle\theta\rangle_T \equiv \langle T^\mu_\mu\rangle_T = \epsilon - 3P$, ϵ the energy density, P the pressure, and $\epsilon_v = \langle\theta\rangle_0/4$ the energy density in vacuum. Now, since

the interaction measure, defined as $\Delta \equiv \langle\theta\rangle^*/T^4$, has a peak near the critical temperature (see Fig. 3.26), it is reasonable to assume the following ansatz for the spectral density [Kha08, Kar08]:

$$\rho_{\theta\theta}(\omega,0) = \frac{9\zeta}{\pi}\frac{\omega\omega_0^2}{\omega_0^2+\omega^2} \ , \tag{3.50}$$

where $\omega_0 \sim 1$ GeV. Using this ansatz one arrives to the relation between the trace anomaly and the bulk viscosity [Kha08]:

$$\zeta(T) = \frac{1}{9\omega_0(T)}\left[T^5\frac{\partial}{\partial T}\frac{\langle\theta\rangle_T - \langle\theta\rangle_0}{T^4} + 16|\epsilon_{\rm v}|\right] \ , \tag{3.51}$$

This equation implies then a large bulk viscosity near the QCD transition, from the $\langle\theta\rangle_T$ peak observed in the lattice [Che08], more or less pronounced depending on the transition order [Kar08]. However, this argument has been recently criticized on the basis of the $\int_0^\infty(\rho/\omega)$ convergence and parametric dependence with the QCD coupling constant [Moo08]. On the other hand, estimates of ζ from lattice data show that $\omega\delta(\omega)$ terms and large-ω non-thermal contributions have to be properly accounted for in spectral functions [Mey08a, Hue08].

It is therefore of great importance to study QCD regimes where one can rely on analytic calculations, in order to clarify the validity of the above proposal without appealing directly to lattice data. In the weak coupling regime, valid for very high temperatures, ζ/η has been found to be parametrically small [Arn06b]. Another regime where one can perform analytic calculations is low-energy QCD, where the system consists primarily of a meson gas and, for low temperatures, one can rely on Chiral Perturbation Theory [Ger89]. As we have seen in the previous sections of this chapter, the usual ChPT power counting must be extended to account for $1/\Gamma_p$ contributions arising in transport coefficients. Here, Γ_p is the thermal width of a pion with three-momentum $\boldsymbol{p}$, in which the $\pi\pi$ total elastic cross section enters linearly in the dilute gas regime (see formula (3.7)). Performing the power counting, which includes a detailed analysis of ladder-type diagrams considered in [Jeo95, Jeo96] (see Section 3.3), the leading-order ChPT contribution comes from the one-loop meson diagram of Fig. 3.10 with $\Gamma_p \neq 0$ internal lines. An essential point, as we have seen, is to include unitarity corrections in Γ_p to describe correctly the temperature behavior as the system approaches chiral restoration.

As it is discussed at the end of Section 3.1.2, the bulk viscosity of the massive pion gas, defined in complete chemical equilibrium by the LRT formula (1.199), is dominated by inelastic processes at low temperatures. However, we shall neglect inelastic $2\pi \leftrightarrow 4\pi$ reactions restoring particle number equilibrium, which are suppressed in our counting and yield chemical relaxation times about ten times larger than the plasma lifetime [Son97]. Thus, our bulk viscosity is meaningful for the pion gas formed in heavy ion collisions, which conserves approximately pion number between the temperatures of chemical and thermal freeze-out, as confirmed by particle spectra data analyses with a pion chemical potential [Hun98, Kol03]. The dominance of elastic processes for ζ in the pion gas, for the temperature regime of interest in heavy-ion collisions, has also been assumed in other

kinetic theory analyses[16] [Pra93, Che09, Gav85]. Using the theoretical basis presented in the previous sections we shall analyze now within ChPT the correlation between bulk viscosity and the conformal anomaly in the pion gas regime, studying the origin of the different contributions to conformal breaking for physical massive pions. Thus, we start with Kubo's formula derived in Section 1.6.3:

$$\zeta(T) = \frac{1}{2} \lim_{\omega \to 0^+} \frac{\partial}{\partial \omega} \int \mathrm{d}^4x \; \mathrm{e}^{\mathrm{i}\omega x^0} \; \langle [\hat{\mathcal{P}}(x), \hat{\mathcal{P}}(0)] \rangle \; , \tag{3.52}$$

where the modified pressure operator is given by $\hat{\mathcal{P}} \equiv -T_i^i/3 - c_{\mathrm{s}}^2 T_{00}$ (when there is no conserved charge in the system or the chemical potential associated is zero[17]), the squared speed of sound is $c_{\mathrm{s}}^2 = \partial P/\partial \epsilon = s/c_v$, the entropy density $s = \partial P/\partial T$, and the specific heat $c_v = \partial \epsilon/\partial T = T \partial s/\partial T$. The speed of sound introduced here is the *exact* (non-perturbative) result for a pion gas (see Section 1.6.3), however we shall use a convenient perturbative approximation for it. As we shall see below, the introduction of the term with the speed of sound in the modified pressure operator is crucial in order to obtain the right asymptotic behavior at high temperatures, and a maximum near the phase transition in the bulk viscosity (corresponding to a minimum in the speed of sound). This form of $\hat{\mathcal{P}}$ is also the adequate one to be used within perturbation theory, as it is obtained in [Hos84, Moo08]. In lattice analyses, one works with the Lorentz invariant θ instead. In our approach these two correlators are not equivalent, since the leading order in $1/\Gamma_p$ for perturbative T_{00} commutators does not vanish for zero spatial momentum. Following the method explained in Section 3.3, we calculate then the spectral function ($\hat{\mathcal{P}}$ commutator) in (3.52) in the imaginary-time formalism, picking up the dominant contribution in $1/\Gamma_p$ (pinching pole) of the analytically continued retarded correlator. That term is purely imaginary and gives the dominant effect in the spectral function at zero momentum and small energy. Thus, to leading order:

$$\zeta^{(0)} = \int_0^\infty \mathrm{d}p \; \frac{3p^2(p^2/3 - c_{\mathrm{s}}^2 E_p^2)^2}{4\pi^2 T E_p^2 \Gamma_p} \, n_{\mathrm{B}}(E_p)[1 + n_{\mathrm{B}}(E_p)] \; , \tag{3.53}$$

where the leading $\mathcal{O}(p^2)$ order in $T^{\mu\nu}$ has been retained in the vertex. Now, we get c_{s}^2 in (3.53) from P calculated up to $\mathcal{O}(T^8)$ in [Ger89]. In Fig. 3.21 we see that to $\mathcal{O}(T^6)$, both the specific heat and the speed of sound increase monotonically, c_{s}^2 approaching the ultra-relativistic limit of $1/3$ corresponding to a gas of free massless pions. To that order, since the distribution function is peaked around $p \sim T$ for $T \gg M_\pi$, we see that (3.53) vanishes asymptotically for large temperatures, as expected for conformally invariant systems [Arn06b, Hos84, Gav85, Pra93]. In fact, from (3.53) we get for massless pions (chiral limit):

$$\zeta^{(0)} = 15(1/3 - c_{\mathrm{s}}^2)^2 \eta^{(0)} \; , \tag{3.54}$$

consistently with [Hor87] and parametrically with high-T QCD [Arn06b]. The crucial point here is that taking one more order in the pressure c_v grows, reaching a maximum at

[16] In particular, in [Che09] it is shown that the elastic scattering processes give the dominant contribution to the bulk viscosity of the massless pion gas at very low temperatures ($T \ll F_\pi$).

[17] In a heavy-ion environment, when chemical freeze-out is reached, the number of pions is approximately conserved but the chemical potential is small if we are close to the phase transition temperature (see Chapter 4). We consider that situation here.

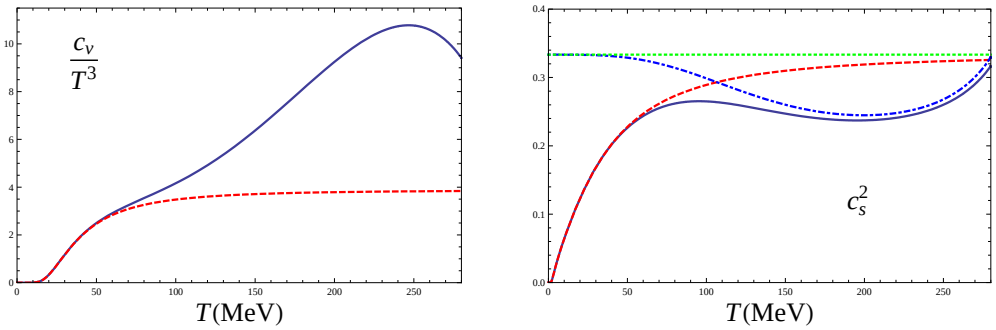

Figure 3.21: Specific heat (left) and speed of sound squared (right) for the pion gas. The red dashed line is the $\mathcal{O}(T^6)$ calculation, and the continuous blue line the $\mathcal{O}(T^8)$ one. The green dotted line is the ultra-relativistic limit $c_s^2 = 1/3$. The dashed-dotted blue line is the chiral limit result to $\mathcal{O}(T^8)$.

about $T_c \simeq 220$ MeV[18]. The speed of sound attains then a minimum at T_c which will alter the behavior of $\zeta(T)$. This is the critical behavior of a $O(4)$-like crossover, as expected for two massive flavors at zero chemical potential. In Figure 3.22 we plot the speed of sound calculated on the lattice for $N_f = 3$ and almost physical quark masses. A physical interpretation is that, although temperature tends to erase mass scales, chiral interactions are enhanced and produce in the critical region a significant, non-perturbative, conformal breaking reflected in $c_s^2 \neq 1/3$. Note that, although in the massive case T_c is near the chiral restoration temperature T_c^χ where the order parameter $\langle \bar{q}q \rangle_T$ vanishes [Ger89], in the chiral limit $T_c^\chi \simeq 170$ MeV, whereas T_c is almost unchanged.

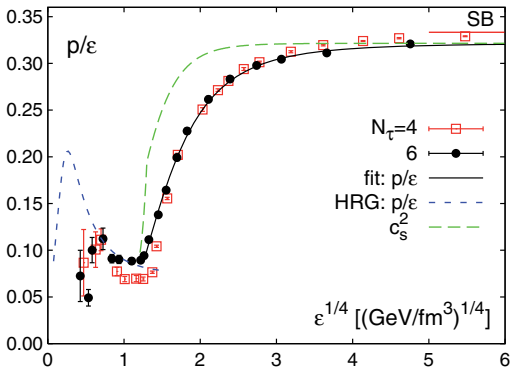

Figure 3.22: Lattice result with almost physical quark masses for the speed of sound squared and the equation of state,from [Che08] ($N_f = 3$).

We plot our result for the bulk viscosity in Fig. 3.23. The effect of including the $\mathcal{O}(T^8)$ in c_s^2 effectively produces a peak around T_c, not present to $\mathcal{O}(T^6)$. The speed of sound is not the only relevant effect yielding a sizable peak: unitarization of the cross section entering Γ_p is also crucial to $\mathcal{O}(T^8)$. Considering unitarized partial waves for $\pi\pi$ scattering (ChPT is only perturbatively unitary) improves the high energy behavior (and therefore

[18]In this section, we denote by T_c the temperature of the anomalous peak in the trace anomaly, do not confuse with T_c^χ, the critical temperature of the chiral phase transition.

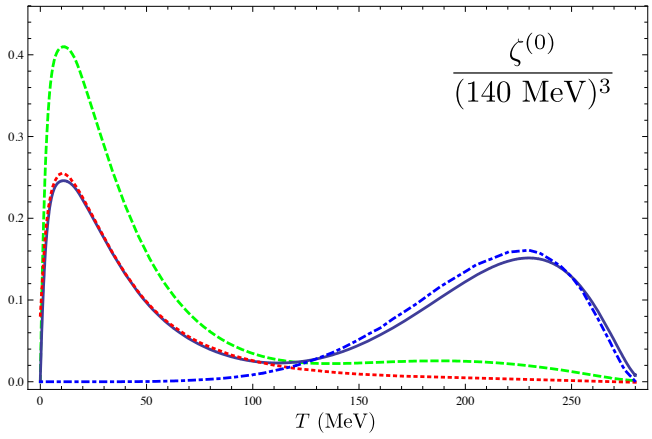

Figure 3.23: Bulk viscosity of the pion gas. The full blue line is the unitarized result with c_s^2 to $\mathcal{O}(T^8)$ and the dashed-dotted blue one is the same calculation in the chiral limit. The dashed green line is the non-unitarized result at the same order. The dotted red line is unitarized with c_s^2 to $\mathcal{O}(T^6)$ and lies very close to the non-unitarized curve, which is not displayed.

the high temperature one) and generates dynamically the $f_0(600)$ and $\rho(770)$ resonance poles. Consistently, we have chosen the values of the low-energy constants $\bar{l}_i$ entering pion scattering (they can be found in Chapter 2) so that the mass and width of the ρ are at their physical values for $T = 0$. As we discuss below, the $\bar{l}_i$ dependence is crucial in the present analysis. In the chiral limit, the transition peak is almost unchanged and so is T_c, unlike T_c^χ, which indicates that chiral restoration is not the main source of this effect. Our massless results are in reasonable agreement with a recent kinetic theory analysis [Che09]. We also obtain a low-T peak, which disappears in the chiral limit. In our regime and for $T \ll M_\pi$, $n_B(E_p) \simeq \mathrm{e}^{-M_\pi/T}\mathrm{e}^{-p^2/2M_\pi T}$ so that three-momenta $p = \mathcal{O}(\sqrt{M_\pi T})$ and taking the leading order for Γ_p given by (3.13) and $c_s^2 \simeq T/M_\pi + \ldots$ [Ger89], Eq. (3.53) becomes:

$$\zeta^{(0)} \simeq 13.3\,\frac{F_\pi^4\sqrt{T}}{M_\pi^{3/2}}\ , \quad \text{for} \quad T \ll M_\pi\ , \tag{3.55}$$

where F_π is the pion decay constant. The above behavior is consistent with non-relativistic kinetic theory [Gav85] where ζ and η are expected to be comparable at low T[19]. Thus, $\zeta(T)$ increases for very low T and has to decrease at some point to match the asymptotic vanishing behavior, thus explaining the low-T maximum. Let us now evaluate conformal-breaking contributions for the pion gas. First, it is instructive to recall the QCD result for the trace anomaly [Col77]:

$$\partial_\mu s^\mu = T^\mu{}_\mu = \frac{\beta(g)}{2g}G^a_{\mu\nu}G^{\mu\nu}_a + (1+\gamma_m(g))\bar{q}Mq\ , \tag{3.56}$$

[19]This would be the correct behavior for ζ at very low temperatures if only elastic processes were available. However, at those temperatures inelastic processes dominate the bulk viscosity of the massive pion gas, as it is discussed at the end of Section 3.1.2. The correct behavior turns out to be $\zeta \propto \exp(2M_\pi/T)$ [Jeo95].

where $s^\mu = T^{\mu\nu}x_\nu$ is the dilation current, and the renormalization group functions are, perturbatively, $\beta(g) = \mathcal{O}(g^3)$ (QCD $\beta-$function), $\gamma_m(g) = \mathcal{O}(g^2)$ (anomalous dimension of the quark mass). The first term is the conformal anomaly proportional to the gluon condensate. The second one comes from the explicit breaking in the QCD lagrangian, M being the quark mass matrix. At finite temperature, the thermal average of the trace anomaly is given in terms of thermodynamical quantities, $\langle\theta\rangle_T \equiv \langle T^\mu{}_\mu\rangle_T = \epsilon - 3P$, and it has already been calculated on the lattice for the pure glue theory [Boy96] as well as for QCD with almost physical quark masses [Che08]. For the pion gas, using the relation between the trace anomaly and the pressure[20]

$$\langle\theta\rangle_T = T^5 \frac{\mathrm{d}}{\mathrm{d}T}\left(\frac{P}{T^4}\right), \tag{3.57}$$

we represent in Fig. 3.24 the trace anomaly to different orders in the pressure, as well as the T-function appearing in the r.h.s. of (3.51). The diagrams contributing to $\mathcal{O}(T^8)$ in the ChPT counting are represented in Fig. 4.2. We observe clearly the same two-peak structure as the bulk viscosity, with similar features. The low-T peak disappears in the chiral limit. Its contribution comes then from explicit conformal breaking. This peak was also obtained in the work [Li08]. In the chiral limit, the trace anomaly has a simple expression at this order [Ger89, Leu88, Leu92]:

$$\langle T^\mu{}_\mu\rangle^* = \frac{\pi^2}{270}\frac{T^8}{F_\pi^4}\left(\ln\frac{\Lambda_\mathrm{p}}{T} - \frac{1}{4}\right), \tag{3.58}$$

with $\Lambda_\mathrm{p} \sim 400$ MeV for our choice of $\bar{l}_i$ given in Section 2.1. The result is very dependent on the choice of $\bar{l}_i$ (see discussion below).

Calculating only the first non-vanishing order in ChPT, either using (3.57) or evaluating directly the energy-momentum correlators, we get:

$$\begin{aligned}\langle\theta\rangle_T - \langle\theta\rangle_0 &= 3M_\pi^2 g_1(M_\pi, T) + \mathcal{O}(F_\pi^{-2}) \\ &= 2m_\mathrm{q}\left(\langle\bar{q}q\rangle_T - \langle\bar{q}q\rangle_0\right) + \mathcal{O}(F_\pi^{-2}),\end{aligned} \tag{3.59}$$

where $m_\mathrm{q} \equiv m_\mathrm{u} = m_\mathrm{d}$ and we formally account for different chiral orders by their F_π power. The function g_1 is the thermal correction to the free pion propagator $G(x=0)$ [Ger89] (see Chapter 4 and Appendix D). Comparing with the QCD expression (3.56) the factor of two in (3.59) for the quark condensate is perfectly consistent with the result [Aga01] showing that the quark and gluon contributions to the trace anomaly are identical at low temperatures. Now, $g_1(T)/T^4$ has a maximum at $T \simeq 2M_\pi/5 \simeq 60$ MeV, which is the low-T peak in Fig. 3.24 and the source for the first peak of the bulk viscosity. The transition peak only shows up at $\mathcal{O}(T^8)$ and survives in the chiral limit, where its origin is purely anomalous. It comes from ChPT interactions involving dimensionful couplings, like F_π, and is therefore suppressed at low temperatures [Leu92]. For massive pions, the value of the peak and its position are almost unchanged with respect to the chiral limit, the difference being even smaller than the simple extrapolation of the quark condensate contribution in (3.59) with $\langle\bar{q}q\rangle_T$ to $\mathcal{O}(T^8)$, which represents around a 10%

[20] This formula is easily obtained from the thermodynamic relations $s = \frac{\mathrm{d}P}{\mathrm{d}T}$, and $\epsilon = Ts - P$.

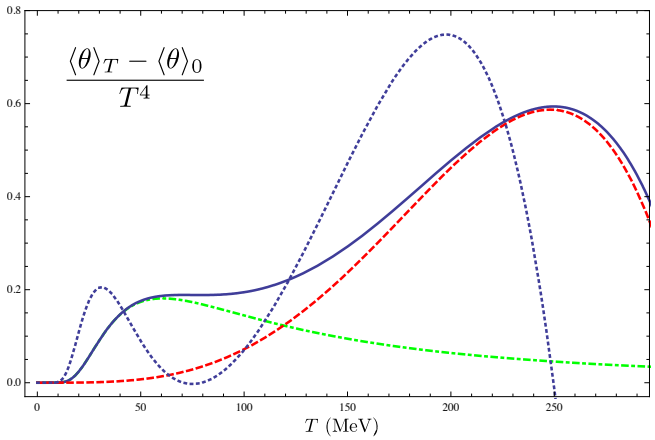

Figure 3.24: Thermal expectation value of the trace anomaly for the pion gas. The dashed-dotted green and continuous blue lines are, respectively, the $\mathcal{O}(T^6)$ and $\mathcal{O}(T^8)$ results. The dashed red line corresponds to the $\mathcal{O}(T^8)$ result for massless pions (the $\mathcal{O}(T^6)$ order vanishes for $M_\pi = 0$). The dotted blue line is $T\frac{\partial}{\partial T}\frac{\langle\theta\rangle_T - \langle\theta\rangle_0}{T^4}$.

correction in the critical region. The fermion contribution is also subdominant in lattice analyses [Che08]. These results show again that the nature of this effect is not likely to be related to chiral symmetry restoration but rather to other QCD critical effects like deconfinement. The correlation with the bulk viscosity is again clear. In fact, in the chiral limit the function between brackets in (3.51) and $15(c_s^2 - 1/3)^2 = \zeta/\eta$ have their maximum at the same $T_c = e^{-5/8}\Lambda_p$ with Λ_p given in [Ger89] in terms of $\bar{l}_1 + 4\bar{l}_2$. We recall that in order to establish the possible correlations between the conformal anomaly and the bulk viscosity, we have used the same set of $\bar{l}_i$ in both figures. For those unitarized values, $T_c \simeq 220$ MeV. Using perturbative values, for instance those given in [Ger89] fixed to reproduce pion scattering lengths, the critical peak is about three times smaller and $T_c \simeq 148$ MeV, while T_c^χ varies only about 10 MeV from one set to another. We get exactly the same drastic reduction of the critical peak and shift of T_c in the bulk viscosity. The presence of resonances is then crucial to yield a sizable effect in the transition peak, whose dominant contribution comes from the gluon condensate in the trace anomaly.

Regarding the $\omega_0(T)$ function defined through (3.51), in the chiral limit it grows linearly with T, reaching $\omega_0 \sim 400$ MeV at the transition. In the massive case, taking $|\epsilon_v| = F_\pi^2 M_\pi^2$, the ChPT lowest order, we get $\omega_0(T_c) \sim 1$ GeV, almost constant from $T \sim 150$ MeV onwards. These values are in reasonable agreement with the estimates in [Kar08]. On the other hand, from (3.55) we get $\omega_0(T) \simeq 0.13 M_\pi^{7/2}/(F_\pi^2\sqrt{T})$ for $T \to 0^+$.

The numerical values of the trace anomaly in Fig. 3.24 are not far from the lattice values [Che08] for low T (see Fig. 3.25), but they are about a factor of 10 smaller near T_c. The increasing of degrees of freedom due to heavier states, not included in our approach, is clearly important in that region. For instance, the $\mathcal{O}(T^8)$ pressure in the chiral limit is proportional to $N_f^2(N_f^2 - 1)$ [Leu92] so that changing from two to three flavors, which are not Boltzmann suppressed near the transition, increases significantly the anomaly. In addition, using a simple free Hadron Resonance Gas approach (see

below), the contributions to the anomaly from the states $\{\pi, \rho, \sigma\}$ amount only to a 5% of all baryon and meson states up to 2.5 GeV (see Fig. 3.26). In fact, although we get $\zeta/s \simeq 0.02$ at the transition peak, still smaller than $\eta/s \simeq 0.25$, we would get a larger value if we assume that the introduction of heavier states increase the anomaly, and that implies an increase of the transition strength and a strong reduction of c_s^2 [Kar08]. As an indication, setting $c_s^2 = 0$ in (3.53) we get $\zeta/s \sim 1$ at T_c.

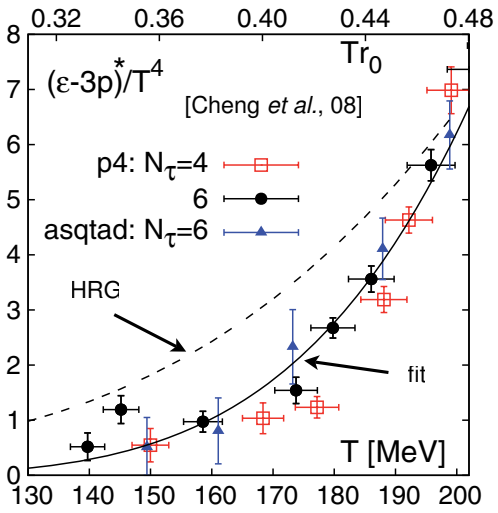

Figure 3.25: Comparison between the lattice results (dots and continuous line) with almost physical quark masses and the HRG approximation (dashed line) for temperatures below the phase transition, from [Che08].

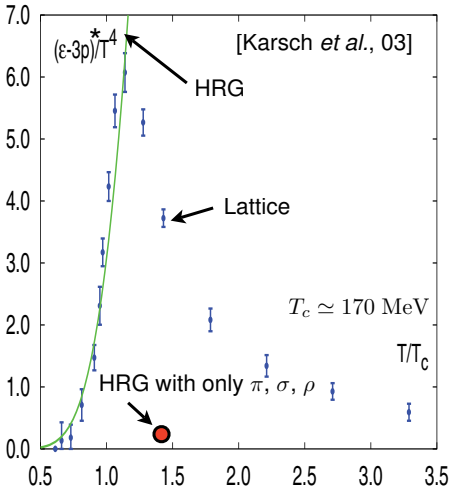

Figure 3.26: Interaction measure calculated on the lattice (dots) and in the HRG approximation (green line, taking into account 1026 states in total, see text), from [Kar03]. The big red dot corresponds to the result from the HRG approximation taking into account only pions, the $f_0(600)$ and the $\rho(770)$ states.

The Hadron Resonance Gas (HRG) approximation considers a free (non-interacting) gas which consists of all the baryonic and mesonic states up to 2 GeV, 1026 in total [Kar03]. Therefore, in this approximation the interaction measure is given by:

$$\Delta \equiv \frac{(\epsilon - 3P)^*}{T^4} = \sum_{i=1}^{1026} \frac{(\epsilon_i - 3P_i)^*}{T^4} = \sum_{i=1}^{1026} \frac{g_i}{2\pi^2} \sum_{k=1}^{\infty} \eta^{k+1} \frac{(\beta m_i)^3}{k} K_1(k\beta m_i) \ , \tag{3.60}$$

where g_i denotes the degeneracy of the state, $\eta = \pm 1$ depending on whether it is a boson or a fermion respectively, and K_1 is the modified Bessel function of the second kind. In Fig. 3.25, from [Che08], the lattice results for the interaction measure are compared with the HRG results for temperatures below the phase transition (for an analysis of the trace anomaly from above the critical temperature see [Meg09]). We see that the HRG approximation fits better the lattice results near the maximum of the peak, while as the temperature decreases they start to separate from each other. This might be due to the values of the quarks masses taken in [Che08], since the HRG approximation and ChPT should coincide for very low temperatures. It is important to remark that although the HRG approximation gives a value for the interaction measure compatible with lattice results near the peak, it is a monotonously increasing curve, so it does not have the shape of a peak, which the ChPT calculation does have because it includes the interaction between the Goldstone bosons (in the HRG the non-zero interaction measure comes from the explicit breaking due to the non-zero mass of the states).

We are also interested in the influence of the in-medium $f_0(600)$ and $\rho(770)$ resonances on the trace anomaly and eventually in the bulk viscosity. For that purpose, we calculate the interaction measure in the Virial Gas Approximation (VGA) which allows us to introduce the unitarized scattering amplitudes in the dilute gas regime. According to the VGA, to the lowest order in the interaction, the pressure of the gas is given by [GM06]:

$$\beta P = \sum_i \left(B_i^{(1)} \xi_i + B_i^{(2)} \xi_i^2 + \sum_{j \geq i} B_{ij}^{\text{int}} \xi_i \xi_j + \dots \right) \ , \tag{3.61}$$

where

$$B_i^{(n)} = \frac{g_i \eta_i^{n+1}}{2\pi^2 n} \int_0^\infty \mathrm{d}p \ p^2 \mathrm{e}^{-n\beta(E_i - m_i)} \ , \tag{3.62}$$

$$B_{ij}^{\text{int}} = \frac{\mathrm{e}^{\beta(m_i+m_j)}}{2\pi^3} \int_{m_i+m_j}^\infty \mathrm{d}E \ E^2 K_1(\beta E) \sum_{I,J,S} (2I+1)(2J+1) \delta_{IJS}^{ij}(E) \ , \tag{3.63}$$

with $\xi_i \equiv \mathrm{e}^{\beta(\mu_i - m_i)}$, and δ_{IJS}^{ij} the phase-shifts for $ij \to ij$ scattering. In Fig. 3.27 we plot the interaction measure for several scattering amplitudes in the VGA. The interaction peak is obtained when considering $\mathcal{O}(p^4)$ amplitudes, and its height is almost equal to the one obtained with the perturbative calculation of Fig. 3.24. We then observe that

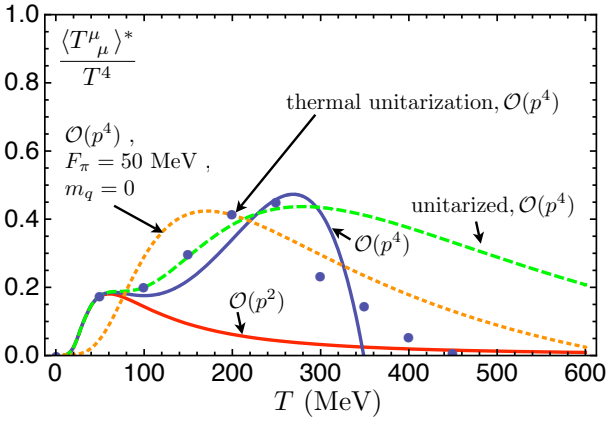

Figure 3.27: Interaction measure in the VGA (see text) for several scattering amplitudes. The in-medium evolution of the $f_0(600)$ and $\rho(770)$ resonances do no change significantly the height of the interaction peak.

the in-medium evolution of the $f_0(600)$ and $\rho(770)$ resonances (see Sections 2.1 and 2.2) does not change significantly the height of the interaction peak.

We have seen that it is crucial to include correctly the effect of the ρ resonance. On the other hand, the $f_0(600)/\sigma$ is expected to be related to chiral restoration. Regarding bulk viscosity, it has been suggested in [Pae06], within mean field theory, that any dynamic scalar field σ should contribute to $\zeta \propto \Gamma_\sigma/m_\sigma^2$, which may be large near the critical region by mass reduction, for instance in the Linear Sigma Model (LSM) context. Within unitarized ChPT, the dynamically generated $f_0(600)$ pole undergoes a significant mass reduction towards $2M_\pi$ governed by chiral restoration, remaining a broad state with sizable width near the transition (see Section 2.1). Interestingly, from the results of Chapter 2, we find that Γ_σ/m_σ^2 has a peak at $T \sim 180$ MeV, where the pole mass reaches threshold. For higher T the width still decreases (by phase space reduction) while the mass remains close to threshold. This critical value is very close to the one obtained in [Pae06] for the LSM assuming a T-independent width. However, as discussed above, these chiral restoration effects are likely to be subdominant for the trace anomaly, and therefore we would not expect a big change in the bulk viscosity due to the in-medium evolution of resonances. In Fig. 3.28 we plot the bulk viscosity calculated using the value for the pion decay constant $F_\pi = 50$ MeV, in order to simulate nuclear density and to force possible symmetry restoration effect (see Section 2.2). As we can see, the influence of these effects on the the bulk viscosity is small.

Finally, in Fig. 3.29 we plot the bulk viscosity over the entropy density. We explicitly show the importance of introducing unitarized scattering amplitudes (resonances) in order to reproduce the peak near the phase transition. Nuclear density effects do not change significantly the height of the anomalous peak, as expected from the previous analysis of the conformal anomaly. Comparing with Fig. 3.20, our result for the ratio $\zeta^{(0)}/s$ is still smaller than $\eta^{(0)}/s$ near the transition, although the correlation with the conformal anomaly is clear, and that allows to predict larger ζ/s values if heavier states are included. Nevertheless, these are extrapolation based on a low-T analysis and must be taken with

a grain of salt.

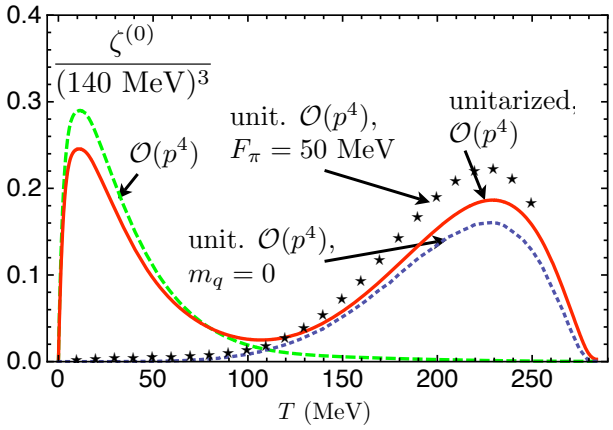

Figure 3.28: Lowest order contribution for the bulk viscosity of a pion gas considering different approximations in the scattering amplitudes.

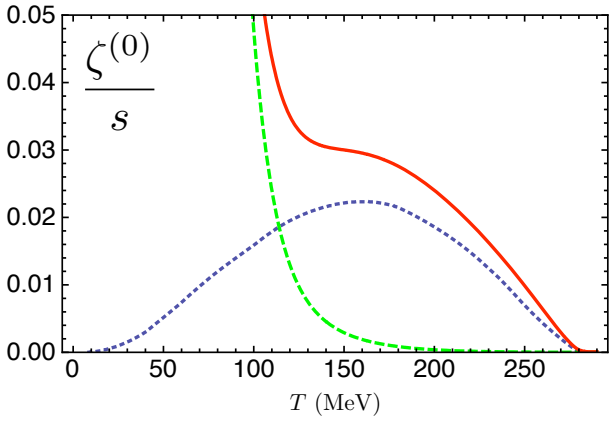

Figure 3.29: Lowest order contribution for the bulk viscosity over the entropy density of a pion gas. The curves correspond to the same cases as in Fig. 3.28.

3.4.5 Large-N_c behavior of transport coefficients

One of the main advantages of our formalism is that we can readily obtain the parametric dependence with the number of colors N_c. This analysis is interesting, given the theoretical relevance of the large N_c limit to describe qualitatively the QCD low-energy sector [Man99]. In addition, it will confirm some of our previous qualitative arguments.

The large-N_c counting of the low-energy constants $\bar{l}_i$ can be extracted from that of the SU(3) ones L_i [Man99, Gas84] in the $N_f = 2$ limit [Gas84], while $F_\pi^2 = \mathcal{O}(N_c)$ (see Section 1.1.2). This gives for the $\pi\pi$ scattering amplitudes $|T|^2 \sim \mathcal{O}(1/N_c^2)$, regardless of whether they are unitarized or not, and therefore, according to (3.6), we get $\Gamma_p \sim \mathcal{O}(1/N_c^2)$. This result, together with the N_c scaling of the thermodynamic quantities $P \sim \epsilon \sim c_s^2 \sim s \sim$

$\mathcal{O}(1)$, which we extract from [Ger89], implies that all transport coefficients scale as $\mathcal{O}(N_c^2)$ for $M_\pi \neq 0$.

However, in the chiral limit, from the expression of the pressure [Ger89]

$$P = \frac{\pi^2}{30} T^4 \left[1 + \frac{T^4}{36 F_\pi^4} \ln \frac{\Lambda_p}{T} + \mathcal{O}(T^6) \right] \ , \tag{3.64}$$

and taking into account that $\ln \Lambda_p \sim \bar{l}_1 + 4\bar{l}_2 \sim \mathcal{O}(N_c)$, we get in this limit $c_s^2 - 1/3 \sim \mathcal{O}(\ln \Lambda_p / F_\pi^4) \sim \mathcal{O}(1/N_c) \sim \langle\theta\rangle_T$. Now, since $\zeta/\eta \sim \mathcal{O}(c_s^2 - 1/3)^2$ in the chiral limit and the previous counting of the width is valid also in this limit, this means that for $M_\pi = 0$, the scaling of the bulk viscosity is $\zeta \sim \mathcal{O}(1)$, unlike the other coefficients which still scale as $\mathcal{O}(N_c^2)$. Summarizing:

$$\sigma \sim \kappa \sim \zeta \sim \eta \sim \zeta/s \sim \eta/s \sim \mathcal{O}(N_c^2) \qquad (M_\pi \neq 0) \ , \tag{3.65}$$

$$\sigma \sim \kappa \sim \eta \sim \eta/s \sim \mathcal{O}(N_c^2) \ , \quad \zeta \sim \zeta/s \sim \mathcal{O}(1) \quad (M_\pi = 0) \ . \tag{3.66}$$

This scaling relations are consistent with the results we obtained in the previous sections. The bulk viscosity is suppressed with respect to the shear viscosity in the chiral limit, as a consequence of scale invariance, although this is only a parametric dependence and it does not take into account the anomalous breaking near the transition. For $M_\pi \neq 0$ the explicit breaking of conformal invariance makes the two coefficients comparable, as we get for very low temperatures, where the mass terms dominate. For higher T, the chiral limit result is again reached asymptotically. Note also that the N_c scaling for $M_\pi \neq 0$ is compatible with our leading expressions (3.23), (3.43), (3.47) and (3.55). We disagree with the chiral limit N_c-counting for ζ given in [Che09], where we believe that the scaling of $\ln \Lambda_p$ discussed above is not properly accounted for. The above N_c behavior is also useful in order to understand the origin of the different conformal-breaking terms near the transition. Taking into account the critical behavior, we have $T_c \sim \mathcal{O}(e^{N_c})$ and $\langle\theta\rangle_{T_c} \sim \mathcal{O}(e^{N_c}/N_c^2)$. This large dependence is another indication of the dominance of confinement over chiral restoration, comparing with the chiral $T_c^\chi = \mathcal{O}(N_c)$. Also, $\langle\theta\rangle \propto L_3$, which in large-$N_c$ includes a term proportional to the gluon condensate [Esp90]. Comparing with the QCD expressions in [Arn06b], we agree except for the overall $\mathcal{O}(N_c^2)$ constants in the pressure which count the degrees of freedom. For massive pions, the above chiral limit scaling is only reached asymptotically for large T, while for any T we get $\zeta/\eta \sim \mathcal{O}(1) \sim \langle\theta\rangle_T - \langle\theta\rangle_0$ with $\zeta \sim \mathcal{O}(N_c^2)$, compatible with (3.55). Finally, comparing with results from high-T QCD is also revealing. From the parametric expressions given in [Arn00, Arn06b] with the scaling $\alpha_s = \mathcal{O}(1/N_c)$, one gets $\eta/s \sim \mathcal{O}(1)$. This is qualitatively compatible with the idea of η/s approaching a minimum when coming from the low-T phase to the critical region, as we also obtain in our approach. In the high-T regime, ζ/η is also suppressed by an additional $(c_s^2 - 1/3)^2$ factor.

3.5 Conclusions

In this chapter we have presented a method for calculating different transport coefficients (DC electrical conductivity, thermal conductivity, and shear and bulk viscosities) in a meson gas at low temperatures within the framework of Chiral Perturbation Theory and

Linear Response Theory. The analysis has been particularized for the case of a pion gas, including also the resonances $f_0(600)$ and $\rho(770)$ dynamically generated through unitarization with the IAM. The non-perturbative nature of transport coefficients is reflected in the need of including the thermal pion width in the calculations, in order to avoid "pinching poles" singularities. Physically, this allows to account for the relevant in-medium pion collisions and gives rise to the leading order contribution in the inverse width consistently with kinetic theory. We have shown that, after a suitable modification of the standard ChPT power counting and including unitarity corrections in the scattering amplitudes in order to improve their high energy behavior, one ends up with a reasonable description of transport coefficients for temperatures below the transition. At very low temperatures, our approach meets the predictions of non-relativistic kinetic theory, while at higher T we get an adequate behavior of transport coefficients when compared with existing studies based on the kinetic approach. To obtain these results, we have just considered the dominant diagram, with unitarized scattering in the thermal width for the internal pion lines.

A very important part of our analysis has been the role of higher order diagrams which, although naively suppressed, are enhanced by powers of the inverse width. As it happens in other theories, the dominant diagrams are the uncrossed ladder ones, which in our case can be interpreted in terms of pion scattering of the internal lines. A careful evaluation of the ladder diagrams shows that they can still be considered perturbative in ChPT at low temperatures. This is particularly important at very low temperatures, $T \ll M_\pi$, where the non-perturbative contributions are larger. In that regime, we have been able to show exactly that ladder diagrams are perturbative, so that they merely renormalize the numerical coefficient of the leading order contribution by subleading corrections in ChPT. Although collinearly enhanced, our numerical analysis shows that the next-to-leading order correction typically amounts to a 5% approximately. As temperature increases, ladder diagrams become more important, the most relevant contributions coming from ladders with derivative vertices. At temperatures near the chiral phase transition it is not clear that ladder diagrams can be neglected (furthermore, strictly, ChPT is not applicable in that regime). In fact, at those high temperatures we expect other effects to become important, like the presence of kaon states.

As mentioned above, another important point concerns unitarity. We have shown that the behavior with temperature of the different transport coefficients changes qualitatively with temperature as a consequence of implementing unitarity for the partial waves in the thermal width. This provides a more physical picture as far as the behavior of partial waves with energy and the presence of resonances in the thermal bath are concerned (the $f_0(600)/\sigma$ and $\rho(770)$). The unitarized conductivity increases slowly for increasing T, which seems to be consistent with lattice and analytical analyses far beyond the transition point. Thermal conductivity and shear viscosity also experiment an increasing behavior with temperature due to unitarity. And the maximum in bulk viscosity near the critical temperature is enhanced by the same effect. In addition, we have discussed phenomenological predictions for the zero-energy photon spectrum and the shear viscosity to entropy ratio, which are in fair agreement with data. On one hand, our analysis implies that there should be sizable effects for very low energy hadronic photon production and

this result is consistent with recent theoretical low-energy analysis and compatible with naive extrapolations of experimental data. On the other hand, we have seen that the quotient η/s for the pion gas respects the universal lower bound conjectured from a AdS/CFT calculation by Kovtun et al. We have also seen that it is very likely that this quotient presents a minimum at the phase transition. Moreover, our estimation of η/s, which enters directly into the sound attenuation length, is in good agreement with a previous analysis of elliptic flow. However, the lack of precise experimental and lattice knowledge about the zero frequency limit, together with the own limitations of our approach do not allow to draw very quantitative conclusions.

Regarding the bulk viscosity, we have shown that the massive pion gas develops a strong correlation between bulk viscosity and the conformal anomaly, as suggested by previous works. Both quantities show a low-temperature peak coming from mass conformal breaking and another one at the critical temperature remaining in the chiral limit and mainly dominated by gluon condensate contributions not related to chiral restoration. In perturbation theory, it is necessary to calculate the partition function to order $\mathcal{O}(T^8)$ in order to obtain an anomalous peak in the interaction measure. We have seen that this peak can also be obtained in the VGA using scattering amplitudes calculated in ChPT at order $\mathcal{O}(p^4)$. The dynamically generated light resonances (σ and ρ) are essential to obtain sizable effects at the transition. In the calculation of the trace anomaly, we have also compared with the results from the HRG approximation, where many more resonances are introduced as free states obtaining a good agreement with lattice calculations. Since resonances do not interact in the HRG approach, there is no maximum in the interaction measure, unlike in the ChPT calculation. Different estimates indicate that heavier states could yield a larger bulk viscosity near the transition, leading to observable effects in heavy ion collisions.

We have also studied the large-N_c limit of the transport coefficients obtained in our approach. The parametric scaling with N_c is consistent with our previous analysis and provides a qualitative description for the behavior of shear and bulk viscosities when approaching the critical region.

Chapter 4

Chemical non-equilibrium in the meson gas

In this chapter we consider an interacting pion gas (although the treatment can be easily extended to consider other mesons) in the regime where thermal but not chemical equilibrium has been reached. Approximate particle number conservation is implemented by a non-vanishing pion chemical potential μ_π within a diagrammatic thermal field theory approach, valid in principle for any (neutral) bosonic field theory in this regime. The resulting Feynman rules are then applied within the context of Chiral Perturbation Theory, to discuss thermodynamical quantities of interest for the pion gas such as the free energy, the quark condensate and thermal self-energy. In particular, we derive the $\mu_\pi \neq 0$ generalization of Luscher and Gell-Mann-Oakes-Renner type relations. We pay special attention to the comparison with the conventional kinetic theory approach in the dilute regime, which allows for a check of consistency of our approach. Several phenomenological applications are discussed, concerning chiral restoration, freeze-out conditions and Bose-Einstein pion condensates. The original formalism and results presented in this chapter essentially correspond to the work [FF09b].

One of the ongoing research lines in Heavy Ion Physics is the thermal and chemical evolution of the expanding hadronic gas. Roughly speaking, the accepted picture is that the thermal evolution of the freezing system reaches chemical freeze-out before the thermal one, so that when hadrons fully decouple the chemical potentials associated to particle number conservation are not zero. The chemical composition of the gas can be determined experimentally by looking at the relative abundances of the different hadron species and their spectra [Kat90, Beb92, Hun98, Kol03, BM04]. The presence of such a chemically not-equilibrated phase is more likely to exist for higher collision energies such as those in RHIC and LHC than for SPS or AGS experiments [BM04]. For the pion component, different estimates based on local thermal equilibrium predict $\mu_\pi \sim 50 - 100$ MeV at a thermal freeze-out temperature $T_{\rm TFO} \sim 100 - 120$ MeV, with chemical freeze-out taking place at about $T_{\rm CFO} \sim 180$ MeV [Beb92, Son97, Hun98, Kol03, Let08].

For low and moderate temperatures, the dominant component is the pionic one. In that phase, the mean free path of pions is small compared to the system size, so that local thermal equilibrium prevails [Goi89, Beb92, Sch93]. On the other hand, the chemical relaxation rate through $2\pi \leftrightarrow 4\pi$ processes is very small [Goi93, Son97] due to a strong

phase space suppression. Therefore, in the range of temperatures $T_{\rm TFO} < T < T_{\rm CFO} \lesssim T_{\rm c}$, with $T_{\rm c}$ the critical temperature of chiral symmetry restoration, the system is in thermal equilibrium and dominated by elastic collisions so that $\mu_\pi \neq 0$. In that temperature range, it is valid to use the theoretical framework of Chiral Perturbation Theory and it is also reasonable to adopt a dilute gas description, since the mean particle density is small. In addition, neglecting dissipative effects such as viscosities, entropy is conserved in the evolution (see Section 1.5).

The system described above, i.e., a pion gas with $\mu_\pi \neq 0$ is the one we will consider here. Clearly, it is an oversimplified version of the real hadron gas, but we will take it as a physically relevant working example for our present analysis. So far, chemical potential effects in such a system have been incorporated basically in two ways. One of them is the limit of free particles (where one has actually exact particle conservation) used for the evaluation of the partition function, including resonances explicitly [Beb92, Son97]. This allows, via entropy conservation requirements, to describe rather accurately the dependence $\mu_\pi(T)$ in the range of temperatures of phenomenological relevance indicated above. The other one is to use kinetic theory arguments and then include the $\mu_\pi \neq 0$ dependence in the distribution function. The latter has been followed for instance in the calculation of the thermal width [Goi89], in the evaluation of transport coefficients [Pra93, Dob04], or in the virial approach for low densities [Dob99]. Finally, it is worth mentioning that there are phenomenological analyses, like that in [Bai97] for the dilepton rate, where the same prescription is followed, i.e., replacing the distribution function, but for propagators at the diagrammatic level, inspired on the non-equilibrium formulation of thermal field theory [Cho85].

We will be interested then in a diagrammatic formulation of this system, i.e, we will derive the Feynman rules to be used when approximate particle number conservation is valid. There are several previous diagrammatic analyses in the context of chiral effective theories for QCD where the effect of chemical potentials associated to exactly conserved charges is studied [Ele93, AE95, Aya02, Aya03, Loe03]. The Feynman rules of thermal field theory with *exact* conserved charges can be obtained straightforwardly [Lan87] (see Section 4.1 below) but this is a completely different situation, since particle number is not exactly conserved in an interacting bosonic field theory (is only conserved in the free case) and therefore there is not a local charge operator to be included in the probability density operator in the usual way. This will also reflect in the impossibility to define a proper Matsubara imaginary-time formalism. The motivation for our field-theory description is twofold: first, it will provide a formal proof of the consistency and validity of the different prescriptions used in the literature and mentioned in the previous paragraph. Second, it will allow to deal in a natural way with pion interactions when $\mu_\pi \neq 0$, which is particularly interesting in order to describe corrections to dynamical quantities such as the thermal pion self-energy, but also to evaluate the effect of interactions in thermodynamical observables.

The chapter is organized as follows: in Section 4.1 we shall review briefly the introduction of chemical potentials in statistical mechanics and thermal field theory, next (Section 4.2) we will describe our formalism, based on holomorphic path integrals, which naturally leads to the relevant Feynman rules. The results in that part are actually valid for any real

scalar field theory provided one neglects the contributions of number-changing processes. As we shall see, those Feynman rules are really meaningful in the real-time formalism of thermal field theory. The second part (Section 4.3) deals with the application of our formalism to the pion gas. We will analyze corrections in both thermodynamical (free energy, entropy, particle number and quark condensate) and dynamical (thermal mass and width) observables, comparing to previous works in the literature and discussing several phenomenological consequences regarding chiral symmetry restoration, Bose-Einstein condensation, and thermal and chemical freeze-out. The Appendix D contains detailed results about thermal propagators mentioned in the main text.

4.1 Chemical potentials in statistical mechanics and thermal field theory

The chemical potential (usually denoted by μ) associated to some conserved charge N (such as the number of particles in classical or quantum mechanics) is introduced in thermodynamics by considering this charge as a further independent variable, so the differentials of thermodynamic potentials must contain a term proportional to $\mathrm{d}N$ [Lan80, LB04]. For instance, the variation of the internal energy is given by:

$$\mathrm{d}E = T\mathrm{d}S - P\mathrm{d}V + \mu\mathrm{d}N \ . \tag{4.1}$$

Therefore,

$$\mu = \left.\frac{\partial E}{\partial N}\right|_{S,V} = -T \left.\frac{\partial S}{\partial N}\right|_{E,V} \ . \tag{4.2}$$

Thus, the chemical potential can be physically interpreted as the energy we must provide to a particle we introduce into the system in order to keep the statistical equilibrium without modifying the volume and the entropy. Analogously to what happens with the temperature, the chemical potential must be constant in a system which is at statistical equilibrium.

More formally, in the derivation of the grand-canonical ensemble in statistical mechanics, the chemical potential can be related to the Lagrange multiplier associated to the conservation[1] of some charge N [LB04, Lan80]. The problem of determining the probability density of this ensemble then consists in maximizing the entropy subject to the constrains of a fixed statistical average for the energy and the charges, i.e., the quantity to maximize is [LB04]

$$\tilde{S} \equiv -\operatorname{Tr}(\hat{\rho}\ln\hat{\rho}) + \sum_i \lambda_i\{\operatorname{Tr}(\hat{\rho}\hat{A}_i) - \langle\hat{A}_i\rangle\} - \lambda_0(\operatorname{Tr}\hat{\rho} - 1) \ , \tag{4.3}$$

where $\hat{\rho}$ is probability density operator which is subject to the constraint $\operatorname{Tr}\hat{\rho} = 1$, and λ_i are the Lagrange multipliers associated to the corresponding constraints on the conserved

[1] The grand-canonical ensemble is in principle derived by considering a subsystem which exchanges energy and some other charge with the rest of the whole system, but it can also be applied to a closed system where the charges remain constant. From the practical point of view, in order to describe a closed system, it is usually more convenient to use the grand-canonical ensemble instead of the micro-canonical one. See discussion in [Lan80].

charges $\hat{A}_i$. The result of this maximization is the density operator

$$\hat{\rho} = \frac{1}{Z} \exp\left(\sum_i \lambda_i \hat{A}_i\right) \ , \quad \text{with} \quad Z \equiv \mathrm{Tr} \exp\left(\sum_i \lambda_i \hat{A}_i\right) \ , \tag{4.4}$$

where Z is the partition function. In the case of considering only the hamiltonian of the system $\hat{H}$ and a conserved charge $\hat{N}$, the probability density operator and the partition function have the form

$$\hat{\rho} = \frac{1}{Z} \mathrm{e}^{-\beta(\hat{H}-\mu\hat{N})} \ , \quad \text{with} \quad Z \equiv \mathrm{Tr}\, \mathrm{e}^{-\beta(\hat{H}-\mu\hat{N})} \ , \tag{4.5}$$

where it can be shown that the Lagrange multipliers λ_1 (associated to $\hat{H}$) and λ_2 (associated to $\hat{N}$) are identified with $-\beta \equiv -1/T$ and $\beta\mu$ respectively. From this probability density operator, the distribution functions satisfying Bose-Einstein and Fermi-Dirac statistics in the presence of a chemical potential can be deduced and they take the form we gave in (1.140) and (1.141).

In a chemical reaction, the chemical potential determines its balance (i.e., whether the concentrations of reactants and products remain constant in time). We represent an arbitrary chemical reaction in the gaseous phase by the equation

$$\sum_{i=1}^{n} c_i B_i = 0 \ , \tag{4.6}$$

where the stoichiometric coefficient c_i is positive or negative depending on whether the component B_i of the reaction is a reactant or a product respectively. For a closed system, $\mathrm{d}E = 0$ and $\mathrm{d}V = 0$, so the equilibrium condition $\mathrm{d}S = 0$ implies

$$\sum_{i=1}^{n} c_i \mu_i = 0 \ . \tag{4.7}$$

The condition (4.7) also applies when we have inelastic processes in the hadron gas instead of chemical reactions, like $\mathrm{N}\bar{\mathrm{N}} \leftrightarrow 4\pi$, what implies $\mu_{\mathrm{N}} = 2\mu_\pi$ in order to have chemical equilibrium [Beb92]. For a multicomponent gas, we say that some component is out of chemical equilibrium when the statistical average of its number of particles (or another conserved charge) does not coincide with the one calculated with the equilibrium density operator. For instance, in a gas of pions (see next sections in this chapter) the total number of pions is not conserved but, if the system expands fast enough so the expansion rate is much larger than the inverse of the typical collision time for these processes, inelastic processes are very scarce and the total number of pions is approximately conserved. In this way, we can have a situation where chemical equilibrium is no longer established whereas thermal equilibrium is kept.

We now consider an arbitrary multi-component covariant complex field ψ^i_α which transforms under some representation $\mathcal{R}_{\alpha\beta}$ of the Lorentz group [Lan87] (the index i denotes the internal degrees of freedom). Lets assume that this field carries the set of conserved charges q^{ij}_A such that

$$[\hat{Q}_A, \hat{\psi}^i_\alpha(x)] = -q^{ij}_A \hat{\psi}^j_\alpha(x) \ . \tag{4.8}$$

The free lagrangian density for this field is given by (we omit some indices for simplicity)

$$\mathcal{L}_0(x) = \bar{\psi}_\alpha(x) \Lambda_{\alpha\beta}(\mathrm{i}\partial) \psi_\beta(x) \ , \tag{4.9}$$

where $\bar{\psi}_\alpha \equiv (\psi^\dagger A)_\alpha$, and the operator $\Lambda(\mathrm{i}\partial)$ satisfies $[A\Lambda(\mathrm{i}\partial)]^\dagger = A\Lambda(-\mathrm{i}\partial)$ and determines the mass spectrum and spin content of the field ψ. The matrix $A_{\alpha\beta}$ intertwines the representations $\mathcal{R}^{-1}$ and $\mathcal{R}^\dagger$.

For this field, the path-integral representation of the free partition function is given by:

$$Z_0[j,\bar{j}] = \mathcal{N} \int \mathcal{D}\bar{\psi}\, \mathcal{D}\psi \ \exp\left(\mathrm{i} \int\limits_C \mathrm{d}^4x \ [\bar{\psi}\Lambda\psi + \bar{j}\psi + \bar{\psi} j] \right) \ , \tag{4.10}$$

where the contraction of indices inside the exponential is understood. The fields in (4.10) have to satisfy the quasi-periodic boundary condition

$$\psi(t_\mathrm{i}, \boldsymbol{x}) = \eta \, \mathrm{e}^{\beta\mu} \, \psi(t_\mathrm{i} - \mathrm{i}\beta, \boldsymbol{x}) \ , \tag{4.11}$$

with $\eta = \pm 1$ for bosons and fermions respectively, and $\mu \equiv \sum_A q_A \mu_A$. The factor $\mathrm{e}^{\beta\mu}$ in (4.11) is consequence of the identity $\langle\psi| \exp(\beta \sum_A q_A \hat{Q}_A) = \langle \mathrm{e}^{\beta\mu}\psi|$. It is sometimes convenient to work with fields which are (anti-)periodic in the time variable (cf. (4.20) below, and the discussion in [Eva96]), and that we define by

$$\tilde{\psi}(x) \equiv \mathrm{e}^{\mathrm{i}t\mu} \psi(x) \ . \tag{4.12}$$

By expressing the path-integral in terms of these re-defined fields, it can be seen that the introduction of a chemical potential amounts to the replacement $\mathrm{i}\partial_0 \mapsto \mathrm{i}\partial_0 + \mu$. So we see that the chemical potential plays the role of the zero-component of a gauge field.

The free propagator, which is the solution of the equation

$$\Lambda_{\alpha\gamma}(\mathrm{i}\partial) D^C_{\gamma\beta}(x - x') = \delta_{\alpha\beta} \, \delta^{(4)}_C(x - x') \ , \tag{4.13}$$

(the label C represents an arbitrary contour in the complex plane for the arguments) can be decomposed as usual as

$$\mathrm{i}D^C_{\alpha\beta}(x - x') \equiv \langle \psi_\alpha(x) \bar{\psi}_\beta(x') \rangle_0 = \theta_C(t - t') \mathrm{i}D^>_{\alpha\beta}(t - t') + \theta_C(t' - t) \mathrm{i}D^<_{\alpha\beta}(t - t') \ , \tag{4.14}$$

where the Wightman functions involved satisfy the KMS relation:

$$D^>_{\alpha\beta}(t - \mathrm{i}\beta) = \eta \, \mathrm{e}^{-\beta\mu} D^<_{\alpha\beta}(t) \ . \tag{4.15}$$

From this derivation we see that the interacting Green functions $G_{\alpha\beta}$ must also verify the KMS condition (4.15). If $d(\mathrm{i}\partial)$ is the Klein-Gordon divisor of the operator $\Lambda(\mathrm{i}\partial)$, i.e.,

$$d_{\alpha\gamma}(\mathrm{i}\partial) \Lambda_{\gamma\beta}(\mathrm{i}\partial) = \Lambda_{\alpha\gamma}(\mathrm{i}\partial) d_{\gamma\beta}(\mathrm{i}\partial) = \delta_{\alpha\beta} \prod_l (-\partial^2 - m_l^2) \ , \tag{4.16}$$

(the m_l's represent the mass spectrum of Λ) then the solution of the propagator can be written as

$$D^C_{\alpha\beta}(x) = d_{\alpha\beta}(\mathrm{i}\partial) D_C(x) \ . \tag{4.17}$$

The propagator D_C is given by [Lan87]

$$\mathrm{i}D_C(x-x') = \int \frac{\mathrm{d}^4p}{(2\pi)^4}\ \rho_0(p)\mathrm{e}^{-\mathrm{i}p\cdot(x-x')}[\theta_C(t-t') + \eta\, n_+(p_0)]\ , \tag{4.18}$$

with $n_\pm \equiv \{\exp[\beta(p_0 \mp \mu)] - \eta\}^{-1}$, and the free spectral function can be expressed as

$$\rho_0(p_0) = \mathrm{i}\,\mathrm{Disc}\prod_l \frac{1}{p^2 - m_l^2}\ , \tag{4.19}$$

where the discontinuity of an arbitrary function $f(p_0)$ is defined by $\mathrm{Disc}\, f(p_0) \equiv f(p_0 + \mathrm{i}0^+) - f(p_0 - \mathrm{i}0^+)$.

In the ITF, the Matsubara propagator with chemical potential is defined as

$$\Delta(\tau, \boldsymbol{x}) \equiv \mathrm{i}\,\mathrm{e}^{\mu\tau} D^{(\mathrm{E})}(-\mathrm{i}\tau, \boldsymbol{x})\ . \tag{4.20}$$

From its definition, it can be easily seen that it verifies $\Delta(\tau - \beta) = \eta\,\Delta(\tau)$ for $\tau \in [0, \beta]$, and $\Delta(\tau + \beta) = \eta\,\Delta(\tau)$ for $\tau \in [-\beta, 0]$. In momentum space, the Matsubara propagator is given by

$$\begin{aligned}\Delta(\mathrm{i}\omega_n, \boldsymbol{p}) &= \int_0^\beta \mathrm{d}\tau \int \mathrm{d}^3\boldsymbol{x}\ \mathrm{e}^{\mathrm{i}(\omega_n\tau - \boldsymbol{p}\cdot\boldsymbol{x})}\Delta(\tau, \boldsymbol{x}) = \int_{-\infty}^{\infty} \mathrm{d}p_0\ \frac{\rho_0(p_0)}{p_0 - \mu - \mathrm{i}\omega_n} \\ &= \prod_l \frac{1}{\boldsymbol{p}^2 + m_l^2 - (\mathrm{i}\omega_n + \mu)^2}\ ,\end{aligned} \tag{4.21}$$

where the Matsubara frequency is $\omega_n = 2n\pi T$ for bosons and $\omega_n = (2n+1)\pi T$ for fermions, with $n \in \mathbb{Z}$. The vacuum limit, $\beta \to \infty$ and $\mu \to 0$, is obtained in Euclidean space by replacing $\beta^{-1}\sum \mapsto \int \mathrm{d}k_4/(2\pi)$ with $k_0 = \mathrm{i}k_4$.

In RTF, the contour C is again the one depicted in Fig. 1.6, and the free propagators are given by the expressions [Lan87] (for bosonic field and $\sigma = 0$, compare with (1.83)–(1.85)):

$$\mathrm{i}D_{\alpha\beta}^{(11)}(p) = [\mathrm{i}\theta(p_0)\Delta_{\mathrm{F}}(p) + \mathrm{i}\theta(-p_0)\Delta_{\mathrm{F}}^*(p) + \eta\rho_0(p)n_+(p_0)]d_{\alpha\beta}(p)\ , \tag{4.22}$$

$$\mathrm{i}D_{\alpha\beta}^{(22)}(p) = [\mathrm{i}D_{\alpha\beta}^{(11)}(p)]^*\ , \tag{4.23}$$

$$\mathrm{i}D_{\alpha\beta}^{(12)}(p) = \eta\,\rho_0(p)\mathrm{e}^{\sigma p_0}n_+(p_0)d_{\alpha\beta}(p)\ , \tag{4.24}$$

$$\mathrm{i}D_{\alpha\beta}^{(21)}(p) = \eta\,\mathrm{e}^{-\beta\mu}\,\mathrm{e}^{(\beta-2\sigma)p_0}\,\mathrm{i}D_{\alpha\beta}^{(12)}(p)\ , \tag{4.25}$$

where

$$\Delta_{\mathrm{F}}(p) = \prod_l \frac{1}{p^2 - m_l^2 + \mathrm{i}0^+}\ , \tag{4.26}$$

and $\rho_0(p) = \mathrm{i}\,\mathrm{sgn}(p_0)[\Delta_{\mathrm{F}}(p) - \Delta_{\mathrm{F}}^*(p)]$.

4.2 Chemical potential for neutral scalar fields

For a neutral boson field theory, particle number is conserved only in the free case. However, as stated in the introduction, we are interested in a regime where interactions approximately respect particle number conservation, in the dilute gas framework. In other words, the only relevant processes are the elastic ones, for which the number of particles in the initial and final state is the same. Our aim here is to provide a field-theory description of such a system, to which we cannot apply the Feynman rules derived from the propagators in Section 4.1. We note that there are fundamental differences between total particle number and other (exactly) conserved numbers such as the net electric charge. In a pion gas for instance, the first one corresponds to the total number of pions $N_{\pi^0}+N_{\pi^+}+N_{\pi^-}$ whereas the second one measures $N_{\pi^+}-N_{\pi^-}$ [Ele93]. The main difference is of course that charge is exactly conserved, but also, from the field-theoretical point of view, there is a local charge operator in terms of the field and its derivatives, which allow for a straightforward derivation of the corresponding Feynman rules, adding the usual $\mu\hat{N}$ term to the probability density operator [Lan87, LB96, Kap06] (see previous section). However, that is not the case for the particle number, which instead has a natural formulation in terms of canonical creation and annihilation operators[2]. For that reason, we will follow a field-theory derivation based on the holomorphic path-integral representation.

4.2.1 Holomorphic path integrals

In first place, we review some of the key aspects of the holomorphic path integral representation which will be used in the formal analysis of this chapter. We will follow the exposition in [ZJ02], to which we refer for more details.

We consider the space $\mathcal{S}$ of complex analytic functions of one complex variable and define the following scalar product:

$$\langle f|g\rangle \equiv \int \frac{\mathrm{d}\bar{z}\ \mathrm{d}z}{2\pi\mathrm{i}}\ \mathrm{e}^{-\bar{z}z}\ \overline{f(z)}g(z)\ , \tag{4.27}$$

where the overline denotes complex conjugation (z and $\bar{z}$ are treated as independent variables), and the notation for the measure means

$$\int \frac{\mathrm{d}\bar{z}\ \mathrm{d}z}{2\pi\mathrm{i}} \equiv \int_{-\infty}^{\infty} \frac{\mathrm{d}x\ \mathrm{d}y}{\pi}\ , \tag{4.28}$$

with $z \equiv x+\mathrm{i}y$. We also define the states $\langle z|$ in the dual space $\mathcal{S}^*$ such that $\langle z|f\rangle \equiv f(z)$, with $|f\rangle \in \mathcal{S}$. Then, the set $\{f_n\}_0^\infty$, with

$$f_n(z) \equiv \frac{z^n}{\sqrt{n!}}\ , \tag{4.29}$$

[2]Although, as we shall see, for this case we can also add to the generating functional a $\mu\hat{N}$ term which is approximately conserved.

constitutes an orthonormal basis for $\mathcal{S}$ with the inner product (4.27). This implies in particular:

$$\int \frac{\mathrm{d}z'\ \mathrm{d}\bar{z}'}{2\pi\mathrm{i}}\ \mathrm{e}^{-z'\bar{z}'}\ \mathrm{e}^{\bar{z}'z}\ f(z') = f(z)\ . \tag{4.30}$$

We can also calculate the scalar product:

$$\langle z|\bar{z}'\rangle = \sum_{n=0}^{\infty}\ f_n(z)\overline{f_n(z')} = \sum_{n=0}^{\infty}\ \frac{1}{n!}(z\bar{z}')^n = \mathrm{e}^{z\bar{z}'}\ , \tag{4.31}$$

where we shall denote the dual of $\langle z|$ by $|\bar{z}\rangle$. Now, from the definition (4.27), the identity operator can be written as:

$$\hat{1} = \int \frac{\mathrm{d}\bar{z}\ \mathrm{d}z}{2\pi\mathrm{i}}\ \mathrm{e}^{-\bar{z}z}\ |\bar{z}\rangle\langle z|\ . \tag{4.32}$$

Since the functions (4.29) constitute an orthonormal basis, we can calculate the trace of an operator as follows:

$$\mathrm{Tr}\{\cdot\} = \sum_{n=0}^{\infty}\ \langle f_n|\cdot|f_n\rangle = \int \frac{\mathrm{d}\bar{z}\ \mathrm{d}z}{2\pi\mathrm{i}}\ \mathrm{e}^{-\bar{z}z}\ \langle z|\cdot|\bar{z}\rangle\ . \tag{4.33}$$

Creation and annihilation operators act over the space of complex analytic functions of one complex variable z. They are identified with:

$$\hat{a}^\dagger \mapsto z, \quad \hat{a} \mapsto \frac{\partial}{\partial z}\ , \tag{4.34}$$

and they satisfy the usual commutation relation $[\hat{a}, \hat{a}^\dagger] = \hat{1}$. The prescription (4.34) defines a representation of the creation and annihilation operators on $\mathcal{S}$. Therefore:

$$\langle z|\hat{a}^\dagger|\bar{z}'\rangle = z\langle z|\bar{z}'\rangle = z\mathrm{e}^{z\bar{z}'}\ , \quad \langle z|\hat{a}|\bar{z}'\rangle = \frac{\partial}{\partial z}\langle z|\bar{z}'\rangle = \bar{z}'\mathrm{e}^{z\bar{z}'}\ . \tag{4.35}$$

For the purpose of obtaining a path integral, we need to know how to calculate the matrix elements (*kernels*) of the kind $\mathcal{O}(z,\bar{z}') \equiv \langle z|\hat{O}(\hat{a}^\dagger,\hat{a})|\bar{z}'\rangle$, where $\hat{O}$ is an operator expressed in terms of creation and annihilation operators. Normal ordering consists in arranging creation operators to the left and annihilation operators to the right by permutations, and we denote it by $:\hat{O}(\hat{a}^\dagger,\hat{a}):$. In addition, every operator $\hat{O}(\hat{a}^\dagger,\hat{a})$ can be written in normal order by using the commutation relation $[\hat{a},\hat{a}^\dagger] = \hat{1}$, and we denote it by $\hat{O}_{\mathrm{N}}(\hat{a}^\dagger,\hat{a})$ (we call it the normal form of the operator), so $\hat{O} = \hat{O}_{\mathrm{N}}$. However, notice that in general $\hat{O}(\hat{a}^\dagger,\hat{a}) \neq\ :\hat{O}(\hat{a}^\dagger,\hat{a}):$ (normal ordering may imply a different operator), but $\hat{O}_{\mathrm{N}}(\hat{a}^\dagger,\hat{a}) = :\hat{O}_{\mathrm{N}}(\hat{a}^\dagger,\hat{a}):$. Therefore, from (4.35), the kernel is given by:

$$\begin{aligned}\mathcal{O}(z,\bar{z}') \equiv\ & \langle z|\hat{O}|\bar{z}'\rangle = \langle z|\hat{O}_{\mathrm{N}}|\bar{z}'\rangle = O_{\mathrm{N}}(z,\partial/\partial z)\mathrm{e}^{z\bar{z}'} \\ & = O_{\mathrm{N}}(z,\bar{z}')\mathrm{e}^{z\bar{z}'}\ .\end{aligned} \tag{4.36}$$

In particular, we will need the kernel corresponding to the "time-evolution" operator:

$$\mathcal{U}(z,\bar{z}';t_{\mathrm{f}}-t_{\mathrm{i}}) \equiv \langle z|\mathrm{e}^{-\mathrm{i}(t_{\mathrm{f}}-t_{\mathrm{i}})\hat{H}_{\mathrm{N}}}|\bar{z}'\rangle\ , \tag{4.37}$$

with $\hat{H}_{\rm N}$ the normal-ordered hamiltonian of the system. For that purpose, as customarily, we divide the interval $t_{\rm f}-t_{\rm i}$ into n subintervals of infinitesimal length ε and we will take the $n\to\infty$ limit at the end. Having in mind the application to thermal field theory, we will take complex times $t\in C$ where C is the contour starting at $t_{\rm i}$ and ending at $t_{\rm f}=t_{\rm i}-{\rm i}\beta$ shown in Figure 4.1 (see discussion in Section 4.2.2).

Now, from (4.36), for an infinitesimal time interval:

$$\mathcal{U}(z_1,\bar{z}_2;\varepsilon)\simeq {\rm e}^{-{\rm i}\varepsilon H_{\rm N}(z_1,\bar{z}_2)}{\rm e}^{z_1\bar{z}_2}\ , \tag{4.38}$$

so that, inserting the identity operator (4.32) $n-1$ times in (4.37) one gets:

$$\mathcal{U}(z,\bar{z}';t_{\rm f}-t_{\rm i})=\int\prod_{k=1}^{n-1}\frac{{\rm d}z_k\ {\rm d}\bar{z}_k}{2\pi{\rm i}}\ \exp\left\{z_1\bar{z}'+\sum_{k=1}^{n-1}\Big[(z_{k+1}-z_k)\bar{z}_k+\varepsilon\hat{H}_N(z_{k+1},\bar{z}_k)\Big]\right\}\ , \tag{4.39}$$

with $z_n=z$. For the Hamiltonian (4.44) one has $\hat{H}=\hat{H}_{\rm N}+\omega/2$ and the previous integral can be explicitly calculated by using the standard formula [ZJ02]:

$$\int\prod_{k=1}^{n}\frac{{\rm d}z_k\ {\rm d}\bar{z}_k}{2\pi{\rm i}}\ {\rm e}^{-\bar{z}Az+\bar{u}z+u\bar{z}}=(\det A)^{-1}{\rm e}^{\bar{u}A^{-1}u}\ , \tag{4.40}$$

which, taking the $n\to\infty$ limit, yields:

$$\mathcal{U}_0(z,\bar{z}';t_{\rm f}-t_{\rm i})=\exp\left(z\bar{z}'{\rm e}^{-{\rm i}\omega(t_{\rm f}-t_{\rm i})}+\Sigma[j]\right)\ , \tag{4.41}$$

where the subscript "0" distinguishes the particular case of the hamiltonian (4.44) and

$$\Sigma[j]={\rm i}\int_C{\rm d}t\ \left[z\frac{{\rm e}^{-{\rm i}\omega(t_{\rm f}-t)}}{\sqrt{2\omega}}j(t)+\bar{z}'\frac{{\rm e}^{{\rm i}\omega(t_{\rm i}-t)}}{\sqrt{2\omega}}j(t)\right]-\int_C{\rm d}t\ {\rm d}t'\ j(t)\theta(t-t')\frac{{\rm e}^{-{\rm i}\omega(t-t')}}{2\omega}j(t')\ . \tag{4.42}$$

4.2.2 The neutral scalar field

The starting point is the partition function (or generating functional when we include source terms) of the system in the grand-canonical ensemble:

$$\tilde{Z}_\beta\equiv{\rm Tr}\left\{{\rm e}^{-\beta(\hat{H}-\mu\hat{N})}\right\}\ , \tag{4.43}$$

where quantities with a tilde will refer always to the $\mu\neq0$ case throughout this chapter. It is well known that for a neutral scalar field the number of particles is not a conserved quantity. However, if the gas is dilute enough and the temperature is not very high, we may expect that most of the collisions are elastic and therefore, the number of particles would remain approximately constant. We can give a more formal definition of this "conservation of the number of particles": suppose that we measure the number of particles in the system at a certain instant of time t_1, then we will say that the number of particles is conserved if at another time t_2, larger than the typical interaction time, we measure

again the same number of particles. And this must be in this way whatever the state of the system is. Of course this situation cannot happen exactly, because the number of particles is not actually conserved, but it can happen approximately (for short enough intervals of time, or during the expansion of the meson gas[3]). Therefore for *any* state of the system $|n(t_1)\rangle$ with n particles at the instant of time t_1, we will have:

$$\hat{N}|n(t_1)\rangle = n|n(t_1)\rangle \ , \quad \hat{N}|n(t_2)\rangle \simeq n|n(t_2)\rangle \quad \Rightarrow \quad \hat{N}(t_1) \simeq \hat{N}(t_2) \ .$$

And since the temporal evolution of the number operator satisfies the Heisenberg equation

$$\mathrm{i}\frac{\mathrm{d}}{\mathrm{d}t}\hat{N}(t) = [\hat{N}, \hat{H}] \ ,$$

this implies

$$0 \simeq \mathrm{i}(\hat{N}(t_2) - \hat{N}(t_1)) = \int_{t_1}^{t_2} [\hat{N}, \hat{H}] \ \mathrm{d}t \quad \Rightarrow \quad [\hat{N}, \hat{H}] \simeq 0 \ .$$

Therefore:

$$\text{approximate particle number conservation} \quad \Leftrightarrow \quad [\hat{N}, \hat{H}] \simeq 0 \ .$$

In order to simplify further the discussion, we will first consider a quantum-mechanical gas of Bose particles and next we will extend it straightforwardly to the QFT case. Let us consider then a single-frequency quantum oscillator (free Hamiltonian) coupled to an external force $j(t)$. The Hamiltonian and number operators are then:

$$\begin{aligned} \hat{H} &= \frac{1}{2}\hat{p}^2 + \frac{1}{2}\omega^2\hat{q}^2 - j(t)\hat{q} \equiv \hat{H}_0 - j(t)\hat{q} \\ &= \frac{\omega}{2}\left(\hat{a}^\dagger\hat{a} + \hat{a}\hat{a}^\dagger\right) - \frac{1}{\sqrt{2\omega}}\left(\hat{a}^\dagger + \hat{a}\right) j(t) \ , \qquad (4.44) \\ \hat{N} &= \hat{a}^\dagger\hat{a} \ , \qquad (4.45) \end{aligned}$$

where $\hat{q}$ and $\hat{p}$ are respectively the position and conjugate momentum operators (whose role will be played by the field and its conjugate momentum) and the creation and annihilation operators are defined in the usual way:

$$\hat{a} = \frac{\mathrm{i}}{\sqrt{2\omega}}(\hat{p} - \mathrm{i}\omega\hat{q}) \ , \quad \hat{a}^\dagger = -\frac{\mathrm{i}}{\sqrt{2\omega}}(\hat{p} + \mathrm{i}\omega\hat{q}) \ . \qquad (4.46)$$

In particular, the partition function for any Hamiltonian $\hat{H}$ reads, from (4.33):

$$\tilde{Z}_\beta = \int \frac{\mathrm{d}z \ \mathrm{d}\bar{z}}{2\pi\mathrm{i}} \ \mathrm{e}^{-\bar{z}z} \ \langle z|\mathrm{e}^{-\beta(\hat{H}-\mu\hat{N})}|\bar{z}\rangle \ . \qquad (4.47)$$

[3]This assumption is physically justified if the typical interaction times associated to number-changing processes are much larger than the inverse expansion rate $R/\dot{R}$, where R is the system size. In this way, one has in practice $N(t_1) \simeq N(t_2)$, with N the total particle number and for all $|t_1 - t_2| < t_{\mathrm{tot}}$ (the system lifetime).

Now, if the number operator is approximately conserved, then $[\hat{H}, \hat{N}] \simeq 0$ and equation (4.47) can be recast, by inserting the identity once, as:

$$\tilde{Z}_\beta \simeq \int \frac{\mathrm{d}z\ \mathrm{d}\bar{z}}{2\pi\mathrm{i}}\ \mathrm{e}^{-\bar{z}z} \int \frac{\mathrm{d}z'\ \mathrm{d}\bar{z}'}{2\pi\mathrm{i}}\ \mathrm{e}^{-\bar{z}'z'}\ \langle z|\mathrm{e}^{\beta\mu\hat{N}}|\bar{z}'\rangle\langle z'|\mathrm{e}^{-\beta\hat{H}}|\bar{z}\rangle\ . \tag{4.48}$$

This is the key step of the derivation, since it contains our main approximation, which is equivalent to consider only up to two-particle states in the trace (4.43). Therefore, it is physically appropriate to describe a dilute regime where elastic collisions dominate.

Now, the first matrix element in (4.48) can be calculated directly, using (4.41) with $j = 0$, $t_\mathrm{f} = t_\mathrm{i} - \mathrm{i}\beta$ and $\omega = -\mu$:

$$\langle z|\mathrm{e}^{\beta\mu\hat{N}}|\bar{z}'\rangle = \exp\left(z\bar{z}'\mathrm{e}^{\beta\mu}\right)\ , \tag{4.49}$$

and so, using (4.30), we arrive to:

$$\tilde{Z}_\beta = \int \frac{\mathrm{d}z\ \mathrm{d}\bar{z}}{2\pi\mathrm{i}}\ \mathrm{e}^{-\bar{z}z}\ \langle z\mathrm{e}^{\beta\mu}|\mathrm{e}^{-\beta\hat{H}}|\bar{z}\rangle\ . \tag{4.50}$$

From this representation of the partition function we define the corresponding generating functional (in the QM case):

$$\tilde{Z}_\beta[j] \equiv \int \frac{\mathrm{d}z\ \mathrm{d}\bar{z}}{2\pi\mathrm{i}}\ \mathrm{e}^{-\bar{z}z}\ \langle z\mathrm{e}^{\beta\mu}|\mathrm{e}^{-\beta(\hat{H}-j\hat{q})}|\bar{z}\rangle\ . \tag{4.51}$$

so that correlators of any function of the position operator $\hat{q}$ (the field operator in the QFT case) can be expressed in terms of functional derivatives of $\tilde{Z}_\beta[j]$ with respect to j at $j = 0$ in the usual way.

We will now proceed to the evaluation of $\tilde{Z}_\beta[j]$ when the Hamiltonian is the free one plus the source term, i.e, $\hat{H} = \hat{H}_0 - j\hat{q}$ in (4.44). Then, as usual, by functional derivation we will get the generating functional for the interacting case. We first separate the normal-ordered part as customarily, i.e, $\hat{H}_0 = \omega/2 + \omega\hat{a}^\dagger\hat{a}$ where the first term is the vacuum energy. Therefore, we have:

$$\tilde{Z}^0_\beta[j] = \mathrm{e}^{-\beta\omega/2} \int \frac{\mathrm{d}z\ \mathrm{d}\bar{z}}{2\pi\mathrm{i}}\ \mathrm{e}^{-\bar{z}z}\ \mathcal{U}_0(z\mathrm{e}^{\beta\mu}, \bar{z}; -\mathrm{i}\beta)\ . \tag{4.52}$$

The quantity $\mathcal{U}$ is defined in (4.37) and for the present case, its expression is given in (4.41)-(4.42). For its evaluation, we have considered the complex time contour shown in Figure 4.1 joining the points t_i and $t_\mathrm{i} - \mathrm{i}\beta$ with $\sigma \in [0, \beta]$, which contains the usual real-time and imaginary-time paths of Thermal Field Theory and satisfies the usual requirements for the path integral to be well defined, i.e., $\mathrm{Im}\, t$ is monotonically decreasing along the contour [Lan87]. The imaginary-time contour runs in a straight line from $t_\mathrm{i} = 0$ down to $-\mathrm{i}\beta$ and is denoted as C_4, while the C_1 and C_2 are the paths used in the real-time formulation (see below).

Now, replacing in (4.41)-(4.42) $z \mapsto z\mathrm{e}^{\beta\mu}$, $\bar{z}' \mapsto \bar{z}$, $t_\mathrm{f} \mapsto t_\mathrm{i} - \mathrm{i}\beta$ is equivalent to replacing:

$$\beta \mapsto \tilde{\beta} \equiv \beta\left(1 - \frac{\mu}{\omega}\right)\ , \tag{4.53}$$

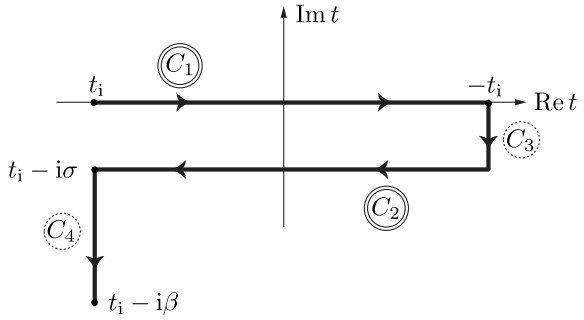

Figure 4.1: Complex time contour including real and imaginary time paths, used in the derivation of the $\mu \neq 0$ Feynman rules, where $\sigma \in [0, \beta]$.

except for the β appearing in the C contour. With this replacement one can follow the same steps as in [ZJ02] for the evaluation of the remaining integral in (4.52). Namely, one goes back to the discretized version of the path-integral (see Section 4.2.1), uses again (4.40) with the modified A matrix and finally takes again the continuum limit. The final result is:

$$\tilde{Z}^0_\beta[j] = \tilde{Z}^0_\beta \exp\left(-\frac{1}{2}\int_C \mathrm{d}t\ \mathrm{d}t'\ j(t)\tilde{G}_\mathrm{F}(t-t')j(t')\right) \ , \tag{4.54}$$

with the free partition function

$$\tilde{Z}^0_\beta = \frac{\mathrm{e}^{-\beta\omega/2}}{1-\mathrm{e}^{-\beta(\omega-\mu)}} \ , \tag{4.55}$$

and the free propagator

$$\tilde{G}(t) = \frac{1}{2\omega}\left[\mathrm{e}^{-\mathrm{i}\omega|t|}(1+n_\mathrm{B}(\omega-\mu)) + \mathrm{e}^{\mathrm{i}\omega|t|}n_\mathrm{B}(\omega-\mu)\right] \ , \tag{4.56}$$

where the Bose-Einstein function:

$$n_\mathrm{B}(x) = \frac{1}{e^{\beta x}-1} \ , \tag{4.57}$$

so that $n_\mathrm{B}(\omega-\mu)$ is the free distribution function at non-zero μ in (D.7). Note that we must restrict to $\mu < \omega$ in order that the previous expressions for the partition function are well defined (see also comments in Appendix D). The case $\mu = \omega$ is the natural Bose-Einstein condensation limit. In the propagator, $|t-t'|$ has to be understood in terms of the relative position of times t and t' with the path routing shown in Figure 4.1.

The result (4.54) is one of the main results of this chapter. Its importance relies on the fact that we can now easily construct the generating functional in the interacting case, say $\hat{H} = \hat{H}_0 + V(\hat{q})$ with V the potential, in the usual way, i.e., by expanding formally in series of V and writing every term in the expansion in terms of functional derivatives of $\tilde{Z}^0_\beta[j]$ with respect to j. From there, the extension to a QFT for a real scalar field with lagrangian density:

$$\mathcal{L} = \frac{1}{2}(\partial_\mu\phi)^2 - \frac{m^2}{2}\phi^2 - \mathcal{V}(\phi) - j\phi \ , \tag{4.58}$$

is direct:

$$\tilde{Z}_\beta[j] = \tilde{Z}^0_\beta \ \exp\left(-\mathrm{i}\int\limits_C \mathrm{d}^4x\ \mathcal{V}\left(\frac{\delta}{\mathrm{i}\delta j(x)}\right)\right) \exp\left(-\frac{1}{2}\int\limits_C \mathrm{d}^4x\ \int\limits_C \mathrm{d}^4x\ j(x)\tilde{G}(x-x')j(x')\right)\ , \tag{4.59}$$

where $\int\limits_C \mathrm{d}^4x\ \equiv \int_C \mathrm{d}t \int \mathrm{d}^3\boldsymbol{x}$.

Note that in the field-theory case, whereas the Hamiltonian can be expressed as a space integral of a local field operator, that is not the case for the number operator when infinite frequencies appear. This is only possible for exactly conserved currents.

The propagator $\tilde{G}$ appearing in (4.59) is the generalization of (4.56) to the QFT case when $\omega \mapsto E_p$ (the particle energy), and therefore we will restrict in the following to $\mu \leq m$. The explicit expression of the propagator coincides, as it should, with the free two-point function (D.8)-(D.11) derived in Appendix D directly within the canonical formalism at $\mu \neq 0$ for $t \in \mathbb{R}$. Recall that the QFT generalization of $\tilde{\beta}$ in (4.53) is the p-dependent $\tilde{\beta}_p$ in (D.13). This p-dependent temperature is a signal of the depart from (chemical) equilibrium and again is related to the absence of a local number operator. Another indication that we are really dealing with a non-equilibrium situation will be the impossibility of defining properly a Matsubara or Imaginary-Time Formalism.

The previous result for the generating functional is valid for any real scalar theory, provided one works in the regime where elastic collisions dominate and particle number is approximately conserved. Therefore, we can define the corresponding Feynman rules for diagrammatic calculations, which in principle can be implemented either in the real-time or imaginary-time formalisms. Let us discuss their main features in the $\mu \neq 0$ case.

4.2.3 Imaginary Time Formalism

The ITF corresponds to the choice $t_\mathrm{i} = \sigma = 0$ for the contour in Fig. 4.1 so that one is left only with purely imaginary times $t = -\mathrm{i}\tau$ with $\tau \in [0, \beta]$. At $\mu = 0$, this formalism is usually best suited to deal with thermodynamic quantities such as the free energy, while retarded Green functions can be derived from it by analytic continuation [LB96]. However, the $\mu \neq 0$ propagator shows a distinctive feature that complicates diagrammatic calculations, generating in some cases not well-defined results. The origin of the problem is that the free propagator is not periodic in imaginary time. In the mixed representation, it satisfies $\tilde{\Delta}_T(\tau + \tilde{\beta}_p, p) = \tilde{\Delta}_T(\tau, p)$, as detailed in Appendix D. This momentum-dependent periodic condition makes it impossible to define properly a Matsubara representation in Fourier space. As discussed in the Appendix, this can only be done for $\tau \in [-\tilde{\beta}_p, \tilde{\beta}_p]$, e.g. Eq. (D.20), instead of the required $[-\beta, \beta]$ interval where time differences appearing in propagators are evaluated (note that $\tilde{\beta}_p < \beta$). In the case of diagrams contributing to the partition function (closed diagrams) this may be a problem whenever there is momentum exchange (time propagation) inside the diagram, i.e, more than one interaction vertex, since in that case the imaginary-time variable running in the internal propagators lies in the interval $[-\beta, \beta]$ while those propagators are only β_p-periodic. When there is just one interaction vertex, time integration factorizes trivially and the answer is proportional to powers of the tadpole-like contribution $\tilde{\Delta}_T(\tau = 0, \boldsymbol{x} = \boldsymbol{0})$ given in Appendix D. That will be the case for all the contributions to leading order $\mathcal{O}(T^6)$ in the calculation of the

ChPT partition function. The diagrams that contribute are given in Figure 4.2, where we follow the same notation as in [Ger89] for the interaction vertices coming from higher order lagrangians (see Section 4.3). However, consider for instance the diagram labelled 8b in Figure 4.2, contributing to the ChPT free energy density to $\mathcal{O}(T^8)$. Taking for simplicity constant vertices, as in the case of $\mathcal{V} = \lambda\phi^4/4!$, this diagram in the ITF would be proportional to:

$$I = \frac{\tilde{G}^2(0)}{\beta} \int \frac{\mathrm{d}^3\boldsymbol{p}}{(2\pi)^3} \int_0^\beta \mathrm{d}\tau' \int_0^\beta \mathrm{d}\tau \; \tilde{\Delta}_T(\tau - \tau', p)\tilde{\Delta}_T(\tau' - \tau, p) \; , \tag{4.60}$$

with $\tilde{G}(0) = \tilde{\Delta}_T(0)$ given in Eqs. (D.21)-(D.23). Now, as commented above, we cannot just replace the Fourier representation for $\tilde{\Delta}_T$ in (D.20) since it is only defined for the $[-\tilde{\beta}_p, \tilde{\beta}_p]$ interval. This obstruction produces additional unnatural terms. The appearance of those terms can be seen by using the mixed representation for Δ_T in terms of $\tilde{G}^>$ and $\tilde{G}^<$ given in (D.10)-(D.11) and performing explicitly the τ, τ' integrals in (4.60). We get:

$$\begin{aligned} I = &- \tilde{G}^2(0)\frac{\partial}{\partial m^2}\tilde{G}(0) + \frac{\tilde{G}(0)}{\beta} \int \frac{\mathrm{d}^3\boldsymbol{p}}{(2\pi)^3} \frac{1}{8E_p^4} \left\{ \left[1 + \tilde{n}_p(E_p)\right]^2 \left[e^{2\beta\mu} - 1\right] \right. \\ &\left. + \left[\tilde{n}_p(E_p)\right]^2 \left[e^{-2\beta\mu} - 1\right] \right\} \; , \end{aligned} \tag{4.61}$$

The first term above gives the standard result for $\mu = 0$ [Ger89] with the replacement of the distribution function $n \mapsto \tilde{n}$, as one would expect from kinetic theory arguments, while this property does not hold for the additional terms. The remaining contributions vanish for $\mu = 0$ but they do not in the $T \to 0^+$ limit where diverge. This contradicts the natural physical expectation that in the $T \to 0^+$ limit and for $\mu < m$, the free energy should reduce to the vacuum contribution. Similar conflictive terms arise when trying to calculate correlation functions.

As we will see in Section 4.3, the appearance of these terms signals the validity limit of our approximation. At the temperatures where the $\mathcal{O}(T^8)$ for the partition function needs to be considered, particle-changing processes start playing an important role so that in practice we should consider $\mu \ll T, m$ for these contributions. Recall that in fact, the conflictive terms in (4.61) are $\mathcal{O}(\mu/T)$ in that expansion so that we will be introducing only small corrections by neglecting them. The fact that these terms appear in the ITF is natural if we note that we are facing a non-equilibrium situation, where the ITF is not appropriate and it must be formulated using a contour including real times [Cho85]. We will indeed see next that one can define a suitable Real-Time Formalism so that these problems are not present and one can calculate properly, to leading order in the interaction, both correlators and the vacuum diagrams leading to the free energy.

4.2.4 Real Time Formalism

We consider now the full contour in Figure 4.1 and, following the standard notation, we denote by $\tilde{D}_{ij} = \tilde{G}(t_i - t_j)$ with $t_i \in C_i, t_j \in C_j$. We then have for the $C_{1,2}$ parts of the

contour (we omit the spatial dependence for simplicity):

$$\begin{aligned}
\tilde{D}_{11}(t-t') &= \tilde{G}^{>}(t-t')\theta(t-t') + \tilde{G}^{<}(t-t')\theta(t'-t) \ , \\
\tilde{D}_{22}(t-t') &= \tilde{G}^{<}(t-t')\theta(t-t') + \tilde{G}^{>}(t-t')\theta(t'-t) \ , \\
\tilde{D}_{12}(t-t') &= \tilde{G}^{<}(t-t'+\mathrm{i}\sigma) = \tilde{D}_{21}(t'-t) \ ,
\end{aligned} \tag{4.62}$$

where $t, t' \in \mathbb{R}$ and $\tilde{G}^{>}, \tilde{G}^{<}$ given in (D.10)-(D.11) and so on for the remaining components.

In order to formulate properly the RTF at $\mu \neq 0$ we take first, as customary, $t_i \to -\infty$. This is necessary if we want to calculate Green functions with arbitrary real time arguments. In principle, this choice implies also that, imposing vanishing asymptotic conditions for the j currents and for the spectral function, which hold also in our case, the generating functional for $\mathcal{V} = 0$ can be factorized as [Lan87]:

$$\tilde{Z}^{\mathcal{V}=0}_{\beta,C}[j] = \mathcal{N}\ \tilde{Z}^{\mathcal{V}=0}_{\beta,C_{12}}[j]\ \tilde{Z}^{\mathcal{V}=0}_{\beta,C_{34}}[j] \ , \tag{4.63}$$

so that one could calculate real-time correlation functions without worrying about the imaginary-leg contributions. However, as it was pointed out in [Nie89, Gel99], there are imaginary-time contributions that still survive in particular diagrams, for instance self-energy insertions, which indeed we will calculate here. Nevertheless, there is a standard rule for collecting all the relevant contributions but using only the propagators in $C_{1,2}$, the so called $|p_0|$-prescription [Nie89, Gel99, LB96]. This prescription amounts to use in Fourier space $n_{\mathrm{B}}(|p_0|)$ instead of the seemingly equivalent $n_{\mathrm{B}}(E_p)$ when multiplied by the on-shell δ-function, as in (D.19). For instance, with this prescription one obtains that a simple constant tadpole-like insertion in the self energy such as the diagram shown in Figure 4.6(a) with a constant vertex, amounts to a redefinition of the mass, as expected. It also guarantees that there are no ill-defined contributions, such as products of δ distributions at the same point which in principle could appear when multiplying the RTF propagators. What we will show here is that for $\mu \neq 0$ there is also a natural prescription that works, now in terms of $n_{\mathrm{B}} \mapsto \tilde{n}_p(p_0)$, which leads to the same properties. This avoids the main obstruction that we faced in the ITF, since the length β of the imaginary leg disappears from the integration limits in momentum space, which Fourier representation is well defined now. Moreover, we also choose $\sigma \to 0^+$. Therefore, for Green functions with real-time arguments for which we neglect (with the above prescription) the $C_{3,4}$ parts, we end up with a Keldysh-like contour characteristic of non-equilibrium Thermal Field Theory [Cho85]. With this procedure we will see that an additional property holds: most results can be written as functionals of $\tilde{n}$, which encodes all the T, μ dependence. This is also a expected property from kinetic theory arguments, at least for the leading order corrections in $\tilde{n}$ (dilute gas regime).

This allows then to calculate properly any real-time correlation function directly, i.e., without appealing to the analytic continuation from the ITF, which is cumbersome for $\mu \neq 0$. In addition, as we will see below, one can also obtain information about the free energy density without using the ITF. Let us then write the propagators (4.62) in momentum space for our choice of contour (note that the $\tilde{D}_{11}$ component corresponds to

the free propagator $\tilde{G}$ in (D.19)):

$$\begin{aligned}
\tilde{D}_{11}(p_0,p) &= \frac{i}{p_0^2-E_p^2+i0^+} + 2\pi\delta(p_0^2-E_p^2)n_{\rm B}(|p_0|-\mu) \ , \\
\tilde{D}_{22}(p_0,p) &= \frac{-i}{p_0^2-E_p^2+i0^+} + 2\pi\delta(p_0^2-E_p^2)n_{\rm B}(|p_0|-\mu) \ , \\
\tilde{D}_{12}(p_0,p) &= 2\pi\delta(p_0^2-E_p^2)\left[\theta(p_0)+n_{\rm B}(|p_0|-\mu)\right] \ , \\
\tilde{D}_{21}(p_0,p) &= 2\pi\delta(p_0^2-E_p^2)\left[\theta(-p_0)+n_{\rm B}(|p_0|-\mu)\right] \ . \qquad (4.64)
\end{aligned}$$

In the above propagators, we have chosen the $|p_0|$ prescription ensuring that the distribution function does not depend explicitly on E_p, as in the $\mu = 0$ case. We will see below that this yields the same expected properties as for $\mu = 0$. It can also be readily checked that our $\mu \neq 0$ RTF propagators above coincide with those given in [Bai97] and used in a dilepton analysis, where they were obtained assuming a direct replacement of the distribution function by the $\mu \neq 0$ non-equilibrium one.

To provide a particularly relevant example of our previous statements, we will consider the tadpole-like correction to the self-energy given by the diagram in Figure 4.6(a) with a constant vertex (the generalization to derivative vertices appearing in ChPT calculations will be straightforward). The external leg is fixed to be of "type 1", since we are calculating the two-point function with real arguments, i.e, the first-order correction to D_{11}. Then, if we consider only the $C_{1,2}$ contributions, this diagram gives in position space:

$$F(x-y) = \mathrm{i}\sum_{j=1,2}\int_{C_j}\tilde{D}_{1j}(x-z)\tilde{D}_{jj}(0)\tilde{D}_{j1}(z-y) \ . \qquad (4.65)$$

Now, we take into account that $\tilde{D}_{11}(0) = \tilde{D}_{22}(0) = \tilde{G}(0)$ in (D.21)-(D.23). Then, the Fourier transform of F is:

$$F(p_0,p) = \mathrm{i}\tilde{G}(0)\left[\tilde{D}_{11}^2(p_0,p) - \tilde{D}_{12}(p_0,p)\tilde{D}_{21}(p_0,p)\right] \ . \qquad (4.66)$$

We replace in the above equation the propagators in (4.64) and use

$$\frac{\delta(x)}{x+\mathrm{i}0^+} = -\frac{\delta'(x)}{2} - \mathrm{i}\pi\delta^2(x) \ ,$$

where as customary we keep the regulator in the definition of

$$\delta(x) = \frac{\mathrm{i}}{2\pi}\left(\frac{1}{x+\mathrm{i}0^+} - \frac{1}{x-\mathrm{i}0^+}\right) \ .$$

Thus, we can write:

$$\begin{aligned}
F(p_0,p) &= \mathrm{i}\tilde{G}(0)\left\{\left[\frac{\mathrm{i}}{p_0^2-E_p^2+\mathrm{i}0^+}\right]^2 - 2\pi\mathrm{i}n_p(|p_0|-\mu)\delta'(p_0^2-E_p^2)\right\} \\
&= -\tilde{G}(0)\frac{\partial}{\partial m^2}\tilde{D}_{11}(p_0,p) \ . \qquad (4.67)
\end{aligned}$$

Note that it is in the last step in the previous equation where it is crucial to use the $|p_0|$ prescription chosen above since $\tilde{n}_p(|p_0|-\mu)$ is independent of m^2. Therefore, the result (4.67) implies that the only modification in the $\tilde{D}_{11}$ propagator is $m^2 \mapsto m^2 - \tilde{G}(0)$, which is the expected result of mass renormalization which in addition is obtained from the $\mu = 0$ case by replacing $n_{\rm B} \mapsto \tilde{n}_p$ in the (finite) thermal correction to the tadpole diagram given by the function $\tilde{g}_1(m,T,\mu)$ in (D.23).

Two more important remarks are in order. The first one is that the spectral properties of the interacting theory are really defined from retarded Green functions, not from time-ordered ones. From the ITF, retarded correlators are defined directly by analytic continuation. However, we have seen that this is not a well defined procedure for $\mu \neq 0$. The solution of the problem of finding retarded Green functions from the RTF time-ordered product was given in [Kob90]. In that work, a set of rules (so-called circling rules) was given in order to define a function that has the required causal retarded properties, namely that satisfies that one of the outgoing lines of the corresponding diagram has the largest time component. It was then shown in several examples that this function coincides with the analytic continuation of the ITF correlator. Now, it can be checked that the same properties of the free propagators used in [Kob90] for the derivation of the circling rules hold for our $\tilde{D}_{ij}$ propagators and therefore the same rules lead to the RTF retarded function. The application of those rules is trivial for the tadpole case discussed above, since there is only one vertex. However, these rules will be of use for the case of higher order contributions to the self energy which we will consider below, like the thermal width arising from diagram 4.6(b).

The second remark has to do with the calculation of thermodynamic quantities within the RTF, i.e., the partition function or the free energy density. In principle, due to the factorization of the imaginary-leg commented above, the contribution to vacuum graphs when summing over fields of type 1 and 2 vanishes identically. However, it was shown in [Fuj84, Mat85] that fixing one of the vertices of a vacuum diagram to be "external" of type 1 and summing over the remaining internal vertices with an overall β factor reproduces the free-energy result and for $\mu = 0$ coincides with the ITF. The functional arguments used in those papers are also applicable to our $\mu \neq 0$ case and in fact, the direct use of that prescription leads to the expected answers. Let us show this for the case of the $\mathcal{O}(T^8)$ diagram 8b in Fig. 4.2, analyzed in Section 4.2.3 in the ITF. Applying the previous prescription and with constant vertices, we get that this diagram is now proportional to:

$$\mathrm{i}\tilde{G}^2(0)\sum_{j=1,2}\int_{C_j}\tilde{D}_{1j}(x-z)\tilde{D}_{j1}(z-x) = \tilde{G}(0)F(0) = -\tilde{G}^2(0)\frac{\partial}{\partial m^2}\tilde{G}(0)\ , \tag{4.68}$$

with F in (4.65). We then see that we arrive to the ITF result (4.61) but without the additional terms discussed in that section, since the proportionality factors between this diagram and (4.68) or (4.60) come only from combinatorics and are therefore identical. We may then use this real-time prescription to define properly our free energy.

4.3 Applications to the pion gas

4.3.1 Evaluation of the ChPT free energy

We apply our previous results to the pion gas, described by ChPT for two light flavors. In the range of temperatures and chemical potentials we are interested, both $T, \mu_\pi = \mathcal{O}(p)$ formally, which corresponds to T below $T_c \sim 200$ MeV. In our approach, we do not perform any formal chiral expansion in μ_π, except in higher order contributions (see our discussion below and in Section 4.2) where it is reasonable to expand in μ_π/T. We will use the same central values for the low-energy constants $\bar{l}_i$ given in [Gas84, Ger89], in order to compare more easily with the results in [Ger89] at $\mu_\pi = 0$. Those values are[4] $\bar{l}_1 = -6.6$, $\bar{l}_2 = 6.2$, $\bar{l}_3 = 2.9$, $\bar{l}_4 = 3.5$. The constant h_1 multiplies a contact term and appears in the vacuum free energy and quark condensate. We use also the estimate in [Gas84, Ger89] of $\bar{h}_1 \simeq 3.4$. The lagrangians of higher orders will only appear through renormalization either of the vacuum energy or the pion mass and therefore the low-energy constants of those orders will not show up once the results are expressed in terms of the physical pion mass (see details below).

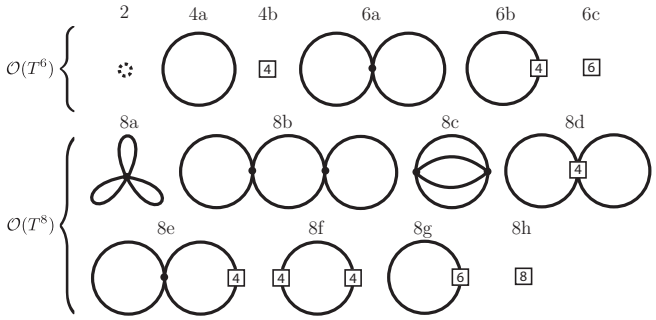

Figure 4.2: Feynman diagrams contributing to the partition function of the pion gas up to and including $\mathcal{O}(T^8)$. The first row includes diagrams up to $\mathcal{O}(T^6)$ while the second and third rows are the $\mathcal{O}(T^8)$ contributions. The dots denote interaction vertices coming from $\mathcal{L}_2$ while those vertices coming from higher order lagrangians are indicated by a square box. The label above each diagram follows the same notation as [Ger89].

The free energy density z, from which thermodynamical observables can be obtained, is defined as customary:

$$\tilde{z}(T, \mu_\pi) = -\lim_{V\to\infty} \frac{T}{V} \ln \tilde{Z}_\beta(T, \mu_\pi) \ . \tag{4.69}$$

We also define the thermodynamic pressure as in [Ger89], i.e, subtracting its $T = 0$ contribution given by the vacuum energy density:

$$\tilde{P}(T, \mu_\pi) = \tilde{z}_0 - \tilde{z}(T, \mu_\pi) \ , \quad \tilde{z}_0 = \lim_{T\to 0^+} \tilde{z} \ . \tag{4.70}$$

[4]These are the perturbative values, which are different from the ones chosen for the analysis of resonances in Chapters 2 and 3 (see also comments in Section 4.3.3).

The diagrams contributing to the free energy in ChPT are the closed diagrams shown in Figure 4.2, where we follow the same convention as [Ger89] to name the diagrams. The number assigned to each diagram indicates the order in the chiral expansion and the numbers inside the boxes in the vertices refer to the lagrangian order, the case of $\mathcal{L}_2$ being indicated solely by a dot. Recall that for a given order of the lagrangian, there are vertices with arbitrary number of (even) pions due to the chiral expansion of the SU(2)-valued chiral field $U = \exp(\mathrm{i}\boldsymbol{\pi}\cdot\boldsymbol{\sigma}/F_0)$ where σ^a are the Pauli matrices (see Appendix B) and π^a the pion field.

The leading order $\tilde{z}_2 = -F_0^2 M_0^2$ comes from the contact term (independent of the pion field) in $\mathcal{L}_2$, is independent of T and μ_π and therefore contributes only to the vacuum energy density $\tilde{z}_0$. Note that, according to our discussion in the previous sections, we will ensure that all our contributions have a well-defined $T \to 0^+$ limit for $\mu_\pi < M_0$, i.e, that the contributions to $\tilde{z}_0$ to any chiral order are μ_π-independent. The next order corresponds to diagrams 4a and 4b. $\tilde{z}_{4\mathrm{a}}$ corresponds to the quadratic pion field contribution in $\mathcal{L}_2$ and is therefore nothing but the free partition function given in (D.26) multiplied by 3 accounting for the three pion degrees of freedom. The divergent contribution to $\tilde{z}_{4\mathrm{a}}$ is T and μ_π independent and therefore it merely renormalizes $\tilde{z}_0$.

The next order in the chiral expansion is $\mathcal{O}(T^6)$ and the diagrams contributing are 6(a,b,c) in Figure 4.2. It is important to remark that this is the first order where pion interactions show up. Graph 6c renormalizes $\tilde{z}_0$, graph 6b is of the same form as 4a and therefore gives rise to the free partition function contribution but with the mass shifted by its tree level $\mathcal{L}_4$ renormalization (see Section 4.3.3) which depends on l_3. As for the diagram 6a, taking into account (D.24), its contribution is proportional to $\tilde{G}^2(0)$. As discussed in Section 4.2, in this case the result is trivially identical in both ITF and RTF and corresponds to the result in [Ger89] replacing $G(0) \mapsto \tilde{G}(0)$:

$$\tilde{z}_{6\mathrm{a}} = \frac{3M_0^2}{8F_0^2}\tilde{G}^2(0)\ . \tag{4.71}$$

The divergent contribution in (4.71), according to (D.21), contains a contribution to $\tilde{z}_0$ and another one which cancels, as it should, with the one in l_3 so that, using (D.27), the total finite result for the pressure to $\mathcal{O}(T^6)$ is:

$$\tilde{P} = \frac{3}{2}\tilde{g}_0(M_\pi, T, \mu) - \frac{3}{8}\frac{M_0^2}{F_0^2}\left[\tilde{g}_1(M_0, T, \mu)\right]^2 + \mathcal{O}(T^8)\ , \tag{4.72}$$

with $\tilde{g}_0$ and $\tilde{g}_1$ given in Appendix D, and where M_π is the physical pion mass at $T = \mu_\pi = 0$, related to the bare mass M_0 to this order as [Gas84]:

$$M_\pi^2 = M_0^2\left[1 - \frac{\bar{l}_3}{32\pi^2}\frac{M_0^2}{F_0^2} + \mathcal{O}(M_0^4)\right]\ . \tag{4.73}$$

Recall that, to this order, the difference between M_π and M_0 is only relevant in the $\tilde{g}_0$ contribution in (4.72). The same applies to the distinction between F_0 and F_π:

$$F_\pi^2 = F_0^2\left[1 + \frac{\bar{l}_4}{8\pi^2}\frac{M_0^2}{F_0^2} + \mathcal{O}(M_0^4)\right]\ . \tag{4.74}$$

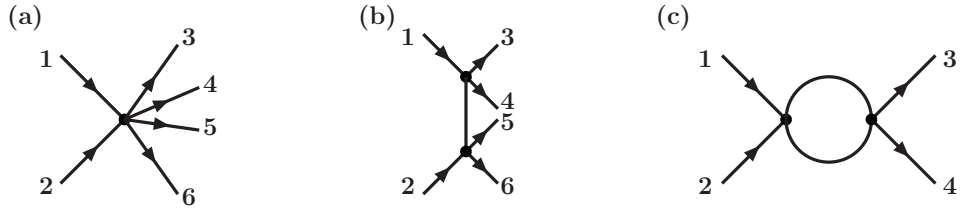

Figure 4.3: (a,b) Diagrams contributing to leading order (tree level) to $2\pi \to 4\pi$ processes. (c) A one-loop contribution to elastic $\pi\pi$ scattering.

We consider now the $\mathcal{O}(T^8)$ contributions shown in Figure 4.2. Now, there are several aspects which make the calculation qualitatively different from the $\mathcal{O}(T^6)$ one. An important point is that to this order we may expect that our approximation of particle number conservation starts breaking up, since vertices entering number-changing processes start showing up. Consider for instance the diagrams contributing to $2\pi \leftrightarrow 4\pi$ processes in the thermal bath, which to leading order in ChPT are given by the tree level diagrams shown in Fig. 4.3(a) and (b). Now, unlike the $\mathcal{O}(T^6)$ case, one can draw vacuum diagrams from these processes by identifying external lines. For instance, joining lines in pairs as 1-2, 3-4, 5-6 and equivalent combinations in the graph in Fig. 4.3(a) leads to diagram 8a in Fig. 4.2. Similarly, joining 1-2, 3-6, 4-5 in Fig. 4.3(b) produces diagram 8c. This is not a one-to-one correspondence. For instance, joining 1-3 and 2-4 lines in the elastic one-loop diagram in Fig. 4.3(c) yields also diagram 8c. Diagram 8b can also be obtained from a elastic process (Fig.4.3(c) joining 1-2, 3-4) or from an inelastic one (Fig. 4.3(b) joining 1-3, 2-6, 4-5). The crucial point is that the lowest order inelastic diagrams in Fig. 4.3(a,b) do not give rise to any $\mathcal{O}(T^6)$ diagram. This distinctive feature can be interpreted as a way to identify the validity range of our approximation. We should bear in mind that these $\mathcal{O}(T^8)$ corrections are meant to be relevant only very near T_c [Ger89] and therefore in the region where chemical equilibrium is nearly restored and $\mu_\pi \to 0$, not surprisingly due to the presence of the particle-changing processes just discussed [Son97]. Precisely for this reason, the μ_π-dependence of these diagrams is suppressed in powers of μ_π/T and μ_π/M_π. Note that, as we have explained in Section 4.2, taking μ_π/T small justifies in practice to get rid of unnatural terms in the ITF formulation.

With the above considerations in mind, we proceed to evaluate the $\mathcal{O}(T^8)$ diagrams in Figure 4.2. Graph 8h renormalizes $\tilde{z}_0$ and graphs 8(f,g) renormalize the pion mass to $\mathcal{O}(M_0^6)$. Graph 8a, similarly to graph 6a, is proportional to a third power of the propagator at the origin, with the same coefficient as in [Ger89]:

$$\tilde{z}_{8a} = -\frac{25M_0^2}{48F_0^4}\tilde{G}^3(0) \ , \tag{4.75}$$

which contains divergent contributions, according to (D.21).

The graph 8b has been analyzed in Section 4.2. The relevant integral contributing to this graph is (4.60) in the ITF and (4.68) in the RTF with the prescription discussed in that section. The difference between both formulations is of $\mathcal{O}(\mu_\pi/T)$ and therefore

expected to be numerically small, for the reasons just discussed. The rest of the contributions to this graph are proportional to $\tilde{G}^3(0)$ and the proportionality constants are the same as in [Ger89]. Thus, adopting the RTF prescription, we get:

$$\tilde{z}_{8\mathrm{b}} = \frac{M_0^2}{16F_0^4}\tilde{G}^2(0)\left(8 + 3M_0^2\frac{\partial}{\partial M_0^2}\right)\tilde{G}(0)\ , \tag{4.76}$$

whose divergent contribution can be also separated using (D.21). Graphs 8d,e have the same form as graph 6a in (4.71), but due to the form of the $\mathcal{L}_4$ lagrangian and following also our previous RTF prescriptions, we arrive to the same structure as in [Ger89]:

$$\tilde{z}_{8\mathrm{d}+8\mathrm{e}} = -\frac{3}{F_0^4}\left\{(2l_1+4l_2)\left[\tilde{G}_{\mu\nu}\right]^2 + \tilde{G}(0)\left[(3l_1+l_2+l_3)\,M_0^4\tilde{G}(0) - \frac{l_3M_0^6}{2}\frac{\partial}{\partial M_0^2}\right]\tilde{G}(0)\right\}\ , \tag{4.77}$$

where $\tilde{G}_{\mu\nu} \equiv \partial_\mu\partial_\nu\tilde{G}(0)$, which has the same properties as in [Ger89], namely, its divergent contribution is the same (T and μ_π independent) while its finite part can be written in the same way in terms of $\tilde{g}_0$ and $\tilde{g}_1$.

The remaining graph is 8c. Following again the RTF prescription, this contribution is:

$$\tilde{z}_{8\mathrm{c}} = \frac{1}{48F_0^4}\left[3M_0^4\tilde{J}_1 - 72\tilde{J}_2 + 16M_0^2\left(\tilde{G}(0)\right)^3\right]\ , \tag{4.78}$$

where:

$$\begin{aligned}
\tilde{J}_1 &= \mathrm{i}\int \mathrm{d}^4x\left[\tilde{D}_{11}^4(x) - \tilde{D}_{12}^4(x)\right] = \int \mathrm{d}^3\boldsymbol{x}\int_0^\infty \mathrm{d}t\left\{\left[\tilde{G}^>(t,\boldsymbol{x})\right]^4 - \left[\tilde{G}^<(t,\boldsymbol{x})\right]^4\right\}\ ,\\
\tilde{J}_2 &= \mathrm{i}\int \mathrm{d}^4x\left[\left(\partial_\mu\tilde{D}_{11}(x)\partial^\mu\tilde{D}_{11}(x)\right)^2 - \left(\partial_\mu\tilde{D}_{12}(x)\partial^\mu\tilde{D}_{12}(x)\right)^2\right]\ .
\end{aligned} \tag{4.79}$$

Written in the above form, it is not difficult to show that for $\mu = 0$, when the propagators are β-periodic, i.e. $G^<(t+\mathrm{i}\beta) = G^>(t)$, one has for instance $J_1 = \int \mathrm{d}^3\boldsymbol{x}\int_0^\beta \mathrm{d}\tau\ \Delta_T^4(\tau,\boldsymbol{x})$ and similarly for $\tilde{J}_2$, as in [Ger89]. As we have seen, for $\mu \neq 0$ the periodicity condition does not hold. However, for this diagram, instead of working directly with the RTF expression (4.79), we will make use of the fact that $\tilde{G}^<(t+\mathrm{i}\beta) = \tilde{G}^>(t) + \mathcal{O}(\beta\mu)$ and neglect the non-periodic terms, so that we end up with $\tilde{J}_1 \simeq \int \mathrm{d}^3\boldsymbol{x}\int_0^\beta \mathrm{d}\tau\ \tilde{\Delta}_T^4(\tau,\boldsymbol{x})$ and $\tilde{J}_2 \simeq \int \mathrm{d}^3\boldsymbol{x}\int_0^\beta \mathrm{d}\tau\ \left(\partial_\mu\tilde{\Delta}_T(\tau,\boldsymbol{x})\partial^\mu\tilde{\Delta}_T(\tau,\boldsymbol{x})\right)^2$. The reason is that the renormalization of the RTF expression is rather cumbersome, whereas for the previous ITF formulation, we can follow the same steps as in [Ger89]: first we separate $\tilde{\Delta}(\tau,\boldsymbol{x}) = \tilde{G}^>(-\mathrm{i}\tau,\boldsymbol{x}) = \tilde{\Delta}(\tau,\boldsymbol{x})^{T=\mu=0} + \delta\tilde{\Delta}(\tau,\boldsymbol{x})$ using the representation (D.10)-(D.11). The divergent contributions in the integrals (4.79) are then contained in the $(\delta\tilde{\Delta}\tilde{\Delta}^0)^2$, $\delta\tilde{\Delta}(\tilde{\Delta}^0)^3$ and $(\tilde{\Delta}^0)^4$ terms and can be renormalized with the same counter-terms as in [Ger89] replacing the $g_{0,1}$ by $\tilde{g}_{0,1}$. The finite part of the $\tilde{J}_{1,2}$ integrals can be evaluated numerically. A crucial point is that this approximation is consistent, as far as renormalization is concerned, with our previous evaluation of the 8(a,b,d,e) diagrams since the divergent parts of the terms proportional to $\tilde{g}_0^2, \tilde{g}_0\tilde{g}_1$ and $\tilde{g}_1^2$ arising from the $\tilde{J}_{1,2}$ integrals cancel exactly with those

coming from the other four diagrams, while the terms proportional to $\tilde{g}_1$ add together to renormalize the physical pion mass according to the definition

$$M_\pi = -\lim_{T\to 0^+} T \ln \tilde{P}(T, \mu_\pi = 0) \ . \tag{4.80}$$

In addition, as it happens for $\mu_\pi = 0$, this ensures that neither the tree level constants from $\mathcal{L}_6$ nor the T, μ_π independent renormalization constants needed to render $\tilde{J}_{1,2}$ finite appear in the final expression for the free energy once it is expressed in terms of M_π. We remark that with our representation, not only the renormalization procedure is consistent, but the final answer for the full $\mathcal{O}(T^8)$ contribution amounts to replace $n_{\rm B}(E_p) \mapsto n_{\rm B}(E_p - \mu)$ in all the spatial momentum integrals, without dealing with unnatural terms, like those discussed in Section 4.2.

After the previous detailed evaluation, we arrive finally to a finite expression for the free energy, suitable for numerical evaluation, with the approximations discussed above implying that the $\mathcal{O}(T^8)$ corrections are reliable only for small μ_π. From this expression we proceed to present our results for the μ_π dependence of several relevant observables.

4.3.2 Results for thermodynamical observables

From the energy density, we obtain the quark condensate (the order parameter of the chiral transition), the entropy density and the pion number density in the standard way:

$$\langle \bar{q}q \rangle(T, \mu_\pi) = \langle \bar{q}q \rangle(0,0) \left[1 + \frac{c}{F_0^2} \frac{\partial \tilde{P}(T,\mu_\pi)}{\partial M_\pi^2} \right] \ , \quad \tilde{s}(T,\mu_\pi) = \frac{\partial \tilde{P}(T,\mu_\pi)}{\partial T} \ ,$$
$$\tilde{n}(T,\mu_\pi) = \frac{\partial \tilde{P}(T,\mu_\pi)}{\partial \mu_\pi} \ , \tag{4.81}$$

where $c = 1 - M_0^2(4\bar{h}_1 + \bar{l}_3 - 1)/(32\pi^2 F_0^2) + \mathcal{O}(M_0^4)$.

We plot our results in Figure 4.4. The first feature we observe is that the $\mathcal{O}(T^6)$ and the ideal gas curves are very close for all the range of temperatures and chemical potentials shown. Sizable differences due to the interactions only show up numerically when including the $\mathcal{O}(T^8)$. This is a also a feature of the $\mu_\pi = 0$ calculation [Ger89]. For instance, in the chiral limit ($M_\pi = 0$) and for $\mu_\pi = 0$, the $\mathcal{O}(T^6)$ in (4.72) vanishes identically, while the $\mathcal{O}(T^8)$ survives, producing conformally anomalous contributions to the pressure (cf. Section 3.4.4). In Figure 4.4 we also compare our results with the virial gas approach [Dob99] (see also Section 3.4.4 for a short description of the VGA), where the pressure can be written at low pion density in terms of the pion scattering phase shifts. In the curves shown in Figure 4.4, the phase shifts have been calculated perturbatively to $\mathcal{O}(p^4)$ in ChPT and using the same set of low-energy constants that for our perturbative results with the approach of the present chapter. We see that our $\mathcal{O}(T^8)$ results with $\mu_\pi \neq 0$ lie reasonably close to the virial result, at least for not very high μ_π. This is a good consistency check of our present approach.

Another general feature that we observe in the curves is that the effect of the pion chemical potential is always to increase thermal effects. Effectively, it acts as similarly as a reduction of the effective pion mass (this is strictly true for $T \ll M_\pi$ where the typical

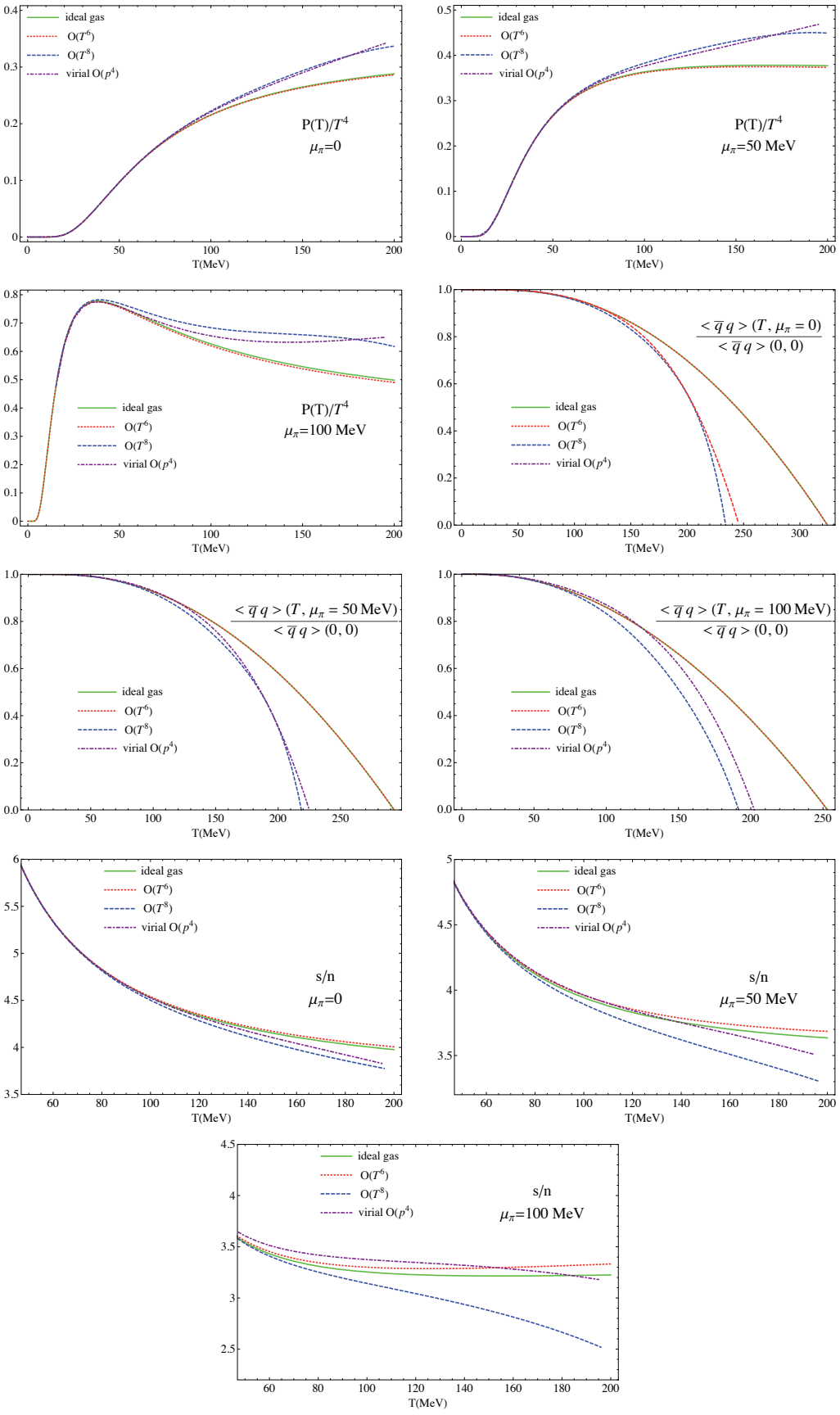

Figure 4.4: Results for thermodynamical observables at different chemical potentials and to different orders in the ChPT interactions.

momenta in the distribution functions are $p = \mathcal{O}(\sqrt{T/M_\pi})$ and therefore for a fixed T, the results for increasing μ_π go qualitatively in the same direction as for increasing T with $\mu_\pi = 0$. For instance, we see that the pressure increases for increasing μ_π and approaches faster the asymptotic limit $P = \pi^2 T^4/30$ [Ger89] expected in the chiral limit ($T \gg M_\pi, \mu_\pi$). The effect of interactions is also to increase the pressure, producing additive contributions in the ChPT expansion.

The curves for the quark condensate show that the chiral restoration temperature goes down for $\mu_\pi \neq 0$. This is also a consequence of the above discussed qualitative behavior, since the system for $\mu_\pi \neq 0$ is closer to chiral restoration, as for $\mu_\pi = 0$ with increasing temperature. With the numerical values we get, we see that if chemical freeze-out takes place for temperatures below the chiral phase transition, then we do not expect to see any change in the value of T_c. On the contrary if $T_{\rm CFO} > T_c$ (which is less likely with the available experimental information) we would expect a reduction in T_c compared with the estimates taking $\mu_\pi = 0$.

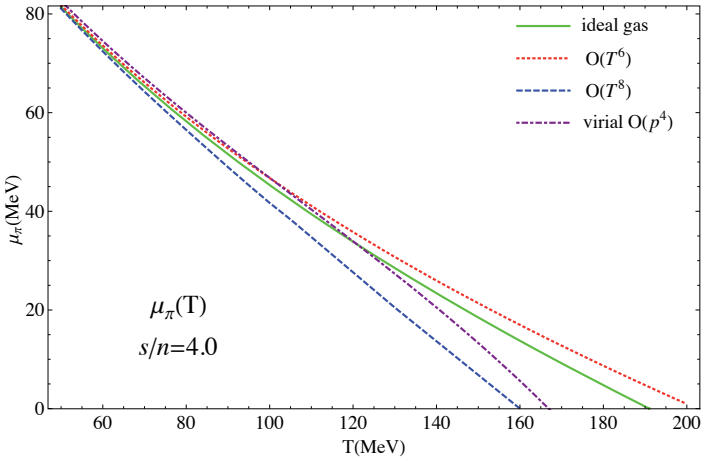

Figure 4.5: Dependence of $\mu_\pi(T)$ in the isentropic approximation, with the fixed value $s/n = 4$.

A very interesting observable in order to describe the evolution of $\mu_\pi(T)$ is the ratio of entropy density to pion density, also plotted in Figure 4.4. As pointed out in [Beb92, Son97] on general grounds one expects this ratio to remain almost constant during the expansion. This is the isentropic expansion approximation, which is exact in the high T limit $T \gg M_\pi, \mu_\pi$ for the ideal gas. We remark that we are restricting here to the gas of pions. If heavier degrees of freedom are included, such as the ρ, one has to account for the total number of pions $\bar{n}_\pi = n_\pi + 2n_\rho + \ldots$ which includes those "stored" in the ρ if the channel $\rho \to \pi\pi$ is considered as the only source of pion number changing, and similarly with other resonances (see details in [Beb92, Son97]). The idea is then that by fixing s/n to a given value at the chemical freeze out temperature $T_{\rm CFO}$ where $\mu_\pi = 0$, going down in the temperature scale one can keep s/n fixed by increasing μ_π, as it can be seen in Figure 4.4. This provides the dependence $\mu_\pi(T)$, which is given in [Beb92, Son97] in the ideal gas approximation. We plot in Figure 4.5 the isentropic curves $\mu_\pi(T)$ with a reference value $s/n = 4$, for which $T_{\rm CFO} \simeq 190$ MeV for the ideal gas. The most significant

effect we observe is the reduction of $T_{\rm CFO}$ when $\mathcal{O}(T^8)$ interactions are included. This is a very natural effect since, as we have discussed in previous sections, that order in the interaction is the one where particle-changing processes begin to be relevant and drive the system back to chemical equilibration. The virial curve lies reasonably close to our perturbative $\mathcal{O}(T^8)$ since the two approaches differ significantly only for rather high values of μ_π and T, which are not reached along the curve $\mu_\pi(T)$. In fact, in the isentropic evolution our $\mathcal{O}(T^8)$ approach is better justified since those corrections are only important for temperatures such that $\mu_\pi(T) \ll T, M_\pi$. We also remark that the same effect of faster equilibration is seen when comparing the curves of the ideal pion gas with that of the ideal pion+resonances gas, as done in [Beb92]. One can check that the curves in that paper for s/n as a function of T for different μ_π are systematically lower when including resonances, as in our case in Figure 4.4 when including the $\mathcal{O}(T^8)$ or in the virial case and therefore the free pion and resonance gas equilibrates faster, which is the feature that we are able to reproduce here including higher order pion interactions.

4.3.3 Self-energy: pion thermal mass and width

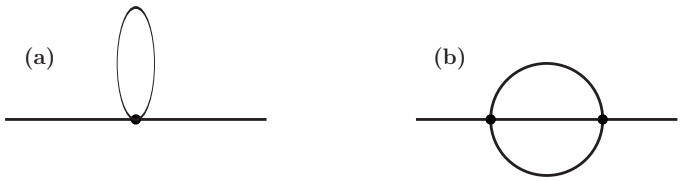

Figure 4.6: Diagrams contributing to leading order to the real (a) and imaginary (b) parts of the self-energy.

Within the real-time formalism developed in Section 4.2.4, we can calculate the pion self-energy, whose leading order corrections to its real and imaginary parts are given by the diagrams in Figure 4.6(a) and 4.6(b), respectively, all vertices coming from the $\mathcal{L}_2$ lagrangian.

Consider first diagram 4.6(a). It includes a contribution with a constant vertex proportional to $M_0^2\tilde{G}(0)\partial\tilde{D}_{11}(p)/\partial M_0^2$ which directly renormalizes the pion mass, following the prescriptions explained in Section 4.2.4, and derivative vertices, which contribute either proportional to $\Box\tilde{G}(0) = -M_0^2\tilde{G}(0)$ (mass renormalization) or as $\tilde{G}(0)p^2\partial\tilde{D}_{11}(p)/\partial M_0^2 = \tilde{G}(0)[\tilde{D}_{11}(p)+M_0^2\partial\tilde{D}_{11}(p)/\partial M_0^2]$ (mass and wave function renormalization). One can then follow similar steps as in the standard derivation of the thermal corrections to the pion self-energy to this order [Sch93, Gas87], the wave function renormalization being directly related to the thermal F_π through the usual definition in terms of the residue of the axial-axial current correlator. The ultraviolet divergences arising in the calculation are absorbed by the renormalization of the low-energy constants l_3 and l_4. We finally obtain:

$$M_\pi^2(T,\mu_\pi) = M_\pi^2 + \frac{M_0^2}{2F_0^2}\tilde{g}_1(M_0,T,\mu_\pi) + \mathcal{O}(M_0^4)\ , \tag{4.82}$$

$$F_\pi^2(T,\mu_\pi) = F_\pi^2 - 2\tilde{g}_1(M_0,T,\mu_\pi) + \mathcal{O}(M_0^4)\ , \tag{4.83}$$

with M_π and F_π the $T=\mu_\pi=0$ physical values given in (4.73) and (4.74) in terms of M_0 and F_0 to this order.

Taking into account now the corrections to the quark condensate to the same chiral order, i.e., $\mathcal{O}(T^6)$, which is given from (4.81) and (4.72) using (D.27):

$$\langle\bar{q}q\rangle(T,\mu_\pi)=\langle\bar{q}q\rangle(0,0)\left[1-\frac{3}{2F_0^2}\tilde{g}_1(M_0,T,\mu_\pi)\right]+\mathcal{O}(T^8)\ , \tag{4.84}$$

we obtain that the Gell-Mann-Oakes-Renner (GOR) relation [GM68] holds also for $\mu_\pi\neq 0$ to this order (one-loop ChPT):

$$\frac{F_\pi^2(T,\mu_\pi)M_\pi^2(T,\mu_\pi)}{\langle\bar{q}q\rangle(T,\mu_\pi)}=\frac{F_\pi^2(0,0)M_\pi^2(0,0)}{\langle\bar{q}q\rangle(0,0)}=-m_{\rm q}\ . \tag{4.85}$$

The GOR relation in terms of thermal quantities at $T\neq 0$, $\mu_\pi=0$ had been verified to one-loop in [Tou97]. To this order, the thermal mass varies little, also at $\mu_\pi\neq 0$ (see below) so that the evolution of F_π follows that of the quark condensate and both behave as order parameters. However, beyond one-loop, the GOR does not hold for thermal quantities [Tou97].

Another important observation is that the shift (4.82) in the mass to this order can be written, as in the $\mu_\pi=0$ case [Sch93] in terms of the pion forward scattering amplitude, from (D.23):

$$M_\pi^2(T,\mu_\pi)-M_\pi^2=-\int\frac{{\rm d}^3\boldsymbol{p}}{(2\pi)^3}\ \frac{1}{2E_p}\frac{1}{{\rm e}^{\beta(E_p-\mu_\pi)}-1}\,{\rm Re}\left[T^{\rm f}_{\pi\pi}(s=(E_p+M_\pi)^2-|\boldsymbol{p}|^2)\right]\ , \tag{4.86}$$

where $E_p^2=M_\pi^2+|\boldsymbol{p}|^2$ and $T^{\rm f}_{\pi\pi}(s)$ is the isospin averaged forward scattering amplitude, which to lowest order $\mathcal{O}(p^2)$ (tree level diagrams with $\mathcal{L}_2$ vertices) is given by:

$$\begin{aligned}T^{\rm f}_{\pi\pi}(s)\equiv T_{\pi\pi}(s,0,u)&=\frac{1}{3}\sum_{I=0}^{2}(2I+1)T_I(s,0,u)=\frac{32\pi}{3}\sum_{I=0}^{2}\sum_{J=0}^{\infty}(2I+1)(2J+1)t_{IJ}(s)\\&\simeq\frac{32\pi}{3}\left[t_{00}(s)+9t_{11}(s)+5t_{20}(s)\right]=-\frac{M_0^2}{F_0^2}+\mathcal{O}(s^2,M_0^4)\ .\end{aligned} \tag{4.87}$$

Here, $T_I(s,t,u)$ are the projections of the scattering amplitude with definite isospin I, s,t,u are the Mandelstam variables satisfying $s+t+u=4M_\pi^2$, and t_{IJ} are the partial waves, defined in the center of mass frame with definite isospin I and angular momentum J. We follow the conventions in [Gas84]. In the previous expression, we have included only the partial waves with lowest angular momentum $J\leq 1$. Those with $J>1$ are negligible below inelastic thresholds such as $\rm K\bar{K}$ and the temperatures involved here [Sch93].

The result in (4.86) is the generalization to $\mu_\pi\neq 0$ of the formula relating the shift in the self-energy with the density of states and the scattering amplitude to lowest order in the density (dilute gas regime) [Sch93]. These type of relations were first derived by Luscher [Lus86] for the finite-volume dependence of the mass. A very interesting point is that it admits a natural extension [Sch93] by considering (in the dilute gas regime) not only the perturbative tree-level $\mathcal{O}(p^2)$ amplitude, but also higher orders, including

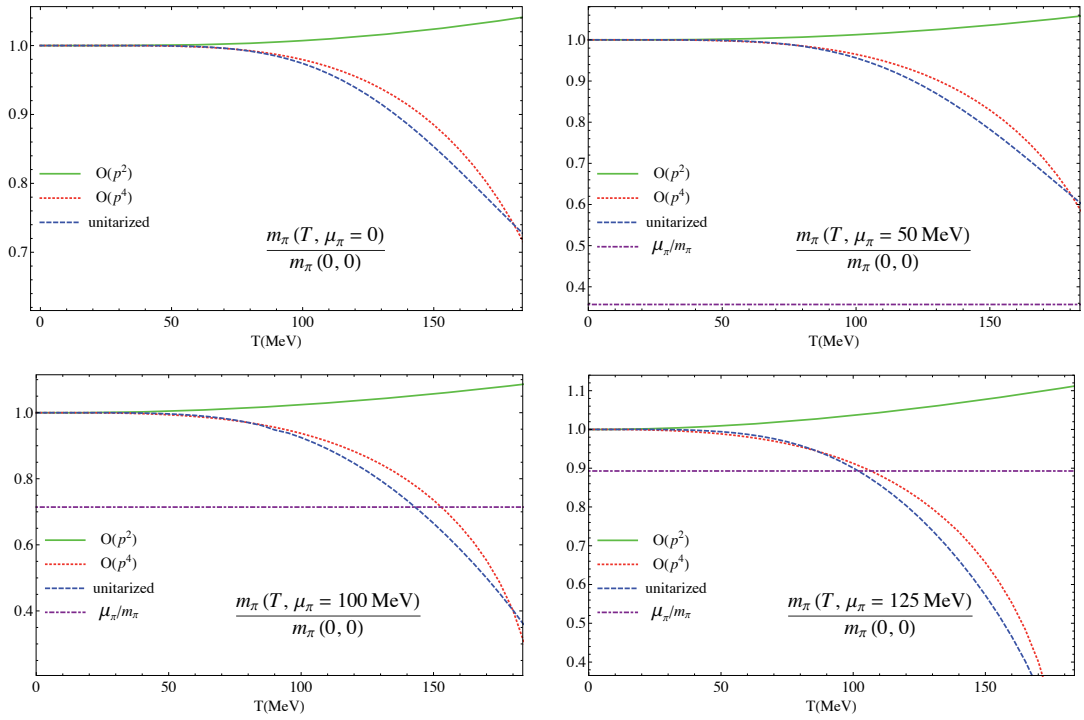

Figure 4.7: Results for the thermal mass dependence on temperature and pion chemical potential, considering different orders in the scattering amplitude in (4.86).

unitarized amplitudes. In the latter case, unitarized partial waves $t^{\rm U}_{IJ}(s)$ for $\pi\pi$ scattering can be constructed to satisfy exactly the unitarity relation (see Chapter 2):

$$\mathrm{Im}\, t^{\rm U}_{IJ}(s) = \sqrt{1-\frac{4M_\pi^2}{s}}|t^{\rm U}_{IJ}|^2 \ , \tag{4.88}$$

matching at the same time the perturbative ChPT expansion and providing expressions that can be analytically continued to the complex s plane. As we saw in detail in Chapter 2, all these features are satisfied by the Inverse Amplitude Method scattering amplitudes [Tru88, Tru91, Dob90, Dob93, Dob97, GN02a], which reproduces scattering data up to $\sqrt{s} \sim 1$ GeV and all the low-lying resonances, which in the pure pion case considered here reduce to the $\rho(770)$ and the $f_0(600)$ or σ. Recall that the ChPT amplitudes satisfy the unitarity relation (4.88) only perturbatively order by order, violating the unitarity bounds for higher energies and thus not being able to reproduce resonances.

In Figure 4.7 we show our results for the thermal mass, considering $\mathcal{O}(p^2)$, $\mathcal{O}(p^4)$ and IAM unitarized amplitudes in (4.86). We have used the same set of low-energy constants as in our previous calculations, i.e, the $\bar{l}_i$ given at the beginning of Section 4.3.1. For the case of the unitarized amplitudes, this set is adequate to compare with the perturbative ChPT expressions, although it does not give the best results for the mass and width of the resonances generated with the IAM. We have checked that our results do not change qualitatively by changing for instance to the set used in Chapters 2 and 3, which gives better physical values for the mass and width of the $\rho(770)$ and the $f_0(600)$.

Our results show that the leading order, the ChPT $\mathcal{O}(p^2)$ given by the tadpole di-

agram in Figure 4.6(a), produces a thermal mass slightly increasing with temperature and chemical potential. However, including the $\mathcal{O}(p^4)$ or unitarized corrections to the amplitude, the mass tends to decrease significantly with T and μ_π. Our results at $\mu_\pi = 0$ agree with [Sch93]. The difference between the $\mathcal{O}(p^4)$ and the unitarized curve is not very relevant here. Our $\mathcal{O}(p^2)$ curve agrees reasonably with a linear-sigma model calculation [Aya02, Aya03] which agrees with ChPT to this order at $\mu_\pi = 0$ and where the chemical potential is introduced by analogy with the charged scalar field case.

These results suggest an interesting scenario: the pion system could undergo Bose-Einstein (BE) condensation driven by the dropping of the thermal mass by interactions. Recall that we are dealing with BE condensation of both neutral and charged pions, since we are considering an electrically neutral system with finite pion density. The physical situation is then different from the charged pion or kaon condensation taking place in nuclear matter [Saw72, Kap86] or isospin chemical potential [Son01, Loe03] scenarios, although the feature of dropping mass is similar to the former. BE condensation for pion number and its possible phenomenological consequences in heavy ion collisions has been extensively studied in the literature [Zim79, Gre93, Led00, Beg07]. Among the possible observable consequences are the anomalous enhancement of the low-$p_{\rm T}$ pion spectrum and of number fluctuations in high multiplicity events.

In our grand-canonical interacting approach we can describe the corrections to BE condensation due to pion interactions. In the standard free case, the BE limit is reached when $\mu_\pi \to M_\pi$ from below (by definition the system is below the condensed phase). Those values for the pion chemical potential seem too high compared with those measured in heavy ion collisions at thermal freeze out $T_{\rm ther} \sim 100$ MeV [Beb92, Hun98, Kol03]. In other words, the required pion densities for BE condensation might not be reached. However, if the effective particle mass $M_\pi(T, \mu_\pi)$ drops by interactions among the medium constituents, the value $\mu_\pi = M_\pi(T, \mu_\pi)$ would be reduced. We show that line in Figure 4.7. In Figure 4.8 (left) the resulting $\mu_\pi^{\rm BE}(T) = M_\pi(T, \mu_\pi^{\rm BE}(T))$ curve is represented and compared with the isentropic curves corresponding to different values of s/n. We see that the BE curve thus defined lies not very far from the isentropic approach and the expected phenomenological values. Those curves correspond to the $\mathcal{O}(p^4)$ amplitudes, both for the thermal mass and for s and n (in the virial approach). In Figure 4.8 (right) we show also the density-temperature curves corresponding to $\mu_\pi \to M_\pi^-$ for different orders in the interaction. The $\mathcal{O}(T^6)$ allows for lower density values, but the virial contribution points in the opposite direction. We also show the curve corresponding to the BE limit by lowering of the mass, as we have just explained, for the same virial approach, which produces a considerable lowering of the required densities. In any case, the corrections due to interactions are small near thermal freeze-out. We also remark that some of our previous results, including those regarding BE condensation by mass reduction, rely on the validity of the dilute gas regime, for instance when using (4.86), but corrections might be important for temperatures close to the chiral transition or chemical potentials close to M_π.

Finally, we turn to the calculation of the leading order imaginary part of the pion self-energy, given in ChPT by diagram (b) in Figure 4.6. This is the leading order contribution to the thermal collisional width Γ_p given by (3.3).

As we have commented in Section 4.2.4, we shall evaluate the retarded correlator in

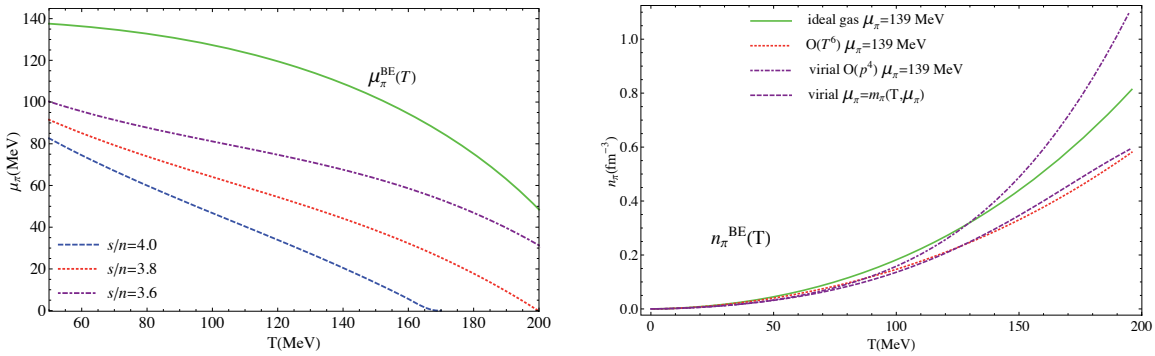

Figure 4.8: Bose-Einstein condensation lines. Left: the curve $\mu_\pi^{\rm BE} = M_\pi(T, \mu_\pi)$ with the thermal mass from the $\mathcal{O}(p^4)$ amplitudes, compared to the isentropic expansion curves for the virial case to the same order and for different s/n values. Right: pion density versus temperature in the BE limit $\mu_\pi \to M_\pi^-$ for different orders in the interaction, compared to the ideal gas and to the virial case with thermal mass.

the real-time formalism, following the circling rules in [Kob90], which also apply to the $\mu_\pi \neq 0$ case. Applying those rules to diagram 4.6(b) we have:

$$\text{Im}\,\Sigma_{\rm R}(p_0, |\boldsymbol{p}|) = -\frac{1}{2}\left[\tilde{H}^{>}(p_0, |\boldsymbol{p}|) - \tilde{H}^{<}(p_0, |\boldsymbol{p}|)\right] \ , \tag{4.89}$$

where $\tilde{H}^{>(<)}$ are obtained by using for the three internal lines in the diagram the $\tilde{G}^{>(<)}$ RTF propagators, which, according to our discussion in Section 4.2.4 and in Appendix D satisfy:

$$\tilde{G}^{>}(k) = 2\pi\delta(p_0^2 - E_p^2)\left[\theta(p_0) + n_{\rm B}(|p_0| - \mu_\pi)\right] = \mathrm{e}^{\tilde{\beta}_k k_0}\tilde{G}^{<}(k) = \mathrm{e}^{\beta[k_0 - \mu_\pi\,\mathrm{sgn}(k_0)k_0]}\tilde{G}^{<}(k) \ , \tag{4.90}$$

so that we get for the thermal width:

$$\begin{aligned}\Gamma_p(T, \mu_\pi) = \frac{1}{4E_p}\int\left(\prod_{i=1}^{3}\frac{\mathrm{d}^4k_i}{(2\pi)^4}\right)\Lambda(k_1, k_2, k_3, p)\tilde{G}^{>}(-k_1)\tilde{G}^{>}(k_2)\tilde{G}^{>}(k_3) \\ \times\left(1 - \mathrm{e}^{-\beta[E_p - \mu_\pi f(k_1,k_2,k_3)]}\right)(2\pi)^4\delta(E_p + k_1^0 - k_2^0 - k_3^0)\delta^{(3)}(\boldsymbol{p} + \boldsymbol{k}_1 - \boldsymbol{k}_2 - \boldsymbol{k}_3) \ ,\end{aligned} \tag{4.91}$$

where $k_{1,2,3}$ label the three internal lines, Λ is the squared vertex function coming from the $\mathcal{L}_2$ lagrangian and:

$$f(k_1, k_2, k_3) = \mathrm{sgn}(k_2^0) + \mathrm{sgn}(k_3^0) - \mathrm{sgn}(k_1^0) \ . \tag{4.92}$$

Recall that in the $\mu_\pi = 0$ case, the f-term is absent so that one ends up with a prefactor $e^{-\beta E_p} - 1 = 1/(1 + n_{\rm B}(E_p))$ in the thermal width. The natural expectation from replacing just the distribution function $n_{\rm B} \mapsto \tilde{n}_{\rm B}$ for $\mu_\pi \neq 0$ would be then $E_p \mapsto E_p - \mu_\pi$ in that factor, as well as the modifications of the internal distribution functions $n_{\rm B}(E_i) \mapsto n_{\rm B}(E_i - \mu_\pi)$ where E_i is short for E_{k_i}. This is indeed the result found in [Goi89] derived

from kinetic theory. In our case, it is not obvious that the answer is the same, since the function f above is not equal to one for the eight possible combinations of signs of the three internal k_i^0. We denote them by $s_1 s_2 s_3$, with $s_i = \mathrm{sgn}(k_i^0)$. Now, we take into account that the δ functions in each of the internal lines put them on-shell, i.e., $k_i^0 = \pm E_i$ and global energy-momentum conservation in the diagram imposed by the δ-functions in (4.91). Thus, the combination $+--$ giving $f = -3$ is excluded by energy conservation $E_p + E_1 > 0 > -E_2 - E_3$. On the other hand, from three-momentum conservation and the on-shell conditions we have that for any combination it should hold $A = B$ where we denote $A \equiv E_p^2 + E_1^2 - E_2^2 - E_3^2$ and $B \equiv 2(\boldsymbol{k}_2 \cdot \boldsymbol{k}_3 - \boldsymbol{p} \cdot \boldsymbol{k}_1)$ and, in addition $-C \leq B \leq C$ with $C = 2(pk_1 + k_2 k_3)$ and where k_i, p are short for $|\boldsymbol{k}_i|$ and $|\boldsymbol{p}|$ respectively. Therefore, the case $++-$ ($f = -1$) is also excluded, since for that combination $E_p + E_1 = E_2 - E_3$ so that $A = -2(E_p E_1 + E_2 E_3) < -C$. The same reason excludes $+-+$ ($f = -1$). Combinations $-++$ ($f = 3$) and $---$ ($f = -1$) give $A = 2(E_p E_1 + E_2 E_3) > C$ and are thus excluded as well. Therefore, the only combinations remaining are $+++$, $-+-$ and $--+$, the three of them giving $f = 1$ and the same contribution from the vertices as for $\mu_\pi = 0$, given in [Sch93]. In conclusion, we find with our diagrammatic method the same result as in kinetic theory [Goi89], which, after relabeling $k_1 \leftrightarrow -k_3$ in $-+-$ and $k_1 \leftrightarrow -k_2$ in $--+$ and performing the three integrals in k_i^0 in (4.91) using the on-shell δ-functions, can be written as:

$$\begin{aligned} \Gamma_p(T, \mu_\pi) = \frac{1}{8E_p} \frac{1}{1 + n_{\mathrm{B}}(E_p - \mu_\pi)} \int \left(\prod_{i=1}^{3} \frac{\mathrm{d}^3 \boldsymbol{k}_i}{(2\pi)^3 2E_i} \right) n_{\mathrm{B}}(E_1 - \mu_\pi) \left[1 + n_{\mathrm{B}}(E_2 - \mu_\pi) \right] \\ \times \left[1 + n_{\mathrm{B}}(E_3 - \mu_\pi) \right] |T_{\pi\pi}(s,t)|^2 (2\pi)^4 \delta^{(4)}(p + k_1 - k_2 - k_3) \ , \end{aligned} \tag{4.93}$$

where $T_{\pi\pi}$ is the isospin averaged elastic pion scattering amplitude with $s = (E_p + E_1)^2 - |\boldsymbol{p} + \boldsymbol{k}_1|^2$, $t = (E_p - E_2)^2 - |\boldsymbol{p} - \boldsymbol{k}_2|^2$.

Taking now the dilute gas regime in the previous expression, which amounts to neglect all the Bose-Einstein functions $n_{\mathrm{B}} \ll 1$ except $n_{\mathrm{B}}(E_1 - \mu_\pi)$, gives rise to the extension of Luscher's formula in terms of the forward scattering amplitude, as in (4.86) but now for the imaginary part of the self-energy through the pion thermal width (which vanishes at $T = 0$):

$$\begin{aligned} \Gamma_p^{\mathrm{DG}}(T, \mu_\pi) &= \frac{1}{2E_p} \int \frac{\mathrm{d}^3 \boldsymbol{k}}{(2\pi)^3} \, n_{\mathrm{B}}(E_k - \mu_\pi) \frac{\sqrt{s(s - 4M_\pi^2)}}{2E_k} \, \sigma_{\pi\pi}(s) \\ &= \frac{1}{2E_p} \int \frac{\mathrm{d}^3 \boldsymbol{k}}{(2\pi)^3 2E_k} \, n_{\mathrm{B}}(E_k - \mu_\pi) \, \mathrm{Im}\, T_{\pi\pi}^{\mathrm{f}}(s) \ , \end{aligned} \tag{4.94}$$

where we have relabeled $k_1 \mapsto k$ and $\sigma_{\pi\pi}$ is the total $\pi\pi$ cross section

$$\sigma_{\pi\pi}(s) = \frac{32\pi}{3s} \sum_{IJ} (2I+1)(2J+1) |t_{IJ}(s)|^2 = \frac{1}{\sqrt{s(s - 4M_\pi^2)}} \, \mathrm{Im}\, T_{\pi\pi}^{\mathrm{f}}(s) \ , \tag{4.95}$$

where the last equality is the optical theorem, following from exact unitarity (4.88).

We remark that our final results both for the real and imaginary parts of the self-energy to this order correspond to the replacement $n \to \tilde{n}$ evaluated at positive energies. This is not only natural from the kinetic theory viewpoint but it is also formally obtained by performing such replacement in the analytically continued $\mu_\pi = 0$ ITF self-energies.

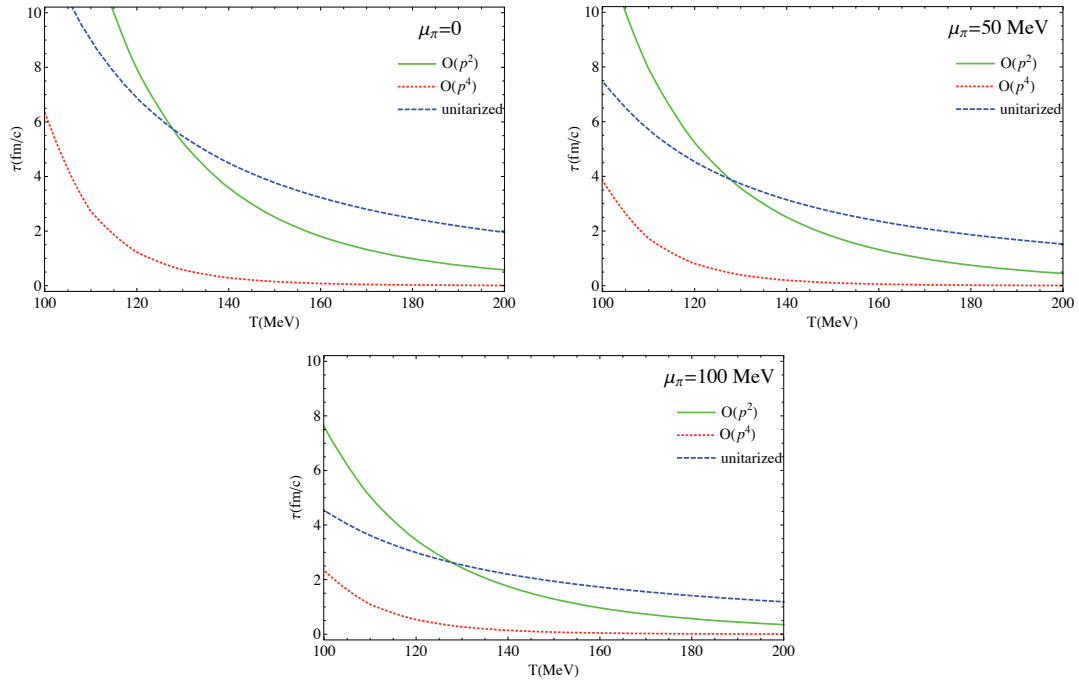

Figure 4.9: Mean collision time in the elastic and dilute limit, considering different orders for the pion scattering amplitude and different values for the pion chemical potential.

The thermal width is of phenomenological relevance, since it enters directly in the calculation of transport coefficients in the meson gas (see Chapter 3). It is then important to estimate pion chemical potential effects in the width during the phase of chemical non-equilibrium where particle number is approximately conserved and transport phenomena can be described relying on the dominance of elastic collisions, which is also consistent with the dilute gas regime. On the other hand, in this regime the mean collision time defined for ultra-relativistic particles as $\tau = 2/\bar{\Gamma}$ [Goi89, Son97, Hun98] with the averaged width:

$$\bar{\Gamma}(T,\mu_\pi) = \frac{\displaystyle\int \mathrm{d}^3\boldsymbol{p}\; \Gamma_p(T,\mu_\pi) n_{\mathrm{B}}(E_p-\mu_\pi)}{\displaystyle\int \mathrm{d}^3\boldsymbol{p}\; n_{\mathrm{B}}(E_p-\mu_\pi)}\,, \tag{4.96}$$

provides direct information about thermal relaxation. We represent τ in the dilute approach in Figure 4.9, using the scattering amplitude in (4.94) to different orders, including the unitarized case. We use the same set of $\bar{l}_i$ constants than in the rest of the chapter.

We see in the figure that the effects of reproducing correctly the energy behavior of the scattering amplitude is important for evaluating the collision time. In particular, the unitarized curve shows important differences with the perturbative ones in the temperature range shown. This was also noticed in [Sch93] at $\mu_\pi = 0$ and the importance of including unitarized corrections to the width for transport coefficients in the meson gas has already been highlighted in Chapter 3 and in [Dob09], for instance regarding violations of AdS/CFT bounds for the shear viscosity over entropy ratio or correlations between the bulk viscosity and the conformal anomaly.

Another clear effect that we observe is the reduction of the mean time with the pion chemical potential, also observed in [Goi89] with $\mathcal{O}(p^2)$ amplitudes. Physically, in the temperature regime where τ is much smaller than the typical plasma lifetime (~ 10 fm/c) which at the same time is small compared to the inelastic collision time driving the system to chemical equilibrium, the system remains in thermal but not chemical equilibrium. From the estimates of the inelastic collision rates given for instance in [Son97] and the results in Figure 4.9, this would happen at $\mu_\pi = 0$ typically between $120 - 180$ MeV. However, precisely in that regime, and as we have explained in this chapter, $\mu_\pi \neq 0$, its typical values being given by the isentropic curve in Figure 4.5, which means that the range of thermal equilibrium enlarges from below, from the commented reduction of τ with μ_π. In fact, estimating the thermal freeze out temperature $T_{\rm TFO}$ as that where this approximation ceases to be valid, i.e., where $\tau \sim 10$ fm/c would give about $T_{\rm TFO} \simeq 130$ MeV without taking into account μ_π effects ($\mu_\pi = 0$) but reduces to about $T_{\rm TFO} \simeq 100$ MeV, closer to experimental values, for $\mu_\pi \neq 0$ following approximately the isentropic values in Figure 4.5.

4.4 Conclusions

In this chapter we have developed a path-integral diagrammatic formalism in order to deal with chemical non-equilibrium effects in interacting scalar field theories, in the regime where particle number is approximately conserved. Within the theoretical framework of holomorphic path integrals and thermal field theory, we have derived the relevant Feynman rules for non-zero particle number chemical potential μ, whose validity is restricted to the temperature regimes where one can neglect particle-changing processes.

We have addressed some subtleties related to the choice of contour in complex times, leading to the extension of real and imaginary time formalisms at $\mu \neq 0$. We have shown that the consistent formulation is the real-time one, in agreement with other non-equilibrium formulations. The imaginary-time formalism can lead to spurious contributions related to the loss of periodicity or global KMS conditions. These problems are not present in the real-time formalism, once a proper energy representation for the propagators is chosen, in accordance with the standard $\mu \equiv 0$ choice. In addition, following previous studies in the literature at $\mu \equiv 0$, we have been able to construct the combinations of real-time diagrams leading to retarded correlators and to closed diagrams contributing to the free energy.

We have applied this formalism to the case of a pion gas, relevant for Relativistic Heavy Ion Collisions between thermal and chemical freeze-out with non-zero pion number chemical potential μ_π. The relevant diagrammatic scheme for temperatures below chiral restoration is Chiral Perturbation Theory. Within our scheme, we have calculated the leading corrections in chiral interactions to the ideal gas. To leading order $\mathcal{O}(T^6)$ the corrections to the pressure can be expressed in terms of tadpole diagrams and are numerically rather small up to $T_{\rm c}$. To next-to-leading order $\mathcal{O}(T^8)$, closed diagrams contributing to the free energy can be obtained from particle-changing processes, which signals the onset of the number conservation approximation break-up. Nevertheless, since μ_π is small for temperatures where those ChPT corrections become important, they can be reliably calculated. In fact, the results to that order agree reasonably well with a virial expansion

analysis. Our results for thermodynamical observables show that both, chiral interactions and μ_π, tend to increase the pressure. The chiral restoration critical temperature decreases with increasing μ_π, which would only be of relevance if chiral restoration takes place for lower temperatures than chemical freeze-out. We have also calculated the isentropic $\mu_\pi(T)$ curve for different orders in the interactions. The corrections to the ideal gas show a significant reduction of the chemical freeze-out temperature.

Our approach also allows to derive the thermal corrections to the pion self-energy at $\mu_\pi \neq 0$ from the leading-order ChPT diagrams, both for the real and imaginary parts of the retarded correlator. The imaginary part comes from a two-loop diagram, and in this case the use of the RTF rules for the construction of the retarded function is crucial. After a detailed evaluation, our diagrammatic result is shown to coincide with the expected expressions from kinetic theory arguments. The real part gives the thermal mass which, together with the condensate and the pion decay constant to the same order, satisfy the $\mu_\pi \neq 0$ extension of the Gell-Mann-Oakes-Renner relation. In addition, both the real and imaginary parts satisfy a Luscher-like relation in terms of the forward pion scattering amplitude. This relation allows to calculate in the dilute regime the self-energy corrections for higher orders in the ChPT amplitudes, including unitarized amplitudes which have the physically expected energy behavior and reproduce the lightest resonance states. The results for the thermal mass show a clear decreasing both with T and μ_π for $\mathcal{O}(p^4)$ and unitarized amplitudes. This suggests the interesting possibility of achieving Bose-Einstein condensation when the effective thermal mass approaches the chemical potential. We have discussed this possibility, which is a purely interacting effect, within the isentropic values and comparing the pion densities with those in the standard approach of considering the ideal gas BE limit $\mu \to M_\pi^-$ with M_π the vacuum mass. Our mass-dropping BE curve is not far, but still above the isentropic ones for reasonable values of chemical freeze-out. Finally, using also the scattering amplitudes, we have evaluated the corrections to the mean collision time at $\mu_\pi \neq 0$. The mean time decreases with T and μ_π for all orders in the interaction, which implies a sizable reduction of the thermal freeze-out temperature estimated as that where τ equals the typical plasma lifetime, within the isentropic approximation.

Conclusions of the thesis

In this thesis we have studied, in the context of unitarized Chiral Perturbation Theory, spectral properties of in-medium resonances, transport coefficients, and effects of conservation of the number of particles for a gas of light mesons. Most of calculations have been particularized for a gas of pions and its corresponding resonances, $\rho(770)$ and $f_0(600)/\sigma$, although the extension to the more general three-flavor case is direct.

In first place, we have presented an analysis of the behavior of $\pi\pi$ scattering amplitudes in Unitarized Chiral Perturbation Theory with medium effects incorporated in several ways. In particular, we have been focused on the behavior with finite temperature and nuclear density of the $\rho(770)$ and $f_0(600)$ resonances, which are generated dynamically with the Inverse Amplitude Method. In the channel of the σ, we have also studied nuclear-density effects using a many-body approach and unitarizing by means of the Bethe-Salpeter equation.

By considering only thermal effects on the IAM $\pi\pi$ amplitudes, the ρ exhibits a considerable broadening with a small mass decrease as temperature increases, whereas the σ mainly decreases its mass, effectively signaling chiral symmetry restoration, although it still remains as a broad resonance even at the transition temperature. The broadening obtained in our approach for the ρ meson at finite temperature is compatible with the spectral function analysis from dilepton spectra in the recent experiment by the NA60 Collaboration. The evolution of the ρ mass with temperature does not scale as the condensate, which renders our results in quantitative disagreement with the Brown-Rho scaling scenario. The fact that the σ pole remains far from the real axis even at the two-pion threshold when only temperature effects are considered implies no significant threshold enhancement for the scattering amplitude, which has been advocated as a precursor of chiral symmetry restoration. We neither observe a scaling of the σ mass with the quark condensate, which indicates that the $f_0(600)/\sigma$ resonance dynamically generated in our unitarized chiral approach has a non-$\bar{q}q$ component which is relevant near the phase transition.

By introducing finite nuclear density the picture changes dramatically. In a first approximation, we have incorporated the effect of a nuclear medium by decreasing F_π according to the GOR relation to linear order in the density. At sufficiently low (high) values of F_π (density), the ρ and σ poles collapse onto the real energy axis at the threshold energy, which is preceded by a significant threshold enhancement in the scattering amplitudes. We have discussed these effects in the context of recent results from resonance production in finite nuclei and our results are in line with the experimental observations. A detailed analysis reveals that when the resonance pole is close to the real axis it splits

into two states in separated Riemann sheets. The properties of these double poles allow us to classify the σ resonance according to its internal structure: it exhibits a "molecular" behavior (one of the poles stays close to threshold, well separated from the other one which evolves to lower energies to become degenerated with the pion). On the order hand, according to these arguments the ρ would correspond to a $\bar{q}q$, non-molecular, scenario. However, this criterium of classification is in principle only applicable to scalar resonances. Nevertheless, the $\bar{q}q$ nature of the ρ has been supported by other analyses based on different methods, such as large-N_c scaling [Pel04, Pel06]. The mass scaling from the σ and ρ pole with $F_\pi(\rho)$ follows the quark condensate evolution and therefore is compatible with a Brown-Rho scaling scenario, although one should keep in mind that relevant finite density mechanisms are neglected in this approximation.

We have also improved our implementation of finite nuclear density (and temperature) effects by considering a microscopic calculation of many-body pion dynamics in $\pi\pi$ scattering. We have chosen a different unitarization scheme for the $\pi\pi$ scattering amplitude, namely to solve the Bethe-Salpeter equation for the lowest order ChPT interaction. Despite differences in the amplitudes at $\mathcal{O}(p^4)$, this scheme essentially provides the same results as the IAM and allows a systematic analysis and resummation of a relevant class of pion interaction mechanisms with the nuclear medium. The pion interactions with the medium are encoded in the single-particle pion self-energy, which accounts for the excitation of p-wave particle-hole and Delta-hole components as well as short distance correlation effects from nucleon-nucleon and Delta-nucleon interactions. The opening of baryon-related channels on top of $\sigma \to \pi\pi$ at finite density extends the available phase space to lower energies and therefore the $\pi\pi$ scattering amplitude exhibits an increased strength at and below the two-pion threshold, which is magnified at finite temperature as a consequence of Bose enhancement on the low energy modes of the $\pi\pi$ intermediate states. Such an effect has been found to provide a satisfactory description of the data from the two-pion photo-production reaction in nuclei when comparing the mass spectrum in the neutral- vs charged-pion channels for different nuclei [Roc02, Mes02], where nuclear densities of the order of ρ_0 and below are explored. In our analysis we have considered both finite temperature and nuclear density, thus extending the applicability of the present approach to other experimental scenarios such as the forthcoming Heavy-Ion physics program at FAIR. As compared to the purely thermal calculation, the attractive interaction mechanisms of the pion at finite density accelerate the migration of the σ pole towards the two-pion threshold. The threshold enhancement observed in the $\pi\pi$ amplitude is correlated to the evolution of the σ pole towards (and below) $2M_\pi$. However, differently from the reduced-F_π result, the σ pole stays far from the real axis indicating a sizable decay width of the resonance at densities as high as $2\rho_0$ and temperatures close to the transition one.

In second place, we have presented a method for calculating different transport coefficients (DC electrical conductivity, thermal conductivity, and shear and bulk viscosities) in a meson gas at low temperatures within the framework of Chiral Perturbation Theory and Linear Response Theory. The analysis has been particularized for the case of a pion gas, including also the resonances $f_0(600)$ and $\rho(770)$ dynamically generated through unitarization with the IAM. The non-perturbative nature of transport coefficients is re-

flected in the need of including the thermal pion width in the calculations, in order to avoid "pinching poles" singularities. Physically, this allows to account for the relevant in-medium pion collisions and gives rise to the leading order contribution in the inverse width consistently with kinetic theory. We have shown that, after a suitable modification of the standard ChPT power counting and including unitarity corrections in the scattering amplitudes in order to improve their high energy behavior, one ends up with a reasonable description of transport coefficients for temperatures below the transition. At very low temperatures, our approach meets the predictions of non-relativistic kinetic theory, while at higher T we get an adequate behavior of transport coefficients when compared with existing studies based on the kinetic approach. To obtain these results, we have just considered the dominant diagram, with unitarized scattering in the thermal width for the internal pion lines.

A very important part of our analysis has been the role of higher order diagrams which, although naively suppressed, are enhanced by powers of the inverse width. As it happens in other theories, the dominant diagrams are uncrossed ladder ones, which in our case can be interpreted in terms of pion scattering of the internal lines. A careful evaluation of the ladder diagrams shows that they can still be considered perturbative in ChPT at low temperatures. This is particularly important at very low temperatures, $T \ll M_\pi$, where the non-perturbative contributions are larger. In that regime, we have been able to show exactly that ladder diagrams are perturbative, so that they merely renormalize the numerical coefficient of the leading order contribution by subleading corrections in ChPT. Although collinearly enhanced, our numerical analysis shows that the next-to-leading order correction typically amounts to a 5% approximately. As temperature increases, ladder diagrams become more important, the most relevant contributions coming from ladders with derivative vertices. At temperatures near the chiral phase transition it is not clear that ladder diagrams can be neglected (furthermore, strictly, ChPT is not applicable in that regime). In fact, at those high temperatures we expect other effects to become important, like the presence of kaon states.

As mentioned above, another important point concerns unitarity. We have shown that the behavior with temperature of the different transport coefficients changes qualitatively with temperature as a consequence of implementing unitarity for the partial waves in the thermal width. This provides a more physical picture as far as the behavior of partial waves with energy and the presence of resonances in the thermal bath are concerned (the $f_0(600)/\sigma$ and $\rho(770)$). The unitarized conductivity increases slowly for increasing T, which seems to be consistent with lattice and analytical analyses far beyond the transition point. Thermal conductivity and shear viscosity also experiment an increasing behavior with temperature due to unitarity. And the maximum in bulk viscosity near the critical temperature is enhanced by the same effect. In addition, we have discussed phenomenological predictions for the zero-energy photon spectrum and the shear viscosity to entropy ratio, which are in fair agreement with data. On one hand, our analysis implies that there should be sizable effects for very low energy hadronic photon production and this result is consistent with recent theoretical low-energy analysis and compatible with naive extrapolations of experimental data. On the other hand, we have seen that the quotient η/s for the pion gas respects the universal lower bound conjectured from a

AdS/CFT calculation by Kovtun et al. We have also seen that it is very likely that this quotient presents a minimum at the phase transition. Moreover, our estimation of η/s, which enters directly into the sound attenuation length, is in good agreement with a previous analysis of elliptic flow. However, the lack of precise experimental and lattice knowledge about the zero frequency limit, together with the own limitations of our approach do not allow to draw very quantitative conclusions.

Regarding the bulk viscosity, we have shown that the massive pion gas develops a strong correlation between bulk viscosity and the conformal anomaly, as suggested by previous works. Both quantities show a low-temperature peak coming from mass conformal breaking and another one at the critical temperature remaining in the chiral limit and mainly dominated by gluon condensate contributions not related to chiral restoration. In perturbation theory, it is necessary to calculate the partition function to order $\mathcal{O}(T^8)$ in order to obtain an anomalous peak in the interaction measure. We have seen that this peak can also be obtained in the VGA using scattering amplitudes calculated in ChPT at order $\mathcal{O}(p^4)$. The dynamically generated light resonances (σ and ρ) are essential to obtain sizable effects at the transition. In the calculation of the trace anomaly, we have also compared with the results from the HRG approximation, where many more resonances are introduced as free states obtaining a good agreement with lattice calculations. Since resonances do not interact in the HRG approach, there is no maximum in the interaction measure, unlike in the ChPT calculation. Different estimates indicate that heavier states could yield a larger bulk viscosity near the transition, leading to observable effects in heavy ion collisions.

We have also studied the large-N_c limit of the transport coefficients obtained in our approach. The parametric scaling with N_c is consistent with our previous analysis and provides a qualitative description for the behavior of shear and bulk viscosities when approaching the critical region.

And finally, we have developed a path-integral diagrammatic formalism in order to deal with chemical non-equilibrium effects in interacting scalar field theories, in the regime where particle number is approximately conserved. Within the theoretical framework of holomorphic path integrals and thermal field theory, we have derived the relevant Feynman rules for non-zero particle number chemical potential μ, whose validity is restricted to the temperature regimes where one can neglect particle-changing processes.

We have addressed some subtleties related to the choice of contour in complex times, leading to the extension of real and imaginary time formalisms at $\mu \neq 0$. We have shown that the consistent formulation is the real-time one, in agreement with other non-equilibrium formulations. The imaginary-time formalism can lead to spurious contributions related to the loss of periodicity or global KMS conditions. These problems are not present in the real-time formalism, once a proper energy representation for the propagators is chosen, in accordance with the standard $\mu \equiv 0$ choice. In addition, following previous studies in the literature at $\mu \equiv 0$, we have been able to construct the combinations of real-time diagrams leading to retarded correlators and to closed diagrams contributing to the free energy.

We have applied this formalism to the case of a pion gas, relevant for Relativistic

Heavy Ion Collisions between thermal and chemical freeze-out with non-zero pion number chemical potential μ_π. The relevant diagrammatic scheme for temperatures below chiral restoration is Chiral Perturbation Theory. Within our scheme, we have calculated the leading corrections in chiral interactions to the ideal gas. To leading order $\mathcal{O}(T^6)$ the corrections to the pressure can be expressed in terms of tadpole diagrams and are numerically rather small up to T_c. To next-to-leading order $\mathcal{O}(T^8)$, closed diagrams contributing to the free energy can be obtained from particle-changing processes, which signals the onset of the number conservation approximation break-up. Nevertheless, since μ_π is small for temperatures where those ChPT corrections become important, they can be reliably calculated. In fact, the results to that order agree reasonably well with a virial expansion analysis. Our results for thermodynamical observables show that both, chiral interactions and μ_π, tend to increase the pressure. The chiral restoration critical temperature decreases with increasing μ_π, which would only be of relevance if chiral restoration takes place for lower temperatures than chemical freeze-out. We have also calculated the isentropic $\mu_\pi(T)$ curve for different orders in the interactions. The corrections to the ideal gas show a significant reduction of the chemical freeze-out temperature.

Our approach also allows to derive the thermal corrections to the pion self-energy at $\mu_\pi \neq 0$ from the leading-order ChPT diagrams, both for the real and imaginary parts of the retarded correlator. The imaginary part comes from a two-loop diagram, and in this case the use of the RTF rules for the construction of the retarded function is crucial. After a detailed evaluation, our diagrammatic result is shown to coincide with the expected expressions from kinetic theory arguments. The real part gives the thermal mass which, together with the condensate and the pion decay constant to the same order, satisfy the $\mu_\pi \neq 0$ extension of the Gell-Mann-Oakes-Renner relation. In addition, both the real and imaginary parts satisfy a Luscher-like relation in terms of the forward pion scattering amplitude. This relation allows to calculate in the dilute regime the self-energy corrections for higher orders in the ChPT amplitudes, including unitarized amplitudes which have the physically expected energy behavior and reproduce the lightest resonance states. The results for the thermal mass show a clear decreasing both with T and μ_π for $\mathcal{O}(p^4)$ and unitarized amplitudes. This suggests the interesting possibility of achieving Bose-Einstein condensation when the effective thermal mass approaches the chemical potential. We have discussed this possibility, which is a purely interacting effect, within the isentropic values and comparing the pion densities with those in the standard approach of considering the ideal gas BE limit $\mu \to M_\pi^-$ with M_π the vacuum mass. Our mass-dropping BE curve is not far, but still above the isentropic ones for reasonable values of chemical freeze-out. Finally, using also the scattering amplitudes, we have evaluated the corrections to the mean collision time at $\mu_\pi \neq 0$. The mean time decreases with T and μ_π for all orders in the interaction, which implies a sizable reduction of the thermal freeze-out temperature estimated as that where τ equals the typical plasma lifetime, within the isentropic approximation.

Concerning to possible future lines of research, we would like to extend our study of mesonic resonances in the medium to the three-flavor case, and to analyze the relation between the resonances that a appear in this case with chiral symmetry restoration, at finite temperatures and densities using both approaches, the IAM and the Bethe-

Salpeter equation. A more detailed investigation of possible pole-doubling effects in the Bethe-Salpeter approach is also planned. Another possible continuation would consist in extending also the analysis of transport coefficients to the strangeness sector (which includes kaons, etas, and their corresponding resonances), along with the introduction of the corresponding additional effects of an approximately conserved number of kaons and etas. This would be especially relevant for temperatures close to the phase transition, where the new degrees of freedom are not Boltzmann-suppressed in densities anymore, and it is expected that they play an important role in that regime. The analysis of the resummation of ladder diagrams and the possible cancellations that may occur is interesting as well, specially in the case of the bulk viscosity which, once calculated in full chemical equilibrium, involves more complicated rungs corresponding to inelastic processes.

Appendix A

Notation

- We consider units such that $c = 1$ (speed of light), $\hbar = 1$, and $k_{\mathrm{B}} = 1$ (Boltzmann constant).
- Metric in Minkowski space: $\eta_{\mu\nu} = \mathrm{diag}(1, -1, -1, -1)$.
- In general, vacuum propagators in RT are denoted with the letter D, propagators at finite temperature in the RTF are denoted with the letter G, and propagators at finite temperature in the ITF are denoted with the symbol Δ. However, when there is a change in this convention, as it happens in Chapter 4, it is clearly indicated.
- Fluid quantities evaluated in the LRF are denoted with a tilde, e.g. $\tilde{T}^{ij}$. However, in Chapter 4 a tilde denotes quantities that depend on a chemical potential. And in Section 1.1.2 a tilde denotes quantities rescaled in N_{c}.
- Operators are usually indicated by a hat, e.g. $\hat{O}$, but the hat is sometimes omitted when other indices or symbols have to be placed over the letter.
- Fourier transform (it will be recognized by an argument k, p, or q for momenta, and ω or ν for frequencies):

$$f(k) = \int_{-\infty}^{\infty} \mathrm{d}t \; \mathrm{e}^{\mathrm{i}kt} f(t) \;, \quad f(t) = \int_{-\infty}^{\infty} \frac{\mathrm{d}k}{2\pi} \; \mathrm{e}^{-\mathrm{i}kt} f(k) \;.$$

- The Kronecker delta is also denoted by $\delta_{\mathrm{K}}(\cdot)$.

Appendix B

The SU(2) and SU(3) groups

SU(2)

- Algebra: $[I_a, I_b] = \mathrm{i}\epsilon_{abc} I_c$, with the generators $I_a \equiv \dfrac{\sigma_a}{2}$.

- Pauli matrices:

$$\sigma_1 = \begin{pmatrix} 0 & 1 \\ 1 & 0 \end{pmatrix} , \quad \sigma_2 = \begin{pmatrix} 0 & -\mathrm{i} \\ \mathrm{i} & 0 \end{pmatrix} , \quad \sigma_3 = \begin{pmatrix} 1 & 0 \\ 0 & -1 \end{pmatrix} ,$$

$$\sigma_a^\dagger = \sigma_a , \quad \mathrm{Tr}\{\sigma_a\} = 0 , \quad \mathrm{Tr}\{\sigma_a \sigma_b\} = 2\delta_{ab} , \quad \mathrm{Tr}\{\sigma_a \sigma_b \sigma_c\} = 2\mathrm{i}\epsilon_{abc} ,$$
$$\mathrm{Tr}\{\sigma_a \sigma_b \sigma_c \sigma_d\} = 2(\delta_{ab}\delta_{cd} - \delta_{ac}\delta_{bd} + \delta_{ad}\delta_{bc}) .$$

SU(3)

- Algebra: $[J_a, J_b] = \mathrm{i} f_{abc} J_c$, with the generators $J_a \equiv \dfrac{\lambda_a}{2}$.

- The structure constants f_{abc} are fully antisymmetric, and the non-vanishing values are permutations of:

$$f_{123} = 1 , \quad f_{458} = f_{678} = \frac{\sqrt{3}}{2} , \quad f_{147} = f_{165} = f_{246} = f_{257} = f_{345} = f_{376} = \frac{1}{2} .$$

- Gell-Mann matrices:

$$\lambda_1 = \begin{pmatrix} 0 & 1 & 0 \\ 1 & 0 & 0 \\ 0 & 0 & 0 \end{pmatrix} , \quad \lambda_2 = \begin{pmatrix} 0 & -\mathrm{i} & 0 \\ \mathrm{i} & 0 & 0 \\ 0 & 0 & 0 \end{pmatrix} , \quad \lambda_3 = \begin{pmatrix} 1 & 0 & 0 \\ 0 & -1 & 0 \\ 0 & 0 & 0 \end{pmatrix} ,$$

$$\lambda_4 = \begin{pmatrix} 0 & 0 & 1 \\ 0 & 0 & 0 \\ 1 & 0 & 0 \end{pmatrix} , \quad \lambda_5 = \begin{pmatrix} 0 & 0 & -\mathrm{i} \\ 0 & 0 & 0 \\ \mathrm{i} & 0 & 0 \end{pmatrix} , \quad \lambda_6 = \begin{pmatrix} 0 & 0 & 0 \\ 0 & 0 & 1 \\ 0 & 1 & 0 \end{pmatrix} ,$$

$$\lambda_7 = \begin{pmatrix} 0 & 0 & 0 \\ 0 & 0 & -\mathrm{i} \\ 0 & \mathrm{i} & 0 \end{pmatrix} , \quad \lambda_8 = \frac{1}{\sqrt{3}} \begin{pmatrix} 1 & 0 & 0 \\ 0 & 1 & 0 \\ 0 & 0 & -2 \end{pmatrix} ,$$

$$\lambda_a^\dagger = \lambda_a , \quad \mathrm{Tr}\{\lambda_a\} = 0 , \quad \mathrm{Tr}\{\lambda_a \lambda_b\} = 2\delta_{ab} .$$

Appendix C

Loop integrals

In the analysis of the conductivity, we find loops involving the imaginary-time correlators:

$$I(\mathrm{i}\omega_m, |\boldsymbol{Q}|; k) = \mathrm{i}T \sum_{n=-\infty}^{\infty} \int \frac{\mathrm{d}^3\boldsymbol{p}}{(2\pi)^3} \, \frac{|\boldsymbol{p}|^{2k}}{[\omega_n^2 + |\boldsymbol{p}|^2 + m^2]\,[(\omega_n+\omega_m)^2 + |\boldsymbol{p}+\boldsymbol{Q}|^2 + m^2]} \;, \tag{C.1}$$

with $k = 0, 1$.

Performing the Matsubara sum in the usual way [LB96], one arrives to a function analytical in $\mathrm{i}\omega_m$ off the real axis, so that we find for the retarded correlator:

$$\begin{aligned} \mathrm{Im}\, I^{\mathrm{R}}(\omega, |\boldsymbol{Q}|; k) = \pi \sum_{s_1,s_2=\pm 1} \int \frac{\mathrm{d}^3\boldsymbol{p}}{(2\pi)^3} \, |\boldsymbol{p}|^{2k} \frac{s_1 s_2}{4E_p E_{p+Q}} \left[1 + n_{\mathrm{B}}\left(s_1 E_p\right) + n_{\mathrm{B}}\left(s_2 E_{p+Q}\right)\right] \\ \times \, \delta(\omega - s_1 E_p - s_2 E_{p+Q}) \;, \end{aligned} \tag{C.2}$$

where $E_q^2 = |\boldsymbol{q}|^2 + m^2$. The two $s_1 = s_2$ contributions require $s \geq 4m^2$ ($s = \omega^2 - |\boldsymbol{Q}|^2$) and give the unitarity cut appearing in the analysis of thermal scattering [GN02b]. Performing the angular integrations with the delta function, it can be written as:

$$\left[\mathrm{Im}\, I^{\mathrm{R}}(\omega, |\boldsymbol{Q}|; k)\right]_{\mathrm{unit}} = \frac{\mathrm{sgn}(\omega)\theta(s-4m^2)}{16\pi|\boldsymbol{Q}|} \int_{y_-}^{y_+} \mathrm{d}y \;\; \left(y^2 - m^2\right)^k \left[1 + n_{\mathrm{B}}(y) + n_{\mathrm{B}}(|\omega| - y)\right] \;, \tag{C.3}$$

where $y_\pm = (|\omega| \pm |\boldsymbol{Q}|\sigma_{2\mathrm{p}}(s))/2 \geq m$ for $s \geq 4m^2$ and $\sigma_{2\mathrm{p}}(s) = \sqrt{1 - 4m^2/s}$ is the phase space of two particles of equal mass m.

The case $k = 0$ can be solved in terms of elementary functions:

$$\left[\mathrm{Im}\, I^{\mathrm{R}}(\omega, |\boldsymbol{Q}|; 0)\right]_{\mathrm{unit}} = \frac{\mathrm{sgn}(\omega)\theta(s-4m^2)}{16\pi} \left[\sigma_{2\mathrm{p}}(s) + \frac{2T}{|\boldsymbol{Q}|} \ln\left[\frac{1 - \exp(-y_+/T)}{1 - \exp(-y_-/T)}\right]\right] \tag{C.4}$$

On the other hand, in the limit $|\boldsymbol{Q}| \to 0^+$ (center of mass limit in the scattering case) we find:

$$\left[\mathrm{Im}\, I^{\mathrm{R}}(\omega, |\boldsymbol{Q}| \to 0^+; k)\right]_{\mathrm{unit}} = \frac{\mathrm{sgn}(\omega)\theta(s-4m^2)}{16\pi} \sigma_T(\omega) \left[\left(\frac{|\omega|}{2}\right)^2 - m^2\right]^k \tag{C.5}$$

where $\sigma_T(\omega) = \sigma_{2\mathrm{p}}(\omega^2)\,[1 + 2n_{\mathrm{B}}(|\omega|/2)]$ is the two-particle thermal phase space, which can be interpreted in terms of enhancement and absorption in the thermal bath [GN02b].

Let us analyze now the two $s_1 = -s_2$ contributions. First, it is not difficult to see that these two integrals are identical and contribute only for $s \leq 0$. Unlike the unitarity cut, this cut is purely thermal, i.e, is only present for $T \neq 0$. Integrating the delta function, their contribution to $\mathrm{Im}\, I^{\mathrm{R}}$ is:

$$\begin{aligned}\left[\mathrm{Im}\, I^{\mathrm{R}}(\omega, |\boldsymbol{Q}|; k)\right]_{\mathrm{ther}} = & -\frac{\mathrm{sgn}(\omega)\theta(-s)}{16\pi|\boldsymbol{Q}|}\int_{y_0}^{\infty} \mathrm{d}y\ \left[n_{\mathrm{B}}(y+|\omega|) - n_{\mathrm{B}}(y)\right] \\ & \times \left[(y^2-m^2)^k + ((y+|\omega|)^2-m^2)^k\right]\ , \end{aligned} \tag{C.6}$$

where $y_0 = -y_- = (-|\omega| + |\boldsymbol{Q}|\sigma_{2\mathrm{p}}(s))/2 \geq m$ for $s \neq 0$. For $k = 0$:

$$\left[\mathrm{Im}\, I^{\mathrm{R}}(\omega, |\boldsymbol{Q}|; 0)\right]_{\mathrm{ther}} = \frac{T}{8\pi|\boldsymbol{Q}|}\,\mathrm{sgn}(\omega)\theta(-s)\ln\left[\frac{1-\mathrm{e}^{-(y_0+|\omega|)/T}}{1-\mathrm{e}^{-y_0/T}}\right]\ . \tag{C.7}$$

Now, taking the limit $|\boldsymbol{Q}| \to 0^+$ with m and T fixed implies necessarily $\omega \to 0^+$ since this is a space-like contribution. More precisely, $y_0 \simeq m|\boldsymbol{Q}|/\sqrt{-s}$, so that:

$$\left[\mathrm{Im}\, I^{\mathrm{R}}(\omega \to 0^+, |\boldsymbol{Q}| \to 0^+; k)\right]_{\mathrm{ther}} = -\frac{1}{8\pi}\theta(-s)\frac{\omega}{|\boldsymbol{Q}|}\left[F_k\left[\omega^2/|\boldsymbol{Q}|^2; T\right] + \mathcal{O}\left(\frac{|\omega|}{m}, \frac{|\omega|}{T}\right)\right]\ , \tag{C.8}$$

where:

$$F_k(x;T) \equiv \int_{m/\sqrt{1-x}}^{\infty} \mathrm{d}y\ (y^2-m^2)^k n'_{\mathrm{B}}(y)\ , \tag{C.9}$$

for $0 \leq x < 1$. Note that $F_k(x) < 0$, $\lim_{x\to 1^-} F_k(x) = 0$ and that the small energy and momentum limits (C.8) do not coincide necessarily with taking directly $|\boldsymbol{Q}| = 0$ with $\omega \neq 0$, which gives a vanishing contribution due to the step function.

Following similar steps as above, it is not difficult to obtain the imaginary part of loop integrals with more powers of $\mathrm{i}\omega_n$ in the numerator:

$$J_\alpha(\mathrm{i}\omega_m, |\boldsymbol{Q}|) = \mathrm{i}T\sum_{n=-\infty}^{\infty}\int\frac{\mathrm{d}^3\boldsymbol{p}}{(2\pi)^3}\ \frac{(\mathrm{i}\omega_n)^\alpha}{\left[\omega_n^2 + |\boldsymbol{p}|^2 + m^2\right]\left[(\omega_n+\omega_m)^2 + |\boldsymbol{p}+\boldsymbol{Q}|^2 + m^2\right]}\ , \tag{C.10}$$

with α a positive integer or zero. We have analyzed the $\alpha = 0$ case previously. For arbitrary α we get:

$$\left[\mathrm{Im}\, J^{\mathrm{R}}_\alpha(\omega, |\boldsymbol{Q}|)\right]_{\mathrm{unit}} = \frac{\left[\mathrm{sgn}(\omega)\right]^{\alpha+1}\theta(s-4m^2)}{16\pi|\boldsymbol{Q}|}\int_{y_-}^{y_+}\mathrm{d}y\ (-y)^\alpha\left[1 + n_{\mathrm{B}}(y) + n_{\mathrm{B}}(|\omega|-y)\right]\ , \tag{C.11}$$

$$\begin{aligned}\left[\mathrm{Im}\, J^{\mathrm{R}}_\alpha(\omega, |\boldsymbol{Q}|)\right]_{\mathrm{ther}} = & -\frac{\left[\mathrm{sgn}(\omega)\right]^{\alpha+1}\theta(-s)}{16\pi|\boldsymbol{Q}|}\int_{y_0}^{\infty}\mathrm{d}y\ \left[y^\alpha + (-1)^\alpha(y+|\omega|)^\alpha\right] \\ & \times\left[n_{\mathrm{B}}(y+|\omega|) - n_{\mathrm{B}}(y)\right]\ . \end{aligned} \tag{C.12}$$

Appendix D

Free thermal propagators and partition function at $\mu \neq 0$

In this appendix we review some important aspects of the the propagators in different representations of Thermal Field Theory. Let us consider first a free scalar field theory. In that case, one can evaluate the partition function and the propagator (two-point function) directly in the complete set $|N_1, N_2, \ldots\rangle$, corresponding to eigenstates of the hamiltonian operator with N_1 particles in the state 1, N_2 particles in the state 2, and so on:

$$\begin{aligned} &\langle N_1, N_2, \ldots | N_1', N_2', \ldots\rangle = \delta_{N_1 N_1'} \cdot \delta_{N_2 N_2'} \cdot \ldots \ , \\ &\hat{H}_0 |N_1, N_2, \ldots\rangle = \left(N_1 E_1 + \ldots + \sum_{i=1}^{\infty} \frac{E_i}{2} \right) |N_1, N_2, \ldots\rangle \ , \\ &\hat{N} |N_1, N_2, \ldots\rangle = (N_1 + N_2 + \ldots) |N_1, N_2, \ldots\rangle \ , \end{aligned} \tag{D.1}$$

with $\sum N_i = N$. For non-interacting bosons of mass m, $E_i \equiv \sqrt{m^2 + |\boldsymbol{p}_i|^2}$, and the (infinite) term $\sum_i E_i/2$ represents the *vacuum energy*. As customary, we consider first the system in a finite volume $V = L^3$, which we will later take to infinity, so that spatial momenta are discretized as $|p_i| = \pi n_i / L$ with $n_i \in \mathbb{Z}$ and the energy levels are labeled by $\boldsymbol{n} \equiv (n_x, n_y, n_z)$. The free partition function reads then:

$$\tilde{Z}_\beta^0 = \prod_{\boldsymbol{n}} \sum_{N=0}^{\infty} \mathrm{e}^{-\beta N (E_{\boldsymbol{n}} - \mu)} \mathrm{e}^{-\beta E_{\boldsymbol{n}}/2} = \prod_{\boldsymbol{n}} \frac{\mathrm{e}^{-\beta E_{\boldsymbol{n}}/2}}{1 - \mathrm{e}^{-\beta (E_{\boldsymbol{n}} - \mu)}} \ ,$$

where the condition $\mu < E_{\boldsymbol{n}}$ must be satisfied for all $\boldsymbol{n}$. Thus, in the $V \to \infty$ limit:

$$\ln \tilde{Z}_\beta^0 = -V \int \frac{\mathrm{d}^3 \boldsymbol{p}}{(2\pi)^3} \ \left[\frac{\beta E_p}{2} + \ln \left(1 - \mathrm{e}^{-\beta (E_p - \mu)} \right) \right] \ . \tag{D.2}$$

Therefore, in the following we must restrict to a chemical potential $\mu \leq m$ (Bose-Einstein condensation limit) to ensure the convergence of the previous expressions.

In order to obtain the particle propagator in the canonical formalism, defined as the two-point function:

$$\tilde{G}(x) \equiv \langle \hat{T} \hat{\phi}(x) \hat{\phi}(0) \rangle_{\beta, \mu} \equiv \tilde{Z}_\beta^{-1} \, \mathrm{Tr} \left\{ \mathrm{e}^{-\beta (\hat{H} - \mu \hat{N})} \hat{T} \hat{\phi}(x) \hat{\phi}(0) \right\} \ , \tag{D.3}$$

where $\hat{T}$ is the time-ordering operator, we expand the field as customarily in terms of creation and annihilation operators:

$$\hat{\phi}(\boldsymbol{x}) = \frac{1}{V}\sum_{n}\frac{1}{\sqrt{2E_{\boldsymbol{n}}}}\left(\hat{a}_{\boldsymbol{n}}\mathrm{e}^{\mathrm{i}2\pi\boldsymbol{n}\cdot\boldsymbol{x}/L} + \hat{a}^{\dagger}_{\boldsymbol{n}}\mathrm{e}^{-\mathrm{i}2\pi\boldsymbol{n}\cdot\boldsymbol{x}/L}\right) \ , \tag{D.4}$$

with commutation relation

$$[\hat{a}_{\boldsymbol{n}}, \hat{a}^{\dagger}_{\boldsymbol{n}'}] = V\delta_{\boldsymbol{n},\boldsymbol{n}'} \ . \tag{D.5}$$

The free hamiltonian and the number operator are given in terms of creation and annihilation operators as:

$$\begin{aligned}\hat{H}_0 &= \sum_{\boldsymbol{n}}\frac{1}{V}E_{\boldsymbol{n}}(\hat{a}^{\dagger}_{\boldsymbol{n}}\hat{a}_{\boldsymbol{n}} + \frac{1}{2}V) \ , \\ \hat{N} &= \sum_{\boldsymbol{n}}\frac{1}{V}\hat{a}^{\dagger}_{\boldsymbol{n}}\hat{a}_{\boldsymbol{n}} \ .\end{aligned} \tag{D.6}$$

Now, the *real* time evolution of the field is given by $\hat{\phi}(t,\boldsymbol{x}) \equiv \mathrm{e}^{\mathrm{i}\hat{H}t}\hat{\phi}(\boldsymbol{x})\mathrm{e}^{-\mathrm{i}\hat{H}t}$ with $t \in \mathbb{R}$. We will calculate the trace in (D.3) using

$$\frac{1}{V}\langle\hat{a}^{\dagger}_{\boldsymbol{n}}\hat{a}_{\boldsymbol{n}}\rangle_{\beta,\mu} = \frac{1}{\mathrm{e}^{\beta(E_{\boldsymbol{n}}-\mu)}-1} \equiv n(E_{\boldsymbol{n}}-\mu) \ , \tag{D.7}$$

so that we get for the free propagator, after taking the $V \to \infty$ limit:

$$\tilde{G}(x) = \theta(t)\tilde{G}^{>}(x) + \theta(-t)\tilde{G}^{<}(x) \ , \tag{D.8}$$

with:

$$\tilde{G}^{>(<)}(x) = \int\frac{\mathrm{d}^3\boldsymbol{p}}{(2\pi)^3}\ \mathrm{e}^{\mathrm{i}\boldsymbol{p}\cdot\boldsymbol{x}}\ \tilde{G}^{>(<)}(t,p) \ , \tag{D.9}$$

$$\tilde{G}^{>}(t,\boldsymbol{p}) = \frac{1}{2E_p}\left[\mathrm{e}^{-\mathrm{i}E_pt}(1+\tilde{n}_p(E_p)) + \mathrm{e}^{\mathrm{i}E_pt}\tilde{n}_p(E_p)\right] \ , \tag{D.10}$$

$$\tilde{G}^{<}(t,\boldsymbol{p}) = \frac{1}{2E_p}\left[\mathrm{e}^{\mathrm{i}E_pt}(1+\tilde{n}_p(E_p)) + \mathrm{e}^{-\mathrm{i}E_pt}\tilde{n}_p(E_p)\right] \ . \tag{D.11}$$

Here, we have defined the following useful "modified" distribution function:

$$\tilde{n}_p(x) = \frac{1}{\mathrm{e}^{\tilde{\beta}_px}-1} \ , \tag{D.12}$$

with the p-dependent inverse "temperature":

$$\tilde{\beta}_p \equiv \beta\left(1-\frac{\mu}{E_p}\right) \ . \tag{D.13}$$

Therefore, we have for instance $\tilde{n}_p(E_p) = n(E_p-\mu)$ and the $\tilde{n}_p$ function satisfies:

$$1 + \tilde{n}_p(x) + \tilde{n}_p(-x) = 0 \ . \tag{D.14}$$

Thus, the free propagator satisfies the following KMS-like periodicity condition in the mixed representation:

$$\tilde{G}^{>}(t,p) = \tilde{G}^{<}(t + \mathrm{i}\tilde{\beta}_p, p) \ , \tag{D.15}$$

and in Fourier space we can write a spectral representation:

$$\begin{aligned} \tilde{G}^{>}(p_0,p) &= [1 + \tilde{n}_p(p_0)]\, \rho(p_0,p) \ , \\ \tilde{G}^{<}(p_0,p) &= \mathrm{e}^{-\tilde{\beta}_p p_0} \tilde{G}^{>}(p_0,p) = \tilde{n}_p(p_0)\rho(p_0,p) \ , \end{aligned} \tag{D.16}$$

where

$$\rho(p_0,p) = 2\pi\, \mathrm{sgn}(p_0)\delta(p_0^2 - E_p^2) \ , \tag{D.17}$$

is the free spectral function, which is independent of temperature and chemical potential.

Now, using:

$$\theta(t) = \mathrm{i} \int_{-\infty}^{\infty} \frac{\mathrm{d}k_0}{2\pi} \, \frac{\mathrm{e}^{-\mathrm{i}k_0 t}}{k_0 + \mathrm{i}0^+} \ , \tag{D.18}$$

we can write for the propagator in (D.8) in momentum space:

$$\tilde{G}(p_0,p) = \frac{\mathrm{i}}{p_0^2 - E_p^2 + \mathrm{i}0^+} + 2\pi\delta(p_0^2 - E_p^2) n_{\mathrm{B}}(|p_0| - \mu) \ . \tag{D.19}$$

Note that we have used $\tilde{n}_p(E_p)\delta(p_0^2 - E_p^2) = \tilde{n}_p(|p_0|)\delta(p_0^2 - E_p^2) = n_{\mathrm{B}}(|p_0| - \mu)\delta(p_0^2 - E_p^2)$ and we have chosen the "$|p_0|$-prescription" which, as explained in the main text, guarantees the decoupling of the imaginary-leg contribution to real-time Green functions.

The free propagators in (D.10)-(D.11) can be extended to imaginary times $t = -\mathrm{i}\tau$ corresponding to the imaginary-time leg C_4 in Fig. 4.1. The imaginary time propagators admit a Matsubara-like representation. For $\tau \in [0, \tilde{\beta}_p]$:

$$\tilde{\Delta}_T(\tau,p) = \tilde{G}^{>}(-\mathrm{i}\tau,p) = \frac{1}{\tilde{\beta}_p} \sum_{n=-\infty}^{\infty} \frac{\mathrm{e}^{\mathrm{i}\tilde{\omega}_n \tau}}{\tilde{\omega}_n^2 + E_p^2} \ , \tag{D.20}$$

with $\tilde{\omega}_n = 2\pi n/\tilde{\beta}_p$ and so on for $\tau \in [-\tilde{\beta}_p, 0]$, where $\tilde{\Delta}_T(\tau,p) = \tilde{G}^{<}(-\mathrm{i}\tau,p)$. Therefore, the KMS-like condition (D.15) translates into the imaginary-time propagator as $\tilde{\Delta}_T(\tau + \tilde{\beta}_p, p) = \tilde{\Delta}_T(\tau,p)$.

Most of the results shown in the main text can be written in terms of the above thermal propagators evaluated at the origin in position space and functions related to them. From (D.9)-(D.11) we have (for $\mu \leq m$) at $\tau = t = \boldsymbol{x} = 0$:

$$\tilde{G}^{>}(0) = \tilde{G}^{<}(0) = \tilde{\Delta}_T(0) = \tilde{G}(0) = \Big[\tilde{G}(0)\Big]^{T=\mu=0} + \tilde{g}_1(m,T,\mu) \ , \tag{D.21}$$

where the $T = \mu = 0$ contribution is ultraviolet divergent. In dimensional regularization it is given by:

$$\Big[\tilde{G}(0)\Big]^{T=\mu=0} = \int \frac{\mathrm{d}^{D-1}p}{(2\pi)^{D-1}} \frac{1}{2E_p} = \frac{\Gamma[1 - \frac{D}{2}] m^{D-2}}{(4\pi)^{D/2}} \ , \tag{D.22}$$

while the T, μ-dependent contribution $\tilde{g}_1$ is finite. We are following the same notation as in [Ger89] so that $\tilde{g}_1$ is the $\mu \neq 0$ extension of their function $g_1(T)$, to which it reduces for $\mu = 0$. We have:

$$\tilde{g}_1(m, T, \mu) = \frac{1}{2\pi^2} \int_0^\infty dp \frac{p^2}{E_p} \frac{1}{\mathrm{e}^{\beta(E_p - \mu)} - 1} \ . \tag{D.23}$$

Note that in dimensional regularization one has, as in the $\mu = 0$ case:

$$\begin{aligned} \left[\partial_\tau^2 - \nabla^2\right] \tilde{\Delta}_T(\tau, \boldsymbol{x})\Big|_{\tau=\boldsymbol{x}=0} &= m^2 \tilde{\Delta}_T(0) \ , \\ \Box \tilde{G}(t, \boldsymbol{x})\Big|_{t=\boldsymbol{x}=0} &= -m^2 \tilde{G}(0) \ , \end{aligned} \tag{D.24}$$

and $\partial_\mu \tilde{G}(0) = \partial_\mu \Delta_T(0) = 0$. Let us also define, following again the notation in [Ger89]:

$$\tilde{g}_0(m, T, \mu) = -\frac{T}{\pi^2} \int_0^\infty \mathrm{d}p \ p^2 \ln\left[1 - \mathrm{e}^{-\beta(E_p - \mu)}\right] \ , \tag{D.25}$$

so that, taking into account that $\partial E_p / \partial m^2 = 1/(2E_p)$, we can write the free partition function (D.2) separating its divergent contribution in dimensional regularization as:

$$\ln \tilde{Z}_\beta^0 = \frac{\beta V}{2} \left[\frac{\Gamma\left[-\frac{D}{2}\right] m^D}{(4\pi)^{D/2}} + \tilde{g}_0(m, T, \mu) \right] \ . \tag{D.26}$$

Note that the functions $\tilde{g}_0$ and $\tilde{g}_1$ satisfy:

$$\tilde{g}_1(m, T, \mu) = -\frac{\partial}{\partial m^2} \tilde{g}_0(m, T, \mu) \ . \tag{D.27}$$

List of abbreviations

AdS – Anti de Sitter

BE – Bose-Einstein

BR – Brown-Rho

BS – Bethe-Salpeter

BW – Breit-Wigner

CFT – Conformal field theory

ChPT – Chiral Perturbation Theory

c.m. – Center of mass

DGA – Dilute gas approximation

EM – Electromagnetic

EOM – Equations of motion

EOS – Equation of state

FRS – First Riemann sheet

GOR – Gell-Mann-Oakes-Renner

HE – Hydrodynamic equations

HBT – Hanbury-Brown-Twiss

HRG – Hadron resonance gas

IAM – Inverse Amplitude Method

IT – Imaginary time

ITF – Imaginary-Time Formalism

KMS – Kubo-Martin-Schwinger relation

KT – Kinetic theory

l.h.s. – Left-hand side

LPM – Landau-Pomeranchuk–Migdal

LRF – Local-rest frame

LRT – Linear Response Theory

LSM – Linear Sigma Model

QFT – Quantum Field Theory

QGP – Quark-gluon plasma

QM – Quantum Mechanics

RHIC – Relativistic Heavy-Ion Collider

r.h.s. – Right-hand side

RPA – Random phase approximation

SRS – Second Riemann sheet

VGA – Virial gas approximation

Bibliography

[Aar02] G. Aarts and J. M. Martinez Resco, *Transport coefficients, spectral functions and the lattice*, JHEP 04, (2002) 053.

[Aar03] G. Aarts and J. M. Martinez Resco, *Transport coefficients from the 2PI effective action*, Phys. Rev. D68, (2003) 085009.

[Aar04] G. Aarts and J. M. Martinez Resco, *Shear viscosity in the O(N) model*, JHEP 02, (2004) 061.

[Aar05] G. Aarts and J. M. Martinez Resco, *Transport coefficients in large N_f gauge theories with massive fermions*, JHEP 03, (2005) 074.

[Ada04a] J. Adams et al., *Particle-type dependence of azimuthal anisotropy and nuclear modification of particle production in Au+Au collisions at $\sqrt{s_{NN}}$ = 200 GeV*, Phys. Rev. Lett. 92, (2004) 052302.

[Ada04b] J. Adams et al., *ρ^0 production and possible modification in Au+Au and p+p collisions at $\sqrt{s_{NN}}$=200 GeV*, Phys. Rev. Lett. 92, (2004) 092301.

[Ada05] J. Adams et al., *Experimental and theoretical challenges in the search for the quark gluon plasma: The STAR collaboration's critical assessment of the evidence from RHIC collisions*, Nucl. Phys. A757, (2005) 102.

[Adc05] K. Adcox et al., *Formation of dense partonic matter in relativistic nucleus-nucleus collisions at RHIC: Experimental evaluation by the PHENIX collaboration*, Nucl. Phys. A757, (2005) 184.

[AE95] R. F. Alvarez-Estrada and A. Gomez Nicola, *Effective chiral lagrangian from QCD at nonzero chemical potential*, Phys. Lett. B355, (1995) 288.

[Aga01] N. O. Agasian, *Low temperature relation for the trace of the energy momentum tensor in QCD with light quarks*, JETP Lett. 74, (2001) 353.

[Aga05] G. Agakichiev et al., *e^+e^--pair production in Pb-Au collisions at 158 GeV per nucleon*, Eur. Phys. J. C41, (2005) 475.

[Agg04] M. M. Aggarwal et al., *Interferometry of direct photons in central ^{208}Pb+^{208}Pb collisions at 158A GeV*, Phys. Rev. Lett. 93, (2004) 022301.

[Ala01] J. Alam, S. Sarkar, P. Roy, T. Hatsuda, and B. Sinha, *Thermal photons and lepton pairs from quark gluon plasma and hot hadronic matter*, Annals Phys. 286, (2001) 159.

[Alf00] M. G. Alford and R. L. Jaffe, *Insight into the scalar mesons from a lattice calculation*, Nucl. Phys. B578, (2000) 367.

[Ams04] C. Amsler and N. A. Tornqvist, *Mesons beyond the naive quark model*, Phys. Rept. 389, (2004) 61.

[Ams08] C. Amsler et al., *Review of particle physics*, Phys. Lett. B667, (2008) 1.

[App75] T. Appelquist and J. Carazzone, *Infrared singularities and massive fields*, Phys. Rev. D11, (1975) 2856.

[Arm96] N. Armesto, M. A. Braun, E. G. Ferreiro, and C. Pajares, *Percolation approach to Quark Gluon Plasma and J/ψ suppression*, Phys. Rev. Lett. 77, (1996) 3736.

[Arn00] P. Arnold, G. D. Moore, and L. G. Yaffe, *Transport coefficients in high temperature gauge theories. I: Leading-log results*, JHEP 11, (2000) 001.

[Arn01] P. Arnold, G. D. Moore, and L. G. Yaffe, *Photon emission from ultrarelativistic plasmas*, JHEP 11, (2001) 057.

[Arn03] P. Arnold, G. D. Moore, and L. G. Yaffe, *Transport coefficients in high temperature gauge theories. II: Beyond leading log*, JHEP 05, (2003) 051.

[Arn06a] R. Arnaldi et al., *First measurement of the rho spectral function in high-energy nuclear collisions*, Phys. Rev. Lett. 96, (2006) 162302.

[Arn06b] P. Arnold, C. Dogan, and G. D. Moore, *The bulk viscosity of high-temperature QCD*, Phys. Rev. D74, (2006) 085021.

[Ars05] I. Arsene et al., *Quark Gluon Plasma and Color Glass Condensate at RHIC? The perspective from the BRAHMS experiment*, Nucl. Phys. A757, (2005) 1.

[Aur98] P. Aurenche, F. Gelis, R. Kobes, and H. Zaraket, *Bremsstrahlung and photon production in thermal QCD*, Phys. Rev. D58, (1998) 085003.

[Aya02] A. Ayala, P. Amore, and A. Aranda, *Pion dispersion relation at finite density and temperature*, Phys. Rev. C66, (2002) 045205.

[Aya03] A. Ayala and J. Magnin, *Rho propagation and dilepton production at finite pion density and temperature*, Phys. Rev. C68, (2003) 014902.

[Bac05] B. B. Back et al., *The PHOBOS perspective on discoveries at RHIC*, Nucl. Phys. A757, (2005) 28.

[Bai97] R. Baier, M. Dirks, and K. Redlich, *Thermal dileptons from π-ρ interactions in a hot pion gas*, Phys. Rev. D55, (1997) 4344.

[Bai08] R. Baier, P. Romatschke, D. T. Son, A. O. Starinets, and M. A. Stephanov, *Relativistic viscous hydrodynamics, conformal invariance, and holography*, JHEP 04, (2008) 100.

[Bat67] G. K. Batchelor, *An introduction to fluid dynamics*, Cambridge University Press, 1967.

[Beb92] H. Bebie, P. Gerber, J. L. Goity, and H. Leutwyler, *The role of the entropy in an expanding hadronic gas*, Nucl. Phys. B378, (1992) 95.

[Beg07] V. V. Begun and M. I. Gorenstein, *Bose-Einstein condensation of pions in high multiplicity events*, Phys. Lett. B653, (2007) 190.

[Ber95] V. Bernard, N. Kaiser, and U.-G. Meissner, *Chiral dynamics in nucleons and nuclei*, Int. J. Mod. Phys. E4, (1995) 193.

[Bla05] J.-P. Blaizot and F. Gelis, *Photon and dilepton production in the quark-gluon plasma: Perturbation theory vs lattice QCD*, Eur. Phys. J. C43, (2005) 375.

[BM04] P. Braun-Munzinger, K. Redlich, and J. Stachel, *Particle production in heavy ion collisions*, In "Quark-gluon plasma 3", R. C. Hwa et al. (eds.), pp. 491–599, World Scientific, 2004.

[Bon00] F. Bonutti et al., *The $\pi\pi$ interaction in nuclear matter from a study of the $\pi^+ A \to \pi^+\pi^\pm A'$ reactions*, Nucl. Phys. A677, (2000) 213.

[Boy96] G. Boyd et al., *Thermodynamics of SU(3) Lattice Gauge Theory*, Nucl. Phys. B469, (1996) 419.

[Bro91] G. E. Brown and M. Rho, *Scaling effective lagrangians in a dense medium*, Phys. Rev. Lett. 66, (1991) 2720.

[Bro02] G. E. Brown and M. Rho, *On the manifestation of chiral symmetry in nuclei and dense nuclear matter*, Phys. Rept. 363, (2002) 85.

[Bro04] G. E. Brown and M. Rho, *Double decimation and sliding vacua in the nuclear many-body system*, Phys. Rept. 396, (2004) 1.

[Bro05a] G. E. Brown and M. Rho, *NA60 and BR scaling in terms of the vector manifestation: A model approach*, `nucl-th/0509001`.

[Bro05b] G. E. Brown and M. Rho, *NA60 and BR scaling in terms of the vector manifestation: Formal consideration*, `nucl-th/0509002`.

[Bug03] D. V. Bugg, *Comments on the sigma and kappa*, Phys. Lett. B572, (2003) 1.

[Cab02] D. Cabrera, E. Oset, and M. J. Vicente Vacas, *Chiral approach to the rho meson in nuclear matter*, Nucl. Phys. A705, (2002) 90.

[Cab05] D. Cabrera, E. Oset, and M. J. Vicente Vacas, *Evaluation of the $\pi\pi$-scattering amplitude in the σ-channel at finite density*, Phys. Rev. C72, (2005) 025207.

[Cab08] D. Cabrera, D. Fernandez-Fraile, and A. Gomez Nicola, *Chiral symmetry and light resonances in hot and dense matter*, Eur. Phys. J., DOI:10.1140/epjc/s10052-008-0831-z, `arXiv:0809.5237[hep-ph]`.

[Car98a] M. E. Carrington and R. Kobes, *The general cancellation of ladder graphs at finite temperature*, Phys. Rev. D57, (1998) 6372.

[Car98b] M. E. Carrington, R. Kobes, and E. Petitgirard, *Cancellation of ladder graphs in an effective expansion*, Phys. Rev. D57, (1998) 2631.

[Che07] J.-W. Chen and E. Nakano, *Shear viscosity to entropy density ratio of QCD below the deconfinement temperature*, Phys. Lett. B647, (2007) 371.

[Che08] M. Cheng et al., *The QCD equation of state with almost physical quark masses*, Phys. Rev. D77, (2008) 014511.

[Che09] J.-W. Chen and J. Wang, *Bulk viscosity of a gas of massless pions*, Phys. Rev. C79, (2009) 044913.

[Chi98a] H. C. Chiang, E. Oset, and M. J. Vicente-Vacas, *Chiral nonperturbative approach to the isoscalar S-wave pion-pion interaction in a nuclear medium*, Nucl. Phys. A644, (1998) 77.

[Chi98b] S. Chiku and T. Hatsuda, *Soft modes associated with chiral transition at finite temperature*, Phys. Rev. D57, (1998) 6.

[Cho85] K.-c. Chou, Z.-b. Su, B.-l. Hao, and L. Yu, *Equilibrium and non-equilibrium formalisms made unified*, Phys. Rept. 118, (1985) 1.

[Clo79] F. E. Close, *An introduction to quarks and partons*, Academic Press, 1979.

[Col77] J. C. Collins, A. Duncan, and S. D. Joglekar, *Trace and dilatation anomalies in gauge theories*, Phys. Rev. D16, (1977) 438.

[Col85] S. Coleman, *Aspects of symmetry: selected Erice lectures of Sidney Coleman*, Cambridge University Press, 1985.

[Cse06] L. P. Csernai, J. I. Kapusta, and L. D. McLerran, *On the strongly-interacting low-viscosity matter created in relativistic nuclear collisions*, Phys. Rev. Lett. 97, (2006) 152303.

[Dan85] P. Danielewicz and M. Gyulassy, *Dissipative phenomena in quark-gluon plasmas*, Phys. Rev. D31, (1985) 53.

[Dav96] D. Davesne, *Transport coefficients of a hot pion gas*, Phys. Rev. C53, (1996) 3069.

[Dav00] D. Davesne, Y. J. Zhang, and G. Chanfray, *Medium modification of the pion-pion interaction at finite density*, Phys. Rev. C62, (2000) 024604.

[dB55] J. de Boer, *Transport phenomena in gases at low temperatures*, In "Progress in low temperature physics, Vol. 1", C. J. Gorter (ed.), p. 385, North-Holland, 1955.

[Den09] G. S. Denicol, T. Kodama, T. Koide, and P. Mota, *Effect of bulk viscosity on elliptic flow near QCD phase transition*, `arXiv:0903.3595[hep-ph]`.

[Dob90] A. Dobado, M. J. Herrero, and T. N. Truong, *Unitarized Chiral Perturbation Theory for elastic pion-pion scattering*, Phys. Lett. B235, (1990) 134.

[Dob93] A. Dobado and J. R. Pelaez, *A global fit of $\pi\pi$ and πK elastic scattering in ChPT with dispersion relations*, Phys. Rev. D47, (1993) 4883.

[Dob97] A. Dobado and J. R. Pelaez, *The Inverse Amplitude Method in Chiral Perturbation Theory*, Phys. Rev. D56, (1997) 3057.

[Dob99] A. Dobado and J. R. Pelaez, *Chiral symmetry and the pion gas virial expansion*, Phys. Rev. D59, (1999) 034004.

[Dob02] A. Dobado, A. Gomez Nicola, F. J. Llanes-Estrada, and J. R. Pelaez, *Thermal rho and sigma mesons from chiral symmetry and unitarity*, Phys. Rev. C66, (2002) 055201.

[Dob04] A. Dobado and F. J. Llanes-Estrada, *The viscosity of meson matter*, Phys. Rev. D69, (2004) 116004.

[Dob07a] A. Dobado and F. J. Llanes-Estrada, *The ratio of viscosity to entropy density in a pion gas satisfies the KSS holographic bound*, Eur. Phys. J. C49, (2007) 1011.

[Dob07b] A. Dobado, F. J. Llanes-Estrada, and J. M. Torres Rincon, *Heat conductivity of a pion gas*, `arXiv:hep-ph/0702130`.

[Dob09] A. Dobado, F. J. Llanes-Estrada, and J. M. Torres-Rincon, *η/s and the phase transition of the Non-Linear Sigma Model*, Phys. Rev. D79, (2009) 014002.

[Dus08] K. Dusling and D. Teaney, *Simulating elliptic flow with viscous hydrodynamics*, Phys. Rev. C77, (2008) 034905.

[Ele93] V. L. Eletsky, J. I. Kapusta, and R. Venugopalan, *Screening mass from chiral perturbation theory, virial expansion and the lattice*, Phys. Rev. D48, (1993) 4398.

[Ell98] P. J. Ellis, J. I. Kapusta, and H.-B. Tang, *Low-energy theorems for gluodynamics at finite temperature*, Phys. Lett. B443, (1998) 63.

[Esp90] D. Espriu, E. de Rafael, and J. Taron, *The QCD effective action at long distances*, Nucl. Phys. B345, (1990) 22.

[Eva96] T. S. Evans, *The condensed matter limit of relativistic QFT*, In "Fourth workshop on thermal field theories and their applications", Y. X. Gui et al. (eds.), pp. 283–295, World Scientific, 1996.

[FF06] D. Fernandez-Fraile and A. Gomez Nicola, *The electrical conductivity of a pion gas*, Phys. Rev. D73, (2006) 045025.

[FF07a] D. Fernandez-Fraile and A. Gomez Nicola, *Transport coefficients in Chiral Perturbation Theory*, Eur. Phys. J. A31, (2007) 848.

[FF07b] D. Fernandez-Fraile and A. Gomez Nicola, *Transport properties of a meson gas*, Int. J. Mod. Phys. E16, (2007) 3010.

[FF07c] D. Fernandez-Fraile, A. Gomez Nicola, and E. T. Herruzo, *Pion scattering poles and chiral symmetry restoration*, Phys. Rev. D76, (2007) 085020.

[FF09a] D. Fernandez-Fraile and A. Gomez Nicola, *Bulk viscosity and the conformal anomaly in the pion gas*, Phys. Rev. Lett. 102, (2009) 121601.

[FF09b] D. Fernandez-Fraile and A. Gomez Nicola, *Chemical nonequilibrium for interacting bosons: applications to the pion gas*, Submitted to Phys. Rev. D.

[FF09c] D. Fernandez-Fraile and A. Gomez Nicola, *Transport coefficients and resonances for a meson gas in Chiral Perturbation Theory*, Eur. Phys. J. C, DOI:10.1140/epjc/s10052-009-0935-0, `arXiv:0902.4829[hep-ph]`.

[Fis77] W. Fischler, *Quark - anti-quark potential in QCD*, Nucl. Phys. B129, (1977) 157.

[Fuj84] Y. Fujimoto, H. Matsumoto, H. Umezawa, and I. Ojima, *Mass derivative formula and the sigularity structure in Thermo Field Dynamics*, Phys. Rev. D30, (1984) 1400.

[Gas84] J. Gasser and H. Leutwyler, *Chiral Perturbation Theory to one loop*, Ann. Phys. 158, (1984) 142.

[Gas87] J. Gasser and H. Leutwyler, *Light quarks at low temperatures*, Phys. Lett. B184, (1987) 83.

[Gav85] S. Gavin, *Transport coefficients in ultra-relativistic heavy-ion collisions*, Nucl. Phys. A435, (1985) 826.

[Gel99] F. Gelis, *A new approach for the vertical part of the contour in thermal field theories*, Phys. Lett. B455, (1999) 205.

[Geo99] H. Georgi, *Lie algebras in particle physics*, Perseus Books, 1999.

[Geo09] H. Georgi, *Weak interactions and modern particle theory*, Dover Publications, 2009.

[Ger89] P. Gerber and H. Leutwyler, *Hadrons below the chiral phase transition*, Nucl. Phys. B321, (1989) 387.

[GM68] M. Gell-Mann, R. J. Oakes, and B. Renner, *Behavior of current divergences under $SU(3) \times SU(3)$*, Phys. Rev. 175, (1968) 2195.

[GM06] R. Garcia Martin and J. R. Pelaez, *Chiral condensate thermal evolution at finite baryon chemical potential within Chiral Perturbation Theory*, Phys. Rev. D74, (2006) 096003.

[GN00] A. Gomez Nicola, J. Nieves, J. R. Pelaez, and E. Ruiz Arriola, *Improved unitarized Heavy Baryon Chiral Perturbation Theory for πN scattering*, Phys. Lett. B486, (2000) 77.

[GN02a] A. Gomez Nicola and J. R. Pelaez, *Meson-meson scattering within one loop Chiral Perturbation Theory and its unitarization*, Phys. Rev. D65, (2002) 054009.

[GN02b] A. Gomez Nicola, F. J. Llanes-Estrada, and J. R. Pelaez, *Finite temperature pion scattering to one-loop in Chiral Perturbation Theory*, Phys. Lett. B550, (2002) 55.

[GN05] A. Gomez Nicola, F. J. Llanes-Estrada, and J. R. Pelaez, *Finite temperature pion vector form factors in Chiral Perturbation Theory*, Phys. Lett. B606, (2005) 351.

[GN07] A. Gomez Nicola and D. Fernandez-Fraile, *Electromagnetic fields and transport coefficients in a hot pion gas*, Nucl. Phys. A785, (2007) 166.

[GN08] A. Gomez Nicola, J. R. Pelaez, and G. Rios, *The Inverse Amplitude Method and Adler zeros*, Phys. Rev. D77, (2008) 056006.

[Goi89] J. L. Goity and H. Leutwyler, *On the mean free path of pions in hot matter*, Phys. Lett. B228, (1989) 517.

[Goi93] J. L. Goity, *Chemical relaxation times in a hadron gas at finite temperature*, Phys. Lett. B319, (1993) 401.

[Gre93] C. Greiner, C. Gong, and B. Muller, *Some remarks on pion condensation in relativistic heavy ion collisions*, Phys. Lett. B316, (1993) 226.

[Gro73] D. J. Gross and F. Wilczek, *Ultraviolet behavior of non-abelian gauge theories*, Phys. Rev. Lett. 30, (1973) 1343.

[Gro80] S. R. d. Groot, W. A. v. Leeuwen, and C. G. v. Weert, *Relativistic Kinetic Theory: Principles and applications*, North-Holland Pub. Co., 1980.

[Gup04] S. Gupta, *The electrical conductivity and soft photon emissivity of the QCD plasma*, Phys. Lett. B597, (2004) 57.

[Hal84] F. Halzen and A. D. Martin, *Quarks and leptons: An introductory course in modern particle physics*, Wiley, 1984.

[Han08] C. Hanhart, J. R. Pelaez, and G. Rios, *Quark mass dependence of the rho and sigma from dispersion relations and Chiral Perturbation Theory*, Phys. Rev. Lett. 100, (2008) 152001.

[Har06] M. Harada and C. Sasaki, *Thermal dilepton production from dropping rho based on the vector manifestation*, Phys. Rev. D74, (2006) 114006.

[Hat85] T. Hatsuda and T. Kunihiro, *Fluctuation effects in hot quark matter: Precursors of chiral transition at finite temperature*, Phys. Rev. Lett. 55, (1985) 158.

[Hat95] T. Hatsuda, S. H. Lee, and H. Shiomi, *QCD sum rules, scattering length and the vector mesons in nuclear medium*, Phys. Rev. C52, (1995) 3364.

[Hat99] T. Hatsuda, T. Kunihiro, and H. Shimizu, *Precursor of chiral symmetry restoration in the nuclear medium*, Phys. Rev. Lett. 82, (1999) 2840.

[Hei09] U. W. Heinz, *Early collective expansion: Relativistic hydrodynamics and the transport properties of QCD matter*, `arXiv:0901.4355[nucl-th]`.

[Her92] M. Herrmann, B. L. Friman, and W. Noerenberg, *Rho mesons in dense nuclear matter*, Nucl. Phys. A545, (1992) 267.

[Hid03] Y. Hidaka, O. Morimatsu, T. Nishikawa, and M. Ohtani, *Effect of pion thermal width on the sigma spectrum*, Phys. Rev. D68, (2003) 111901.

[Hid04] Y. Hidaka, O. Morimatsu, T. Nishikawa, and M. Ohtani, *Two-pion bound state in sigma channel at finite temperature*, Phys. Rev. D70, (2004) 076001.

[Hid08a] Y. Hidaka and R. D. Pisarski, *Suppression of the shear viscosity as QCD cools into a confining phase*, Prog. Theor. Phys. Suppl. 174, (2008) 228.

[Hid08b] Y. Hidaka and R. D. Pisarski, *Suppression of the shear viscosity in a "semi"-quark-gluon plasma*, Phys. Rev. D78, (2008) 071501.

[Hor87] R. Horsley and W. Schoenmaker, *Quantum field theories out of thermal equilibrium. 1. General considerations*, Nucl. Phys. B280, (1987) 716.

[Hos84] A. Hosoya, M.-a. Sakagami, and M. Takao, *Nonequilibrium thermodynamics in field theory: Transport coefficients*, Ann. Phys. 154, (1984) 229.

[Hua87] K. Huang, *Statistical mechanics*, Wiley, 1987.

[Hue08] K. Huebner, F. Karsch, and C. Pica, *Correlation functions of the energy-momentum tensor in SU(2) gauge theory at finite temperature*, Phys. Rev. D78, (2008) 094501.

[Hun98] C. M. Hung and E. V. Shuryak, *Equation of state, radial flow and freeze-out in high energy heavy ion collisions*, Phys. Rev. C57, (1998) 1891.

[Ian04] E. Iancu and R. Venugopalan, *The color glass condensate and high energy scattering in QCD*, In "Quark-gluon plasma 3", R. C. Hwa et al. (eds.), pp. 249–363, World Scientific, 2004.

[Isr72] W. Israel, *The relativistic Boltzmann equation*, In "General relativity: papers in honour of J. L. Synge", L. O'Raifeartaigh (ed.), pp. 201–241, Clarendon Press, 1972.

[Isr79] W. Israel and J. M. Stewart, *Transient relativistic thermodynamics and kinetic theory*, Ann. Phys. 118, (1979) 341.

[Itz05] C. Itzykson and J. B. Zuber, *Quantum field theory*, Dover Publications, 2005.

[Jac99] J. D. Jackson, *Classical electrodynamics*, Wiley, 1999.

[Jeo95] S. Jeon, *Hydrodynamic transport coefficients in relativistic scalar field theory*, Phys. Rev. D52, (1995) 3591.

[Jeo96] S. Jeon and L. G. Yaffe, *From quantum field theory to hydrodynamics: Transport coefficients and effective kinetic theory*, Phys. Rev. D53, (1996) 5799.

[Jid01] D. Jido, T. Hatsuda, and T. Kunihiro, *In-medium $\pi\pi$ correlation induced by partial restoration of chiral symmetry*, Phys. Rev. D63, (2001) 011901.

[Kap86] D. B. Kaplan and A. E. Nelson, *Strange goings on in dense nucleonic matter*, Phys. Lett. B175, (1986) 57.

[Kap06] J. I. Kapusta and C. Gale, *Finite-temperature field theory: principles and applications*, Cambridge University Press, 2006, 2nd edition.

[Kar03] F. Karsch, K. Redlich, and A. Tawfik, *Hadron resonance mass spectrum and lattice QCD thermodynamics*, Eur. Phys. J. C29, (2003) 549.

[Kar08] F. Karsch, D. Kharzeev, and K. Tuchin, *Universal properties of bulk viscosity near the QCD phase transition*, Phys. Lett. B663, (2008) 217.

[Kat90] M. Kataja and P. V. Ruuskanen, *Non-zero chemical potential and the shape of the p(T) distribution of hadrons in heavy-ion collisions*, Phys. Lett. B243, (1990) 181.

[Kha08] D. Kharzeev and K. Tuchin, *Bulk viscosity of QCD matter near the critical temperature*, JHEP 09, (2008) 093.

[Kob90] R. Kobes, *A correspondence between imaginary time and real time finite temperature field theory*, Phys. Rev. D42, (1990) 562.

[Kol03] P. F. Kolb and R. Rapp, *Transverse flow and hadro-chemistry in Au+Au collisions at $\sqrt{s_{NN}}$=200 GeV*, Phys. Rev. C67, (2003) 044903.

[Kov05] P. Kovtun, D. T. Son, and A. O. Starinets, *Viscosity in strongly interacting quantum field theories from black hole physics*, Phys. Rev. Lett. 94, (2005) 111601.

[Kra87] K. S. Krane and D. Halliday, *Introductory nuclear physics*, Wiley, 1987.

[Kra04] U. Kraemmer and A. Rebhan, *Advances in perturbative thermal field theory*, Rept. Prog. Phys. 67, (2004) 351.

[Lan80] L. D. Landau, E. M. Lifshitz, and L. P. Pitaevskii, *Statistical physics*, Pergamon Press, 1980.

[Lan87] N. P. Landsman and C. G. van Weert, *Real and imaginary time field theory at finite temperature and density*, Phys. Rept. 145, (1987) 141.

[LB96] M. Le Bellac, *Thermal field theory*, Cambridge University Press, 1996.

[LB04] M. Le Bellac, F. Mortessagne, and G. G. Batrouni, *Equilibrium and non-equilibrium statistical thermodynamics*, Cambridge University Press, 2004.

[Led00] R. Lednicky et al., *Multiboson effects in multiparticle production*, Phys. Rev. C61, (2000) 034901.

[Let08] J. Letessier and J. Rafelski, *Hadron production and phase changes in relativistic heavy ion collisions*, Eur. Phys. J. A35, (2008) 221.

[Leu88] H. Leutwyler, *QCD: Low temperature expansion and finite size effects*, Nucl. Phys. Proc. Suppl. 4, (1988) 248.

[Leu92] H. Leutwyler, *Restoration of chiral symmetry*, In "Effective field theories of the Standard Model: proceedings", U.-G. Meissner (ed.), pp. 193–224, World Scientific, 1992.

[Leu98] S. Leupold and U. Mosel, *On QCD sum rules for vector mesons in nuclear medium*, Phys. Rev. C58, (1998) 2939.

[Li08] B.-C. Li and M. Huang, *Non-conformality and non-perfectness of fluid near phase transition*, Phys. Rev. D78, (2008) 117503.

[Lib03] R. L. Liboff, *Kinetic theory: classical, quantum, and relativistic descriptions*, Springer, 2003.

[Lif81] E. M. Lifshitz and L. P. Pitaevskii, *Physical kinetics*, Pergamon Press, 1981.

[Liu07] W. Liu and R. Rapp, *Low-energy thermal photons from meson-meson bremsstrahlung*, Nucl. Phys. A796, (2007) 101.

[Loe03] M. Loewe and C. Villavicencio, *Thermal pions at finite isospin chemical potential*, Phys. Rev. D67, (2003) 074034.

[Lus86] M. Luscher, *Volume dependence of the energy spectrum in massive quantum field theories. 1. Stable particle states*, Commun. Math. Phys. 104, (1986) 177.

[Luz08] M. Luzum and P. Romatschke, *Conformal relativistic viscous hydrodynamics: Applications to RHIC results at $\sqrt{s_{NN}}$ = 200 GeV*, Phys. Rev. C78, (2008) 034915.

[Man99] A. V. Manohar, *Large N QCD*, In "Les Houches 1997, Probing the Standard Model of particle interactions, Pt. 2", F. David et al. (eds.), pp. 1091–1169, North-Holland, 1999.

[Man05] C. Manuel, A. Dobado, and F. J. Llanes-Estrada, *Shear viscosity in a CFL quark star*, JHEP 09, (2005) 076.

[Man07] C. Manuel and F. J. Llanes-Estrada, *Bulk viscosity in a cold CFL superfluid*, JCAP 0708, (2007) 001.

[Man08] M. Mannarelli and C. Manuel, *Transport theory for cold relativistic superfluids from an analogue model of gravity*, Phys. Rev. D77, (2008) 103014.

[Mat85] H. Matsumoto, Y. Nakano, and H. Umezawa, *The free energy in Thermo Field Dynamics*, Phys. Rev. D31, (1985) 1495.

[McL02] L. D. McLerran, *The color glass condensate and small x physics: 4 lectures*, Lect. Notes Phys. 583, (2002) 291.

[Meg09] E. Megias, E. R. Arriola, and L. L. Salcedo, *Trace anomaly, thermal power corrections and dimension two condensates in the deconfined phase*, `arXiv:0903.1060[hep-ph]`.

[Mei02] U.-G. Meissner, J. A. Oller, and A. Wirzba, *In-medium Chiral Perturbation Theory beyond the mean-field approximation*, Annals Phys. 297, (2002) 27.

[Mes02] J. G. Messchendorp et al., *In-medium modifications of the $\pi\pi$ interaction in photon-induced reactions*, Phys. Rev. Lett. 89, (2002) 222302.

[Mey08a] H. B. Meyer, *A calculation of the bulk viscosity in SU(3) gluodynamics*, Phys. Rev. Lett. 100, (2008) 162001.

[Mey08b] H. B. Meyer, *Computing the viscosity of the QGP on the lattice*, Prog. Theor. Phys. Suppl. 174, (2008) 220.

[Moo04] G. D. Moore, *Electromagnetic emission and energy loss in the QGP*, J. Phys. G30, (2004) S775.

[Moo08] G. D. Moore and O. Saremi, *Bulk viscosity and spectral functions in QCD*, JHEP 09, (2008) 015.

[Mor91] D. Morgan and M. R. Pennington, *$f_0(S^*)$: Molecule or quark state?*, Phys. Lett. B258, (1991) 444.

[Mor92] D. Morgan, *Pole counting and resonance classification*, Nucl. Phys. A543, (1992) 632.

[MR98] J. M. Martinez Resco and M. A. Valle Basagoiti, *The speed of cool soft pions*, Phys. Rev. D58, (1998) 097901.

[MR01] J. M. Martinez Resco and M. A. Valle Basagoiti, *Color conductivity and ladder summation in hot QCD*, Phys. Rev. D63, (2001) 056008.

[Nak05] A. Nakamura and S. Sakai, *Transport coefficients of gluon plasma*, Phys. Rev. Lett. 94, (2005) 072305.

[Nar06] M. Naruki et al., *Experimental signature of the medium modification for rho and omega mesons in 12 GeV p+A reactions*, Phys. Rev. Lett. 96, (2006) 092301.

[Nas07] R. Nasseripour et al., *Search for medium modification of the ρ meson*, Phys. Rev. Lett. 99, (2007) 262302.

[New02] R. G. Newton, *Scattering theory of waves and particles*, Dover Publications, 2002.

[Nie89] A. Niegawa, *Path integral formulation of real time quantum field theories at finite temperature*, Phys. Rev. D40, (1989) 1199.

[Nie99] J. Nieves and E. Ruiz Arriola, *Bethe-Salpeter approach for meson meson scattering in Chiral Perturbation Theory*, Phys. Lett. B455, (1999) 30.

[Nie00] J. Nieves and E. Ruiz Arriola, *Bethe-Salpeter approach for unitarized chiral perturbation theory*, Nucl. Phys. A679, (2000) 57.

[Oll97] J. A. Oller and E. Oset, *Chiral symmetry amplitudes in the S-wave isoscalar and isovector channels and the σ, $f_0(980)$, $a_0(980)$ scalar mesons*, Nucl. Phys. A620, (1997) 438.

[Oll98] J. A. Oller, E. Oset, and J. R. Pelaez, *Non-perturbative approach to effective chiral lagrangians and meson interactions*, Phys. Rev. Lett. 80, (1998) 3452.

[Oll99a] J. A. Oller and E. Oset, *N/D description of two meson amplitudes and chiral symmetry*, Phys. Rev. D60, (1999) 074023.

[Oll99b] J. A. Oller, E. Oset, and J. R. Pelaez, *Meson-meson interaction in a non-perturbative chiral approach*, Phys. Rev. D59, (1999) 074001.

[Oll01] J. A. Oller and U.-G. Meissner, *Chiral dynamics in the presence of bound states: Kaon-nucleon interactions revisited*, Phys. Lett. B500, (2001) 263.

[Ose82] E. Oset, H. Toki, and W. Weise, *Pionic modes of excitation in nuclei*, Phys. Rept. 83, (1982) 281.

[Pae06] K. Paech and S. Pratt, *Origins of bulk viscosity at RHIC*, Phys. Rev. C74, (2006) 014901.

[Paj05] C. Pajares, *String and parton percolation*, Eur. Phys. J. C43, (2005) 9.

[Paj07] C. Pajares, *Deconfinement*, AIP Conf. Proc. 892, (2007) 134.

[Pat02] A. Patkos, Z. Szep, and P. Szepfalusy, *Second sheet sigma pole and the threshold enhancement of the spectral function in the scalar-isoscalar meson sector*, Phys. Rev. D66, (2002) 116004.

[Pat03] A. Patkos, Z. Szep, and P. Szepfalusy, *Universal threshold enhancement*, Phys. Rev. D68, (2003) 047701.

[Pei02] T. Peitzmann and M. H. Thoma, *Direct photons from relativistic heavy-ion collisions*, Phys. Rept. 364, (2002) 175.

[Pel04] J. R. Pelaez, *On the nature of light scalar mesons from their large N_c behavior*, Phys. Rev. Lett. 92, (2004) 102001.

[Pel06] J. R. Pelaez and G. Rios, *Nature of the $f_0(600)$ from its N_c dependence at two loops in unitarized Chiral Perturbation Theory*, Phys. Rev. Lett. 97, (2006) 242002.

[Pes95] M. E. Peskin and D. V. Schroeder, *An introduction to quantum field theory*, Addison-Wesley Pub. Co., 1995.

[Pet98] W. Peters, M. Post, H. Lenske, S. Leupold, and U. Mosel, *The spectral function of the rho meson in nuclear matter*, Nucl. Phys. A632, (1998) 109.

[Pis95] R. D. Pisarski, *Where does the rho go? Chirally symmetric vector mesons in the quark-gluon plasma*, Phys. Rev. D52, (1995) 3773.

[Pis96] R. D. Pisarski and M. Tytgat, *Propagation of cool pions*, Phys. Rev. D54, (1996) 2989.

[Pol73] H. D. Politzer, *Reliable perturbative results for strong interactions?*, Phys. Rev. Lett. 30, (1973) 1346.

[Pol78] A. M. Polyakov, *Thermal properties of gauge fields and quark liberation*, Phys. Lett. B72, (1978) 477.

[Pol87] A. M. Polyakov, *Gauge fields and strings*, Harwood Academic Publishers, 1987.

[Pra93] M. Prakash, M. Prakash, R. Venugopalan, and G. Welke, *Nonequilibrium properties of hadronic mixtures*, Phys. Rept. 227, (1993) 321.

[Ram00] A. Ramos and E. Oset, *The properties of anti-K in the nuclear medium*, Nucl. Phys. A671, (2000) 481.

[Rap97] R. Rapp, G. Chanfray, and J. Wambach, *Rho meson propagation and dilepton enhancement in hot hadronic matter*, Nucl. Phys. A617, (1997) 472.

[Rap99] R. Rapp and J. Wambach, *Low mass dileptons at the CERN-SPS: Evidence for chiral restoration?*, Eur. Phys. J. A6, (1999) 415.

[Rap00] R. Rapp and J. Wambach, *Chiral symmetry restoration and dileptons in relativistic heavy-ion collisions*, Adv. Nucl. Phys. 25, (2000) 1.

[Roc02] L. Roca, E. Oset, and M. J. Vicente Vacas, *The sigma meson in a nuclear medium through two pion photoproduction*, Phys. Lett. B541, (2002) 77.

[Rom07] P. Romatschke and U. Romatschke, *Viscosity information from relativistic nuclear collisions: How perfect is the fluid observed at RHIC?*, Phys. Rev. Lett. 99, (2007) 172301.

[Saw72] R. F. Sawyer, *Condensed π^- phase in neutron star matter*, Phys. Rev. Lett. 29, (1972) 382.

[Sch88] P. Schuck, W. Norenberg, and G. Chanfray, *Bound two pion Cooper pairs in nuclei?*, Z. Phys. A330, (1988) 119.

[Sch93] A. Schenk, *Pion propagation at finite temperature*, Phys. Rev. D47, (1993) 5138.

[Sch03] S. Scherer, *Introduction to Chiral Perturbation Theory*, Adv. Nucl. Phys. 27, (2003) 277.

[Shu99] I. A. Shushpanov, J. I. Kapusta, and P. J. Ellis, *Low-energy theorems for QCD at finite temperature and chemical potential*, Phys. Rev. C59, (1999) 2931.

[Shu09] E. Shuryak, *Physics of strongly coupled Quark-Gluon Plasma*, Prog. Part. Nucl. Phys. 62, (2009) 48.

[Son97] C. Song and V. Koch, *Chemical relaxation time of pions in hot hadronic matter*, Phys. Rev. C55, (1997) 3026.

[Son01] D. T. Son and M. A. Stephanov, *QCD at finite isospin density*, Phys. Rev. Lett. 86, (2001) 592.

[Sta00] A. Starostin et al., *Measurement of $\pi^0\pi^0$ production in the nuclear medium by π-interactions at 0.408 GeV/c*, Phys. Rev. Lett. 85, (2000) 5539.

[Ste96] J. V. Steele, H. Yamagishi, and I. Zahed, *Dilepton and photon emission rates from a hadronic gas*, Phys. Lett. B384, (1996) 255.

[Ste97] J. V. Steele, H. Yamagishi, and I. Zahed, *Dilepton and photon emission rates from a hadronic gas. II*, Phys. Rev. D56, (1997) 5605.

[Str64] R. F. Streater and A. S. Wightman, *PCT, spin and statistics, and all that*, W.A. Benjamin, 1964.

[Sus79] L. Susskind, *Lattice models of quark confinement at high temperature*, Phys. Rev. D20, (1979) 2610.

[Tay06] J. R. Taylor, *Scattering theory: The quantum theory of nonrelativistic collisions*, Dover Publications, 2006.

[Tea03] D. Teaney, *Effect of shear viscosity on spectra, elliptic flow, and Hanbury Brown-Twiss radii*, Phys. Rev. C68, (2003) 034913.

[tH74a] G. 't Hooft, *A planar diagram theory for strong interactions*, Nucl. Phys. B72, (1974) 461.

[tH74b] G. 't Hooft, *A two-dimensional model for mesons*, Nucl. Phys. B75, (1974) 461.

[Tho95] V. Thorsson and A. Wirzba, *S-wave meson-nucleon interactions and the meson mass in nuclear matter from chiral effective lagrangians*, Nucl. Phys. A589, (1995) 633.

[Tol08] L. Tolos, D. Cabrera, and A. Ramos, *Strange mesons in nuclear matter at finite temperature*, Phys. Rev. C78, (2008) 045205.

[Tor08] G. Torrieri, B. Tomasik, and I. Mishustin, *Bulk viscosity driven clusterization of quark-gluon plasma and early freeze-out in relativistic heavy-ion collisions*, Phys. Rev. C77, (2008) 034903.

[Tou97] D. Toublan, *Pion dynamics at finite temperature*, Phys. Rev. D56, (1997) 5629.

[Tru88] T. N. Truong, *Chiral Perturbation Theory and Final State Theorem*, Phys. Rev. Lett. 61, (1988) 2526.

[Tru91] T. N. Truong, *Remarks on the unitarization methods*, Phys. Rev. Lett. 67, (1991) 2260.

[Tur04] S. Turbide, R. Rapp, and C. Gale, *Hadronic production of thermal photons*, Phys. Rev. C69, (2004) 014903.

[Ueh33] E. A. Uehling and G. E. Uhlenbeck, *Transport phenomena in Einstein-Bose and Fermi-Dirac gases. I*, Phys. Rev. 43, (1933) 552.

[Urb98] M. Urban, M. Buballa, R. Rapp, and J. Wambach, *Momentum dependence of the pion cloud for rho mesons in nuclear matter*, Nucl. Phys. A641, (1998) 433.

[Urb00] M. Urban, M. Buballa, and J. Wambach, *Modifications of the rho meson from the virtual pion cloud in hot and dense matter*, Nucl. Phys. A673, (2000) 357.

[Vaf84] C. Vafa and E. Witten, *Restrictions on symmetry breaking in vector-like gauge theories*, Nucl. Phys. B234, (1984) 173.

[VB02] M. A. Valle Basagoiti, *Transport coefficients and ladder summation in hot gauge theories*, Phys. Rev. D66, (2002) 045005.

[Wan99] E. Wang and U. W. Heinz, *Nonperturbative calculation of the shear viscosity in hot ϕ^4 theory in real time*, Phys. Lett. B471, (1999) 208.

[Wei66] S. Weinberg, *Pion scattering lengths*, Phys. Rev. Lett. 17, (1966) 616.

[Wei72] S. Weinberg, *Gravitation and cosmology: principles and applications of the general theory of relativity*, Wiley, New York, 1972.

[Wei79] S. Weinberg, *Phenomenological lagrangians*, Physica A96, (1979) 327.

[Wel93] H. A. Weldon, *Generalization of the Breit-Wigner formula to nonzero temperature and density*, Annals Phys. 228, (1993) 43.

[Wit79] E. Witten, *Baryons in the 1/N expansion*, Nucl. Phys. B160, (1979) 57.

[Yag05] K. Yagi, T. Hatsuda, and Y. Miake, *Quark-gluon plasma: from big bang to little bang*, Cambridge University Press, 2005.

[Zim79] J. Zimanyi, G. I. Fai, and B. Jakobsson, *Bose-Einstein condensation of pions in energetic heavy ion collisions?*, Phys. Rev. Lett. 43, (1979) 1705.

[ZJ02] J. Zinn-Justin, *Quantum field theory and critical phenomena*, Clarendon Press, 2002, 4th edition.

[Zub74] D. N. Zubarev, *Nonequilibrium statistical thermodynamics*, Consultants Bureau, 1974.